

Numerical Characterization of Ultrasound Elastography for the Early  
Detection of Deep Tissue Injuries

by

Kenton David Hamaluik

A thesis submitted in partial fulfillment of the requirements for the degree of

Master of Science

Department of Mechanical Engineering  
University of Alberta

© Kenton Hamaluik, 2014

# Abstract

Deep tissue injuries—casually termed “bedsores”—are a type of wound often suffered as secondary injuries in persons with reduced mobility such as those with spinal cord injuries, the elderly, and people with multiple sclerosis. Deep tissue injuries form when excess pressure is applied to tissue for extended periods of time without relief and begin as the necrotic breakdown of deep tissues at the bone-muscle interface. As these wounds progress, they “tunnel” up toward the surface of the skin where they break open into late-stage pressure ulcers and are completely unnoticeable if the patient lacks sensation. There is currently no clinical tool for detecting these injuries as they form and progress and as such these wounds represent a severe burden on both patients and the health care system alike.

The goal of this work was to numerically characterize the use of three modalities of ultrasound elastography—quasi-static ultrasound elastography, acoustic radiation force impulse imaging, and shear wave speed quantification—for the early detection of deep tissue injuries. Ultrasound elastography is an imaging modality capable of imaging the mechanical stiffness of soft tissue which is a key measure of tissue health. Through combinations of k-space pseudo-spectral techniques, finite-element modelling, and image processing methods, the ability of ultrasound elastography to detect and accurately diagnose deep tissue injuries was explored. Parametric studies were undertaken to

investigate the effect of a wide range of parameters relevant to the detection sensitivity of ultrasound elastography including both device-design parameters and deep tissue injury lesion properties.

Through the numerical characterizations performed in this work, an understanding of the benefits and limitations of using ultrasound elastography to detect deep tissue injuries was achieved. Shear wave speed quantification was found to provide the most accurate measures of tissue health, however its effectiveness may be limited in very deep tissues. The understanding gained from this work may lead to investigating ultrasound elastography as a viable detection modality for early deep tissue injuries in both animal models and human subjects—these real world tests are the next step on the way to clinical adoption of ultrasound elastography for the early detection of deep tissue injuries.

# Preface

Chapter 3 of this thesis has been published as K. Hamaluik, W. Moussa, M. Ferguson-Pell, “Numerical Characterization of Quasi-Static Ultrasound Elastography,” *IEEE Transactions on Medical Imaging*. I was responsible for the study design, data collection, and manuscript composition. W. Moussa and M. Ferguson-Pell were the supervisory authors and assisted with manuscript composition.

# Dedication

This work was written for all those who have lovingly supported me throughout it's creation.

To my mother Meridel, who instilled in me the desire to always better myself and persist through the greatest of difficulties. Even when things got difficult, you gently pushed me to continue even to your own detriment.

To my late father David, who taught me about the world and inspired my combination of creativity, critical analysis, and work ethic. I wasn't able to finish before he left us, but I know he would be proud of what I accomplished in the end.

To my beautiful wife Dennie, who has stood by me and loved me without condition in the face of adversity and struggle. Without you, I would have given up long ago. You supported me above all others and this work exists as much because of you as it does because of me.

# Acknowledgements

This work reflects the endless days I have spent learning, researching, and growing throughout the past several years and would not have been possible without the gracious assistance of the considerable number of people supporting me.

My supervisor, Dr. Waled Moussa has been a constant source of inspiration and learning for me. His enthusiasm and tenacity for research became a model for this work early on in the process. I would like to thank him for providing me with this alongside all the resources and support I needed to complete this work.

I would also like to thank my co-supervisor, Dr. Martin Ferguson-Pell for believing in me since I was an undergrad and continually providing me with opportunities to advance my learning. Despite his tremendous responsibilities, he always made time for me when I needed it and has always provided valuable input and guidance.

I am incredibly grateful for the wonderful guidance, support, and supervision of the entire Project SMART Pressure Ulcer group along with the rest of the PIs and trainees of the Project SMART team. Their gentle leadership, kind friendship, and impressive ability continually inspired me to pursue my best and live up to their remarkable example.

I truly stand as a dwarf upon the shoulders of giants.

# Table of Contents

<b>1</b>	<b>Introduction</b>	<b>1</b>
1.1	Motivation . . . . .	1
1.2	Objective . . . . .	3
1.3	Methodology . . . . .	3
1.4	Thesis Outline . . . . .	4
<b>2</b>	<b>Literature Review</b>	<b>7</b>
2.1	Deep Tissue Injuries . . . . .	7
2.1.1	Aetiology and Histology . . . . .	11
2.1.2	Prevention and Treatment . . . . .	14
2.1.3	Detection . . . . .	16
2.2	Ultrasound Elastography . . . . .	18
2.2.1	Quasi-Static Ultrasound Elastography . . . . .	19
2.2.2	Acoustic Radiation Force Impulse Imaging . . . . .	20
2.2.3	Shear Wave Speed Quantification . . . . .	22
2.3	Conclusion . . . . .	23
<b>3</b>	<b>Numerical Characterization of Quasi-Static Ultrasound Elastography</b>	<b>26</b>
3.1	Introduction . . . . .	26
3.2	Method . . . . .	27
3.2.1	Formation of B-Mode Ultrasound Images . . . . .	29
3.2.2	Finite-Element Model of Tissue Deformation Under Surface Distortion . . . . .	30
3.2.3	Characterizing Quasi-Static Ultrasound Elastography . . . . .	33
3.2.4	Model Validation Using a Commercially Available Phantom . . . . .	33
3.3	Results and Discussion . . . . .	34

3.3.1	Finite Element Models of Ultrasound and Deformation	35
3.3.2	Resulting Elastograms . . . . .	37
3.3.3	Numerical Characterizations . . . . .	38
3.3.4	Physical Phantom Validation . . . . .	53
3.4	Conclusion . . . . .	58
<b>4</b>	<b>Numerical Characterization of Acoustic Radiation Force Impulse Imaging</b>	<b>61</b>
4.1	Introduction . . . . .	61
4.2	Method . . . . .	61
4.2.1	K-Space Pseudo-spectral Model of Acoustic Fields . . .	62
4.2.2	Derivation of Acoustic Radiation Force . . . . .	64
4.2.3	Temporal Finite-Element Model of Soft Tissue Deformation . . . . .	66
4.2.4	Characterizing Acoustic Radiation Force Impulse Imaging	68
4.2.5	Physical Phantom Validation . . . . .	71
4.3	Results . . . . .	72
4.3.1	K-Space Pseudospectral Models of Acoustic Radiation Force . . . . .	72
4.3.2	Temporal Finite-Element Model of Soft Tissue Deformation . . . . .	79
4.3.3	Numerical Characterization of Acoustic Radiation Force Impulse Imaging . . . . .	82
4.3.4	Physical Phantom Validation . . . . .	93
4.4	Conclusion . . . . .	94
<b>5</b>	<b>Numerical Characterization of Shear Wave Speed Quantification</b>	<b>97</b>
5.1	Introduction . . . . .	97
5.2	Method . . . . .	98
5.2.1	Shear Wave Speed . . . . .	98
5.2.2	Model Set Up . . . . .	100
5.2.3	Model Validation . . . . .	102
5.3	Results and Discussion . . . . .	103
5.3.1	Acoustic Radiation Force Impulse Simulations . . . .	103
5.3.2	Sample Shear Wave Speed Measurement . . . . .	104
5.3.3	Lesion Detection Characterization . . . . .	109

5.3.4 Physical Phantom Validation . . . . .	121
5.4 Conclusions . . . . .	123
<b>6 Conclusion</b>	<b>126</b>
6.1 Comparisons Between Methods . . . . .	128
6.2 Recommendations and Future Work . . . . .	138
<b>References</b>	<b>141</b>
<b>Appendix A Data Tables</b>	<b>165</b>
A.1 Quasi-Static Ultrasound Elastography . . . . .	165
A.2 Acoustic Radiation Force Impulse Imaging . . . . .	167
A.3 Shear Wave Speed Quantification . . . . .	171
<b>Appendix B Source Code</b>	<b>172</b>
B.1 Quasi-Static Ultrasound Elastography . . . . .	172
B.2 Acoustic Radiation Force Impulse Imaging . . . . .	178
B.3 Shear Wave Speed Quantification . . . . .	186
<b>Appendix C Experimental Protocols</b>	<b>188</b>
C.1 Quasi-Static Ultrasound Elastography . . . . .	189
C.2 Acoustic Radiation Force Impulse Imaging . . . . .	189
C.3 Shear Wave Speed Quantification . . . . .	190

# List of Tables

3.1	Quasi-static model investigated parameters . . . . .	28
3.2	CIRS phantom model mechanical properties . . . . .	34
4.1	K-Space pseudo-spectral model parameters . . . . .	64
4.2	ARFI model tissue properties . . . . .	66
4.3	ARFI Maxwell model tissue properties . . . . .	66
4.4	ARFI model investigated parameters . . . . .	71
5.1	Shear wave speed quantification model investigated parameters	101

# List of Figures

2.1	NPUAP pressure ulcer staging guidelines . . . . .	9
2.2	Schematic representation of the time course of tissue stiffness changes in a deep tissue injury . . . . .	13
3.1	Quasi-static model geometries . . . . .	29
3.2	Point spread function used for simulating b-mode ultrasound scans . . . . .	30
3.3	Quasi-static finite-element model boundary conditions . . . . .	32
3.4	Sample deformation finite-element model results for a hard spherical lesion . . . . .	36
3.5	Sample strain elastogram for a hard spherical lesion . . . . .	38
3.6	Detection ability as it is related to true lesion stiffness ratio . .	39
3.7	Error characterization for a hard spherical lesion . . . . .	41
3.8	Error characterization for: co-located, blurred boundary, clustered, and visible human lesion models . . . . .	42
3.9	Quasi-static lesion size characterization . . . . .	43
3.10	Quasi-static lesion depth characterization . . . . .	44
3.11	Quasi-static lesion altitude characterization . . . . .	45
3.12	Quasi-static ultrasound probing frequency characterization .	46
3.13	Quasi-static applied strain characterization . . . . .	47
3.14	Quasi-static lesion separation distance characterization . . . . .	48
3.15	Sample elastogram for two co-located lesions . . . . .	49
3.16	Quasi-static lesion blur radius characterization . . . . .	50
3.17	Quasi-static lesion density characterization . . . . .	51
3.18	Sample elastogram for a set of clustered lesions . . . . .	52
3.19	Quasi-static clustered lesion radius characterization . . . . .	53
3.20	Quasi-static Visible Human model lesion width characterization	54
3.21	Sample elastogram of a Visible Human model lesion . . . . .	55

3.22	Quasi-static characterization of lesion depth in a Visible Human model . . . . .	56
3.23	Experimental validation of quasi-static model results . . . . .	57
4.1	ARFI finite-element model boundary conditions . . . . .	68
4.2	ARFI model schematics . . . . .	70
4.3	Sample acoustic radiation force distribution . . . . .	73
4.4	Effect of depth and interrogation frequency on magnitude of acoustic body forces . . . . .	74
4.5	Effect of transducer aperture on the magnitude of acoustic radiation force . . . . .	75
4.6	Magnitude of developed acoustic radiation force in relation to the number of applied pulse cycles . . . . .	76
4.7	Strong dependence on source pressure of focal point force . . . . .	77
4.8	$I_{SPPA}$ safety measures of ARFI pulses . . . . .	79
4.9	ARFI-induced deformation at various depths and interrogation frequencies . . . . .	80
4.10	ARFI-induced deformation at various depths and source pressures	81
4.11	ARFI-induced deformation across various interrogation frequencies and source pressures . . . . .	82
4.12	Numerical characterization of ARFI imaging-acquired stiffness ratio with changing lesion radius . . . . .	83
4.13	ARFI imaging-acquired lesion stiffness mean squared error related to lesion radius . . . . .	84
4.14	Numerical characterization of ARFI imaging-acquired stiffness ratio with changing lesion depth . . . . .	85
4.15	ARFI imaging-acquired lesion stiffness mean squared error related to lesion depth . . . . .	86
4.16	Numerical characterization of ARFI imaging-acquired stiffness ratio with blurred lesions . . . . .	87
4.17	ARFI imaging-acquired lesion stiffness mean squared error related to lesion blurring . . . . .	87
4.18	Numerical characterization of ARFI imaging-acquired stiffness ratio with clustered lesions . . . . .	88
4.19	ARFI imaging-acquired lesion stiffness mean squared error related to small lesion cluster density . . . . .	89

4.20	Numerical characterization of ARFI imaging-acquired stiffness ratio with clustered lesions . . . . .	89
4.21	ARFI imaging-acquired lesion stiffness mean squared error related to small lesion cluster density . . . . .	90
4.22	Numerical characterization of ARFI imaging-acquired stiffness ratio with changing lesion radii in a visible human model . . . . .	91
4.23	ARFI imaging-acquired lesion stiffness mean squared error related to MRI-acquired lesion size in a Visible Human model . . . . .	92
4.24	Experimental ARFI model results . . . . .	93
4.25	Experimental validation of ARFI imaging model results . . . . .	94
5.1	Schematic of shear wave speed quantification-investigated lesions	102
5.2	Sample radiation force distribution in relation to lesion location	104
5.3	Sample shear wave motion through time . . . . .	106
5.4	Sample continuous surface plot of shear wave induced displacement . . . . .	106
5.5	Sample continuous surface plot of shear wave induced axial displacement highlighting the shear wave location in time . . . . .	107
5.6	Sample extracted shear wave position-time trace . . . . .	108
5.7	Sample trace of shear wave speed through the focal line . . . . .	108
5.8	Numerical characterization of shear wave speed measured stiffness ratio with changing lesion radius . . . . .	110
5.9	Shear-wave speed quantified squared error related to lesion radius	110
5.10	Numerical characterization of shear wave speed measured stiffness ratio with changing lesion offsets . . . . .	112
5.11	Shear-wave speed quantified mean squared error related to lesion offset . . . . .	113
5.12	Numerical characterization of shear wave speed measured stiffness ratio with changing lesion depth . . . . .	113
5.13	Shear-wave speed quantified mean squared error related to lesion depth . . . . .	114
5.14	Numerical characterization of shear wave speed measured stiffness ratio with blurred lesions . . . . .	116
5.15	Shear-wave speed quantified mean squared error related to lesion blurring . . . . .	116

5.16	Numerical characterization of shear wave speed measured stiffness ratio with clustered lesions . . . . .	117
5.17	Shear-wave speed quantified mean squared error related to small lesion cluster density . . . . .	118
5.18	Numerical characterization of shear wave speed measured stiffness ratio with clustered lesions . . . . .	119
5.19	Shear-wave speed quantified mean squared error related to small lesion cluster density . . . . .	119
5.20	Numerical characterization of shear wave speed measured stiffness ratio with changing lesion radii in a visible human model	120
5.21	Shear-wave speed quantified mean squared error related to MRI-acquired lesion size in a Visible Human model . . . . .	121
5.22	Experimental shear wave speed quantification results . . . . .	122
5.23	Experimental validation of shear wave speed quantification model results . . . . .	123
6.1	Detection sensitivities of hard-boundaried spherical lesions using the three investigated imaging modalities . . . . .	129
6.2	Percent error of measured stiffness ratios for spherical lesions across the three investigated modalities . . . . .	130
6.3	Detection sensitivities of blurred-boundary spherical lesions using the three investigated imaging modalities . . . . .	131
6.4	Percent error of measured stiffness ratios for blurred lesions across the three investigated modalities . . . . .	132
6.5	Detection sensitivities of clustered lesions using the three investigated imaging modalities . . . . .	133
6.6	Percent error of measured stiffness ratios for clustered lesions across the three investigated modalities . . . . .	134
6.7	Detection sensitivities of MRI-acquired Visible Human lesions using the three investigated imaging modalities . . . . .	135
6.8	Percent error of measured stiffness ratios for MRI-acquired Visible Human lesions across the three investigated modalities . .	136
6.9	Experimental results of the three methodologies investigated .	137
6.10	Experimental validation of the simulation results across all three methodologies investigated . . . . .	138

# Nomenclature

## Mathematical Symbols

Symbol	Meaning
$\alpha$	Acoustic absorption coefficient
$\alpha_0$	Power law prefactor
$B/A$	Acoustic nonlinearity parameter
$b_i$	Body force
$b_r$	Blurred lesion blur radius
$b_\rho$	Clustered lesion density
$C$	Elasticity tensor
$c_0$	Speed of sound
$c_T$	Shear wave speed
$d$	Lesion depth
$d_f$	Focal depth
$\delta_{sep}$	Co-located lesion separation distance
$E$	Young's modulus
$E_{lesion}$	Young's modulus of lesion
$E_{rel,meas}$	Lesion stiffness ratio
$E_{rel,nom}$	Nominal lesion stiffness ratio
$E_{tissue}$	Young's modulus of tissue
$\varepsilon$	Strain
$\varepsilon_{app}$	Transducer-applied strain
$\varepsilon_{lesion}$	Measured lesion strain
$\varepsilon_p$	Percent error
$\varepsilon_{rel,meas}$	Measured lesion strain ratio
$\varepsilon_{rel,true}$	True lesion strain ratio
$\varepsilon_{tissue}$	Measured tissue strain

Symbol	Meaning
$F$	Applied body forces
$f$	Ultrasound frequency
$f_i$	Applied load
$G_m$	Shear modulus of the $m^{\text{th}}$ branch of a Maxwell model
$\Gamma$	Boundary domain
$h$	Lesion altitude
$I$	Acoustic intensity
$I_{SPPA}$	Spatial peak pulse average intensity
$I_{SPTA}$	Spatial peak time average intensity
$K$	Bulk modulus
$k$	Wave number
$\lambda_{\text{tissue}}$	Lamé constant
$\lambda_{\text{wave}}$	Ultrasound wavelength
$MI$	Mechanical index
$MSE$	Mean squared error
$\mu_{\text{tissue}}$	Lamé constant (shear modulus)
$n_c$	Number of acoustic periods
$\nabla$	Del operator
$P_r$	Refractory pressure
$P_{\text{source}}$	Ultrasound transducer source pressure
$p$	Acoustic pressure
$r_{\text{lesion}}$	Lesion radius
$r_{bl}$	Clustered lesion radius
$\rho$	Acoustic density
$\rho_0$	Equilibrium density
$S_M$	Acoustic pressure source term
$\emptyset S$	Lesion diameter
$\emptyset L$	Visible Human lesion width
$\sigma$	Stress tensor
$\sigma_0$	Initial stress distribution
$\sigma_{\text{applied}}$	Stress applied to tissue
$t_{\text{inson}}$	Insonification time
$\tau_m$	Relaxation time of the $m^{\text{th}}$ branch of a Maxwell model
$\vec{u}$	Particle displacement
$\vec{v}$	Particle velocity

Symbol	Meaning
$u_0$	Initial displacement
$v_{max}$	Maximum tissue displacement in the axial direction
$w_{active}$	Total width of active transducer elements
$y$	Power law exponent

## Abbreviations

Abbreviation	Meaning
ARFI	Acoustic radiation force impulse
DTI	Deep tissue injury
IES	Intermittent electrical stimulation
MRI	Magnetic resonance imaging
NPUAP	National Pressure Ulcer Advisory Panel
PU	Pressure ulcer
SCI	Spinal cord injury
USE	Ultrasound elastography

# Chapter 1

## Introduction

### 1.1 Motivation

Pressure ulcers are debilitating wounds often suffered by people with limited mobility such as those undergoing lengthy surgical procedures, the elderly, and those with spinal cord injuries (SCI) [1]—up to 80 percent of people with SCI will develop a pressure ulcer in their lifetime [2]. Pressure ulcers are generally characterized by a deterioration of the skin leading to painful open wounds and while many pressure ulcers may be blamed on excess friction and moisture at the skin surface, many start as “deep tissue injuries” (DTI) which start deep below the skin surface—most often at the bone-muscle interface [3]. DTI are generally thought to be formed due to some combination of excessive deformation and ischemia resulting from sustained loading on localized tissue [4]–[6]. As of the time of writing, there is no clinically feasible method of detecting deep tissue injuries until they begin to damage superficial skin—even the National Pressure Ulcer Advisory Panel’s description of them is largely based on their appearance after the fact [7]. With our inability to detect these forming injuries and subsequently implement deep tissue injury prevention

and mitigation protocols, the injuries may eventually progress to form large subcutaneous cavities which eventually break through the surface of the skin and reveal themselves as stage III or IV pressure ulcers [8], [9].

Currently, the only tool capable of readily detecting early deep tissue injuries is  $T_2^*$ -weighted MRI [6], [10]. Unfortunately, MRI is not cost-effective for detecting the onset of DTI in a clinical population. Alternately, ultrasound is a much more cost-effective, if less sensitive imaging modality. While it has been shown that some DTI may be discerned using classical b-mode ultrasound imaging [3], [11], the sonographic features of DTI are difficult to separate from regular tissue inhomogeneities. To overcome this, ultrasound elastography may provide more reliable results by imaging the mechanical tissue stiffness rather than its acoustic properties. Ultrasound elastography is an imaging modality which utilizes sonographic techniques to determine the localized mechanical stiffness of tissue and is currently used clinically to detect breast and prostate cancer lesions [12], [13] as well as liver fibrosis [14]. It is known that as DTI form, they undergo mechanical stiffness changes throughout their progression [9], [15], [16], with tissue undergoing significant 1.8 – 3.3-fold mechanical stiffening during injury formation [5]. Initially damaged tissues show signs of increased relative stiffness due to edema-related swelling while eventually showing signs of decreased relative stiffness due to decomposition and necrosis [17]. Since ultrasound elastography is capable of imaging these stiffness changes, it follows that the formation and progression of DTI may be imaged using ultrasound elastography. In fact, ultrasound elastography has shown to be a valid technique for imaging the formation of a DTI in a rat model [18]. Before this technique can be fully understood and used in human patients, the various parameters involved in performing ultrasound elastography must be characterized with respect to detecting DTI in humans.

## **1.2 Objective**

The broad objective of this work was to numerically characterize the use of ultrasound elastography to detect and monitor formative and progressive deep tissue injuries. Although it has been shown that ultrasound elastography is capable of imaging DTI [18], the degree of suitability of this technique with regard to DTI is not yet understood. When the effects of numerous interrogation parameters on detection sensitivity and ability are known, the technology may be evaluated on its feasibility and usefulness to detect deep tissue injuries. The ultimate goal of this characterization is to be the first stage in the process of allowing ultrasound elastography to be implemented clinically for detecting DTI. It is reasoned that if early detection modalities are implemented clinically, both patients and the health care system may benefit by lowering the incidence and outright cost of treating fully-formed deep tissue injuries.

## **1.3 Methodology**

In order to investigate the use of ultrasound elastography for the detection of deep tissue injuries, the technology must first be characterized and fully understood. While traditional experimentation provides an opportunity to work with physical subjects it can be severely limiting as absolute control over all investigated parameters is relinquished. Further, subject recruitment may present an insurmountable barrier to the execution of such a study. As such, in this exploratory work, various numerical models of the technology have been utilized to investigate the controlled effect of a broad number of parameters relating to each technology. Specifically, k-space models of ultrasonic wave propagation and finite-element models of tissue deformation have been developed. These models were coupled with tissue strain estimation

algorithms to fully simulate ultrasound elastography procedures. Parametric studies on the detection sensitivity and ability of the various ultrasound elastography modalities were carried out with respect to various lesion and technological parameters. Chief parameters of interest included those related to the physical realities of deep tissue injuries such as lesion depth, size, and relative mechanical stiffness as well as parameters related to the design and development of appropriate ultrasonic transducers such as probing frequency, transducer dimensions, etc.

## 1.4 Thesis Outline

In this work, three methods of ultrasonic elastogram image formation have been investigated: quasi-static ultrasound elastography, acoustic radiation force impulse imaging, and shear wave speed quantification. While all three methods may be used to interrogate tissue stiffness, each does so in a distinctively unique way. The academic background leading to the motivation for this work and the development of the numerical models is presented in Chapter 2.

Quasi-static ultrasound elastography estimates tissue strain by tracking inhomogeneities across pre- and post- compression b-mode scans where the compression is generated by manual indentation of the transducer against the surface of the skin. Naturally, mechanically stiffer regions of tissue will strain significantly less than the relatively unstiff surrounding tissue. To investigate this technique, two-dimensional b-mode ultrasound scans of simulated pre- and post-compressed tissue were generated. A finite-element model of tissue deformation was utilized to generate the post-compression simulated scans. A published tissue strain estimation algorithm was utilized to then generate elastograms for the parametric study. The models and results pertaining to

this technique are presented in Chapter 3.

After performing experiments using quasi-static ultrasound elastography on a phantom model, it became clear that quasi-static methods present significant challenges that acoustic radiation force impulse imaging may overcome. Chief amongst these challenges is the repeatability and inter-operator reliability of the technique as quasi-static elastography is heavily reliant upon manual force generation. Acoustic radiation force impulse imaging estimates tissue strain by applying an acoustic radiation force body load to deep tissue, causing the interrogated tissue region to deform which is then tracked using conventional ultrasound beams fired at a high frame rate. The magnitude of deformation and tissue relaxation time may then be correlated to tissue stiffness. This technique presents an advantage over quasi-static elastography in that the interrogation process is entirely automated, hence more repeatable and reliable. To simulate acoustic radiation force impulse imaging, a k-space pseudo-spectral method was used to generate simulated acoustic body loads which were then combined with a finite-element model of tissue deformation to analyze the sensitivity of ARFI imaging to investigate formative DTI. The models and results for this technique are presented in Chapter 4.

Although acoustic radiaton force impulse imaging has some advantages over quasi-static elastography, it only provides qualitative measures of relative tissue stiffness which is limited utility. To provide a quantitative measure of tissue stiffness and subsequently, tissue health, shear wave speed quantification may be used. Shear wave speed quantification quantifies tissue stiffness by tracking shear waves generated by an acoustic radiation force impulse and correlating the speed of the relatively slow-moving generated shear waves to the mechanical stiffness of the tissue. To simulate shear wave speed quantification, the k-space pseudo-spectral method of simulating acoustic body loads

adopted in Chapter 4 was used in combination with a finite-element model of tissue deformation to investigate the interaction between lesions and shear wave speed. The models and results for this technique are presented in Chapter 5.

Finally, the conclusions derived from this work and their implications along with suggestions for future studies are discussed in Chapter 6. Data tables for all the characterization plots that are presented in this work are given in Appendix A, while the MATLAB<sup>®</sup> source code for performing the simulations are given in Appendix B. Lastly, experimental protocols used in the acquisition of experimental validation data are given in Appendix C.

# Chapter 2

## Literature Review

In order to understand the need for a clinical method of detecting deep tissue injuries, the full scope of the issue must be explored. To this end, the current state of the literature regarding deep tissue injuries, how they form, what factors characterize them, and how they are currently treated is explored here. In order to relate this disease to the detection modalities proposed in this work, the mechanics and history of ultrasound elastography are also explored and related back to the problem at hand. The major gaps in the current literature regarding the use of ultrasound elastography for detecting and monitoring deep tissue injuries are presented as this work attempts to partially fill those gaps and bring the technology one step closer to clinical implementation.

### 2.1 Deep Tissue Injuries

Pressure ulcers, commonly referred to as “bedsores”, are an extraordinarily large problem facing the health care system today. At least \$11 billion is spent in the United States of America alone treating approximately 500,000 injuries annually [19], [20] while only a minute fraction of that is spent toward pressure ulcer research [21]. Compared to hospital stays for all other conditions, pa-

tients with at least a secondary diagnosis of a pressure ulcer were more often discharged to a long-term care facility and more likely resulted in death [20]. These injuries place an extremely significant burden on the people who suffer from them—pressure ulcers were found to have a profound impact on people's lives including: altering their physical, social, and financial status; changing their body image; losing independence and control; and subjecting them to the grieving process [22], [23]. These debilitating wounds are often suffered by people with limited mobility such as those undergoing lengthy surgical procedures, the elderly, and those with spinal cord injuries (SCI) [1]—approximately 80 percent of people with spinal cord injuries (SCI) will develop at least one pressure ulcer during their lifetime [2] and approximately 19 percent of elderly patients in long-term care facilities will develop one [24]. Pressure ulcers exist throughout the entire health-care system and are often formed when undergoing hospitalization [25]. These injuries have a tendency to become chronic, non-healing wounds and many patients die from complications related to them [26]. Furthermore, patients who have developed at least one pressure ulcer in their life are at a significantly greater risk of developing a second one [27].

Pressure ulcers generally form over boney prominences with approximately 64% occurring over the ischial tuberosities, trochanter, or sacrum [28] and typically start at the surface of the skin and progress deep in the tissue. Deep tissue injuries—currently defined as a type of pressure ulcer—form in the same regions as pressure ulcers but generally form at the bone-muscle interface deep in the tissue [3]. In general, these injuries are characterized by some manner of tissue loss through necrosis of the tissue, though there is currently some debate on the exact nature of these wounds as well as the accuracy of the clinical descriptions attributed to them by the National Pressure Ulcer Advisory Panel (NPUAP).

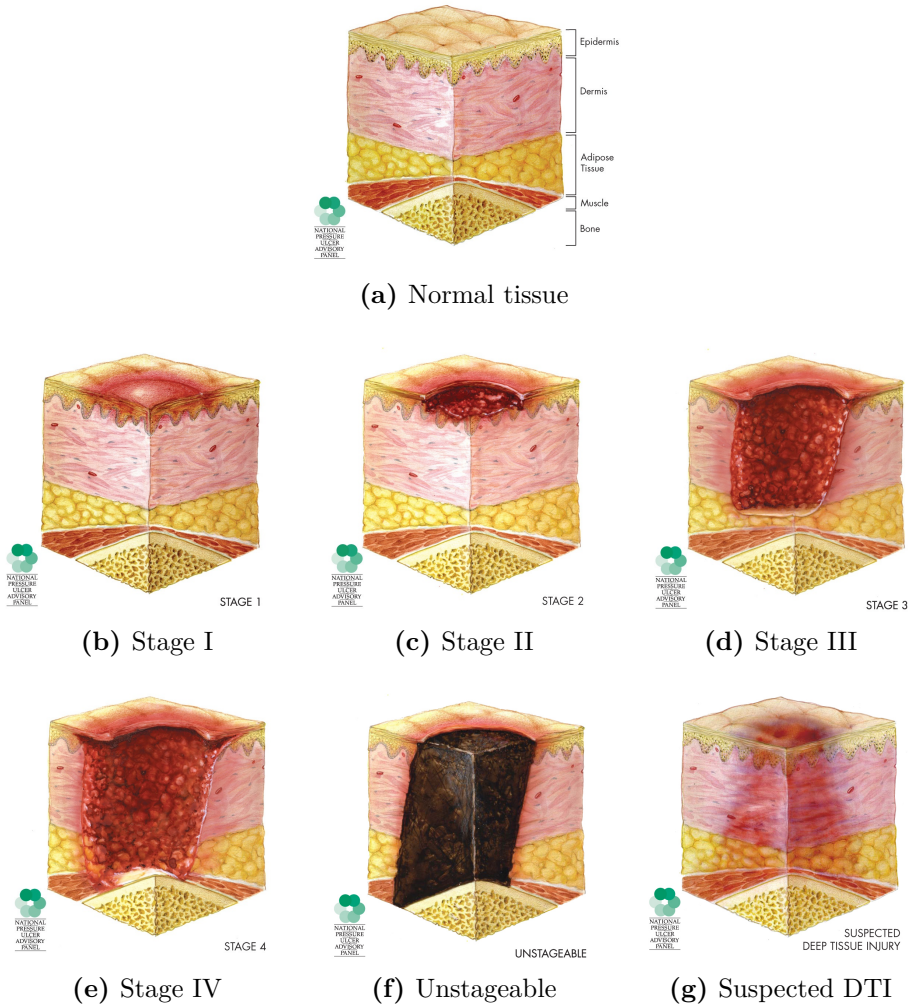


**Fig. 2.1:** The NPUAP staging guideline illustrations of the various stages / severities of pressure ulcers. © National Pressure Ulcer Advisory Panel, used with permission.

The NPUAP defines pressure ulcers as a “localized injury to the skin and / or underlying tissue usually over a bony prominence, as a result of pressure, or pressure in combination with shear and / or friction” and are generally staged according to a tiered system of increasing damage [7]. The various stages of pressure ulcer classifications are depicted in Fig. 2.1 and described as follows [7]:

### Suspected Deep Tissue Injury

Purple or maroon localized area of discoloured intact skin or blood-filled

blister due to damage of underlying soft tissue from pressure and / or shear. The area may be preceded by tissue that is painful, firm, mushy, boggy, warmer or cooler as compared to adjacent tissue.

### **Stage I**

Intact skin with non-blanchable redness of a localized area usually over a bony prominence. Darkly pigmented skin may not have visible blanching; its colour may differ from the surrounding area.

### **Stage II**

Partial thickness loss of dermis presenting as a shallow open ulcer with a red pink wound bed, without slough. May also present as an intact or open / ruptured serum-filled blister.

### **Stage III**

Full thickness tissue loss. Subcutaneous fat may be visible but bone, tendon or muscle are not exposed. Slough may be present but does not obscure the depth of tissue loss. *May* include undermining and tunnelling.

### **Stage IV**

Full thickness tissue loss with exposed bone, tendon or muscle. Slough or eschar may be present on some parts of the wound bed. Often include undermining and tunnelling.

### **Unstageable**

Full thickness tissue loss in which the base of the ulcer is covered by slough (yellow, tan, grey, green, or brown) and / or eschar (tan, brown or black) in the wound bed.

The NPUAP's definitions of pressure ulcers arise from clinical experiences

with them and are largely based on the ulcer’s appearance after they have formed and do not necessarily reflect the true aetiological factors that lead to these conditions. For example, a significant body of literature scientifically describes deep tissue injuries as being much more insidious than a “localized area of discoloured intact skin” and suggests that many Stage III and IV pressure ulcers are actually advanced deep tissue injuries rather than advanced Stage I or II ulcers [17]. This chasm between the clinically accepted and scientifically observed definitions of deep tissue injuries is likely due to the lack of any clinical detection ability [29]. What is agreed upon is that deep tissue injuries are a major problem and more needs to be done to facilitate preventing and treating them [30], [31]. One of the largest hurdles to preventing and treating DTI is the lack of any substantial early detection ability [32], [33].

### 2.1.1 Aetiology and Histology

Deep tissue injuries are thought to occur through the combinatory effects of three distinct but related mechanisms: ischemia, insufficient lymph drainage, and cell deformation. Ischemia is a condition where the blood supply to tissue has been cut off, rendering the tissue unable to function appropriately. Insufficient lymph drainage refers to how waste products may accumulate in tissue when the lymph vessels that normally carry them away become occluded. Cell deformation occurs when mechanical strains are imparted upon the tissue, causing excessive deformation in not only the extracellular matrix, but in the cells as well. Taken together, the presence of these factors has been shown to greatly increase the risk of developing a deep tissue injury [4].

For quite some time, ischemia was regarded as the chief acute risk factor for developing late-stage pressure ulcers [34]–[36]. Although studies have shown that healthy tissue is able to survive complete ischemia for approximately 4

hours before severe necrosis sets in [37], [38], deep tissue injuries are clinically found when loading times are substantially less than this [25], [39]. The model of ischemic damage alone could not account for the rate of late-stage pressure ulcers that we were witnessed.

Once it was realized that ischemia alone could not be the culprit behind deep tissue injury formation, ischemia-induced reperfusion injury became implicated in the formation of DTI [40]–[42]. An ischemia-induced reperfusion injury is caused when blood is allowed to flow back into a region of tissue that was previously ischemic. While seeming somewhat contrary to its expected effect, the restoration of circulation results in a swelling and inflammatory effect which causes extensive microvascular damage [41]. The effect of reperfusion was confirmed when comparing pure ischemic conditions in tissue to a cycle of ischemic-reperfused conditions over the same period of time, where it was found that significantly greater damage was caused by repeated loading and unloading rather than simple constant loading [42], [43]. While ischemia-reperfusion injuries provide a more complete explanation about the formation of deep tissue injuries, they still do not account for those injuries acquired under constant pressure over short time periods.

In order for cells to function in a healthy manner, the waste they produce must be constantly carried off and processed via the lymphatic system and its series of lymph vessels that perfuse tissue. If the magnitude of pressure applied to tissue reaches a threshold level, the pressure occludes the lymph vessels and lymphatic drainage ceases [44]. Once lymphatic drainage ceases, cell waste accumulates in the tissue and is thought to initiate necrosis in the cells [45]–[47].

In order to account for deep tissue injuries that form over short time periods, a model of cell deformation leading to necrosis has more recently been

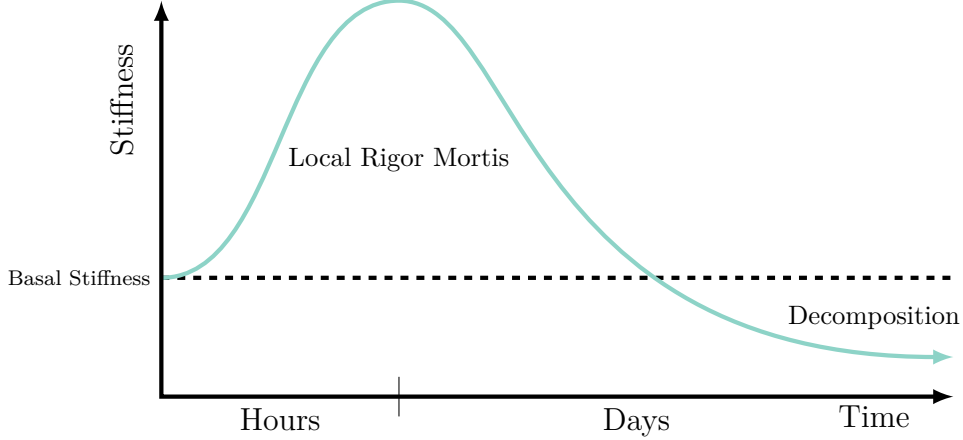


**Fig. 2.2:** Schematic representation of the time course of tissue stiffness changes in a deep tissue injury site. The estimate for the time-course for local rigor mortis was obtained from animal model studies [60] and the estimate for the time-course for tissue decomposition was obtained from the forensic literature [59]. (Adapted from Gefen 2009 [17], used with permission.)

proposed [48]–[50]. It has constantly been observed that tissue regions which eventually form deep tissue injuries exhibit signs of locally increased strains [10], [16], [51]–[53], with greater degrees of deformation correlating to greater degrees of damage. To account for these results, it has been proposed that excessively deforming strains applied to cells over extended periods of time can alter the permeability of the cell’s plasma membranes, leading to an overall reduced cell viability [54]. Further, it has been shown both in finite-element models and experimentally that the stiffness of soft tissue and the corresponding strains that are developed within them are closely related [5], [55]–[57]. Not only does the amount of deformation depend on the stiffness of tissue, but the stiffness of tissue was found to correlate to the level of deep tissue injury damage seen in the resulting histology [58] with immediate 1.6-fold to 3.3-fold stiffening of the tissue occurring immediately after injury [5], [15]. Further, the stiffness of tissue severely drops below that of healthy tissue when it begins to decompose [5], [59], leading to a relationship between injury progression and stiffness as shown in Fig. 2.2 (adapted from [17]).

There have been many models of deep tissue injury formation throughout the years, each relating to different mechanisms, though all relating to mechanical stress of the tissue, either through vessel occlusion or direct cellular strain. The truth is most likely a combination of these effects, with cell deformation dominating the damage on shorter time scales with increased applied pressure and vessel occlusion type injuries dominating on longer time scales [4]. In order to further investigate the etiology of PU and DTI, a combination of experimental and numerical studies has been suggested to provide better fundamental knowledge besides existing clinical experience [8]. There is also significant evidence in the literature that suggests that the current NPUAP definitions of PU and DTI are insufficient and not based on scientific evidence and that updating the clinical definitions to better reflect what exists in the literature is crucial to increasing the success of diagnosis and treatment of PU and DTI [17], [29].

### **2.1.2 Prevention and Treatment**

The current state of deep tissue injury treatment and prevention largely reflects the lack of a quantifiable detection modality. One of the most commonly used preventions is called “turning” whereby patients are repositioned in their beds or wheelchairs such that individual regions of tissue are intermittently relieved of pressure. Although commonly implemented in health care settings, turning has repeatedly been found to be inadequate at reducing the incidence of pressure ulcers [61], [62]. A more technological means of reducing the mechanical loads on tissue lies in support surface design [63]. Unlike turning, pressure-redistribution foam mattresses have repeatedly shown their ability to reduce the incidence of pressure ulcers in a cost-effective manner [64], [65]. Despite the effectiveness of these surfaces, the overall prevalence of pressure

ulcers has not changed significantly—suggesting that appropriate preventions are not being utilized in health-care settings [31].

An emerging technology in the realm of pressure ulcer prevention is intermittent electrical stimulation (IES). IES is the process by which electrical impulses are utilized to activate muscle fibres and contract the muscle. IES has been found to not only increase the oxygenation in deep tissue [66], but also significantly reduce the damage caused from excessive loading [67]. IES prevention paradigms are still being developed but the technology may prove to be an extremely effective preventative therapy for DTI.

While various technologies exist or are in development for preventing pressure ulcers, little is available to treat them when they occur. Generally, pressure ulcer treatment involves optimizing regional blood flow, managing underlying illnesses, and providing adequate nutrition [26]. If a pressure ulcer has become chronic, treatment switches to controlling the symptoms and preventing complications [26]. Negative pressure wound therapy is a process by which a slight vacuum is applied to the open wound for several weeks and has shown some success in reducing the severity of late-stage pressure ulcers [68]. Surgical techniques such as debriding may also be used in an attempt to remove necrotic tissue from the wound and prevent it from growing any larger [69], [70]. Skin-flap surgery is often used on chronic ulcers in an attempt to protect the wound bed [71].

When various prevention and treatment paradigms are implemented, the incidence of hospital-acquired pressure ulcers may decrease dramatically [72]–[74]. However, one of the key required areas of improvement is in the detection and monitoring of pressure ulcers [33]—without the ability to continually monitor a wound, the true effectiveness of any given therapy is ultimately indeterminate.

### 2.1.3 Detection

As previously mentioned, there is a lack of means for detecting the early onset of deep tissue injuries in a clinical setting [32], [33]. Currently, when attempting to detect and diagnose a deep tissue injury or pressure ulcer, clinicians generally rely upon a risk-factor scale for patients rather than actually detecting a lesion. Popular risk assessment tools include the Norton, Braden, and Risk Assessment Pressure Sore scales which each attempt to predict the formation of a pressure ulcer in a patient given their scores in a series of relatively subjective variables such as “general physical condition” and “mental state” [75]–[77]. Aside from these main risk-assessment scales, multiple other scales have been proposed for specific populations such as SCI patients [2] and oncology patients [78]. While these tools assist health-care practitioners to manage their limited resources with regards to patient care, at best they only provide guesses as to who will develop pressure ulcers or not. The sensitivity—the ability to correctly diagnose an existing condition—of these techniques ranges from approximately 42 % – 87 % while the specificity—the ability to correctly determine that no condition is present—ranges from 57 % – 88 % [79]. Other studies have shown that nurses have great difficulty detecting and diagnosing suspected deep tissue injuries given the current frameworks they are provided [80], while physicians may be even worse [81]. While these scales are “better than nothing” at diagnosing patients with pressure ulcers, they are far from ideal and are simply not capable of actually diagnosing this disease—for that, a quantifiable detection technology is required.

In pressure ulcer research it is common to evaluate the extent of deep tissue injury formation through the use of  $T_2^*$ -weighted MRI [6], [10], [16].  $T_2^*$ -weighted MRI is able to detect deep tissue injury by investigating tissue oxygenation as a proxy for detecting the lack of cellular activity due to necro-

sis. Although this technique is well suited for research purposes, it is simply not viable for detecting and monitoring the progression of DTI in the large population of at-risk patients. At the time of writing, MRI scans can easily cost thousands of dollars and take over an hour to complete [82]–[84]. Further, a large proportion of the at-risk population cannot undergo MRI scans for various reasons such as having medical implants or being unable to relocate from their hospital beds to a stationary MRI machine. Of the alternative diagnostic imaging modalities that currently exist, ultrasound provides the most promise due to its ability to noninvasively interrogate tissues in a mobile and cost-effective manner.

B-mode ultrasound scans involve the sonographic interrogation of a tissue's acoustic properties by transmitting sound waves on the order of multiple MHz and “listening” to the waves as they are reflected in tissue. B-mode ultrasound imaging has been used to identify hypo-echoic regions in sub-epidermal tissue related to DTI [3], [11], [85], however the results from these studies are somewhat unclear and require a degree of interpretation of the results. After combining thermographic techniques with b-mode imaging, it may be possible to increase the accuracy of early deep tissue injury detection [86]. As a more reliable alternative, ultrasound elastography—a sonographic technique for interrogating tissue strains rather than acoustic properties—has been proposed as a possible tool for clinical diagnosis of DTI [17], [87], [88]. Some exploratory studies have successfully used this technique to quantify deep tissue injury formation not only numerically, but in PVA-cryogel phantoms as well as in a rat model [18], [89]. While these studies show promise, they are only the beginning for the adoption of ultrasound elastography as a viable clinical detection modality for deep tissue injuries.

Recently, another possible avenue for DTI detection has arisen which lies

in the biochemical markers present in a patient's blood or urine. Rhabdomyolysis refers to the process when myoglobin proteins from damaged skeletal muscle enter the bloodstream due to a breakdown of muscle fibres in the body. Although this condition may be caused by numerous factors such as hyperthermia, ingestion of various drugs, alcohol abuse, toxins, autoimmune disease, or physical damage [90], [91], it may also be an indicator of formative DTI in at-risk patients who do not present with any of the aforementioned risk factors. Myoglobin proteins present in the blood get filtered in the kidneys and as such can present in the urine, turning it tea-brown [92].

With the many avenues of DTI detection currently being explored and utilized, it is most likely that a combination of all the techniques will provide the most utility. For example, upon hospital admission or with a reasonably high risk assessment score, a patient may be given a blood test which confirms the presence of a forming injury or not. Patients with forming injuries may then be scanned using ultrasound technology to locate and quantify the injury. That patient may then receive more targeted care, of which the effectiveness may be continually monitored using both blood and ultrasound tests. It is expected that the targeted care that this approach would provide would increase patient health and well-being while at the same time decreasing the overall load on the health-care system.

## 2.2 Ultrasound Elastography

Ultrasound elastography is a relatively new imaging modality which is capable of imaging the stiffness of soft tissue using ultrasound waves [93] and has its roots in the millennia-old clinical practise of manually palpating tissues to detect localized changes in the mechanical properties of the tissue [94]. In

general, the principle of ultrasound elastography is to visualize the deformation of soft tissue in response to an externally applied force [95]. This is in contrast to traditional ultrasound images which are created by interrogating tissue with high-frequency acoustic waves and “listening” to their echoes as they reflect off of tissue boundaries and small tissue irregularities (scattering centres) [96]. The externally applied force in ultrasound elastography may come from manual indentation of the ultrasound probe, a secondary external vibrator, or as an acoustic radiation force impulse (ARFI) generated by the ultrasound transducer itself [93]. Ultrasound elastography is a proven technology when it comes to detecting very stiff lesions against relatively unstiff backgrounds—it has successfully been used to detect breast and prostate cancer lesions [12], [13], liver fibrosis [14], [97], and atherosclerosis [98]. There are generally three distinct methodologies or algorithms for generating soft tissue elastograms: quasi-static methods which rely upon the manual indentation of the transducer probe; ARFI imaging which measures the dynamic response of tissue due to ARFI excitation; and shear wave speed quantification which measures shear wave speeds developed in tissue due to ARFI excitation.

### 2.2.1 Quasi-Static Ultrasound Elastography

Quasi-static ultrasound elastography was the earliest and most simple form of ultrasound elastography [99], [100] and generally operates by cross-correlating axial scan lines of tissue in pre- and post- deformed states. The term “quasi-static” is used in this method as the deformation applied to the tissue is very slow compared to the measurement time. Quasi-static ultrasound elastography provides a qualitative measure of stiffness as the mechanical conditions involved during quasi-static interrogation cannot be fully known. Despite this, it is possible to obtain relative stiffness estimates by comparing lesionous re-

gions against background tissue with a high spatial resolution and without modification to conventional ultrasound hardware [101], [102]. While quasi-static elastography originally relied upon one-dimensional ultrasound A-lines, the technique has since advanced to two-dimensional B-mode images [103] and even three-dimensional B-mode images [89], [104].

The cross-correlation foundation of quasi-static ultrasound elastography works by tracking the displacement of scattering centres which are inherently anchored to the tissue they are embedded within [105], [106] in much the same manner as contact free strain measurements may be obtained using optic means [107]. There have been numerous different quasi-static strain estimation algorithms developed, each with various advantages and disadvantages [102]. The most common algorithm involves simple cross-correlation maximization and was among the first algorithms to be proposed [103]. One of the most promising algorithms models compressed regions of interest as both scaled and translated versions of their uncompressed counterparts [95], [108] which can overcome poor correlations in simpler algorithms due to warping of the tissue under compression. This technique has successfully been used to investigate a deep tissue injury in: a finite-element model; a tissue phantom; and a rat model [18].

### 2.2.2 Acoustic Radiation Force Impulse Imaging

Acoustic radiation force impulse imaging is a more recent alternative to quasi-static ultrasound elastography which may greatly increase the inter-operator reliability of the technique by precisely controlling the externally applied mechanical interrogation force [109], [110]. While quasi-static ultrasound elastography relies upon the ultrasound operator to manually indent the tissue, ARFI imaging generates spatially focused ultrasound waves for relatively long

periods of time (10s to 100s of  $\mu\text{s}$ ) compared to typical diagnostic procedures in order to generate an acoustic radiation force at the focal region [111]–[113]. Once the acoustic radiation force is generated within the tissue, the procedure is extremely similar to the technique used in quasi-static ultrasound elastography—the deformation in the tissue caused by the externally applied force is tracked using classical ultrasound beams at high sampling frequencies. Although the magnitude of the resulting deformation is generally less than  $20 \mu\text{m}$  [111], ultrasound beams are still able to detect deformations of less than  $2 \mu\text{m}$  [114], [115]. By comparing the level of deformation throughout the tissue to a homogeneous interrogation force, the relative stiffness of individual regions of tissue may be ascertained—relatively stiff regions of tissue will deform less than relatively unstiff regions of tissue.

Since the development of acoustic radiation force within deep tissue requires greater amounts of applied pressure for longer durations than classical ultrasound b-mode imaging, the safety of the technique becomes an important consideration. Health Canada guidelines assert that ultrasound technologies be applied to patients only when medically necessary and exposures should be kept as low as reasonably achievable in any imaging mode [116]. Health Canada also places a limit on the derated spatial-peak time-average intensity,  $I_{SPTA}$  of  $720 \text{ mW cm}^{-2}$  which is derived from FDA regulations [117]. Since  $I_{SPTA}$  is a temporal average, the compliance of this value can be easily controlled by controlling the repetition time of scans—simply disabling ultrasonic push beams for long enough that the tissue has a chance to recover from the initial burst of pressure will allow the device to operate with safety in regards to this parameter. A much more critical parameter is the derated spatial-peak pulse-average intensity,  $I_{SPPA}$ , which is not considered by Health Canada but limited to  $190 \text{ W cm}^{-2}$  by the FDA [117] for classical diagnostic imaging. This

measure is important as it relates to the peak intensity developed in the tissue during an interrogation pulse and is a limit that may need to be pushed in order to develop adequate deformation in deep tissues. Later revisions to FDA guidelines have allowed greater values of  $I_{SPPA}$  for alternate imaging modes, with values up to  $933 \text{ W cm}^{-2}$  being allowed for combined B and M-mode imaging [96].

### 2.2.3 Shear Wave Speed Quantification

Shear wave speed quantification represents the most complicated method of interrogating tissue stiffness using ultrasound technology, however these added complications come with the ability to obtain quantitative measures of tissue stiffness instead of the qualitative measures presented by quasi-static elastography and ARFI imaging. Unlike the longitudinal waves that are used in classical ultrasound imaging, shear waves travel perpendicular to the direction of particle motion and travel at relatively low speeds of  $1 \text{ m s}^{-1} - 10 \text{ m s}^{-1}$ . The speed of travel of shear waves is highly dependent on the density and stiffness of tissue as per equation 2.1 where  $\mu_{tissue}$  is the shear modulus of the tissue and  $\rho$  is the density. Since density cannot be measured *in vivo*, the measurement of shear speed and an assumption of tissue density can be used to calculate the shear modulus [96].

$$c_T = \sqrt{\frac{\mu_{tissue}}{\rho}} \quad (2.1)$$

In order to generate shear waves in tissue, a focused acoustic radiation impulse force must be applied to the tissue to generate shear waves which radiate from the focal point, much like creating ripples in a pond or ringing a bell [118]. As these shear waves travel outwards from the ARFI focal point, the

deformation they create in the tissue can be tracked using classical ultrasound beams sampled at extremely high frequencies. In order to image a large region of tissue at once using generated shear waves, a series of progressively deepening acoustic radiation impulses may be applied in an axial line to generate a “mach cone” of shear waves throughout an entire region of tissue [119].

Shear wave speed quantification has been successfully used to noninvasively determine the mechanical properties of not only tissue mimicking materials [120] but numerous human soft tissues *in vivo* [121]. Further work has been done to construct various viscoelastic models of soft tissue behaviour based on shear wave speed elastography including Kelvin-Voigt, Maxwell, and Zener models [122], [123]. Even more complete models have been constructed by combining shear wave speed quantification with ultrasonic computed tomography to calculate not only the shear modulus of tissue but the bulk modulus as well [124]. Finally, shear wave speed elastography has successfully been used to investigate crush injuries in rabbits which are aetiologically similar to deep tissue injuries [125].

## 2.3 Conclusion

Pressure ulcers and deep tissue injuries are severe wounds that place a tremendous burden not only on those who suffer from them, but on the health care system as well. These injuries are generally caused by some combination of ischemia and reperfusion injury as well as excessive cell deformation. Deep tissue injuries are substantially more difficult to detect than pressure ulcers due to where they form—DTI generally form deep in tissue immediately superior to boney prominences and follow a “bottom-to-top” tunnelling pattern that is hardly detectable until it is “too late” and the wound has broken open

as a late-stage pressure ulcer. Deep tissue injury prevention generally relies upon mechanically offloading at-risk tissue areas by “turning” the patient or by utilizing special pressure-redistribution support surfaces, while deep tissue injury treatment is somewhat limited and relies upon increasing a patient’s overall health or resorting to surgical techniques. Recent research suggests that intermittent electrical stimulation may provide substantial benefits for preventing deep tissue injuries, however without a feasible means of reliably detecting them, the effectiveness of these treatments cannot be adequately gauged.

While detection of deep tissue injuries may be done in a research setting by using  $T_2^*$ -weighted MRI, this is not a cost-effective approach and is generally not used clinically. Instead, health-care practitioners rely upon risk-assessment scales which provide a somewhat subjective and qualitative measure of a patient’s chance of forming a pressure ulcer or DTI instead of actually detecting the disease. Relatively recent advances in ultrasound technology may be able to bridge this gap by imaging the relative stiffness of tissue since it is known that deep tissue injuries undergo significant stiffness changes through their lifetime. The technique of using ultrasound to image tissue stiffness is called “ultrasound elastography” and it works through the estimation of relative local tissue deformations under a commonly applied load. Ultrasound elastography generally encompasses three main techniques of interrogating tissue: manually by indenting the transducer head and tracking displacement of scattering centres before and after the deformation; utilizing an acoustic radiation force to specifically displace a region of tissue and measuring its dynamic response; and utilizing an acoustic radiation force to generate shear waves in the tissue and measuring the shear wave speeds as they travel through the tissue.

While preliminary work has shown that quasi-static ultrasound elastogra-

phy has the potential to be used for the early detection of deep tissue injuries [18], the technique is not yet fully understood in this regard. Further, the use of ARFI imaging and shear wave speed quantification have not yet been explored as a means of detecting DTI. In order to advance the science and move closer to a clinical implementation of this technology, all modes of ultrasound elastography must be characterized with regards to their use in detecting deep tissue injuries.

# **Chapter 3**

## **Numerical Characterization of Quasi-Static Ultrasound Elastography**

### **3.1 Introduction**

The goal of this study was to numerically characterize various important parameters related to detecting DTI using quasi-static ultrasound elastography (such as lesion geometry, material properties, and transducer characteristics) in order to examine the feasibility of using the technique to detect early DTI in humans. Quasi-static ultrasound elastography involves displacing the surface of the skin such that internal tissues are placed under a strain field. Ultrasound signals are used to track internal strains which then relate to the localized mechanical stiffness of the tissue—local regions that are significantly more or less stiff than surrounding tissue may be classified as either undergoing rigor mortis or necrosis and may present cause for concern.

## 3.2 Method

In order to evaluate the sensitivity of using quasi-static ultrasound elastography to detect deep tissue injuries, a numerical model of these injuries was created such that a subset of the investigated cases mimicked a physical phantom model which was used for validation. This numerical model allowed the rapid modification of numerous parameters related to DTI to examine their effect on the method’s detection sensitivity where detection sensitivity is defined as the slope of the given characterization plot. An ideal detection sensitivity would resemble a unary mapping between the measured lesion stiffness ratio and the true lesion stiffness ratio. Lesions are considered to be “detectable” when the measured strain ratio of the lesion is significantly greater than or less than 1. Lesions with measured strain ratios of 1 would appear the same as healthy tissue and would most likely not be detected in the elastogram. To fully understand the problem, 5 general model cases were studied with each case generating numerous sub-studies on the effect of various parameters relating to that case. These parameters included: lesion depth; lesion altitude (distance of the lesion above deep bone); lesion diameter; ratio of the stiffness between the lesion and the surrounding tissue; ultrasound probing frequency; strain level applied by the transducer; the separation distance between two co-located lesions; radius of a circular averaging filter applied to the lesion boundaries; the number of smaller clustered lesions per unit area—noting that the small lesions in this model may overlap each other; the radius of each individual clustered lesion; the width of the lesion in a Visible Human [126] model and the depth of the lesion in a Visible Human model. The range of values for the tested parameters are given in Table 3.1 which resulted in a total of 144 model cases that were analyzed. The geometry of the models shown in Fig. 3.1 include: a cross-section of a simple spherical lesion embedded

within a 2-dimensional rectangular zone of soft tissue; two lesions located at the same depth separated laterally by a finite dimension,  $\delta_{sep}$ ; a cross-section of a spherical lesion without hard boundaries; a cluster of small lesions which together form a larger lesion area; and a lesion with MRI-acquired geometry [67] embedded in geometry obtained from a Visible Human slice [126].

In Fig. 3.1e, the lesion is located superficial to the left ischial tuberosity in the transverse plane. The lesion geometry was obtained from an MRI scan of a real deep tissue injury induced in a porcine model [67]. The generic soft tissue in this model is modelled after muscle, with a layer of adipose tissue residing at the surface of the model.

Note that the axial direction referred to henceforth as the “axial” direction of an ultrasound transducer placed along the top (superficial) surface of the domain such that it becomes the “vertical” direction.

**Table 3.1:** Range of values of investigated parameters

Parameter	Symbol	Values	Units
Lesion depth	$d$	3.5, 6.5, 8.5, 10.0	cm
Lesion altitude	$h$	1.25, 2.50, 3.75	cm
Lesion diameter	$\phi S$	0.5, 1.0, 2.0, 2.5	cm
Lesion stiffness ratio	$E_{rel}$	0.32, 0.56, 1.80, 3.20	—
Ultrasound frequency	$f$	2, 4, 8	MHz
Transducer-applied strain	$\varepsilon_{app}$	2.5, 5.0, 10.0	%
Co-located separation distance	$\delta_{sep}$	1.25, 1.50, 1.75, 2.00	cm
Blurred lesion blur radius	$b_r$	1.0, 2.5, 5.0, 7.5	mm
Clustered lesion density	$b_\rho$	10, 20, 30, 40	$\text{cm}^{-2}$
Clustered lesion radius	$r_{bl}$	0.5, 1.0, 1.5	mm
Visible human lesion width	$\phi L$	0.5, 1.0, 2.0, 2.5	cm
Visible human lesion depth	$d$	6.25, 6.75, 7.25	cm

Simulated ultrasound images were acquired through the convolution of a point spread function with a normally distributed background map of scattering centres [127]. These images were then combined with a finite-element deformation model of the strained tissue to generate both pre- and post- com-

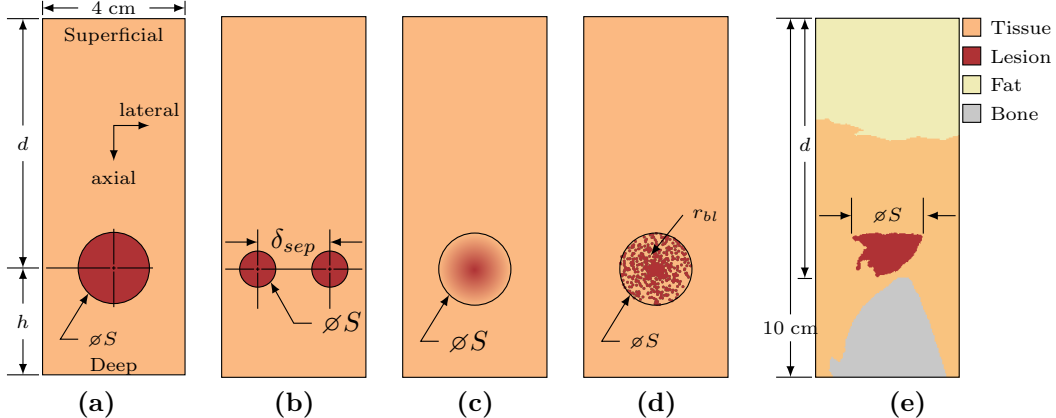


**Fig. 3.1:** Model geometry showing the investigated lesions embedded in a 4 cm wide soft tissue domain. Axial and lateral directions mimic that of a typical ultrasound transducer placed along the top boundary of the domain. The simplest case of a circular lesion embedded in a soft tissue domain located superior to hard underlying bone is shown in (a). In order to investigate the interference caused by closely-located lesions, the case shown in (b) was investigated. Because of the relatively unknown and variable geometric properties of deep tissue injury lesions, cases (c) and (d) were investigated where the lesion edges were blurred and the lesion was actually a large collection of small lesions, respectively. Finally, to investigate detection sensitivity in a realistic setting, case (e) was investigated where an MRI-acquired deep tissue injury was overlaid on a slice from the Visible Human Project such that the injury lesion was located immediately superior to an ischial tuberosity.

pression images of the lesions and surrounding tissue. These images were fed into a tissue strain estimation algorithm to determine the detection sensitivity of the technique. Finally, the technique was validated against a physical phantom model using a subset of the simulated cases.

### 3.2.1 Formation of B-Mode Ultrasound Images

Through the convolution of a point spread function and a normal random distribution of scattering centres, simulated ultrasound images were generated. The point spread function was defined axially as a cosine function operating at the ultrasound probing frequency modulated by a Gaussian distribution defined by  $\mu = 2\lambda_{wave}$  and  $\sigma = 2\lambda_{wave}$  where  $\lambda_{wave}$  is the wavelength of the ultrasonic probing waves. Laterally, the point spread function was modelled

as a Gaussian distribution defined with a mean of 0 and a standard deviation of  $0.25w_{active}$  where  $w_{active}$  is the total width of the active transducer elements during scan-line acquisition. This resulted in the point spread function given in Fig. 3.2. Resulting images were composed of 192 scan lines each sampled at 50 MHz.

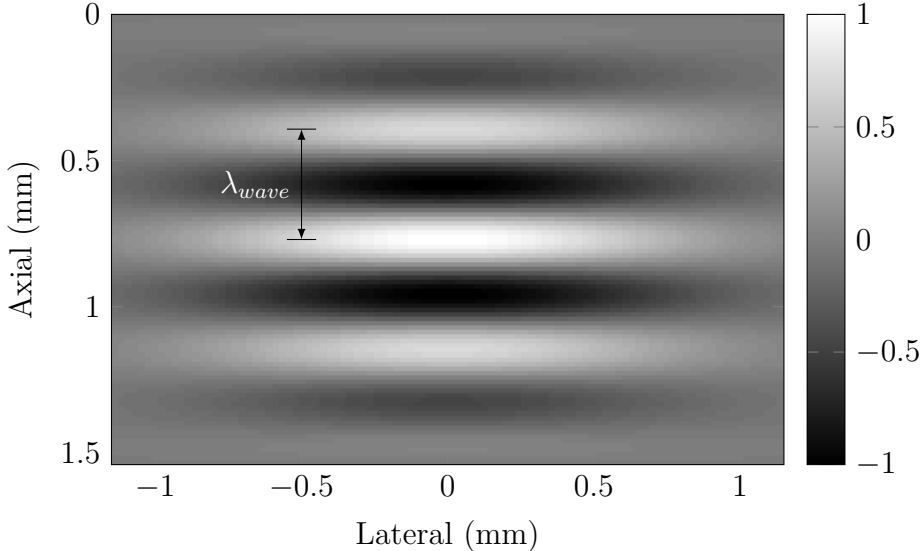


**Fig. 3.2:** Point spread function used for simulating b-mode ultrasound scans. The function is defined axially by a cosine function at the probing frequency and modulated by a Gaussian function both axially and laterally.

### 3.2.2 Finite-Element Model of Tissue Deformation Under Surface Distortion

As a response to an external load being applied to the boundary of a domain, internal structures deform. In the case of a relatively stiff deep tissue injury embedded within surrounding soft tissues, this implies that when the surface of the skin is depressed, the relatively stiff lesion will not strain to the same magnitude that the surrounding soft tissue does. In order to simulate the deformation of interrogated tissue, the displacement field for the simulated models was calculated according to equation 3.1 where  $\sigma$  is the Cauchy stress

tensor and  $F$  are the applied body forces. Simulations were performed assuming a 2-dimensional linearly elastic material deformation model under plane strain conditions.

$$-\nabla \cdot \sigma = F \quad (3.1)$$

A 3-dimensional model was also considered, however the deformations differed from the 2-dimensional simulation by less than 1% so a 2-dimensional model was deemed adequate. Soft tissue was modelled using a Young's modulus of elasticity of 25 kPa, Poisson's ratio of 0.499, and density of  $998 \text{ kg m}^{-3}$  [128]–[130]. Bone was modelled in the Visible Human model with a Young's modulus of elasticity of 18.6 GPa, Poisson's ratio of 0.15 and density of  $297 \text{ kg m}^{-3}$  [131]–[133]. The only difference in lesion mechanical properties from the surrounding soft tissue was the modulus of elasticity which varied according to the simulation parameters. The bottom of the domain was held fixed such that equation 3.2 held true.

$$\vec{u} = 0, \quad \Gamma = \Gamma_{bottom} \quad (3.2)$$

While this boundary condition represents an idealized scenario, it may be likened to that of tissue located superficial to a relatively stiff anchoring bone below since the stiffness of bone is several orders of magnitude greater than soft tissue and will not significantly deform under the loads explored in this model. This lower region is where deep tissue injuries generally form and is therefore of special importance. Compressive strains were applied to the top of the domain so as to induce strain along the top boundary as per equation 3.3. A visual representation of these boundary conditions is given in Fig. 3.3.

$$\vec{u} = (0, -u_0), \quad \Gamma = \Gamma_{top} \quad (3.3)$$

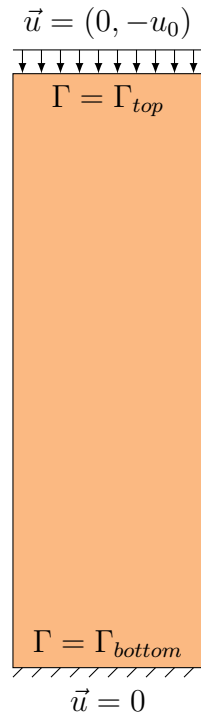


**Fig. 3.3:** Boundary conditions used in the finite-element calculations of soft tissue deformation.

From these simulations, displacement fields throughout the domain were calculated which were then used to displace tissue (including scattering centres) in the simulated ultrasound images in both the axial and lateral directions. This process resulted in pairs of pre- and post- compression simulated b-mode images of lesions of varying parameters which could then be analyzed and characterized. Sample source code for calculating these finite-element models using COMSOL Multiphysics® is given in listing B.2 in Appendix B.

### **3.2.3 Characterizing Quasi-Static Ultrasound Elastography**

Utilizing a 2-D locally regularized tissue strain estimation algorithm [108], pairs of pre- and post- compression images were used to calculate elastogram estimations for the full range of parameter values of the simulated lesions. The algorithm consists of sweeping the image domain with a series of overlapping regions of interest (ROI). ROI are compared between pre- and post-compression images, with ROI in the post- compression images being axially scaled and translated and laterally translated versions of the same ROI in the pre-compression images.

Qualitatively, the noise and computation time of the resulting elastograms were found to be minimum when using an axial ROI size of approximately 10 times the ultrasound wavelength. Axial ROI overlap was held at 99 % to produce elastograms with minimal noise, even though this introduced significant increases in computation time. Due to the extreme anisotropic nature of ultrasound signals, lateral ROI size was kept to 5 signal widths with lateral ROI overlaps of 80 %.

### **3.2.4 Model Validation Using a Commercially Available Phantom**

Utilizing a CIRS Elasticity QA Phantom model 049, a subset of the results obtained from the finite-element simulations and numerical characterizations were compared against their physical phantom equivalents. The phantom mimics acoustically homogeneous soft tissue with embedded lesions which vary in depth, size, and mechanical stiffness. Nominal mechanical properties of the phantom as given by manufacturer specifications are summarized in Table 3.2.

Pre- and post- compression b-mode ultrasound images were obtained of lesions in the phantom and the resulting strain ratios for each lesion were compared to the simulated strain ratios for the specific combination of parameters. Specifically, lesions at a depth of 3.5 cm, a diameter of 2.0 cm, and with true stiffness ratios of 0.56, 1.80, and 3.20 were examined. Surface indentation was performed manually with the transducer indenting approximately 0.5 cm (6.25 %) at the surface. The detailed experimental protocol that was followed for these validations is given in Section C.1 in Appendix C.

**Table 3.2:** CIRS phantom model mechanical properties

Property	Symbol	Value	Units
Nominal basal elastic modulus	$E_{tissue}$	25	kPa
Lesion elastic modulus	$E_{lesion}$	8, 14, 45, 80	kPa
Speed of sound	$c_0$	1540	$\text{m s}^{-1}$
Acoustic attenuation	$\alpha$	0.5	$\text{dB cm}^{-1} \text{MHz}^{-1}$
Lesion diameter	$\varnothing S$	10 and 20	mm
Lesion depth	$d$	15 and 35	mm

### 3.3 Results and Discussion

Following the procedure outlined in Section 3.2, finite-element models of ultrasonic b-mode image formation and tissue deformation were synthesized. The results of these models were then fed into the local strain estimation algorithm described in Section 3.2.3. The resulting numerical characterizations of the relationship between measured and true strain ratios in the simulated tissue and their dependence on the various lesion parameters given in Table 3.1 were examined. Finally, the local strain estimation algorithm was carried out on a physical phantom and compared against a subset of the simulated cases.

### 3.3.1 Finite Element Models of Ultrasound and Deformation

Sample images generated using both the acoustic and deformation finite-element models are given in Figs. 3.4c – 3.4d. In Fig. 3.4c, a sample generated b-mode ultrasound scan is given. Fig. 3.4a shows the lateral displacement field generated by the deformation finite-element model while Fig. 3.4b shows the axial displacement field. The entire top surface of the model has been displaced axially by 6.25 mm (5 %), which caused deformation of both the soft tissue and embedded lesion within. Since the lesion was modelled as being 3.2 times stiffer than the surrounding tissue, the lesion underwent less strain which consequently resulted in the lesser displacement depicted. Fig. 3.4d shows the resultant b-mode image generated by applying the displacement field given in Figs. 3.4a and 3.4b to the tissue and embedded scattering centres used to create Fig. 3.4c. What results is a locally scaled and translated version of Fig. 3.4c that corresponds to indenting the surface of the skin above a stiff lesion. The large anechoic region located at the bottom of the domain is tissue that was not modelled in the pre-compression image as it was outside of the original domain. This area represents the region of tissue that is undetectable with the strain-estimation algorithm given in Section 3.2.3 as the information contained there is only available in one of the two input images and so is considered incomplete data. Sample source code for generating the b-mode images seen in Fig. 3.4 is given in listing B.1 in Appendix B.

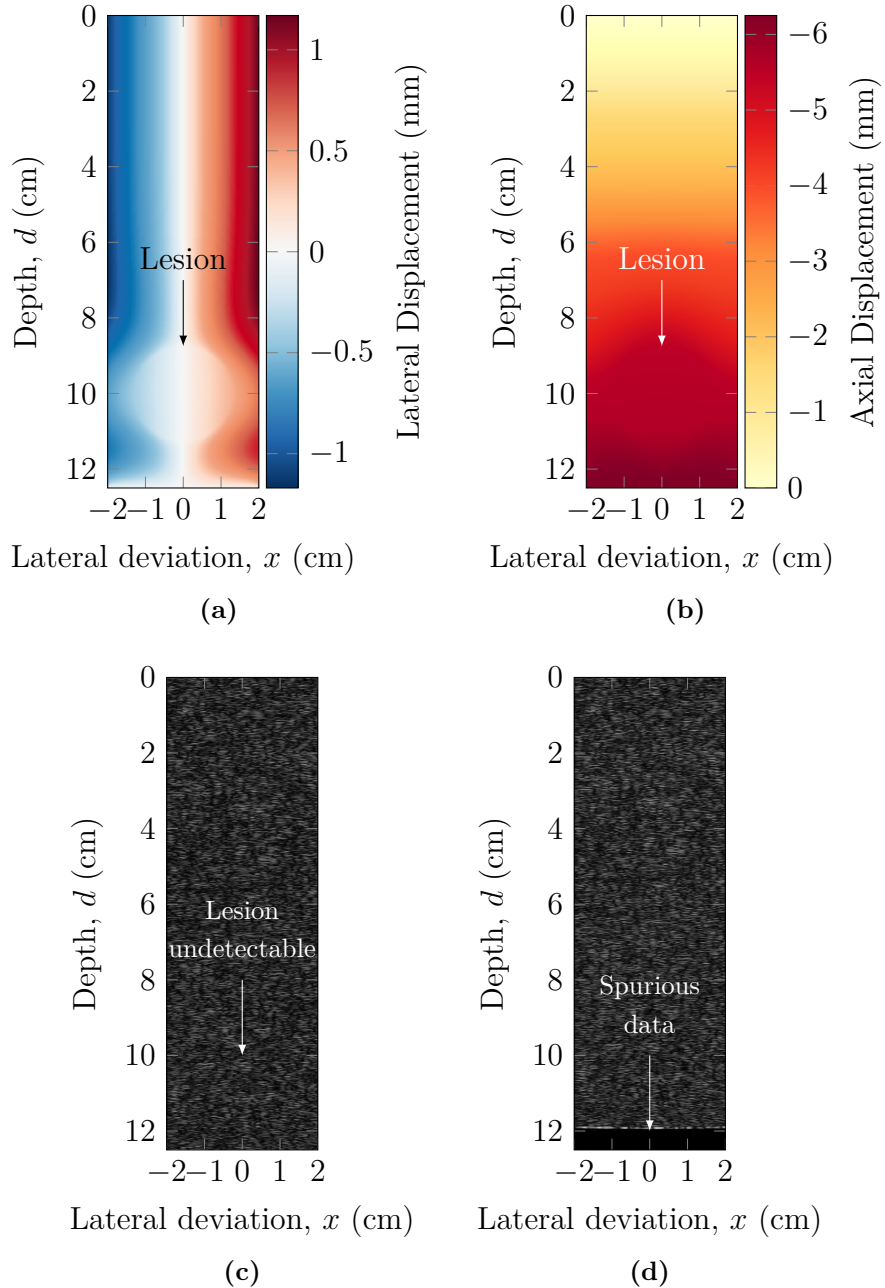


**Fig. 3.4:** Finite-element model results for the case when  $d = 10\text{ cm}$ ,  $\phi S = 2.5\text{ cm}$ ,  $\varepsilon_{rel} = 3.20$ , and  $f = 4\text{ MHz}$  showing (a) the lateral displacement field and (b) the axial displacement field induced by compressive strain applied to the top of the boundary, (c) a generated b-mode image of the pre-compressed tissue domain, and (d) a generated b-mode image of the post-compressed tissue domain. The included lesion is not visible in (c) and (d) as its acoustic properties were no different than surrounding tissues. An anechoic region is visible along the bottom of the domain in (d) which represents tissue outside of the domain visible in (c).

### 3.3.2 Resulting Elastograms

The 2-D locally regularized tissue strain estimation algorithm described in Section 3.2.3 was used in combination with the simulated resultant b-mode ultrasound images (Figs. 3.4c and 3.4d) in order to generate elastogram images which were used in the subsequent analysis. Sample source code for generating these elastograms is given in listing B.3 in Appendix B. An example elastogram resulting from the simulation presented in Fig. 3.4 is shown in Fig. 3.5. Throughout the entire domain on this sample elastogram, regions outside of the stiff lesions showed compressive strains of approximately 5 % as expected due to the compression applied to the upper boundary of the model. The entire lesion region showed relatively consistent low strain amounts of approximately 2.5 %, which is consistent with the lesion being stiffer (and so straining less) than the surrounding tissue. Of note is the increased strain pattern which appeared both axially and laterally around the lesion. While generally symmetric about the axial direction, this stress field was largely concentrated above the lesion when the lesion was deep (close to the bone). This may be explained as a stress concentration brought about by the sudden change in mechanical material properties of the tissue and may serve to fuel the conditions of excessive cell deformation and ischemia which initiated the formation of a deep tissue injury in the first place, exacerbating the wound and assisting its expansion toward the surface. Further, a largely variable strain field artifact is seen along the superior surface of the elastogram shown in Fig. 3.5. While this field does not appear to affect the remainder of the generated elastogram, it will serve to mask any extremely shallow lesions in the tissue, though given as deep tissue injuries generally form immediately superior to boney prominences, this is unlikely to be the case. It is hypothesized that this variable strain field may be due to the large deformations present along the

superior surface of the domain.

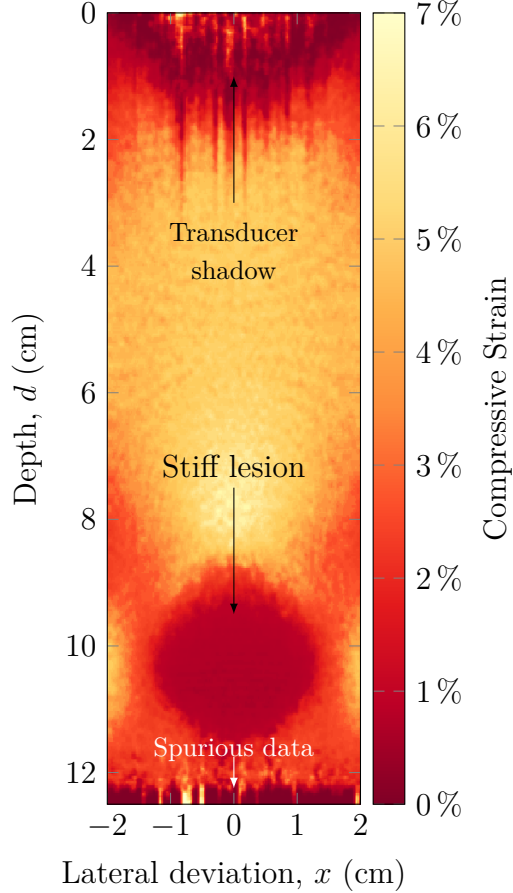


**Fig. 3.5:** Sample strain elastogram showing estimated strain values for  $d = 10$  cm,  $\phi S = 2.5$  cm,  $\varepsilon_{rel} = 3.20$ ,  $f = 4$  MHz. While undetectable on a single b-mode image, the elastogram clearly shows a low-strain (stiff) lesion located approximately 10 cm from the surface.

### 3.3.3 Numerical Characterizations

In order to determine the sensitivity of using quasi-static ultrasound elastography to detect deep tissue injuries, elastograms such as the example that was calculated in Section 3.3.2 were calculated for the full range of parameters given in Table 3.1. “Measured” strain ratios for each elastogram were obtained by comparing the mean strain within each lesion with the mean engineering

strain of the surrounding tissue such that:

$$\varepsilon_{rel,meas} = \frac{\varepsilon_{tissue}}{\varepsilon_{lesion}} \quad (3.4)$$

$\varepsilon_{tissue}$  was sampled as the mean strain in the region of tissue with the same geometry as the lesion located immediately superficial to the lesion in all cases.

In order to characterize how each parameter of interest affects the detection sensitivity of quasi-static ultrasound elastography, measured strain ratios for various lesions were calculated and compared against  $\varepsilon_{rel,true}$ .  $\varepsilon_{rel,true}$  is derived from the relative Young's modulus of elasticity of the lesion such that:

$$\varepsilon_{rel,true} = \frac{\varepsilon_{tissue}}{\varepsilon_{lesion}} = \frac{\left(\frac{\sigma_{applied}}{E_{tissue}}\right)}{\left(\frac{\sigma_{applied}}{E_{lesion}}\right)} = \frac{E_{lesion}}{E_{tissue}} \quad (3.5)$$

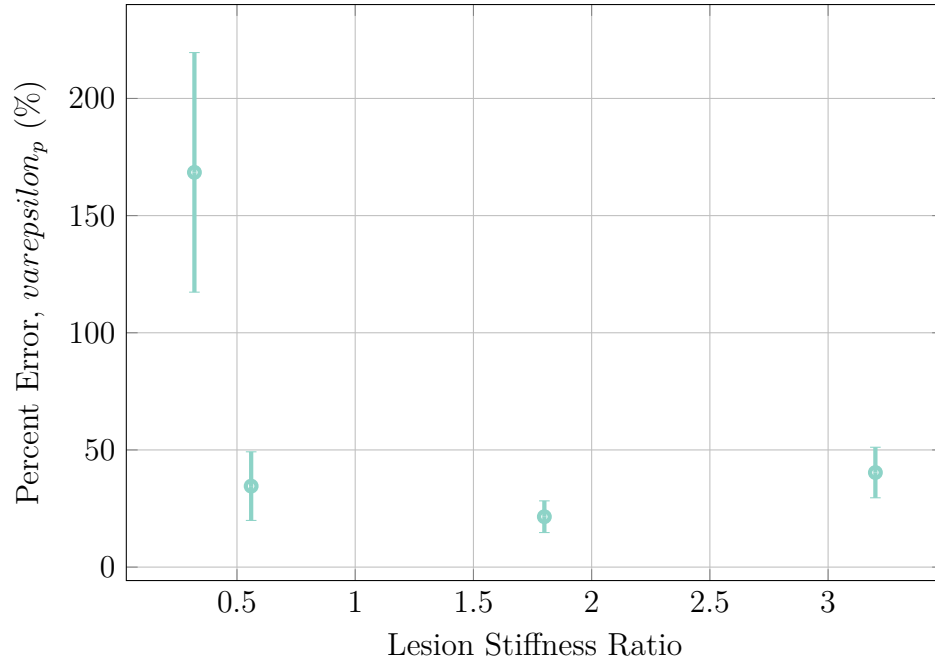


**Fig. 3.6:** Detection ability as it is related to true lesion stiffness ratio. For all but small lesion stiffness ratios (very unstiff lesions), results are linear and predictable. For small lesion stiffness ratios (0.32), the lesion becomes severely misrepresented. This is likely due to the algorithm “losing track” of scattering centres for the relatively large displacements induced in the significantly less stiff tissue.

Fig. 3.6 portrays the severe error involved with using the methods described in Section 3.2 to investigate extremely low stiffness lesions where the percent error was calculated as per equation 3.6 where  $Y_i$  are the measured values for the true / nominal values  $\hat{Y}_i$ . In nearly all investigated cases where the true lesion stiffness ratio was 0.32, the algorithms described severely misrepresented the measured strain ratio of the lesion, often portraying these extremely low stiffness regions as being more stiff than they truly were. It is hypothesized that the excessively large localized deformations in these lesions interrupted the algorithm's ability to sufficiently track the displacement of scattering centres within the tissue, lowering the magnitude of displacement within the lesion and subsequently increasing it's "measured" strain ratio.

$$\varepsilon_p = \left| \frac{Y_i - \hat{Y}_i}{\hat{Y}_i} \right| \times 100 \% \quad (3.6)$$

In order to broadly investigate the critical parameter-values of the investigated models, each parameter was normalized to its investigated range and the error resulting over these ranges is given in Figs. 3.7 and 3.8.

In Fig. 3.7, it is clear to see that the most sensitive error-inducing situations occur when either the lesion is very small or if large strains are used to deform the tissue. Similarly, it is expected that if the lesion depth were increased much further, significant errors would arise with increasing depth. Logically, this may be explained due to the decreasing magnitude of displacement with increasing depth—at a certain point, the magnitude of displacement of scattering centres will be on par with the measurement noise, and the lesion will cease to be detectable.

From Fig. 3.8 it can be seen that small lesions in the Visible Human-MRI model as well as co-located lesions with large separation distances produce greater measurement errors. Conversely, lesion depth in the Visible Human-

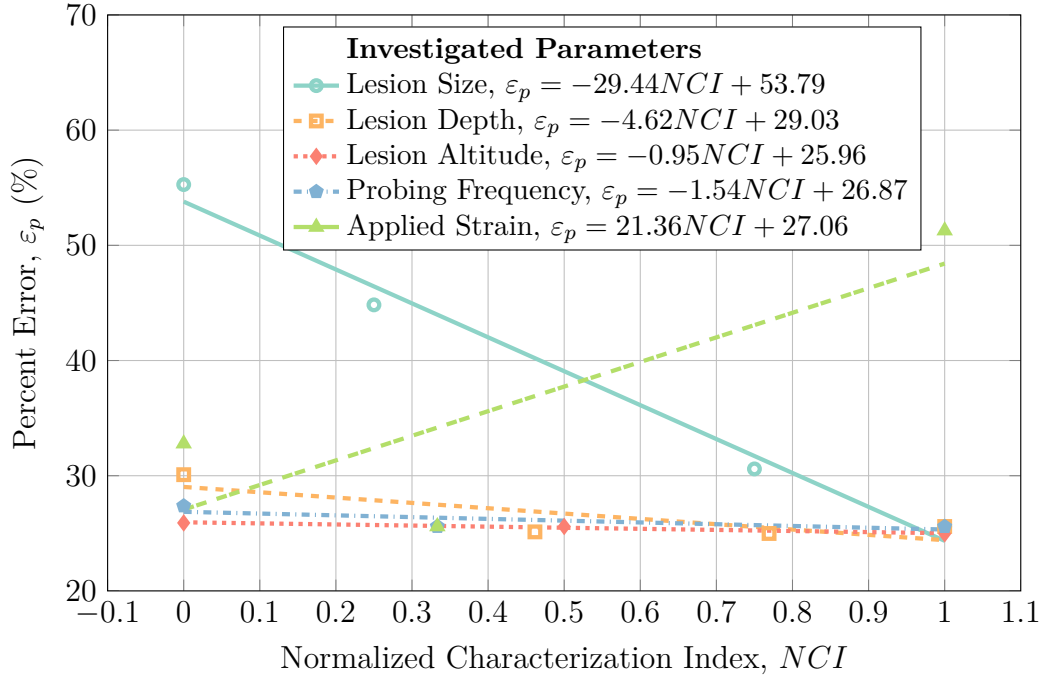


**Fig. 3.7:** Error characterization for range of studied parameters for the simple model of a spherical lesion embedded within soft tissue as seen in Fig. 3.1a. Each parameter has been normalized to the range studied so overly-sensitive regions may be readily distinguished. Lines represent linear regressions of the data points.

MRI model; lesion density and individual lesion size in the clustered lesion model; and boundary blur radius in the blurred-edges model do not seem to affect the measurement error significantly. Of note is the relatively large amount of static error present in the boundary blur radius model which is hypothesized to be due to lesser mean tissue stiffness in the investigated region than expected.

Fig. 3.9 shows the relationship between lesion size and detection sensitivity for lesions at a depth of 10 cm in a model depth of 12.5 cm interrogated at 4 MHz with 5 % applied strain. Specifically, Fig. 3.9 shows the decreasing detection sensitivity with decreasing lesion size with the best detection sensitivity being with the largest investigated lesions with a diameter of 2.5 cm. On the opposite end, the detection sensitivity of lesions at or below 0.5 cm in diameter is questionable. Although data is lacking on the true size of forma-

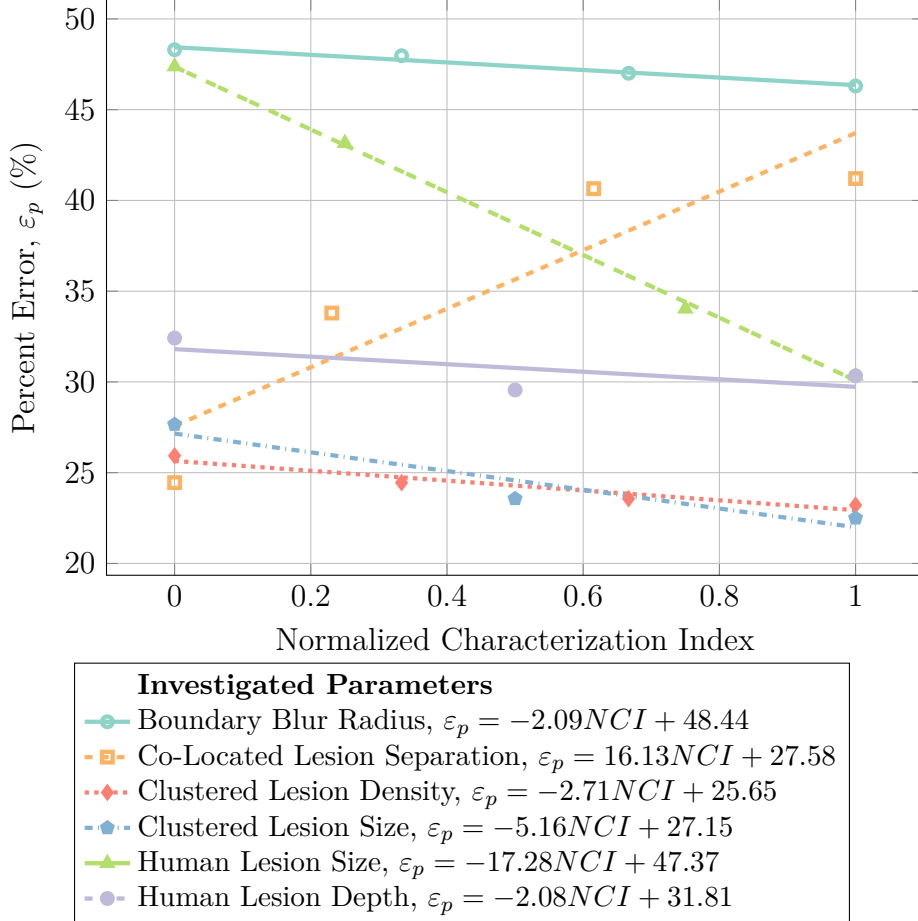


**Fig. 3.8:** Error characterization for range of studied parameters for the co-located lesions, blurred boundary lesions, clustered lesions, and visible human lesion models as seen in Figs. 3.1b – 3.1e. Each parameter has been normalized to the range studied so overly-sensitive regions may be readily distinguished. Lines represent linear regressions of the data.

tive DTI, MRI results indicate that untreated DTI are on the scale of multiple centimetres [67]. Thus, the ability to detect lesions of at least 1 cm in diameter should prove to be adequate to both detect and monitor DTI.

In order to investigate the effect of lesion depth on the detection sensitivity, measured strain ratios for circular lesions with a diameter of 2.5 cm located at various depths were interrogated with a 4 MHz probing frequency, and strained by 5 %. The results of this investigation are seen in Fig. 3.10.

In Fig. 3.10, it can be seen that there was little interplay between detection sensitivity and measured strain ratios at the various depths examined for all

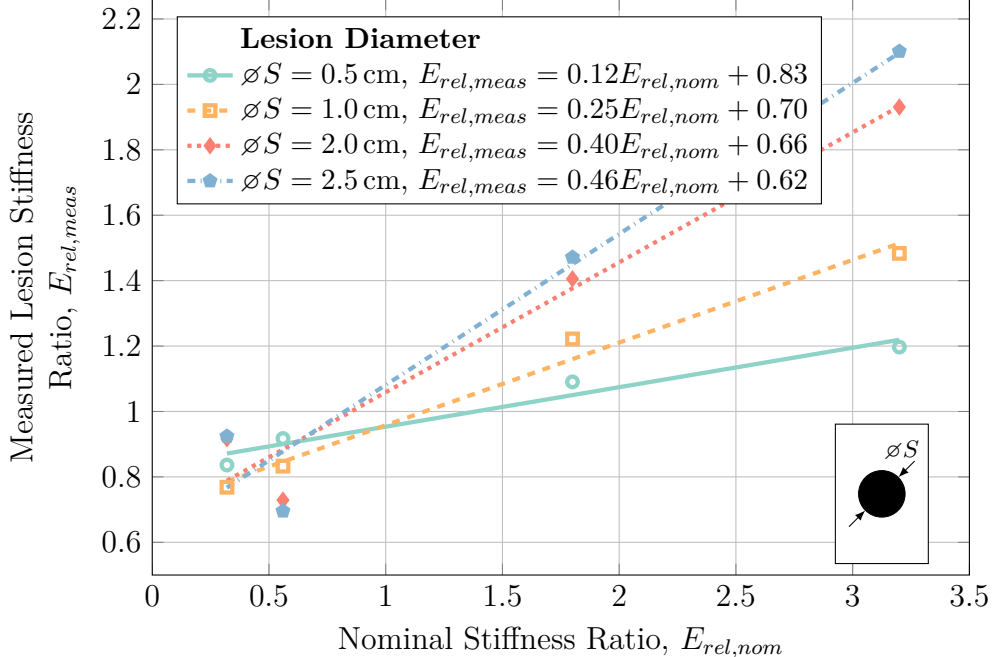


**Fig. 3.9:** Lesion size characterization at a depth of 10 cm with a 4 MHz ultrasound probing frequency showing increasing detection sensitivity of the lesion with increasing lesion size. Detection sensitivity is less than ideal for all cases, with the best case being for lesions approximately 2.5 cm in diameter. Lines represent linear regressions to the data.

but the case of very unstiff (unstiff) lesions (with a stiffness ratio of 0.32). At such low stiffness ratios, the excessive tissue deformation interrupts the tissue strain estimation algorithm's ability to adequately track the induced displacements in the lesion.

Since the strain field caused by compressive forces near an extremely rigid structure embedded within a relatively unstiff domain will be significantly heterogeneous, the effect of lesion altitude above the underlying stiff bone was examined with the hypothesis that if the lesion were too close to the hard bone, it would be masked by the strain field caused by the bone's existence. A 2.5 cm diameter lesion was interrogated with a 4 MHz probing frequency and 5 % applied strain. The results of this characterization are given in Fig. 3.11.

In Fig. 3.11, it can be seen that the lesion altitude above the underlying bone had very little effect on the detection sensitivity. Although larger strain

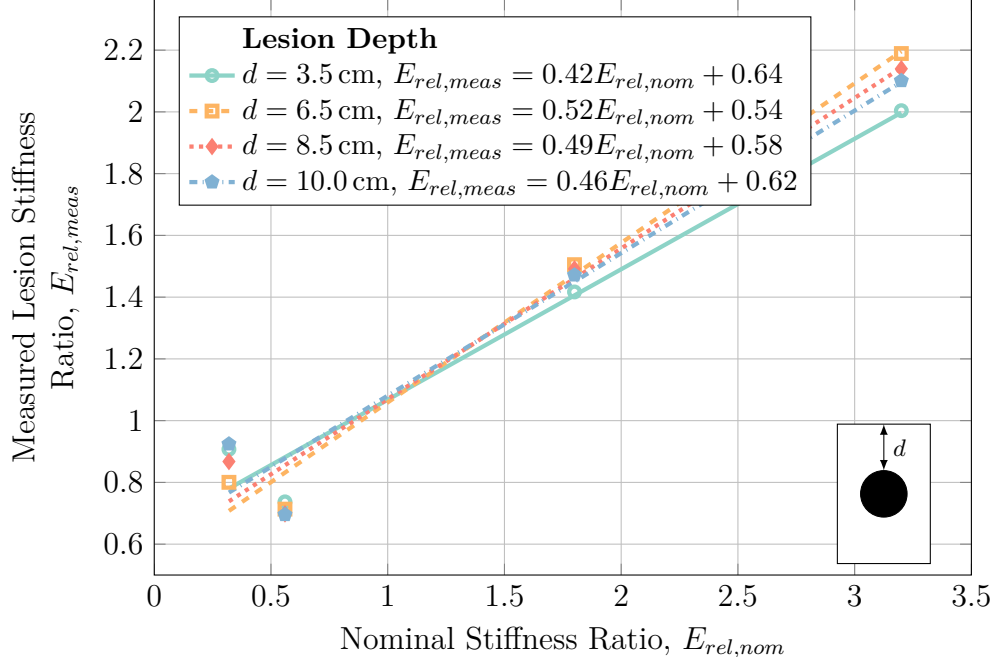


**Fig. 3.10:** Lesion depth characterization at a lesion diameter of 2.5 cm with a 4 MHz ultrasound probing frequency generally showing general independence of detection sensitivity on lesion depth in the tissue. Lines represent linear regressions of the data.

fields may be generated near the bone, it is hypothesized that the larger fields also extend larger and so affect healthy tissue to more or less the same degree as the forming lesion.

In order to characterize the effect of using alternate ultrasound probing frequencies, simulations were carried out on lesions using probing frequencies of 2 MHz, 4 MHz, and 8 MHz. The simulated lesions had a diameter of 2.5 cm, were located at a depth of 10 cm and were strained at 5 %. The results of this study are given in Fig. 3.12.

As can be seen from Fig. 3.12, there is very little effect on the detection sensitivity from the ultrasound probing frequency that was used, therefore an appropriate frequency should be chosen so as to reach the full depth of the bone-muscle interface at suspected DTI locations while retaining the best image resolution.

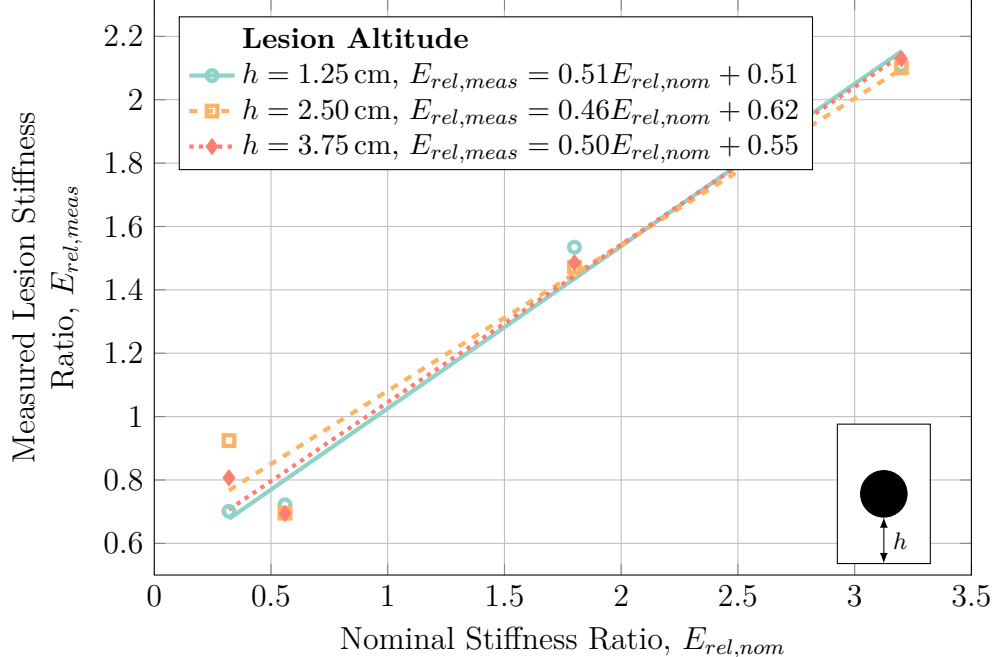


**Fig. 3.11:** Effect of lesion altitude above the underlying bone. Aside from erroneous results at very low lesion stiffness ratios, the effect is negligible. Lines represent linear regressions of the data.

As quasi-static ultrasound elastography is most likely to be performed via manual indentation where the exact magnitude of applied deformation is unknown, it is important to study the effect of applied strain magnitude on the detection sensitivity. Applied strains of 2.5 %, 5.0 %, and 10 % were investigated on a 2.5 cm diameter lesion at a depth of 10 cm using a probing frequency of 4 MHz; the results are given in Fig. 3.13.

While Fig. 3.13 shows a relatively constant detection sensitivity for compressive strains of 2.5 % and 5 %, compressive strains of 10 % generate significant measurement error for both very unstiff and very stiff lesions. Under large compressive strains, the tissue (either in the lesion as in the unstiff lesion case, or the surrounding tissue as in the stiff lesion case) deforms considerably which again interferes with the algorithm's ability to properly track the displacement of tissue. It should also be noted that applying overly large strains to an already forming deep tissue injury may cause additional unwarranted

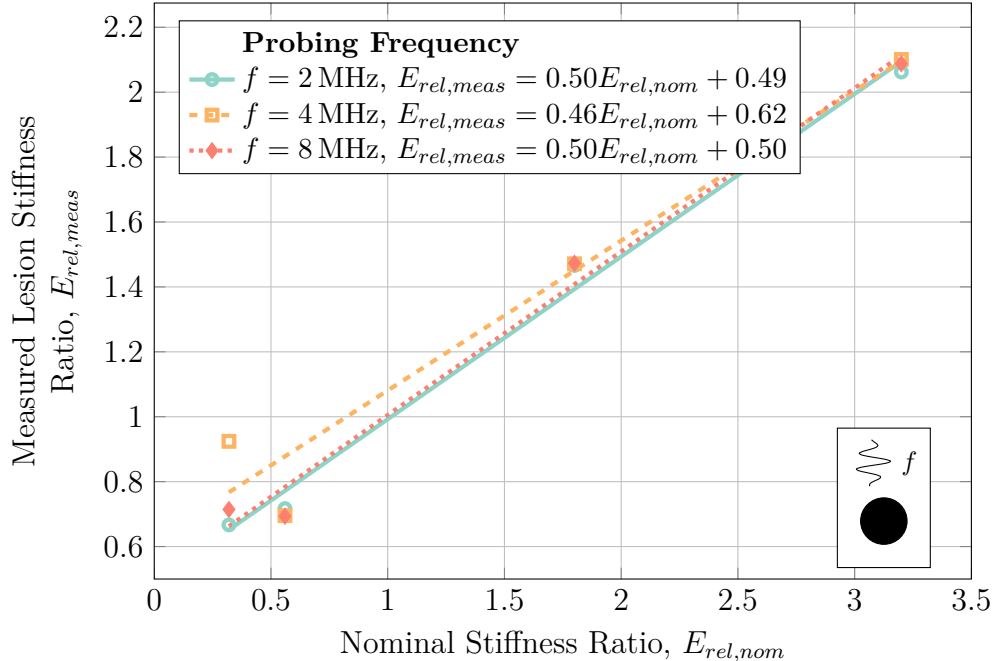


**Fig. 3.12:** Characterization of ultrasonic probing frequency on detection sensitivity. Apart from the requirement of using an ultrasonic frequency low enough to interrogate the desired tissue, probing frequency has negligible effect on the detection sensitivity. Lines represent linear regressions of the data.

damage. Thus it is imperative that applied surface indentation be kept to reasonable bounds (2.5 % – 5 %, or 0.25 cm – 0.50 cm in 10 cm deep domains), not only for safety of the tissue but also for clarity of the diagnostic test.

To study the effect that closely spaced lesions will have on the detection sensitivity as well as how discernible the lesions will be from each other, the separation distance between two 1.0 cm diameter co-located lesions at a depth of 10 cm was examined using a 4 MHz probing frequency with 5% applied strain magnitude. The results of this study are shown in 3.14.

While Fig. 3.14 shows that the separation distance between co-located lesions causes a negligible effect on the detection sensitivity, Fig. 3.15 shows regions of decreased strain above and below the centreline of the lesions. While these regions had the same basal stiffness as the bulk tissue, the decreased strain pattern may obfuscate the true results by introducing “phantom lesions”

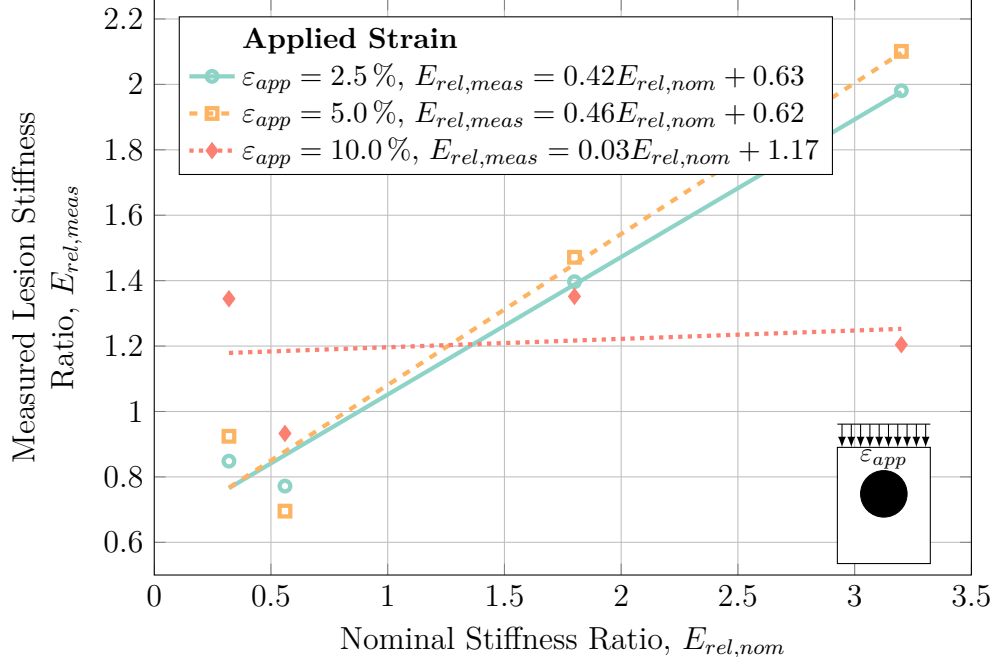


**Fig. 3.13:** Applied strain characterization plot for lesions with a diameter of 2.5 cm located at a depth of 10 cm interrogated at 4 MHz. There is little difference between 2.5 % and 5.0 % applied strain, while large-magnitude strains of 10 % generate significant error for both very unstiff and very stiff lesions. Lines represent linear regressions of the data.

which are not actually present but merely the result of the existing lesions.

While the simulations performed thus far assumed that lesions were perfect spheres with hard boundaries in order to isolate specific parameters of interest, this assumption may not always be accurate. Rather, due to the nature of injury formation, lesions may form gradual boundaries that “fade” from stiff or necrotic tissue to healthy tissue. To investigate the effect of this phenomenon on the detection sensitivity, lesions with “blurred boundaries” were investigated. Hard spherical lesions were blurred by convolving the lesion domain with a disc blurring kernel of varying radius. The results for this investigation on lesions with a diameter of 2.5 cm, at a depth of 10 cm and interrogated with a 4 MHz probing frequency with 5 % applied strain are given in Fig. 3.16.

Fig. 3.16 shows that there is relatively little dependence of the lesion detection sensitivity on the lesion blur radius. No matter the blur radius,

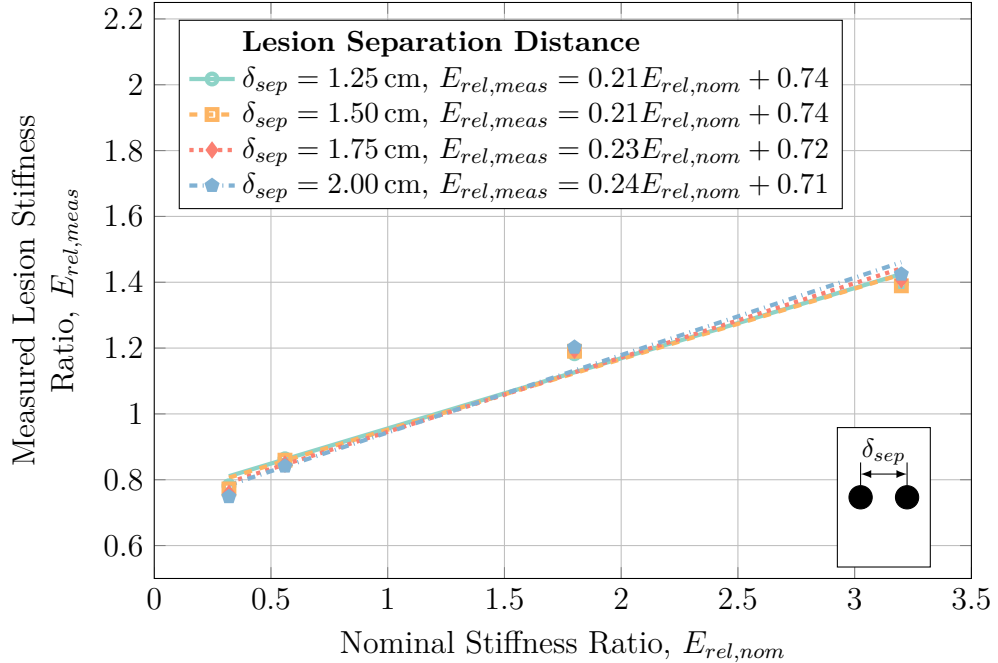


**Fig. 3.14:** Effect of lesion separation distance on two 1.0 cm diameter lesions co-located at a depth of 10 cm interrogated with a 4 MHz probe with 5 % applied strain. There is no negligible difference between separation distances on the detection sensitivity. Lines represent linear regressions of the data.

quasi-static elastography substantially overestimated the stiffness of stiff lesions and underestimated the stiffness of unstiff lesions. This technique was unable to discern differences in lesion stiffness due to blur radius for the least stiff lesions—lesions with a nominal stiffness ratio of 0.32. Further, quasi-static elastography was generally unable to detect unstiff lesions ( $E_{rel,nom} \leq 1$ ) whatsoever.

Similar to how lesions may have “blurred boundaries” rather than hard ones, so too may lesion composition not be homogeneous. In order to study the effect of heterogeneous regions of injured tissue, the detection sensitivity of a set of numerous small lesions located within close proximity to each other so as to form a large, heterogeneous area of diseased tissue was examined. Fig. 3.17 shows the results for this model for varying numbers of 2 mm diameter lesions in a 2.5 cm diameter circle located at a depth of 10 cm with a probing

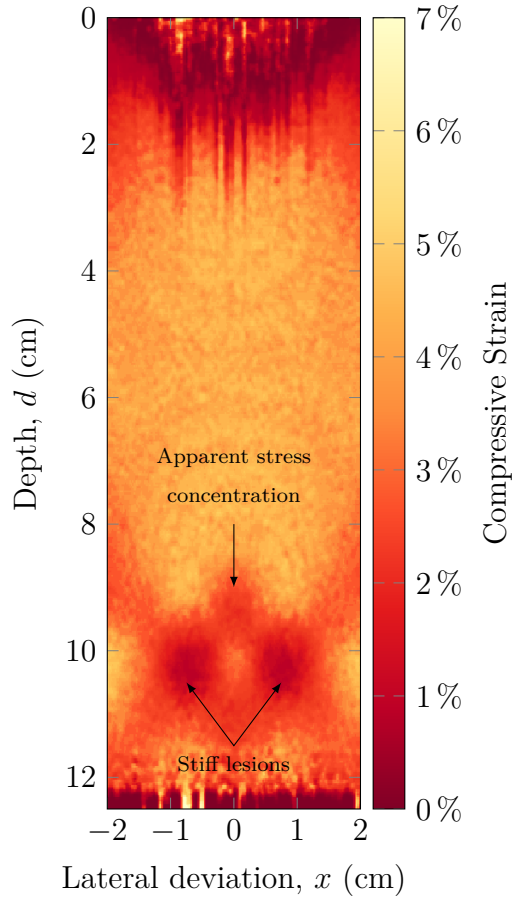


**Fig. 3.15:** Elastogram for two co-located lesions of 1.0 cm diameter at a depth of 10 cm interrogated using a 4 MHz probing frequency with 5 % applied strain. A pattern of decreased strain is present above and below the centerline between the two lesions while the lesions themselves are not affected by each other.

frequency of 4 MHz and 5 % applied strain. Fig. 3.19 further explores this model by investigating the case where there are 30 small lesions per square cm with individual lesions ranging in diameter from 0.5 mm to 1.5 mm.

The characterization plot in Fig. 3.17 for small lesion density is less linear than previous characterization plots, with lesion density having a significant effect on the detection sensitivity. Specifically, for low lesion densities, the detection sensitivity is much lower than for high lesion densities. However, this observation is warranted after examination of the elastogram produced from these results, given in Fig. 3.18, which shows how the small lesions are

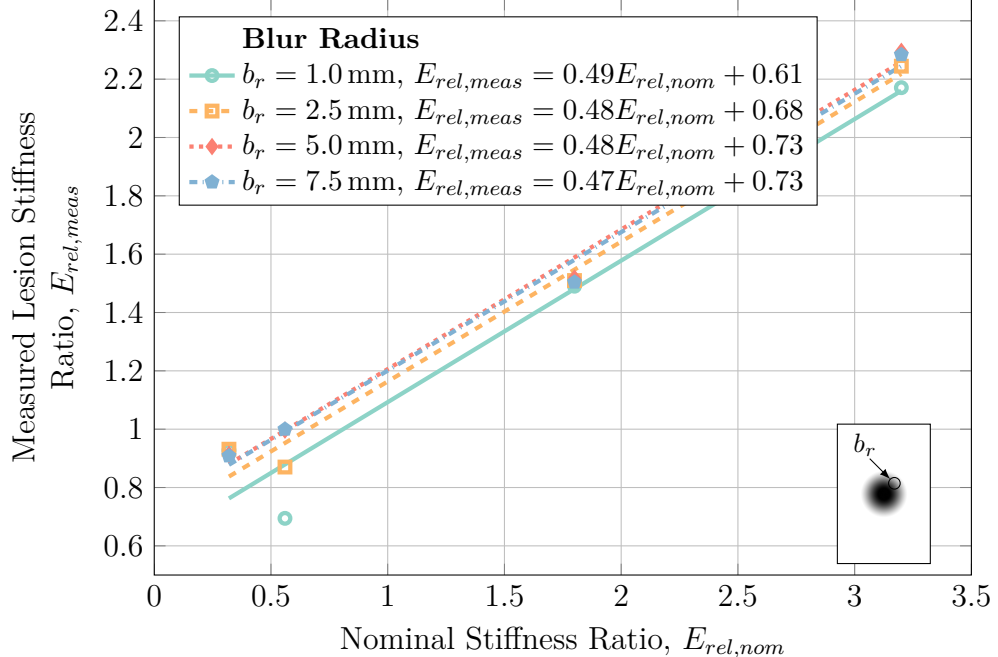


**Fig. 3.16:** Characterization of the effect of lesion blur radius on lesion detection sensitivity for a 2.5 cm diameter lesion at a depth of 10 cm using a probing frequency of 4 MHz and applied strain of 5 %. While there is negligible effect of the blur radius on stiff lesions, the strain ratio for unstiff lesions is considerably over-estimated. Lines represent linear regressions of the data.

not individually detected but rather the entire region is detected as one large lesion. Since the average stiffness ratio over this region is less than the stiffness ratio of individual lesions, it makes sense that the “measured” strain ratio will be less than expected.

Similar to the results shown in Fig. 3.17, changing the size of the individual small lesions does have an effect on the measured strain as seen in Fig. 3.19. In this case, when individual lesions are small, the total area occupied by lesions is lesser which results in a lesser average tissue stiffness over the grouped lesion region.

Note that although the elastography algorithm was able to detect the larger lesion-filled regions in these simulations, it was completely unable to discern the individual lesions comprising those regions. This is not surprising due to both the generated strain fields in the healthy tissue throughout the larger

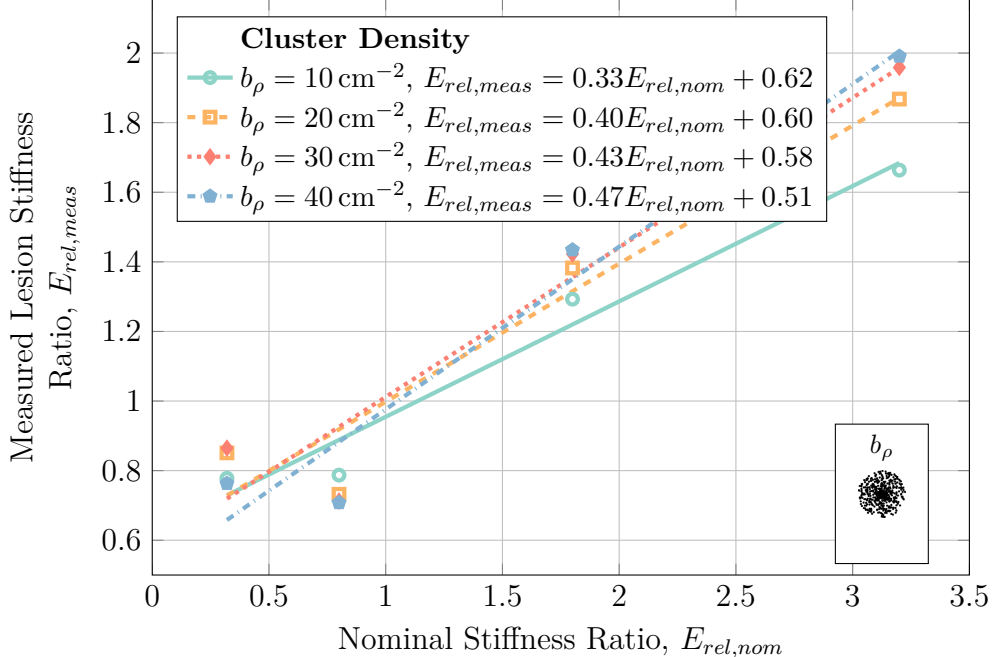


**Fig. 3.17:** Characterization of lesion density for a group of numerous smaller 2 mm diameter lesions comprising a large area with a diameter of 2.5 cm at a depth of 10 cm interrogated with a 4 MHz probing frequency and 5% applied strain. Detection sensitivity decreases with decreasing lesion density, as expected. Lines represent linear regressions of the data.

lesion area as well as the results presented in Fig. 3.9 showing poor detection sensitivity for lesions with diameters  $\leq 1$  cm while the individual lesions in this simulation had diameters of the scale of 0.5 mm – 1.5 mm.

Finally, in order to place these results within the context of a real scenario in humans, a more complicated model utilizing an MRI-acquired lesion and slides from the Visible Human Project [126] was developed. Specifically, lesion geometry was taken from a real deep tissue injury in a pig model imaged using  $T_2^*$ -weighted MRI. The human geometry was taken from a transverse plane slice across the left ischial tuberosity such that the lesion was placed immediately superficial to the boney prominence. For this model, the overall lesion width and lesion depth were examined with results shown in Figs. 3.20 and 3.22 respectively.

In Fig. 3.20, it is clear to see than small lesions (with a diameter  $\leq 1.0$  cm)

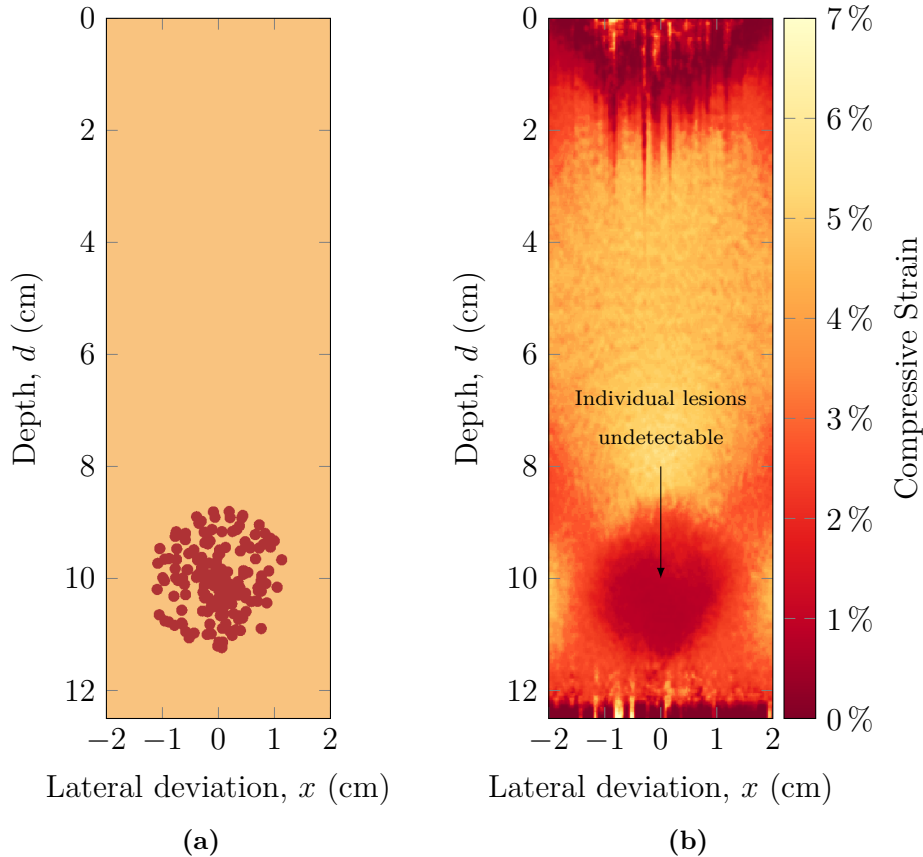


**Fig. 3.18:** Stiffness map (a) and corresponding elastogram (b) for a group of small lesions with a density of 10 lesions per  $\text{cm}^2$  grouped in a 2.5 cm diameter circle at a depth of 10 cm interrogated with a 4 MHz probing frequency and 5 % applied strain. In (a), white regions are regular tissue while black regions are the small lesions. In the elastogram, individual lesions do not stand out, rather the entire region of lesions appears as one large region of unhealthy tissue.

are almost impossible to adequately detect (although larger lesions will be adequately detectable). It is hypothesized that this phenomenon is due to the excessive strain apparent above the bony prominence that is seen in the resultant elastogram given in Fig. 3.21 such that the lesion is “washed out” by the strain field developed by the relatively stiff bone nearby.

In Fig. 3.22, there is little to no dependence of the detection sensitivity on the lesion depth in the Visible Human-MRI model with all depth curves displaying the same profile. However, deeper lesions (lesions closer to the

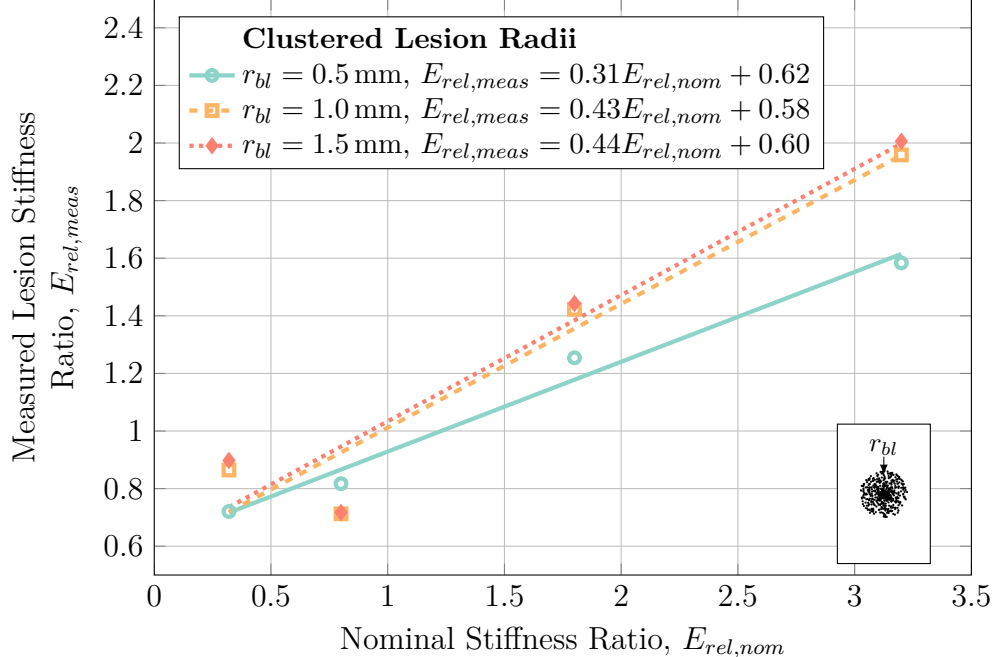


**Fig. 3.19:** Characterization of lesion radius for a group of numerous smaller lesions with a density of 30 lesions per  $\text{cm}^2$  comprising a large area with a diameter of 2.5 cm at a depth of 10 cm interrogated with a 4 MHz probing frequency and 5% applied strain. Detection sensitivity decreases with decreasing individual lesion size, as expected. Lines represent linear regressions of the data.

bony prominence) have stiffnesses that are over-estimated with respect to their superficial counterparts. This is hypothesized to be due to the increased strain field present in all of the soft tissue located immediately superior to the bony prominence, but should not pose a serious problem for imaging lesions of this nature.

Numerical values for the characterization plots presented here are given in Section A.1 of Appendix A.

### 3.3.4 Physical Phantom Validation

In order to ensure that the models presented here represented physical realities, a small subset of the cases studied were modelled in a physical phantom, specifically for three lesions with stiffness ratios of 0.56, 1.80, and 3.20 with

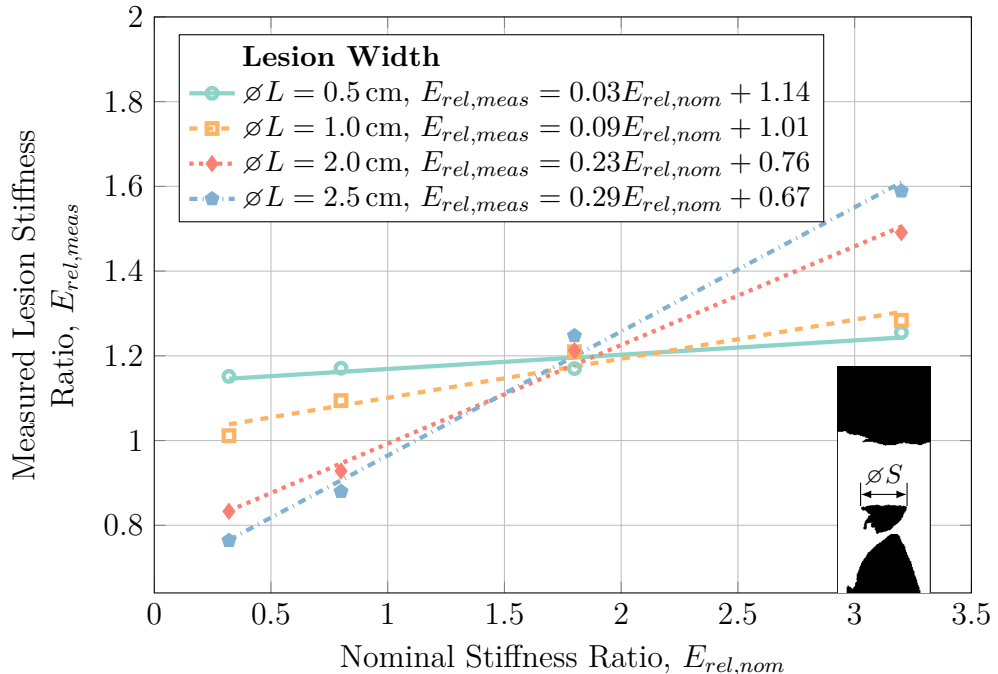


**Fig. 3.20:** Characterization of lesion width in a Visible Human-MRI model for lesions at a depth of 7.25 cm interrogated with a 4 MHz probing frequency with 5 % applied strain. Small lesions (with a width  $\leq 1.0 \text{ cm}$ ) are severely misrepresented and portray general over-estimation of lesion stiffness larger lesions. Lines represent linear regressions of the data.

a diameter of 2.0 cm and at a depth of 3.5 cm, interrogated at 8 MHz with approximately 5 % applied strain. The results of this study are summarized in Fig. 3.23.

As can be seen in Fig. 3.23, a relatively simple (although inexact) relationship between simulated and experimental measured strain ratios exists. It must be noted that the finite-element simulations of b-mode image formation and tissue deformation presented here are idealizations of reality and idealization errors such as the ultrasound pulse profile and plane-strain assumption no doubt contributed to the difference seen in Fig. 3.23.

It must be noted that in order to acquire quasi-static elastography results in the physical phantom, the ultrasound transducer was required to be manually manipulated to cause indentation in the phantom, as the technique would most

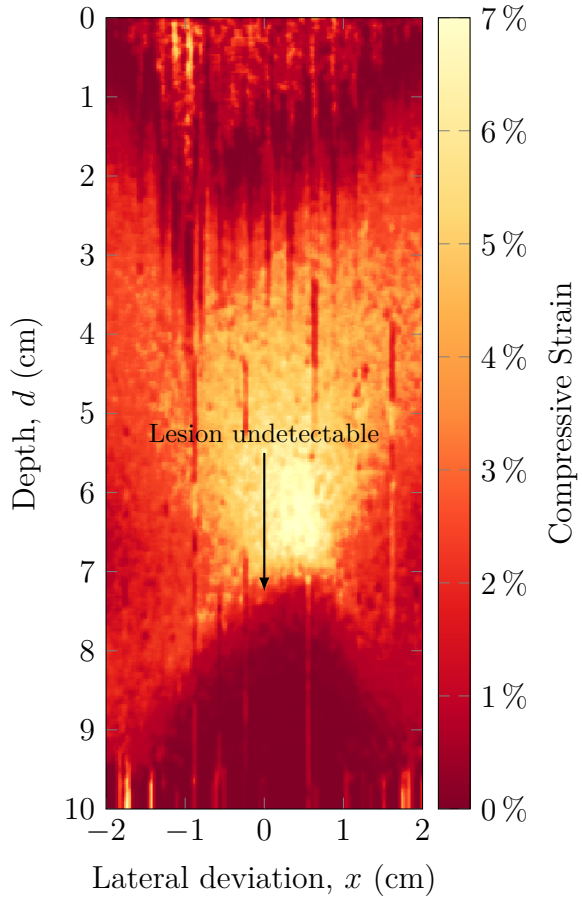


**Fig. 3.21:** Elastogram for a 0.5 cm wide lesion embedded in the Visible Human-MRI model domain at a depth of 7.25 cm interrogated at 4 MHz with an applied strain of 2.5 %. The lesion is not visible in the resultant elastogram.

likely be performed in a clinical setting. This was found to be problematic as the ultrasound transducer was difficult to maintain perfectly perpendicular and in-plane during the compression (largely due to the necessity of using coupling ultrasonic gel). This difficulty suggests that acoustic radiation force impulse (ARFI) elastography would be a more appropriate method to acquire DTI elastograms. ARFI elastography works on the same principles as quasi-static elastography with the exception that tissue deformation is caused by localized large-amplitude acoustic waves generated by the transducer such that human factors play a far less substantial role in image acquisition.

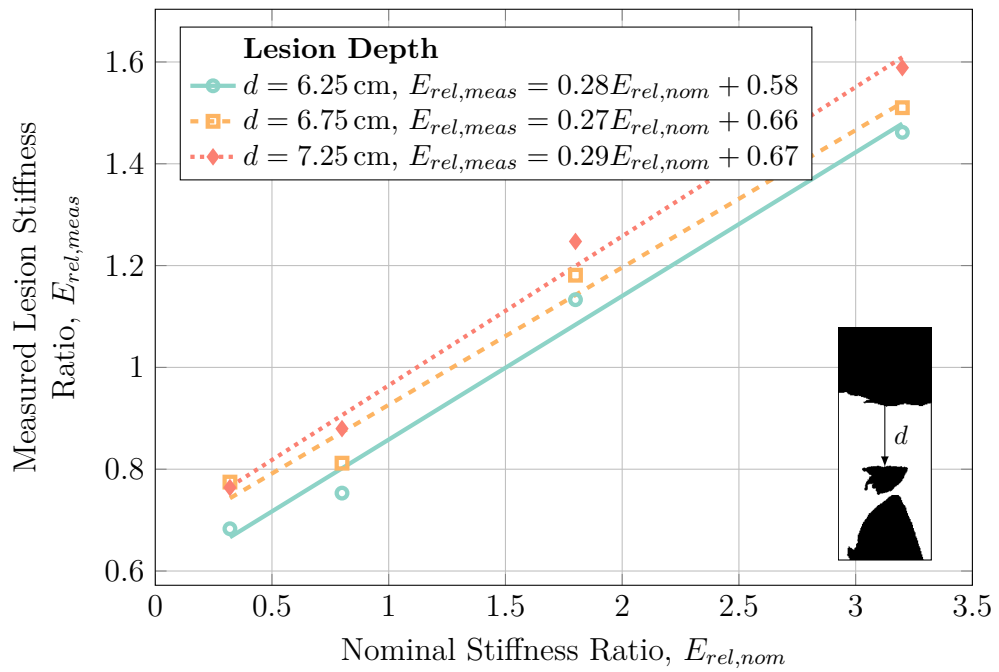


**Fig. 3.22:** Characterization of lesion depth in a Visible Human-MRI model for lesions with a width of 2.5 cm interrogated with a 4 MHz probing frequency and 5% applied strain. Deeper lesions (closer to the bony prominence) are have slightly overestimated lesion stiffness ratios as opposed to more superficial lesions while detection sensitivity is not affected by lesion depth. Lines represent linear regressions of the data.

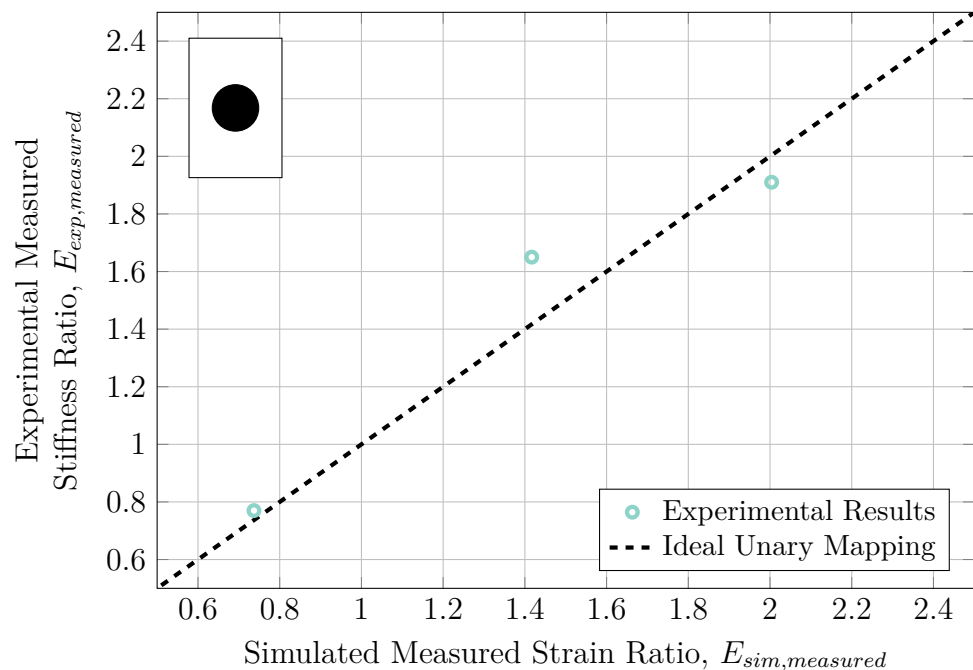


**Fig. 3.23:** Relation between simulated measured strain ratios and experimental measured strain ratios for a lesion at a depth of 3.5 cm and diameter of 2.0 cm showing general agreement between simulated and experimental cases. Idealization errors are the most likely the cause of the differences seen between simulated and experimental cases.

### 3.4 Conclusion

This work represents a numerical characterization of the use of quasi-static ultrasound elastography for the early detection of deep tissue injuries (DTI). There is a real clinical need for an objective tool that is capable of detecting the formation and progression of DTI in human subjects as these wounds are generally not visible from the surface of the skin until they have broken through and already caused substantial damage.

Through this numerical characterization, quasi-static ultrasound elastography was found to be an effective tool for detecting and monitoring DTI in theoretical simulations. Overall, detection sensitivity was less than expected. Small lesions (with diameters  $\leq 1.0\text{ cm}$ ) were more difficult to differentiate due to the low lesion detection sensitivity. While lesion depth, altitude above the underlying bone, and probing frequency did not have significant effect on the lesion detection sensitivity, it was found that applying high levels of compressive strain (10 %) introduced severe error for both very unstiff and very stiff lesions, thus it is recommended that diagnosticians only apply moderate ( $\leq 5\%$ ) compressive strain when interrogating potential lesions. Larger strains may alternately be induced by slowly palpating the tissue with very minor strains frame-by-frame and cumulating the displacement fields across these smaller palpations. Care must be used when palpating the tissue, lest “vigorous” palpations cause harm to the already sensitive injury. In the more complicated model of co-located lesions, while the separation distance between adjacent lesions did not affect the detection sensitivity, the placing of adjacent lesions generated “phantom” lesion regions with altered strain that may appear to be diseased tissue when they are in fact healthy. In a model lesion with gradual blurred boundaries, the effect of blur radius only affected the detection sensitivity and ability to differentiate unstiff lesions. Specifically,

unstiff lesions with large blur radii became nearly impossible to differentiate as these lesions all showed a measured lesion stiffness ratio of approximately 1 which would show up as regular, healthy tissue. In the case of numerous clustered small lesions, both decreased lesion density and decreased individual lesion size caused a decrease in lesion detection sensitivity, likely due to the averaging effect of healthy tissue and diseased tissue in near proximity. Finally, in the Visible Human-MRI acquired lesion model, lesions with widths  $\leq 1.0$  cm are nearly impossible to differentiate as they are hidden by the strain field generated by the bony prominence. Lesion depth did not have an effect on the detection sensitivity, though deeper lesions (lesions which were closer to the bony prominence) had overestimated stiffnesses with respect to their more superficial counterparts.

Although the studies presented here resulted in less-than-ideal detection sensitivities, the technique was still able to pick out lesions from the surrounding unstiff (and hard) tissue. Work done by Solis et al. [67] has shown that untreated DTI are multiple centimetres in size, while work done by Gefen et al. [5] has shown that deep tissue injuries exhibit 1.8-fold to 3.3-fold mechanical stiffening. The work presented here has shown that quasi-static ultrasound elastography is adequate at detecting deep tissue injury lesions in these ranges of parameters and will thus be adequate to detect and monitor progress DTI. However, without further real-world experimentation on the exact nature of newly-forming DTI, the detection sensitivity required to detect newly-forming DTI is indeterminate.

A subset of the results found through simulation were compared with similar experiments done using a tissue mimicking phantom model. The experimental results using the phantom model generally agreed with those found from simulation cases. It was also noted that the manual skin indentation tech-

nique involved with quasi-static ultrasound elastography proved to be difficult to produce reliable images. This difficulty suggests that an alternate method of performing ultrasound elastography may be preferable to quasi-static ultrasound elastography with manual indentation. Acoustic radiation force impulse (ARFI) elastography may be a more appropriate method to acquire DTI elastograms as although ARFI elastography works on the same principles as quasi-static elastography, the difference lays in the fact that tissue deformation is caused by localized large-amplitude acoustic waves generated by the transducer. This means that human factors play a far less substantial role in image acquisition and would likely improve repeatability and inter-operator reliability. Nevertheless, the work done here to characterize the use of quasi-static ultrasound elastography is an important step along the path of generating a useful clinical tool for detecting formative and monitoring progressive deep tissue injuries.

# **Chapter 4**

## **Numerical Characterization of Acoustic Radiation Force Impulse Imaging**

### **4.1 Introduction**

Acoustic radiation force impulse imaging presents a chief benefit over quasi-static ultrasound elastography in that since the external deformation force is applied by the transducer itself rather than through manual indentation of the transducer by the diagnostician, the inter-operator reliability may be greatly increased. The net effect of this is an expected decrease in the required amount of training of diagnosticians as well as an expected increase in the sensitivity and specificity of early deep tissue injury detection.

### **4.2 Method**

In order to numerically characterize acoustic radiation force impulse imaging for the early detection of deep tissue injuries, a combinatory model of acoustic

radiation force simulations and time-domain finite-element models of tissue deformation were used. Acoustic radiation force distributions were calculated using a k-space pseudo-spectral model of ultrasonic acoustics which simulated the acoustic intensities and subsequent radiation force developed by an ultrasonic transducer applying deep body loads to soft tissue. These forces were then combined with a temporal finite-element model of tissue deformation to model the response of the tissue to the body force impulses generated by the transducer. The use of these models allowed extensive simulation and parameter sensitivity analysis in order to numerically characterize the use of acoustic radiation force impulse imaging for detecting deep tissue injuries.

#### 4.2.1 K-Space Pseudo-spectral Model of Acoustic Fields

In order to simulate the body loads generated within deep tissue by a continuous ultrasound beam, a k-space pseudo-spectral model of acoustic field intensities was generated. The body load fields that were generated as a result of this model were fed into a temporal soft tissue deformation model to investigate the dynamic response of tissue to ARFI loads.

The governing equations used for the k-space pseudo-spectral model were the set of coupled first-order partial differential equations 4.1a – 4.1c. These equations are the first-order equivalents of the wave equation given in equation 4.2 taking into account acoustic absorption, tissue heterogeneities, and acoustic wave non-linearities [134]. Equations 4.1a, 4.1b, and 4.1c represent the momentum conservation, mass conservation, and pressure-density relation terms respectively.

$$\frac{\partial \vec{v}}{\partial t} = -\frac{1}{\rho_0} \nabla p \quad (4.1a)$$

$$\frac{\partial p}{\partial t} = -(2\rho + \rho_0) \nabla \cdot \vec{v} - \vec{v} \cdot \nabla \rho_0 \quad (4.1b)$$

$$p = c_0^2 \left( \rho + \vec{u} \cdot \nabla \rho_0 + \frac{B}{2A} \frac{\rho^2}{\rho_0} - \mathbf{L}\rho \right) \quad (4.1c)$$

In equations 4.1,  $\vec{v}$  is the acoustic particle velocity,  $p$  is the acoustic pressure,  $\rho$  is the acoustic density,  $\rho_0$  is the equilibrium density,  $c_0$  is the acoustic sound speed,  $\vec{u}$  is the acoustic particle displacement, and  $B/A$  is a nonlinearity parameter which models alterations to the sound speed [135].

$$\nabla^2 p - \frac{1}{c_0^2} \frac{\partial^2 p}{\partial t^2} = 0 \quad (4.2)$$

The  $\mathbf{L}$  operator used in equation 4.1c accounts for acoustic absorption and dispersion which follows a frequency power law and is defined as per equations 4.3a – 4.3c where  $\alpha_0$  is the power law prefactor and  $y$  is the power law exponent of the tissue.  $\tau$  and  $\eta$  represent absorption and dispersion proportionality coefficients respectively.

$$\mathbf{L} = \tau \frac{\partial}{\partial t} (-\nabla^2)^{\frac{y}{2}-1} + \eta (-\nabla^2)^{\frac{y+1}{2}-1} \quad (4.3a)$$

$$\tau = -2\alpha_0 c_0^{y-1} \quad (4.3b)$$

$$\eta = 2\alpha_0 c_0^y \tan\left(\frac{\pi y}{2}\right) \quad (4.3c)$$

In order to integrate pressure sources in equations 4.1a – 4.1c, equation 4.1b is modified to include a mass source term,  $S_M$  which counts as a pressure source term through changing density to form equation 4.4.

$$\frac{\partial p}{\partial t} = -(2\rho + \rho_0) \nabla \cdot \vec{v} - \vec{v} \cdot \nabla \rho_0 + S_M \quad (4.4)$$

The k-Wave MATLAB® toolbox version 1.0 was used to solve for the time-variant intensities resulting from simulated acoustic radiation force impulses applied to heterogeneous soft tissue using equations 4.1a, 4.4, and 4.1c with the acoustic properties listed in Table 4.1. Sample source code for performing these simulations using the k-Wave toolbox is given in listing B.4 in Appendix B.

**Table 4.1:** K-Space pseudo-spectral model parameters

Property	Symbol	Value	Units
Nonlinearity parameter	$B/A$	8	—
Power law prefactor	$\alpha_0$	0.7	$Np \text{ (rad/s)}^{-y} \text{ m}^{-1}$
Power law exponent	$y$	0.95	—
Density	$\rho_0$	1,060	$\text{kg m}^{-3}$

### 4.2.2 Derivation of Acoustic Radiation Force

Acoustic radiation force arises as the result of absorption of linear momentum within tissue as acoustic waves travel through it with the requirement that the tissue is a viscoelastic medium—no energy would be absorbed in a purely linear elastic model. Further, at the super-MHz frequencies involved in ultrasound interrogation, tissue may be considered a viscous fluid [113].

Using a perturbative expansion of the general equation of linear momentum given in equation 4.5, acoustic radiation force can be expressed as per equations 4.6 [136]. In equations 4.6,  $\langle \rangle$  represents the time-average operator,  $\vec{v}_1$  and  $\vec{v}_2$  are the first and second order terms in the perturbative expansion of particle velocity,  $p_2$  is the second order pressure term in the perturbative expansion, while  $\vec{F}$  represents the acoustic radiation force developed in the tissue.

$$\sigma_{ij,j} + \rho b_i = \rho f_i \quad (4.5)$$

$$\vec{F} = \nabla p_2 - \mu_{tissue} \nabla^2 \vec{v}_2 \quad (4.6a)$$

$$\vec{F} = \rho \langle \vec{v}_1 \nabla \cdot \vec{v}_1 + \vec{v}_1 \nabla \cdot \vec{v}_1 \rangle \quad (4.6b)$$

For a plane wave, equation 4.6b can be reduced to equation 4.7. Further, substituting the generalized wave particle velocity solution given in equation 4.8 in equation 4.7, the magnitude of acoustic radiation force may be calculated as per equation 4.9.

$$\vec{F} = 2\rho \langle \vec{v} \vec{v}_{,x} \rangle \quad (4.7)$$

$$\vec{v} = i\omega A e^{-\alpha x + i(\omega t - kx)} \hat{x} \quad (4.8)$$

$$|\vec{F}| = A^2 e^{-2\alpha x} \rho \alpha \quad (4.9)$$

Further using the acoustic field intensity, the acoustic radiation force may be calculated as per equation 4.10 where  $\alpha$  is the absorption coefficient of the tissue in  $\text{Np m}^{-1}$ ,  $I$  is the temporal average acoustic intensity in  $\text{W m}^{-2}$ , and  $c$  is the longitudinal speed of sound in the tissue in  $\text{m s}^{-1}$  [113].

$$|\vec{F}| = \frac{2\alpha I}{c} \quad (4.10)$$

Once acoustic radiation force body loads were calculated as per equation 4.10, they were used as initial conditions to the temporal finite-element model

of soft tissue deformation described in Section 4.2.3.

### 4.2.3 Temporal Finite-Element Model of Soft Tissue Deformation

In response to the relatively short duration (“impulse”) acoustic radiation force body load applied to tissue in ARFI imaging, the interrogated tissue will exhibit a dynamic response—namely that tissue deformation will propagate outwards as the absorbed acoustic energy diffuses through the soft tissue.

In order to simulate the dynamic tissue deformation generated by the acoustic impulse force, a generalized Maxwell viscoelastic model of tissue deformation was used [137]. The simulated tissue properties are summarized in Tables 4.2 and 4.3.

**Table 4.2:** ARFI model tissue properties

Property	Symbol	Value	Units
Bulk Modulus	$K$	515.7	kPa
Shear Modulus	$\mu_{tissue}$	1.0	kPa
Density	$\rho$	1,060	$\text{kg m}^{-3}$

**Table 4.3:** ARFI Maxwell model tissue properties

Branch	Shear Modulus (Pa)	Relaxation Time (s)
1	791.0	2
2	66.5	40
3	0.6	80

The time-dependent displacement fields were calculated according to equation 4.11 where  $\sigma$  is the Cauchy stress tensor,  $\vec{F}$  are the applied body forces, and  $\vec{u}$  is the particle displacement, and  $\rho$  is the density.

$$\rho \frac{\partial^2 \vec{u}}{\partial t^2} - \nabla \cdot \sigma = \vec{F} \quad (4.11)$$

In order to include viscoelastic effects through a generalized Maxwell model of soft tissue, equation 4.12 was used where  $\sigma_0$  is the initial stress distribution in the tissue,  $C$  is the 4<sup>th</sup> order elasticity tensor,  $\varepsilon$  is the strain,  $G_m$  and  $\tau_m$  are the shear modulus and relaxation time of the  $m^{\text{th}}$  branch of the Maxwell model respectively, and  $\gamma_m$  is an additional auxiliary degree of freedom used to represent the extension of the abstract springs in the Maxwell model.

$$\sigma - \sigma_0 = C : \varepsilon + \sum_m 2G_m \tau_m \dot{\gamma}_m \quad (4.12)$$

In the simulations, the boundary equations 4.13 were used to apply a fixed boundary condition to the both the bottom (deep) and top (superficial) boundaries of the model in the axial direction at both boundaries and in the lateral direction at the deep boundary. All other boundaries of the model were free to translate in all dimensions. A visual representation of these boundary conditions is given in Fig. 4.1. The acoustic radiation force was applied as a body load to the tissue in the model with the distribution calculated by the k-space pseudo-spectral model and resultant body forces described in Sections 4.2.1 and 4.2.2. In order to prevent reflections from the model boundaries that might affect the simulation results, the model geometry extended laterally by 5 cm in either direction from the centreline. Simulations were run until the axial displacement at the focal point returned to 1 % of it's maximal value during the entire simulation—at this point, the tissue was considered to be “relaxed” after being disturbed by the acoustic radiation force. Sample source code for calculating these finite-element models using COMSOL Multiphysics® is given in listing B.5 in Appendix B.

$$\vec{u} = 0, \quad \Gamma = \Gamma_{bottom} \quad (4.13a)$$

$$u_y = 0, \quad \Gamma = \Gamma_{top} \quad (4.13b)$$

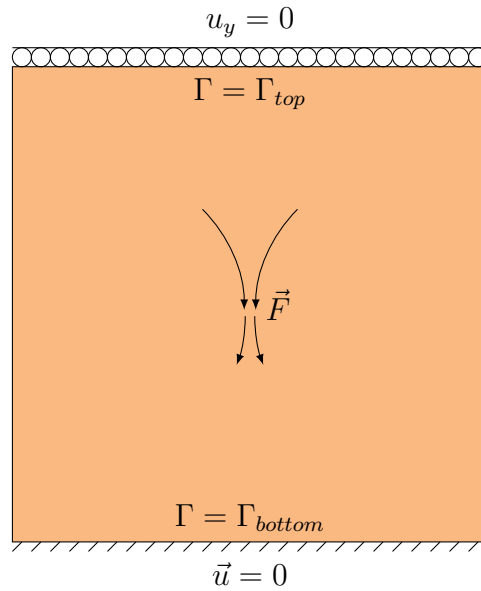


**Fig. 4.1:** Boundary conditions used in the finite-element calculations of soft tissue deformation.

#### 4.2.4 Characterizing Acoustic Radiation Force Impulse Imaging

In order to fully understand the suitability of using ARFI imaging to detect and monitor deep tissue injuries, 1 model of unlesioned tissue and 4 general models of deep tissue injury lesions were modelled. Each model was investigated over a range of parameters in order to determine the relationship between the detection sensitivity and the various parameters that were studied. The unlesioned model was used to investigate the general effects of acoustic radiation force impulse forces in soft tissue. The investigated lesionous models included

a hard-boundaried spherical lesion embedded in a homogeneous soft tissue domain, a lesion with blurred boundaries that “fades” into the homogeneous soft tissue background, a cluster of small lesions which together comprise a greater lesionous region, and a lesion with MRI-acquired geometry [67] embedded in geometry obtained from a Visible Human slice [126]. Schematics of the four investigated models are given in 4.2.

In order to characterize ARFI imaging, ranges of parameters pertinent to each investigated model were studied. The parameters relating to general soft tissue response to acoustic body loads included: the ARFI interrogation frequency used to excite the tissue with acoustic radiation force; the transducer width which applies the acoustic radiation force to the tissue; the number of pulse cycles (loading time) applied by the transducer; and the pressure applied by the transducer. The lesionous models investigated yet more parameters including: lesion depth; lesion diameter; lesion relative stiffness ratio; lesion blur radius; the number of tightly-packed lesions in a clustered lesion model; the radii of the individual tightly-packed lesions in a clustered lesion model; and the width (and overall size) of the MRI-acquired lesion in the Visible Human model. The range of values of these investigated parameters are listed in Table 4.4.

In order to calculate the measured lesion stiffness ratios that are presented in Section 4.3.3, equations 4.14 may be applied. Assuming a constant force applied to both the lesionous region and the soft tissue reference point, the stiffness ratio of the lesion may be calculated as the ratio between the measured tissue deformation and the measured lesion deformation. As the acoustic radiation force impulse interrogation process is highly dynamic, the maximum induced deformation in the region of interest after application of the acoustic radiation force ceased was used in all characterizations.

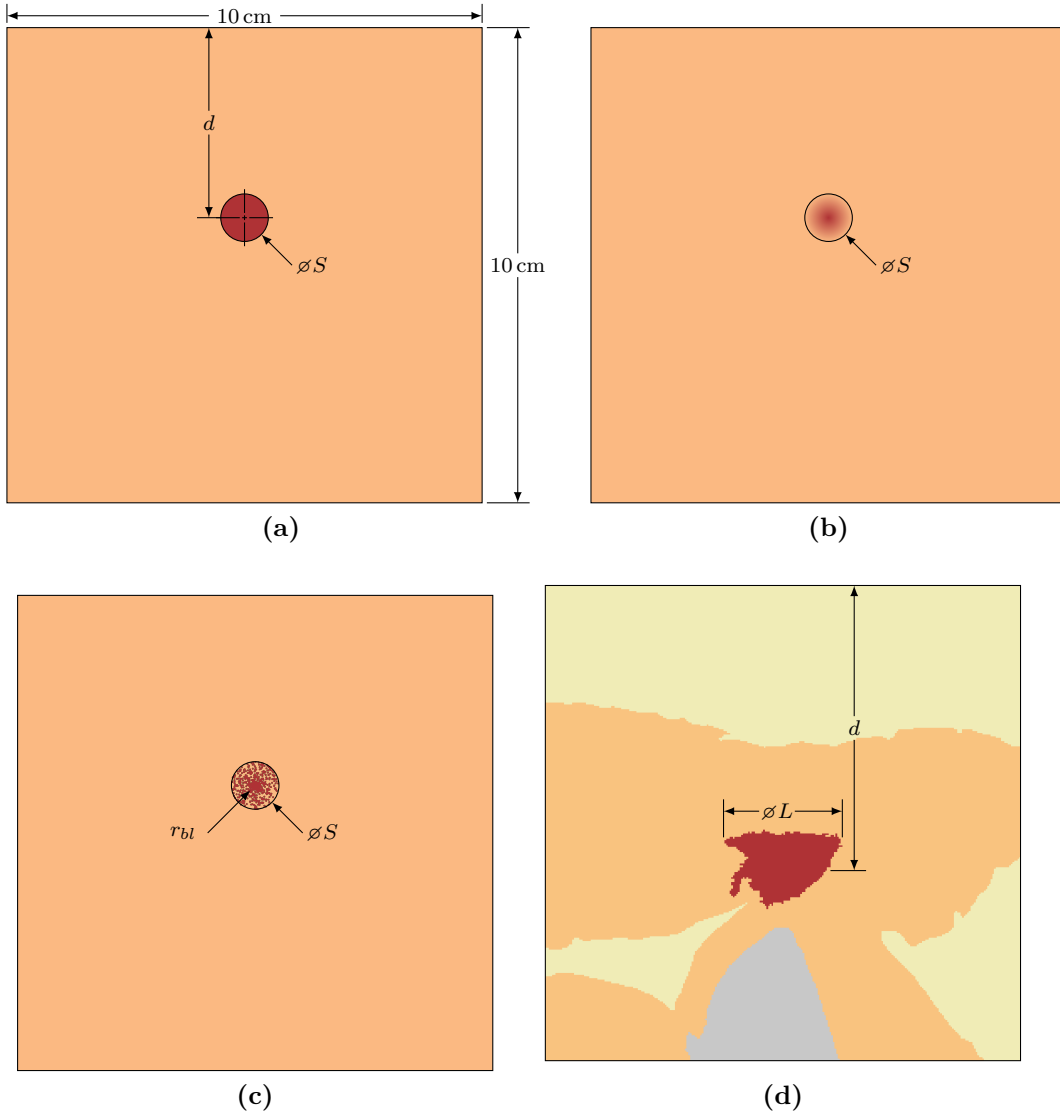


**Fig. 4.2:** Schematics of the lesion models that were investigated using acoustic radiation force impulse imaging showing (a) a spherical hard-boundaried lesion, (b) a spherical blurred-boundary lesion, (c) a cluster of numerous small lesions composing a larger lesionous region, and (d) the geometry from an MRI-acquired deep tissue injury overlaid on a slice from the Visible Human Project such that the injury lesion was located immediately superior to an ischial tuberosity.

$$\sigma = E\varepsilon \quad (4.14a)$$

$$\sigma_{lesion} = \sigma_{tissue} \quad (4.14b)$$

$$E_{lesion}\varepsilon_{lesion} = E_{tissue}\varepsilon_{tissue} \quad (4.14c)$$

$$E_{rel} = \frac{E_{lesion}}{E_{tissue}} = \frac{\varepsilon_{tissue}}{\varepsilon_{lesion}} = \frac{\Delta L_{tissue}}{\Delta L_{lesion}} \quad (4.14d)$$

**Table 4.4:** Range of values of investigated parameters in the various ARFI models that were studied.

Parameter	Symbol	Values	Units
ARFI interrogation frequency	$f$	1, 2, 4, 6	MHz
Transducer width	$w_{trans}$	4, 8, 10	cm
ARFI pulse cycles	$n_c$	3, 100, 300, 500, 700	—
ARFI source pressure	$P_{source}$	4, 5, 6, 7, 8	MPa
Lesion depth	$d$	1, 2, 3, 4, 5, 6, 7, 8, 9	cm
Lesion diameter	$\phi S$	0.5, 1.0, 2.0, 2.5	cm
Lesion stiffness ratio	$E_{rel}$	0.32, 0.56, 1.80, 3.20	—
Blurred lesion blur radius	$b_r$	1.0, 2.5, 5.0, 7.5	mm
Clustered lesion density	$b_p$	10, 20, 30, 40	$\text{cm}^{-2}$
Clustered lesion radius	$r_{bl}$	0.5, 1.0, 1.5	mm
Visible human lesion width	$\phi L$	0.5, 1.0, 2.0, 2.5	cm

#### 4.2.5 Physical Phantom Validation

The same CIRS Elasticity QA Phantom model 049 that was used in the quasi-static studies described in Chapter 3 was used to experimentally validate a subset of the ARFI simulations described here. Using a Siemens ACUSON S2000™ portable ultrasound machine with a Siemens 9L4 transducer, ARFI images were acquired of lesions within the phantom. The 9L4 transducer is a compounding transducer which operates from 4 MHz – 9 MHz and with the ACUSON S2000™ is capable of performing quasi-static elastography, ARFI imaging, and shear wave speed quantification. The stiffness ratios of these lesions according to the acquired ARFI telemetry across 10 trials for each nominal lesion stiffness were then compared with their simulated counterparts in an effort to validate the work completed. The results of this characterization are presented in Section 4.3.4. The detailed experimental protocol that was followed for these validations is given in Section C.2 in Appendix C.

## 4.3 Results

Using the k-space pseudo-spectral model of ultrasound acoustics described in Section 4.2.1, acoustic radiation force distributions were acquired and analysed for the range of input parameters give in Table 4.4. These force distributions were then fed into the time-domain finite-element model of soft tissue deformation described in Section 4.2.3 to examine the difference in relationships between the true and measured tissue stiffness ratios due to the various lesion and transducer parameters that were investigated. The result of these characterizations are presented here.

### 4.3.1 K-Space Pseudospectral Models of Acoustic Radiation Force

In order to adequately simulate complete ARFI imaging sequences, the magnitude and distribution of acoustic radiation force impulses was simulated according to the procedure outlined in Sections 4.2.1 and 4.2.2. By calculating the temporal average of the intensity distributions, the spatially-varying acoustic body load was obtained. A sample generated force distribution is depicted in Fig. 4.3 for the case when a 2 MHz beam focused at a depth of 4 cm was applied to the tissue for 300 pulse cycles, or 150  $\mu$ s.

As expected, the force distribution is strongly concentrated around the focal point, extending axially below the focal point as per typical b-mode ultrasound acoustic beams. The net effect of the force distribution depicted in Figs. 4.3a and 4.3b is to push the tissue deeper axially and toward the focal point laterally. This resulted in a peak acoustic radiation force of approximately  $175 \text{ kN m}^{-3}$  located at the focal point.

Since the k-space pseudo-spectral models employed to simulate acoustic

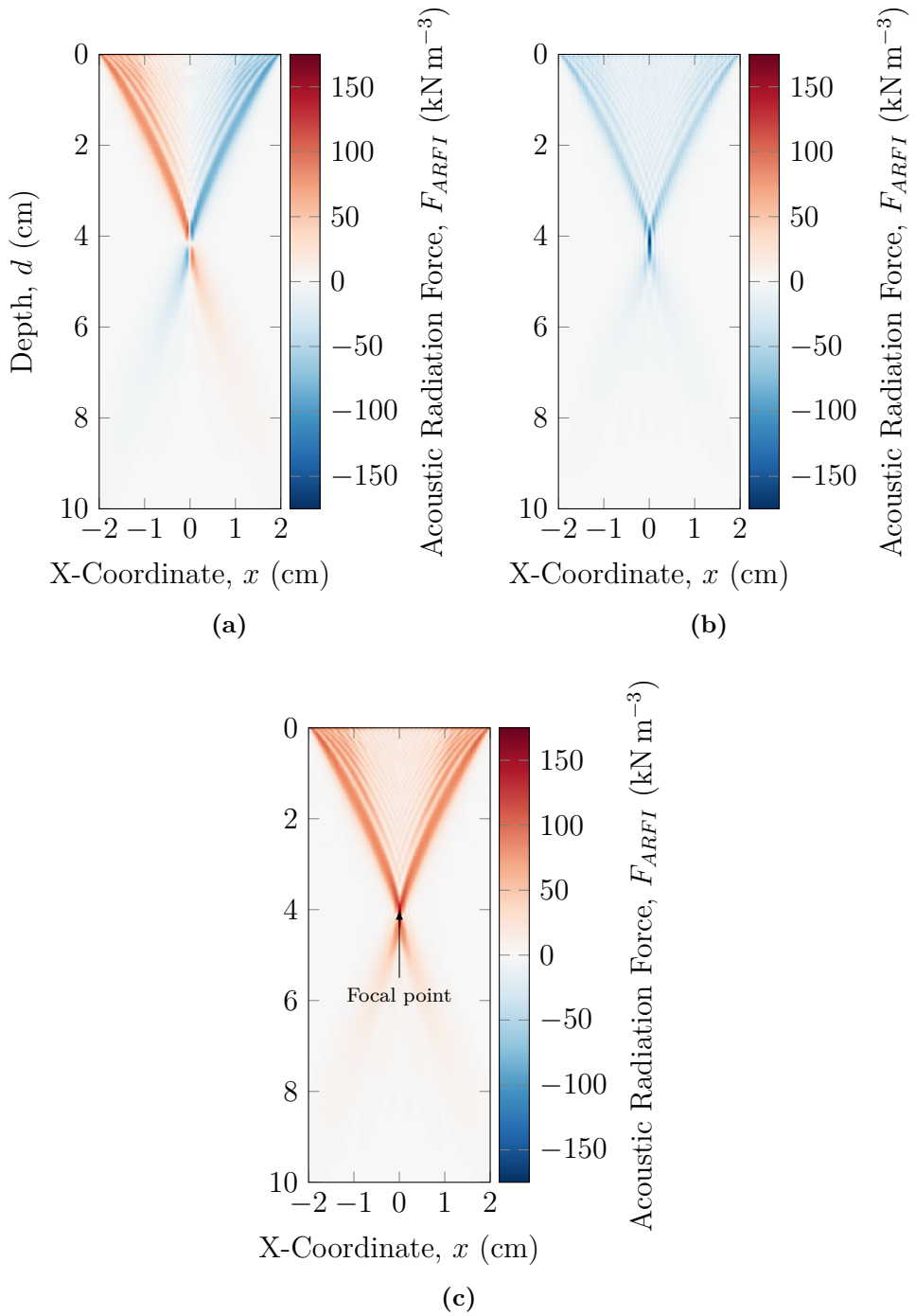


**Fig. 4.3:** Sample acoustic radiation force distribution in the (a) lateral and (b) axial directions, and (c) the resultant  $L^2$ -norm generated by a 2 MHz transducer operating with an aperture of 4 cm focusing an acoustic beam at a depth of 4 cm continuously for 150  $\mu\text{s}$  applying a pressure of 3.35 MPa.

radiation force impulse distributions included absorption and attenuation of the ultrasound waves according to the effects seen in real soft tissues, the depth at which the probe is focused at becomes a critical parameter—the greater the focal depth, the more tissue that the ultrasound must pass through and therefore the more attenuated the signal becomes. This effect is less noticeable with lower frequency ultrasound waves as less energy is absorbed when the particle motion is limited. The resulting acoustic body force generated in the tissue at the focal point for a range of depths of interrogation frequencies is presented in Fig. 4.4.

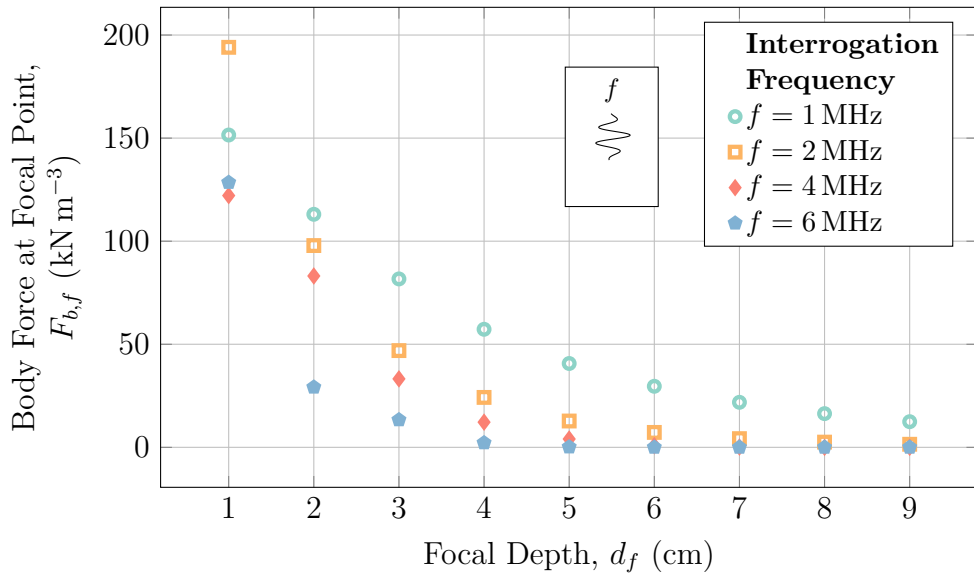


**Fig. 4.4:** Effect of depth and interrogation frequency on the magnitude of acoustic body forces developed in tissue. Increasing the interrogation frequency or the focal depth results in lesser body loads experienced by the tissue at the focal point, with the greatest loss of magnitude resulting from focal depth.

As Fig. 4.4 shows, increasing focal depth and probing frequency drastically decreases the magnitude of the force at the focal point of the tissue. In general, forces that are greater in magnitude are ideal as the deflection in the tissue that they cause must be detectable by the same transducer that is applying the forces—if the resulting deflections are too low, the tracking waves sent by the transducer will not be able to distinguish the motion. For the Siemens

ACUSON S2000<sup>TM</sup> machine used in the validation of these studies, this lower limit is quoted as being  $1/100$  of the applied wavelength, or approximately  $1.7\text{ }\mu\text{m}$  for a  $9\text{ MHz}$  probing frequency [114].

Since the forces developed in the tissue represent a transfer of energy, theoretically increasing the amount of energy input into the system should increase, or at least assist in greater amount of energy being transferred to the tissue. One way of increasing the amount of energy applied to the tissue by the transducer is to increase the size, or the “aperture” of the transducer—an aperture of  $8\text{ cm}$  will use twice as many physical pulsing elements than an aperture of  $4\text{ cm}$ . To study this, the magnitude of the body force at the focal point was studied in simulation as the aperture changed. The results of this study are shown in Fig. 4.5.

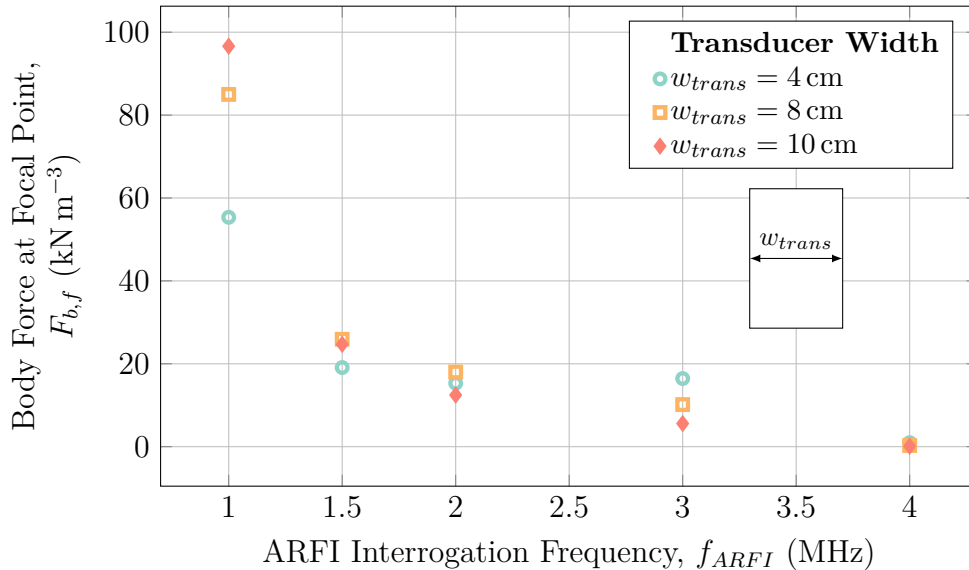


**Fig. 4.5:** Effect of transducer aperture on the magnitude of developed acoustic radiation force at the focal depth of  $6\text{ cm}$  for a range of ultrasound interrogation frequencies.

Surprisingly, there was little consistent effect of the transducer aperture size on the magnitude of the acoustic radiation force that was seen at the focal point. As expected, the greatest and least forces were developed with the

lowest and highest frequencies studied, respectively, as per the results found in Fig. 4.4. The greatest effect of the transducer aperture size occurred at a frequency of 1 MHz while the least effect of the transducer aperture size occurred at a frequency of 4 MHz which correlate to the greatest and least amount of energy input into the system respectively.

Another method of increasing the amount of energy transferred into the system is to increase the duration of time that the system is applying pressure to the tissue. In other words, increasing the number of pulse cycles (insonification time) should generate more energy until tissue is under quasi-steady-state insonification. To investigate this, the effect of the number of acoustic pulse cycles—related to the insonification time by equation 4.15—was investigated, with the results shown in Fig. 4.6.

$$t_{\text{inson}} = \frac{n_c}{f_{\text{applied}}} \quad (4.15)$$

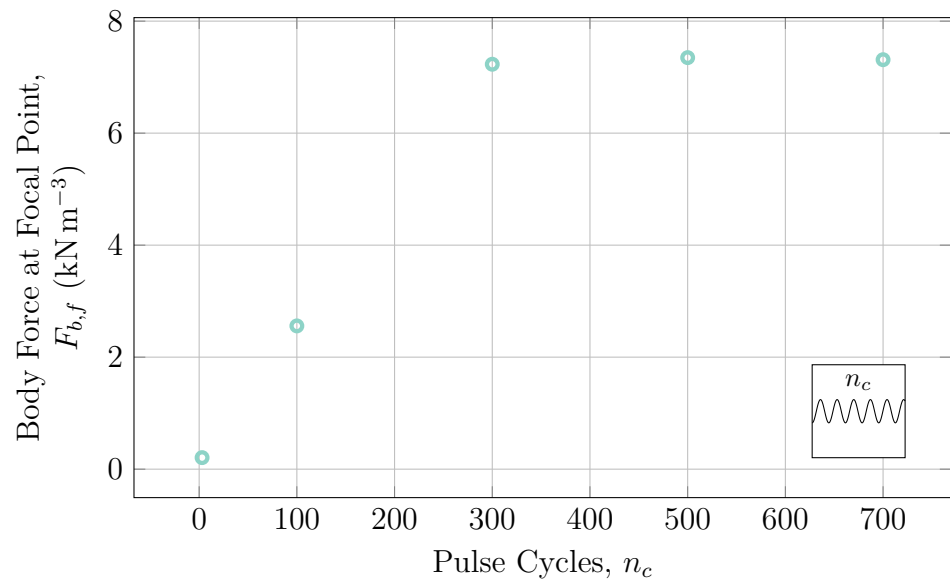


**Fig. 4.6:** Magnitude of the developed acoustic radiation force in relation to the number of applied pulse cycles in tissue at a focal depth of 6 cm using a transducer aperture of 4 cm and source pressure of 3.35 MPa.

As expected, increasing the number of pulse cycles increased the magnitude of the acoustic radiation force seen at the focal point until the domain reached quasi-steady-state at approximately 300 pulses, or 150  $\mu$ s of insonification. At this point, since the calculation of the acoustic radiation force given in equation 4.10 relies on the *average* intensity during the insonification time, increasing the number of pulse cycles has little to no effect on the resulting acoustic radiation force.

One further way of increasing the energy in the system and thereby increasing the magnitude of the acoustic radiation force at the focal point is to increase the amount of pressure applied by the individual transducer elements. To investigate this technique, a range of acoustic pulsing element pressures were applied across a range of focal depths and the resulting acoustic radiation force at the focal point was monitored. The results of this study are shown in Fig. 4.7.

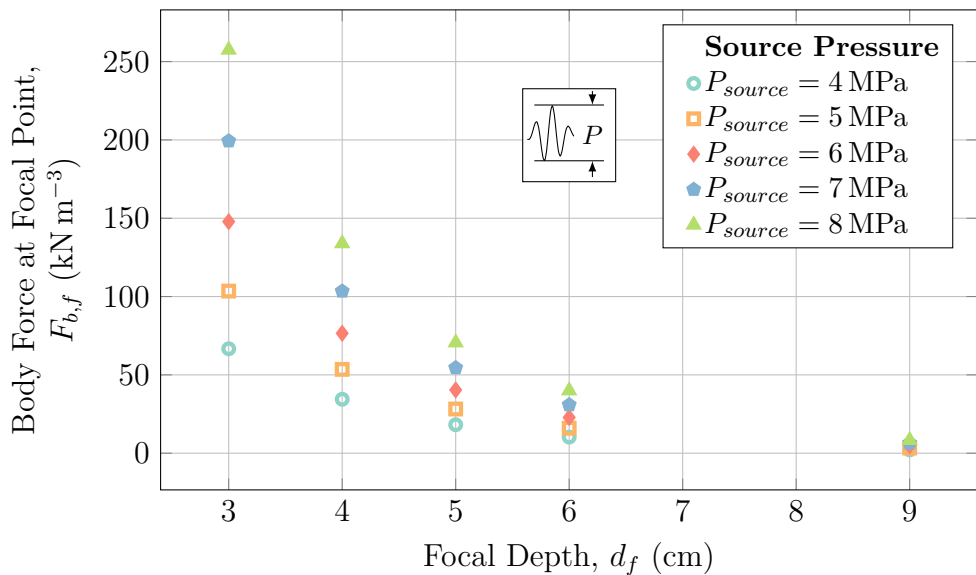


**Fig. 4.7:** Strong dependence on source pressure of focal point force

As Fig. 4.7 shows and as was expected, increasing the applied pressure results in greatly increasing the magnitude of the resultant acoustic radiation

force developed in the tissue—doubling the applied pressure results in nearly quadrupling the magnitude of the acoustic radiation force at all depths. Note however that a critical measure of the safety of ultrasound is the cavitation pressure of the ultrasonic wave as it travels through the tissue. The safety of cavitation is described by the “mechanical index”,  $MI$ , which is calculated according to equation 4.16 [96] where  $P_r$  is the peak rarefaction pressure in the tissue and  $f$  is the ultrasound frequency. While an  $MI$  less than 0.7 generally means that no cavitation may occur, cavitation is largely only a concern in tissues where cavitation is real possibility—only tissues with embedded gas bodies may cavitate. Since deep tissue injuries are largely focused around the sacrum and heels of tissue, the effects of cavitation in ARFI imaging are not largely relevant.

$$MI = \frac{P_r}{\sqrt{f}} \quad (4.16)$$

Maximizing the forces developed in the tissue can be detrimental to that tissue’s health and well-being. To investigate this, the spatial peak pulse average intensity ( $I_{SPPA}$ ) of the acoustic body load simulations was calculated for the range of depths and frequencies investigated in Fig. 4.4 and is shown in Fig. 4.8. Based on a maximum  $I_{SPPA}$  exposure of  $933 \text{ W cm}^{-2}$  [96], the use of ultrasound probes operating at or above 1 MHz and focused at depths greater than 3 cm should be safe for use in examining deep tissue injuries which are generally well separated from the much more sensitive cardiovascular and fetal imaging.

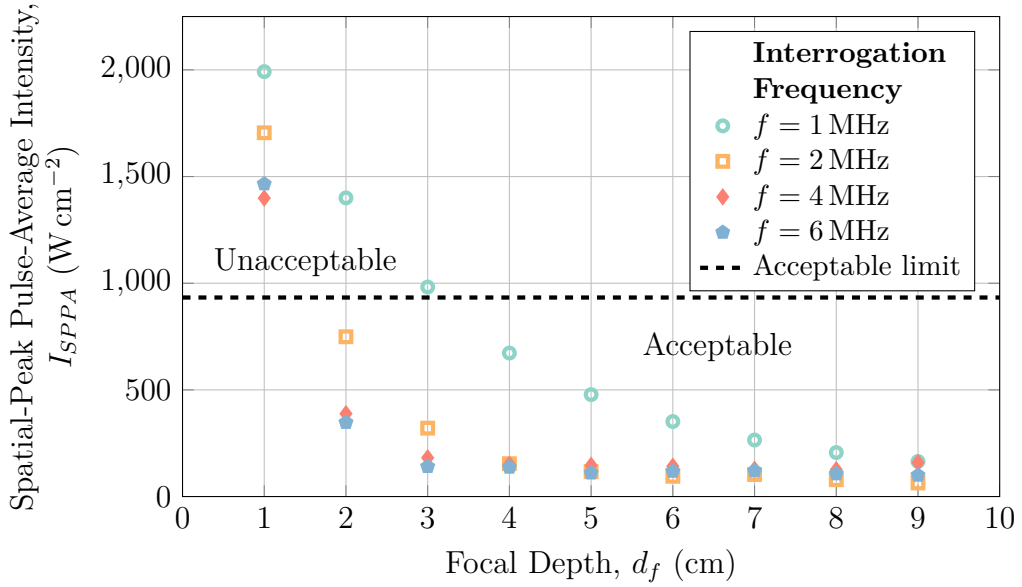


**Fig. 4.8:** The effect of depth and interrogation frequency on the spatial peak pulse average intensity,  $I_{SPPA}$ .  $I_{SPPA}$  is a measure of the safety of high-intensity ultrasound applications, with  $I_{SPPA}$  values below  $933 \text{ W cm}^{-2}$  considered acceptable for non-cardiovascular and non-fetal imaging.

### 4.3.2 Temporal Finite-Element Model of Soft Tissue Deformation

As ARFI imaging relies upon the detection of soft tissue deformation in response to the transducer-applied acoustic radiation force, a key parameter of interest is the magnitude of the deformation generated in the tissue in response to the applied loads. To this end, the temporal finite-element model of soft tissue deformation described in Section 4.2.3 was used to determine the magnitude of the deformation caused by varying acoustic radiation force parameters.

Fig. 4.9 show the relationship between the maximum induced tissue displacement,  $|v|_{max}$ , generated by acoustic radiation forces in soft tissue for a range of focal depths and interrogation frequencies. As expected, significantly greater deformation is generated with shallower focal depths. Further, increases in the interrogation frequency generally resulted in lesser displacement

induced in the tissue. The results obtained using a 1 MHz interrogation frequency stood apart from the higher frequencies investigated. This is likely due to the excess acoustic radiation force produced at such low frequencies shown in Figs. 4.4 and 4.8.

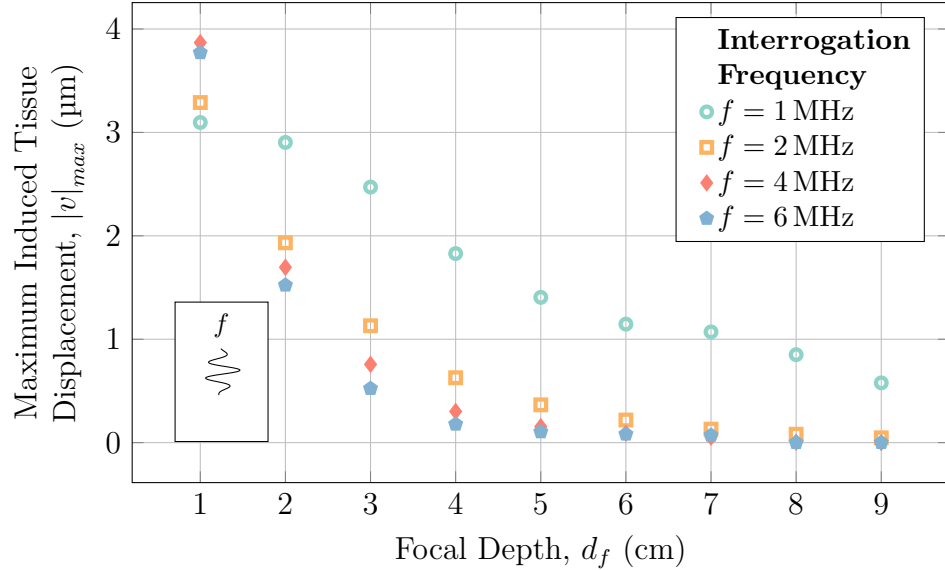


**Fig. 4.9:** Magnitude of deformation resulting from ARFI interrogation at various focal depths and interrogation frequencies with a transducer aperture of 4 cm and source pressure of 3.35 MPa.

To reiterate the results seen in Fig. 4.7, the maximum induced tissue displacement generated by the applied acoustic radiation force at various focal depths for various source pressures was investigated, the results of which are given in Fig. 4.10. These results echo the results seen in Fig. 4.7, where doubling the applied pressure resulted in approximately quadrupling the maximum displacement seen in the tissue across all focal depths as was expected.

The results given in Fig. 4.10 were further investigated by examining the effect of the interrogation frequency on the maximum induced tissue displacement. As expected, increasing the interrogation frequency resulted in decreases in the magnitude of deformation experienced by the tissue across all source pressures investigated. Further, increasing the amount of source

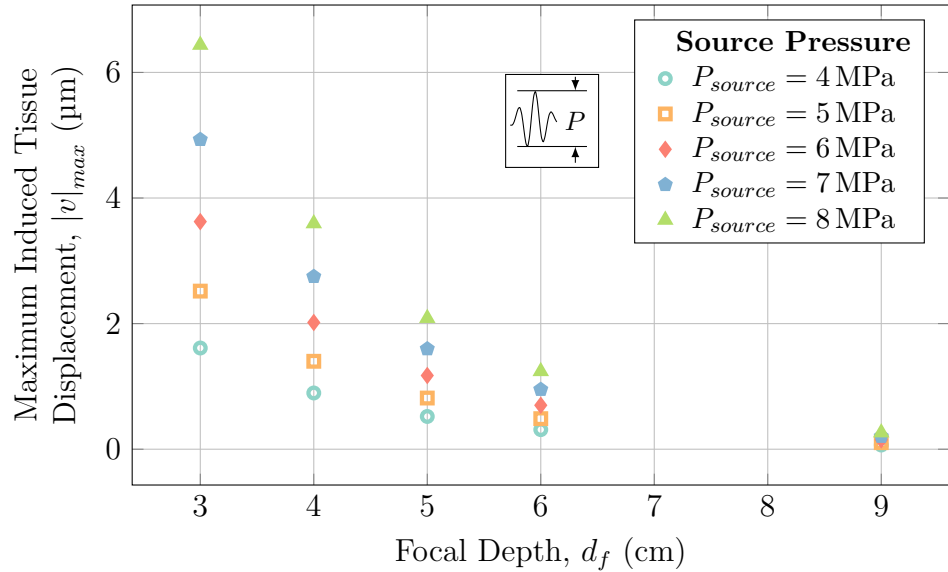


**Fig. 4.10:** Magnitude of deformation resulting from ARFI interrogation at various focal depths and source pressures at an interrogation frequency of 2 MHz with a transducer aperture of 4 cm and source pressure of 3.35 MPa.

pressure applied by the transducer into the tissue resulted in greater levels of tissue deformation. Of note is that the use of a 1 MHz interrogation frequency affected the magnitude of tissue deformation across the different source pressures much more than any of the higher interrogation frequencies studied, further echoing the results seen in Fig. 4.9.

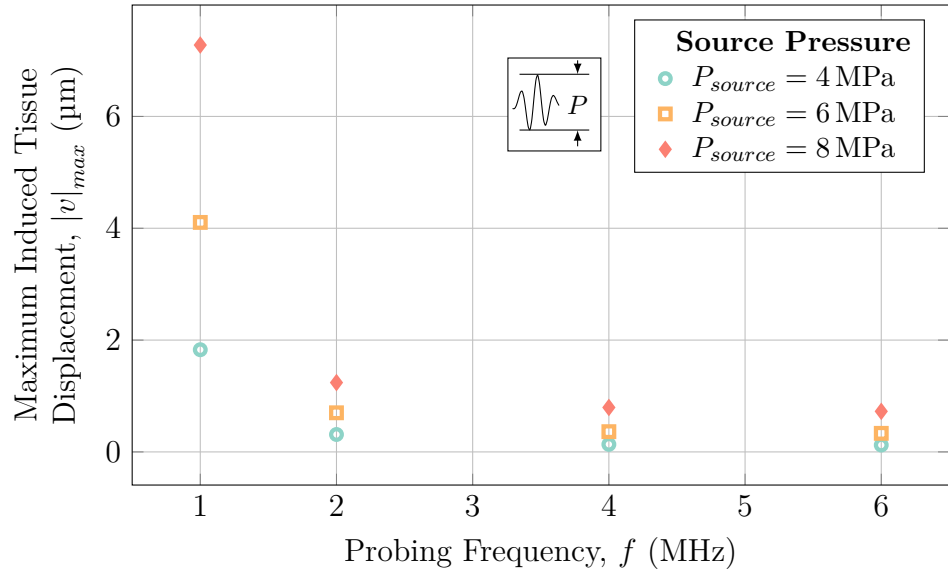


**Fig. 4.11:** Magnitude of deformation resulting from ARFI interrogation at various interrogation frequencies and source pressures at a depth of 6 cm with a transducer aperture of 4 cm and source pressure of 3.35 MPa.

### 4.3.3 Numerical Characterization of Acoustic Radiation Force Impulse Imaging

Beyond understanding the general nature of acoustic radiation forces in soft tissue, the effects of these forces in the presence of deep tissue injuries must also be characterized for ARFI imaging to become a useful diagnostic tool for such injuries. In order to investigate the suitability of ARFI imaging for the detection of DTI, the procedure outlined in Section 4.2.4 was carried out on a range of models with varying parameters of interest. The results of these characterizations are presented here.

In order to understand the effect of general lesion size on the detection sensitivity of ARFI imaging, hard-boundaried spherical lesions of various radii were placed in a soft tissue domain at a depth of 4 cm and insonated at 2 MHz with an aperture of 4 cm and pressure of 3.35 MPa for 150 μs (300 pulse cycles). The results of this characterization are presented in Fig. 4.12.

As Fig. 4.12 shows, ARFI imaging was able to detect the presence of

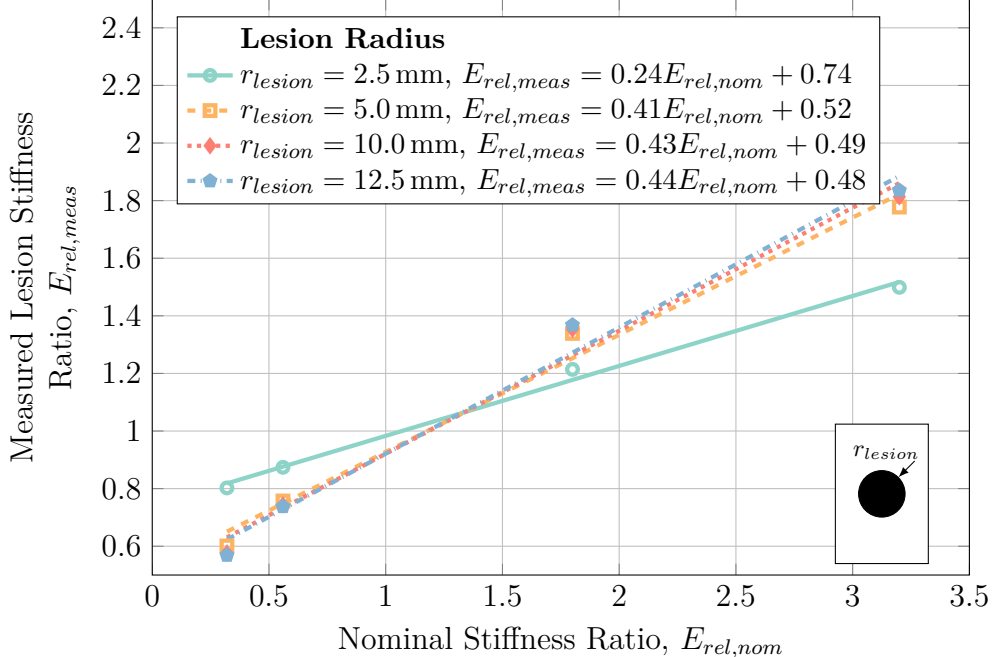


**Fig. 4.12:** Numerical characterization of the ARFI imaging-acquired stiffness ratios acquired with varying lesion radii for a hard-boundaried lesion at a depth of 4 cm using an ARFI probing frequency of 2 MHz.

both stiff and unstiff lesions of all sizes, however the technique both severely underestimated the stiffness of stiff lesions and overestimated the stiffness of unstiff lesions—leading to the observation that ARFI imaging has a relatively low detection sensitivity with regards to both stiff and unstiff deep tissue injury lesions. Fig. 4.12 also shows that above lesion radii of approximately 2.5 mm, the lesions size does not have any appreciable effect on the detection sensitivity of the technique. Below this limit, however, lesions will be much more difficult to detect as the differences between them and the surrounding tissue are minimized.

To further corroborate these results, the mean-squared error associated with the various lesion radii was calculated according to equation 4.17 where  $\hat{Y}_i$  are the true lesion stiffness ratios and  $Y_i$  are the measured lesion stiffness ratios. The results of this calculation with regards to lesion radius are given in Fig. 4.13. Figure 4.13 explicitly depicts a greater degree of error for lesions

with radii of 2.5 mm, with only marginal improvements in measurement error resulting from increasing the lesion radius beyond 5.0 mm.

$$MSE = \frac{1}{n} \sum_{i=1}^n (\hat{Y}_i - Y_i)^2 \quad (4.17)$$

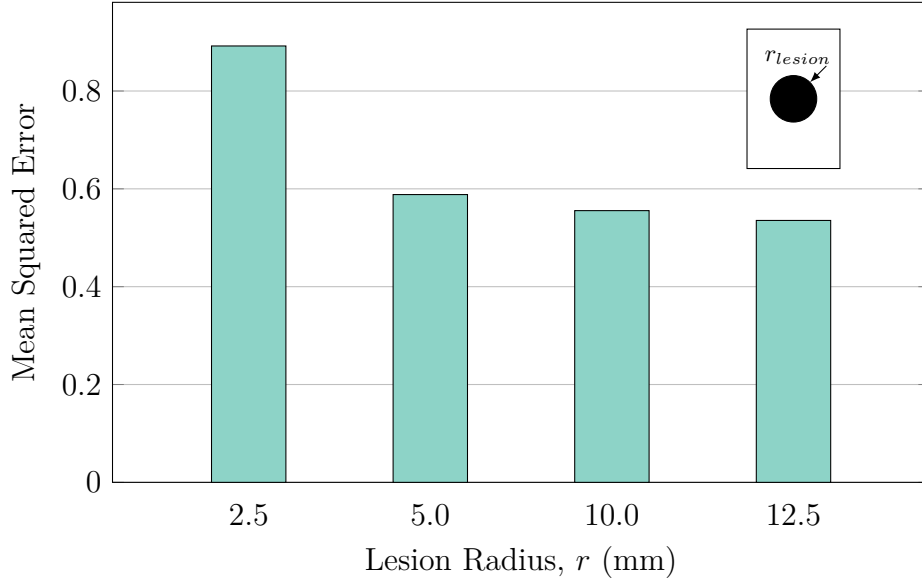


**Fig. 4.13:** Mean squared error between the true and measured lesion stiffness ratios for increasing lesion radii for a hard-boundaried lesion at a depth of 4 cm using an ARFI interrogation frequency of 2 MHz.

In order to investigate the effect of lesion depth on detection sensitivity, the use of ARFI imaging to distinguish spherical hard-boundaried lesions with radii of 10 mm was investigated at a range of depths, with the results shown in Fig. 4.14. As Fig. 4.14 shows, there is almost no dependence of the detection sensitivity on the depth of the lesion. However, it must be noted that the deformations resulting from acoustic radiation force impulses will be of such small magnitudes that they will not be detectable using current ultrasound technology. To understand the limitations of depth in ARFI imaging, please refer to Section 4.3.2.

Fig. 4.15 portrays the mean-squared-error of the measured lesion stiffness

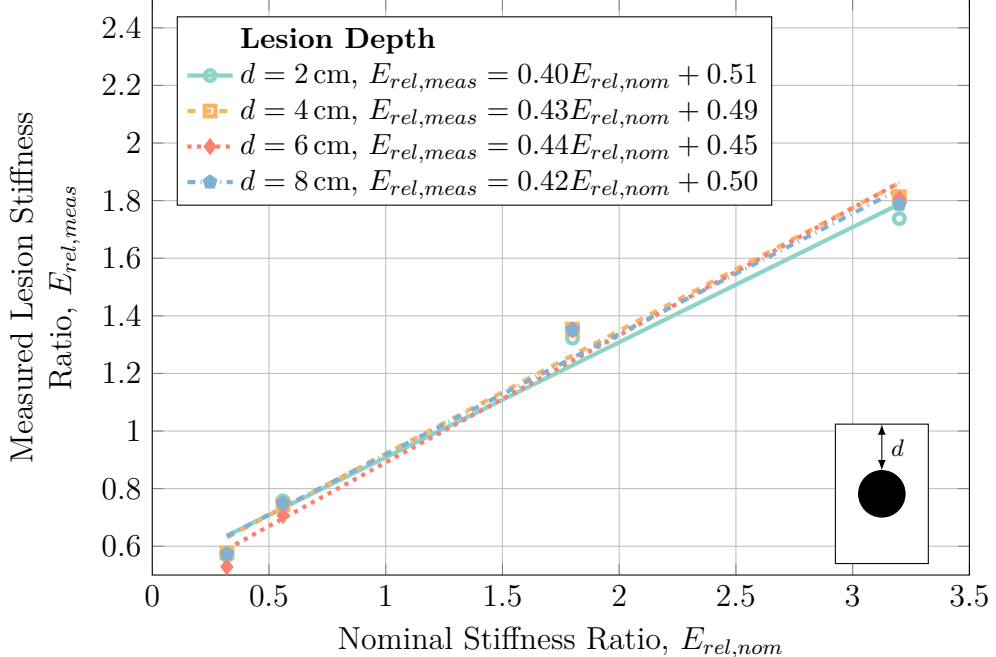


**Fig. 4.14:** Numerical characterization of the ARFI imaging-acquired stiffness ratios acquired with varying lesion and focal point depths for a hard-boundaried 0.5 cm radius lesion using an ARFI probing frequency of 2 MHz.

across the various depths examined. Although the variance in error between the different depths is not substantial, both very shallow—lesions at a depth of 2 cm or less—and very deep—lesions at a depth of 8 cm or more—were found to have the greatest measurement error. In shallow tissue, this increase in error may be due to an inability to appropriately focus the acoustic radiation force so close to the transducer whereas in deep tissue, the increase in error is likely due to the reduced magnitude of radiation force present due to the relatively large amount of tissue absorption.

Since the aforementioned hard-boundaried, spherical lesion cases represent simplifications of reality designed to obtain a general understanding of the ARFI technique, models representing more complicated geometry were also studied. Fig. 4.16 shows the simulated lesion stiffness ratios for a set of lesions with radii of 10 mm at a depth of 4 cm with blurred boundaries as described in Section 4.2.4. As Fig. 4.16 shows, there is no reliance of the detection

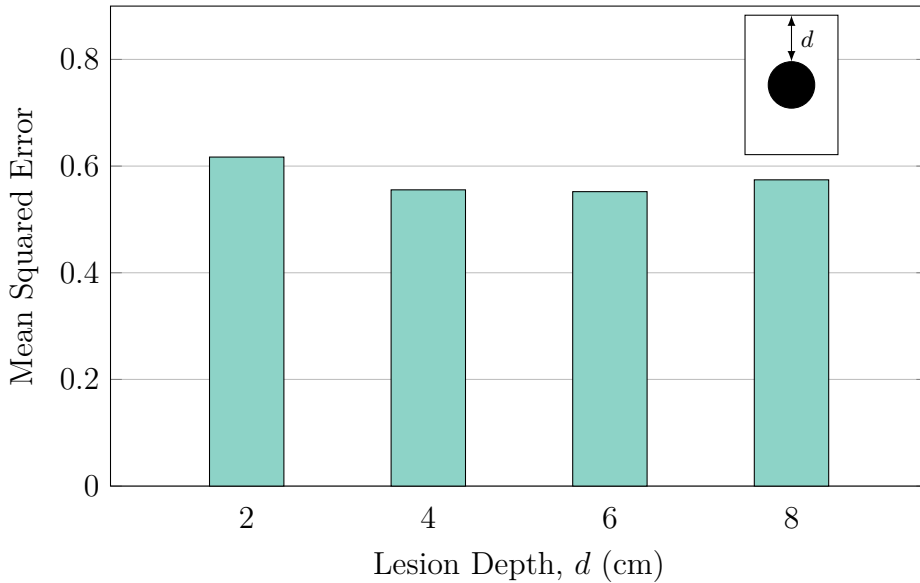


**Fig. 4.15:** Mean squared error between the true and measured lesion stiffness ratios for increasing lesion depths for a hard-boundaried 0.5 cm radius lesion using an ARFI interrogation frequency of 2 MHz.

sensitivity on the blur radius of the lesion, with the results shown repeating the results seen in Figs. 4.12 and 4.14.

The mean-squared error shown in Fig. 4.17 further supports this conclusion, with the error between different blur radii differing by just over 1%. This lack of sensitivity on the degree of lesion blurring presents a significant advantage over quasi-static elastography as it allows even lesions without well-defined boundaries to be detected.

It may also be possible that a diseased region of tissue is not a singular, continuous lesionous region, but rather an amalgamation of numerous small lesions or damaged tissue which collectively compose a larger lesionous region. To investigate the effect such a phenomenon would have on the detection sensitivity of ARFI imaging, the density and size of numerous small, clustered lesions were varied in models and the resulting measured stiffness ratios were investigated. Fig. 4.18 shows the characterization of the lesion cluster density—how many lesions are present per unit area—for densities ranging

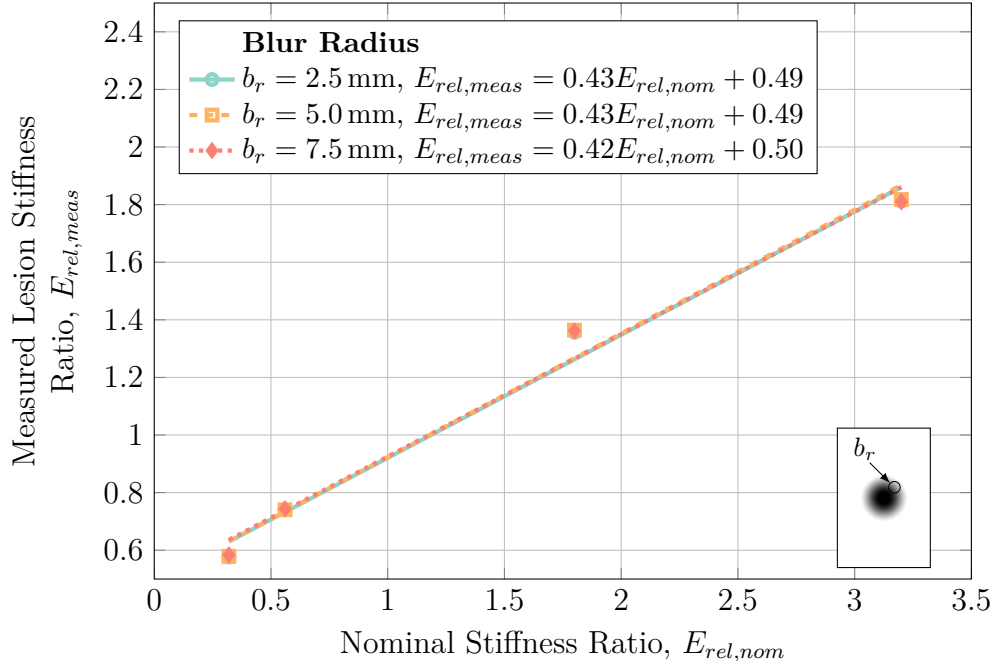


**Fig. 4.16:** Numerical characterization of the ARFI imaging-acquired stiffness ratios acquired with varying lesion and focal point depths for a blurred 1.0 cm radius lesion at a depth of 4 cm using an ARFI interrogation frequency of 2 MHz.

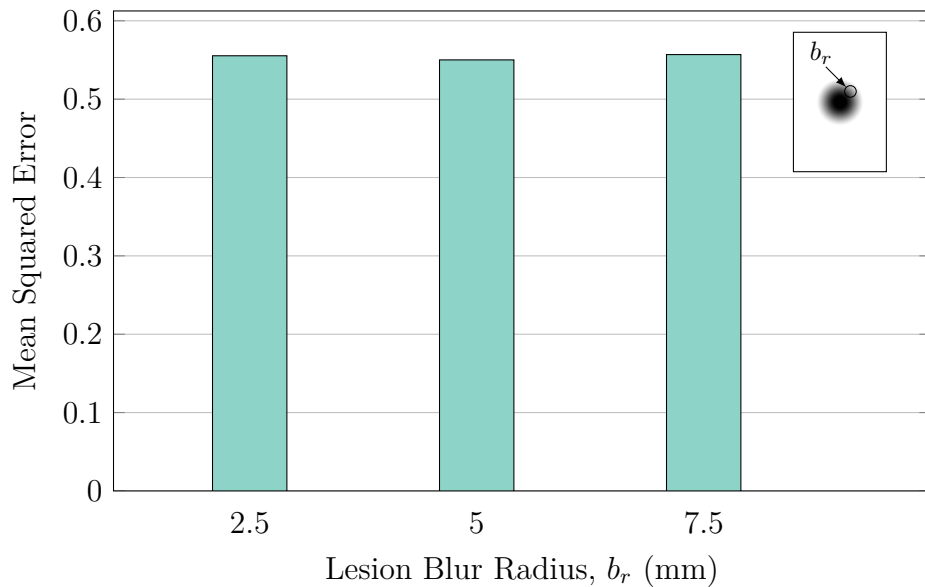


**Fig. 4.17:** Mean squared error between the true and measured lesion stiffness ratios for increasing lesion depths for a blurred 1.0 cm radius lesion at a depth of 4 cm using an ARFI interrogation frequency of 2 MHz.

from  $10 \text{ cm}^{-2}$  to  $40 \text{ cm}^{-2}$  with small lesions of radius 1.0 mm. The centre of the lesionous regions were located at a depth of 4 cm in an overall region with

a radius of 10 mm.

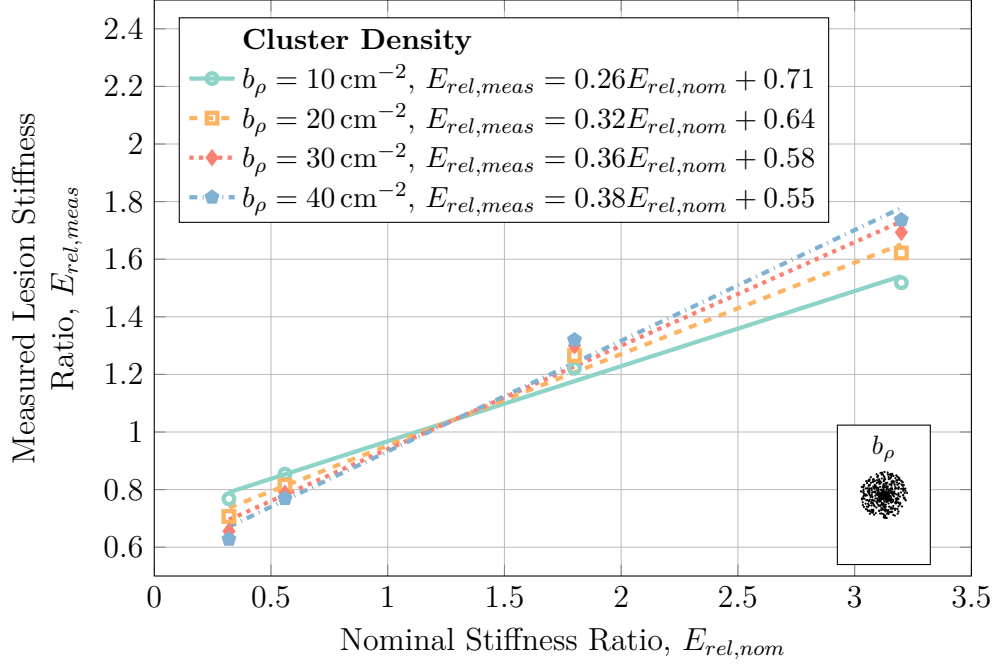


**Fig. 4.18:** Numerical characterization of the ARFI imaging-acquired stiffness ratios acquired with varying cluster densities for clustered 1 mm radius lesions within a 1.0 cm radius at a depth of 4 cm using an ARFI interrogation frequency of 2 MHz.

As Fig. 4.18 shows, increasing the cluster density results in monotonically increasing the detection sensitivity of the ARFI technique. This is as expected, as increasing the cluster density increases the total area contributing to the modified tissue stiffness in the region, which in turn allows the ARFI technique to more readily distinguish the lesion. These results are further shown by the mean-squared error shown in Fig. 4.19 which shows the decrease in error attributed to increases in lesion cluster densities.

Another method to alter the ratio of damaged to healthy tissue within the lesionous region is to alter the size of the individual lesions that comprise that region. This characterization was carried out using small lesions with radii ranging from 0.5 mm to 1.5 mm at a cluster density of  $30 \text{ cm}^{-2}$ , with the results given in Fig. 4.20.

As Fig. 4.20 shows, decreasing the individual lesion radii in the clustered

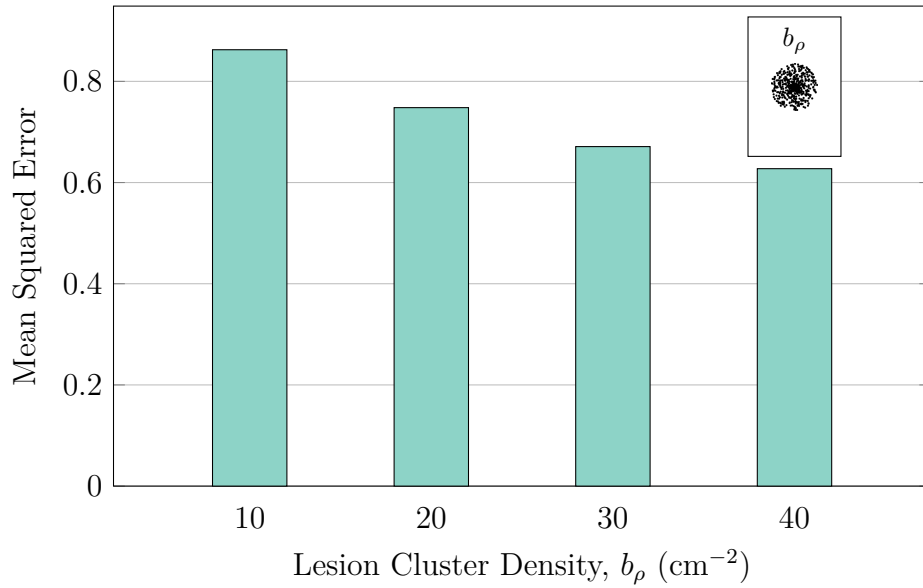


**Fig. 4.19:** Mean squared error between the true and measured lesion stiffness ratios for increasing lesion cluster density for clustered 1 mm radius lesions within a 1.0 cm radius at a depth of 4 cm using an ARFI interrogation frequency of 2 MHz.

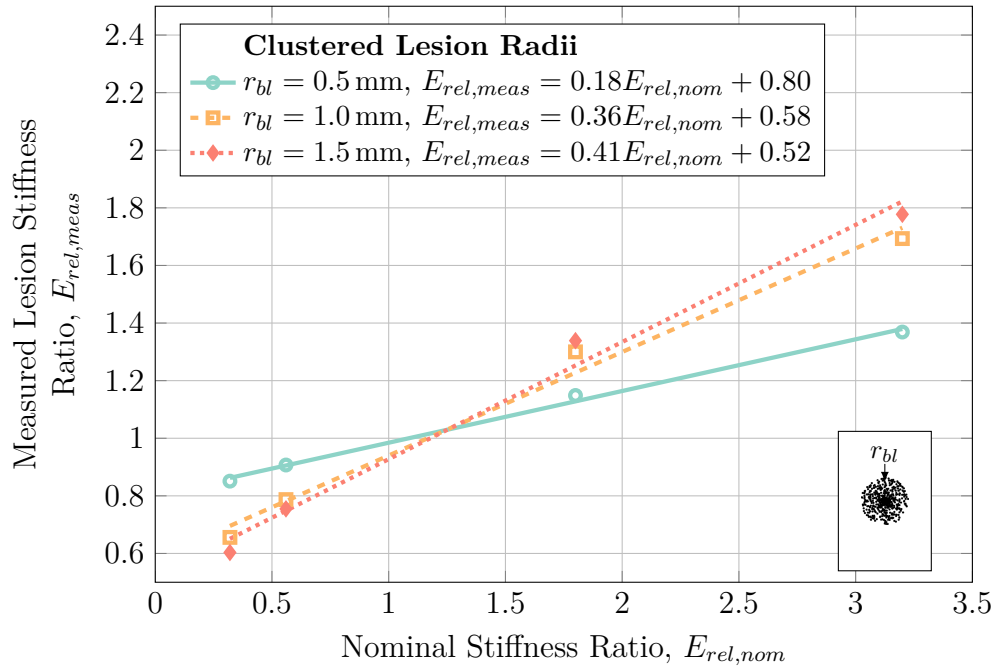


**Fig. 4.20:** Numerical characterization of the ARFI imaging-acquired stiffness ratios acquired with varying clustered lesion radii for clustered lesions with a density of  $30 \text{ cm}^{-2}$  within a 1.0 cm radius at a depth of 4 cm using an ARFI interrogation frequency of 2 MHz.

model substantially decreased the detection sensitivity of the ARFI technique, again echoing the previous results where decreasing the ratio of damaged to healthy tissue in the lesionous region results in lesser detection sensitivity. This is confirmed by examining the mean-squared error of the results, which shows monotonically decreasing errors for monotonically increasing individual lesion radii.

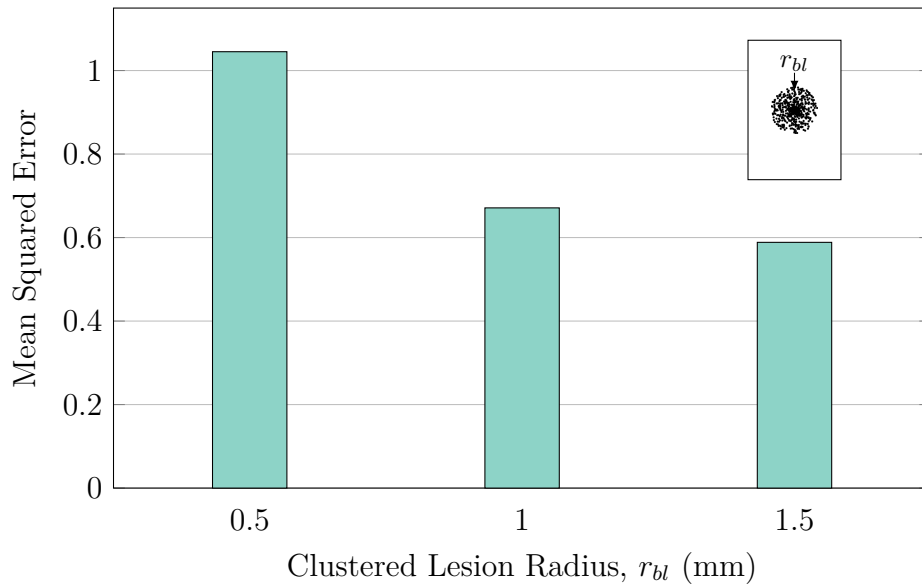


**Fig. 4.21:** Mean squared error between the true and measured lesion stiffness ratios for increasing clustered lesion radii for clustered lesions with a density of  $30 \text{ cm}^{-2}$  within a  $1.0 \text{ cm}$  radius at a depth of  $4 \text{ cm}$  using an ARFI interrogation frequency of  $2 \text{ MHz}$ .

While the aforementioned studies investigated generally spherical lesionous regions, this is unlikely to be the case in a real soft tissue domain. To further investigate ARFI imaging, a model utilizing complicated geometry arising from the combination of the MRI-acquired geometry of a deep tissue injury with the anatomical distribution of fat, muscle, and bone obtained from the Visible Human project [126] was created as described in Section 4.2.4. To investigate the effect of lesion size in this model, the lesion size,  $\varnothing L$ , was varied between  $2.5 \text{ mm}$  and  $12.5$  with the lesion being placed at a depth of  $6 \text{ cm}$ . The results

of this characterization are shown in Fig. 4.22.

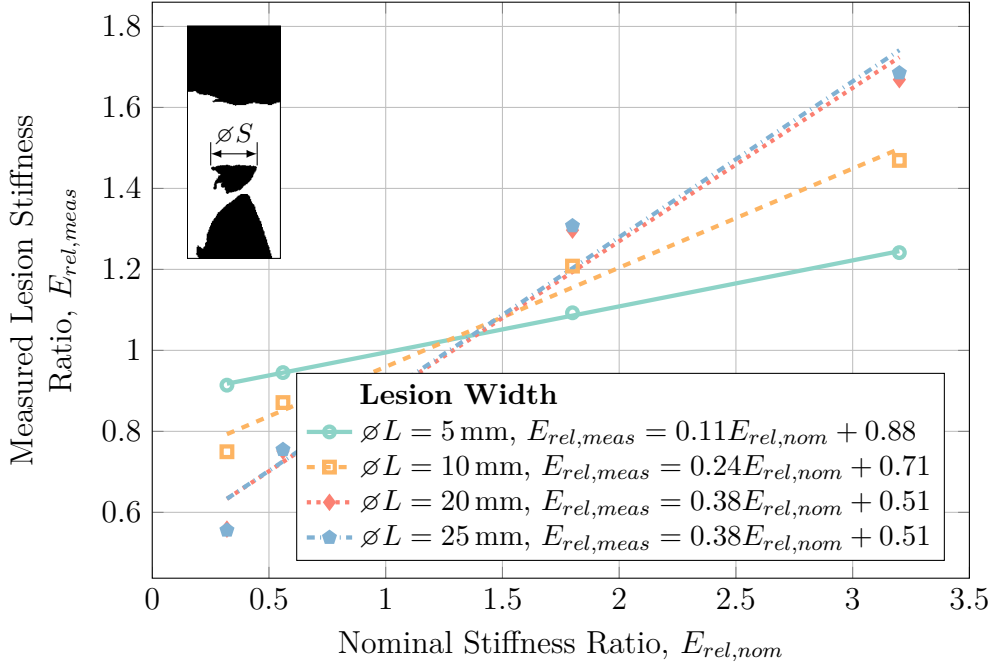


**Fig. 4.22:** Numerical characterization of ARFI imaging-acquired stiffness ratio with changing lesion radii for MRI-acquired lesion geometry in a Visible Human model at a depth of 6 cm using an ARFI interrogation frequency of 2 MHz.

As Fig. 4.22 shows, decreasing the lesion width in the Visible Human model resulted in a decreased detection sensitivity which was echoed by the mean-square error of the results shown in Fig. 4.23. The detection sensitivity decreases with half-widths less than 10 mm in the Visible Human model as opposed to radii of 5 mm as found with the spherical lesion embedded in general soft tissue seen in Fig. 4.12. Although the reason for this is not immediately clear, possible differences lay in the depth at which the lesions were imaged at: the Visible Human model placed the lesion at a depth of 6 cm so as to have it lay immediately superior to the ischial tuberosity while the results for the spherical lesion were taken at a depth of 4 cm. Further, comparing the half-width of the Visible Human lesion to the radius of the spherical lesion may introduce errors as the overall area of lesionous tissue were different.

Numerical values for the characterization plots presented here are given in

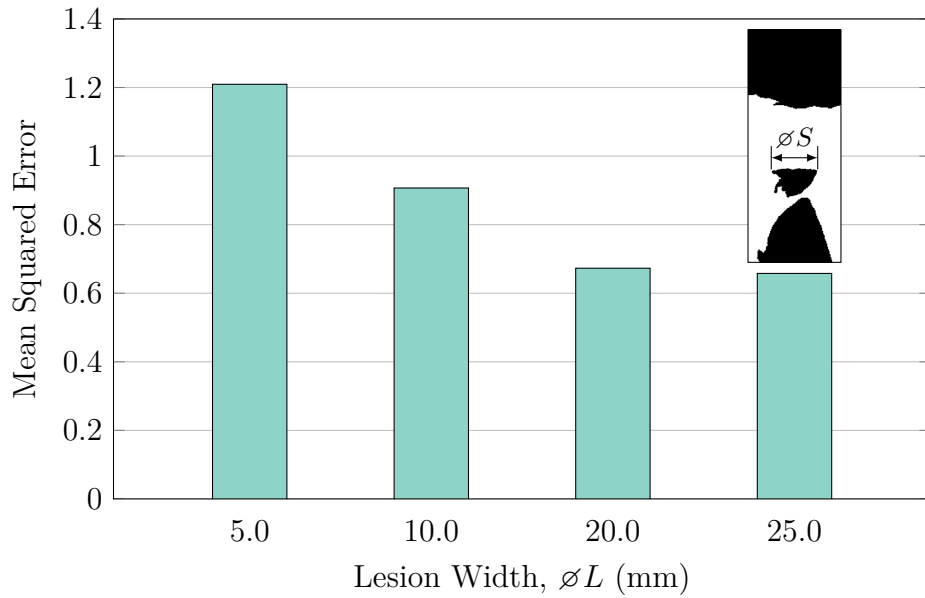


**Fig. 4.23:** Mean squared error between the true and measured lesion stiffness ratios for increasing lesion radii for MRI-acquired lesion geometry in a Visible Human model at a depth of 6 cm using an ARFI interrogation frequency of 2 MHz.

Section A.2 of Appendix A.

#### 4.3.4 Physical Phantom Validation

In order to determine if the results presented in Section 4.3.3 represent valid simulations, validation experiments were carried out on a physical tissue mimicking phantom as described in Section 4.2.5. Fig. 4.24 shows the result of these experiments.

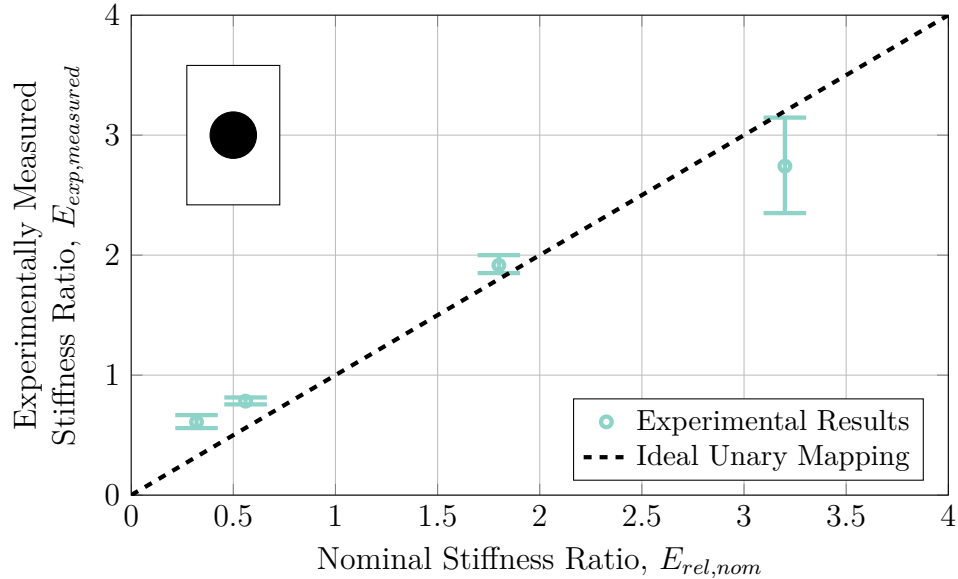


**Fig. 4.24:** Relation between nominally reported strain ratios of the tissue mimicking phantom and experimentally measured strain ratios for a lesion at a depth of 3.5 cm and diameter of 2.0 cm. Error bars represent the range of measurements acquired.

As the results seen in Fig. 4.24 show, ARFI imaging was found experimentally to significantly underestimate the stiffness of the stiffest lesions investigated—lesions with nominal stiffnesses of 3.2. For all other lesions investigated, ARFI imaging was shown to overestimate the lesion stiffness slightly. Although it is possible that the true stiffness ratio of the lesions in the phantom do not perfectly align with the manufacturer-reported nominal values, it is also possible that the acoustic radiation force developed by the ARFI transducer was not enough to substantially deform the stiffest of lesions, leading to the stiffness being underestimated.

Fig. 4.25 compares the experimentally-acquired lesion stiffness ratios against measured stiffness ratios arising from parametrically identical simulated lesions. As Fig. 4.25 shows, although the experimentally measured stiffness ratios align well with the simulated stiffness ratios for relatively unstiff lesions ( $E_{rel} < 1$ ), the simulated ARFI procedure was found to underestimate the stiffness of the stiff lesions that were investigated ( $E_{rel} > 1$ ). The exact cause of this disparity is unclear and future work must be done in order to remedy this in the simulations that were performed in order to accurately understand ARFI imaging.

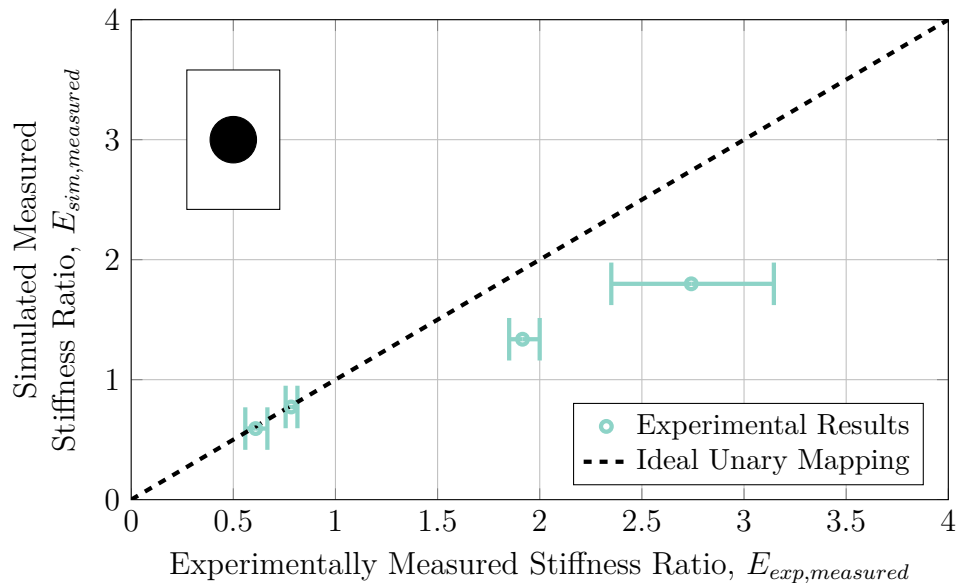


**Fig. 4.25:** Relation between simulated measured strain ratios and experimental measured strain ratios for a lesion at a depth of 3.5 cm and diameter of 2.0 cm.

## 4.4 Conclusion

The results presented in Section 4.3 represent a numerical characterization of the use of acoustic radiation force impulse imaging for the detection of deep tissue injuries including: the distribution of acoustic radiation force generated by transducers; the generalized tissue response to these acoustic radiation

forces; and the use of ARFI imaging to distinguish both early and formative deep tissue injuries from surrounding healthy tissue. Although the principles of operation for ARFI imaging and quasi-static ultrasound elastography are the same—detecting the relative magnitude of deformation in regions of tissue in response to externally applied forces—ARFI imaging presents a key advantage over quasi-static ultrasound elastography in that it allows much greater inter-operator reliability and repeatability. ARFI imaging generates deformation within tissue automatically and without dependence on the operator which is key to developing a successful diagnostic modality.

A key parameter relating to the ability of acoustic radiation force impulses to generate adequate body loads in tissue is the depth at which the radiation force is focused at—increasing depth was found to induce the greatest reduction in the magnitude of the radiation forces and the subsequent magnitude of tissue deformation. This is of concern, as once the magnitude of tissue deformation becomes small enough these deformations will no longer be able to be tracked using conventional ultrasound beams. In order to counteract this, lower frequencies and greater transmit pressures may be used, however care must be taken to ensure the safety of patients undergoing such techniques as the energy resulting from acoustic radiation has the potential to result in tissue damage.

The results shown in Section 4.3.3 show that ARFI imaging is a suitable technique for differentiating both stiff and unstiff lesions from surrounding healthy tissue which may be indicative of deep tissue injury formation and progression. Overall, the detection sensitivity of ARFI imaging is less than ideal with the stiffness of stiff lesions consistently underestimated and the stiffness of unstiff lesions consistently overestimated. ARFI imaging was found to not be dependent on lesion radius above radii of approximately 2.5 mm and

aside from issues with deformation magnitude, the depth of the lesions has no appreciable effect on their detection ability. The amount of lesion blur also did not affect the detection sensitivity, which is advantageous for detecting lesions without clearly defined boundaries. Regions of clustered deep tissue injury lesions were detectable however decreasing the ratio of diseased to healthy tissue area in the lesion resulted in lower detection sensitivities. Lesions were still detectable in the complicated model of MRI-acquired geometry embedded within soft tissue layout extracted from the Visible Human project, although to a slightly lesser extent than uncomplicated hard-boundaried spherical lesions. The overall technique was experimentally validated, however it was found that the simulated lesions underestimated the lesion stiffness compared to their parametrically-identical experimental counterparts.

Future work involving ARFI imaging should investigate the disparity between the experimentally-acquired lesion stiffness ratios and the simulated lesion stiffness ratios in order to increase the validity of the models. In order to truly advance the technology toward its clinical adoption, experimental studies in animals and humans with known deep tissue injuries must be carried out to determine the applicability of ARFI imaging in a real-world setting.

# **Chapter 5**

## **Numerical Characterization of Shear Wave Speed Quantification**

### **5.1 Introduction**

Shear wave speed quantification offers the most desirable method of detecting early deep tissues injuries as it takes the transducer-generated external deformation force that is the chief benefit of ARFI imaging and combines it with a quantitative measure of tissue elasticity rather than the qualitative measures used in both quasi-static elastography and ARFI imaging. Specifically, monitoring the speed of shear waves that are generated in the tissue as a response to a localized acoustic radiation force allows the calculation of tissue stiffness which may again be used as an analogue of tissue health. Further, since the technique is quantitative in nature, tissue stiffness may be accurately tracked over time, enabling physicians to appropriately monitor the progression and treatment of a given deep tissue injury on a per-patient basis.

## 5.2 Method

In order to investigate the sensitivity and applicability of shear wave speed quantification for the early detection of deep tissue injuries, a combination of k-space pseudo-spectral models of acoustic wave propagation and time-domain finite-element models of tissue deformation were employed. The theory and procedure behind both the generalized acoustic simulations using k-space pseudo-spectral models and time-dependent solid mechanics finite-element models used here were presented in Chapter 4. As an alternative to monitoring the dynamic response of tissue at the focal point as in ARFI imaging, shear wave speed quantification tracks the velocity of shear waves which radiate laterally outward from the focal point of an ARFI load. If the focal point is positioned such that the generated shear waves propagate through a lesionous region and the speed of the generated shear wave is monitored, the stiffness of that region may be calculated.

### 5.2.1 Shear Wave Speed

The foundation of shear wave speed quantification with regards to detecting lesionous regions lies in the quantifiable relationship between shear wave speed and tissue stiffness. This relationship is derived here, assuming a linear elastic, isotropic material. Soft tissue is generally considered a viscoelastic material and as such modifications to the linear elastic wave speed are taken into account.

Equation 5.1 represents the constitutive equation of a linear elastic material where the strain tensor is defined as per equation 5.2 such that equation 5.3 holds true.

$$\sigma_{ij} = \lambda_{tissue} \delta_{ij} \varepsilon_{kk} + 2\mu \varepsilon_{ij} \quad (5.1)$$

$$\varepsilon_{ij} = \frac{1}{2} (u_{i,j} + u_{j,i}) \quad (5.2)$$

$$\sigma_{ij} = \lambda_{tissue} \varepsilon_{ii} \delta_{ij} + \mu (u_{i,j} + u_{j,i}) \quad (5.3)$$

Neglecting time-invariant body loads, the balance of linear momentum is given for a linear elastic continuum is given in equation 5.4.

$$\sigma_{ij,j} = \rho \ddot{u}_i \quad (5.4)$$

Substituting equation 5.3 into equation 5.4 yields equation 5.5 which may be rearranged into equation 5.6 by noting that  $\varepsilon_{ii,j} = u_{j,ij}$ .

$$\lambda_{tissue} \varepsilon_{ii,j} + \mu (u_{i,jj} + u_{j,ij}) = \rho \ddot{u}_i \quad (5.5)$$

$$\rho \ddot{u}_i = (\lambda_{tissue} + \mu) u_{j,ji} + \mu u_{i,jj} \quad (5.6)$$

Utilizing the Helmholtz decomposition of the particle displacement given in equation 5.7, equation 5.6 becomes equation 5.8.

$$u_i = \partial_i \phi + \varepsilon_{ijk} \partial_j \psi_k \quad (5.7)$$

$$\nabla [(\lambda_{tissue} + 2\mu) \nabla^2 \phi - \rho \ddot{\phi}] + \nabla \times [\mu \nabla^2 \vec{\psi} - \rho \ddot{\vec{\psi}}] = 0 \quad (5.8)$$

Examining the transverse propagation component of equation 5.8 in one direction yields the familiar shear wave equation given in equation 5.9 such

that the shear wave speed is given by equation 5.10.

$$0 = \frac{\partial^2 \vec{\psi}}{\partial x^2} - \frac{\rho}{\mu} \frac{\partial^2 \vec{\psi}}{\partial t^2} \quad (5.9)$$

$$c_T = \sqrt{\frac{\mu}{\rho}} \quad (5.10)$$

While the above equation holds for linear elastic materials, soft tissues in the human body are generally considered viscoelastic [138], [139]. In the case of viscoelastic tissues, complex Lamé parameters must be used, such that the shear wave speed is represented by equation 5.11 [123]. Note that viscoelastic shear wave speeds of viscoelastic tissues are generally acquired through empirical measurements rather than any sort of mathematical derivation [140], [141].

$$c_T = \sqrt{\frac{\mu^*}{\rho}} \quad (5.11)$$

### 5.2.2 Model Set Up

In order to study the feasibility of using shear wave speed quantification to detect and monitor deep tissue injuries, a collection of deep tissue injury models were investigated including: spherical lesions with hard and unstiff boundaries, clusters of small lesions that make up a larger lesionous region, and a lesion with MRI-acquired geometry [67] embedded in geometry obtained from a Visible Human slice [126]. Each model investigated numerous parameters relating to the detection of lesions including ARFI focal depth, ARFI interrogation frequency, lesion size, distance of the focal point from the lesion (lesion offset), lesion blur radius, clustered lesion density, the size of individual lesions in the clustered lesion model, and the size and altitude of the lesion in the Vis-

ible Human model. The range of parameters investigated for each model are summarized in Table 5.1.

Figs. 5.1 portray the schematics of the lesion models investigated. Note that shear wave speed quantification typically applies the acoustic radiation force impulse to a location of tissue adjacent to the desired region such that the shear waves are fully developed by the time they reach the investigated region.

**Table 5.1:** Range of values of investigated parameters

Parameter	Symbol	Values	Units
Lesion depth	$d$	1, 2, 3, 4, 5, 6, 7, 8, 9	cm
Lesion diameter	$\phi S$	0.5, 1.0, 2.0, 2.5	cm
Lesion offset	$d_{off}$	0.00, 1.25, 2.50, 3.75	cm
Lesion stiffness ratio	$E_{rel}$	0.32, 0.56, 1.80, 3.20	
Blurred lesion blur radius	$b_r$	1.0, 2.5, 5.0, 7.5	mm
Clustered lesion density	$b_\rho$	10, 20, 30, 40	$\text{cm}^{-2}$
Clustered lesion radius	$r_{bl}$	0.5, 1.0, 1.5	mm
Visible human lesion width	$\phi L$	0.5, 1.0, 2.0, 2.5	cm

In all the shear wave speed quantification models, the acoustic radiation force and time-domain finite-element models of tissue deformation were the same as were used in the ARFI imaging simulations in Chapter 4 and described in Sections 4.2.1 – 4.2.3. The difference with the shear wave speed quantification presented here and the ARFI imaging presented in Chapter 4 lies in the the data that was extracted and processed from the time-domain finite-element models of tissue displacement. A discussion of how shear wave speeds are tracked in the finite-element model of tissue deformation is given in Section 5.3.2 by working though a sample dataset result.

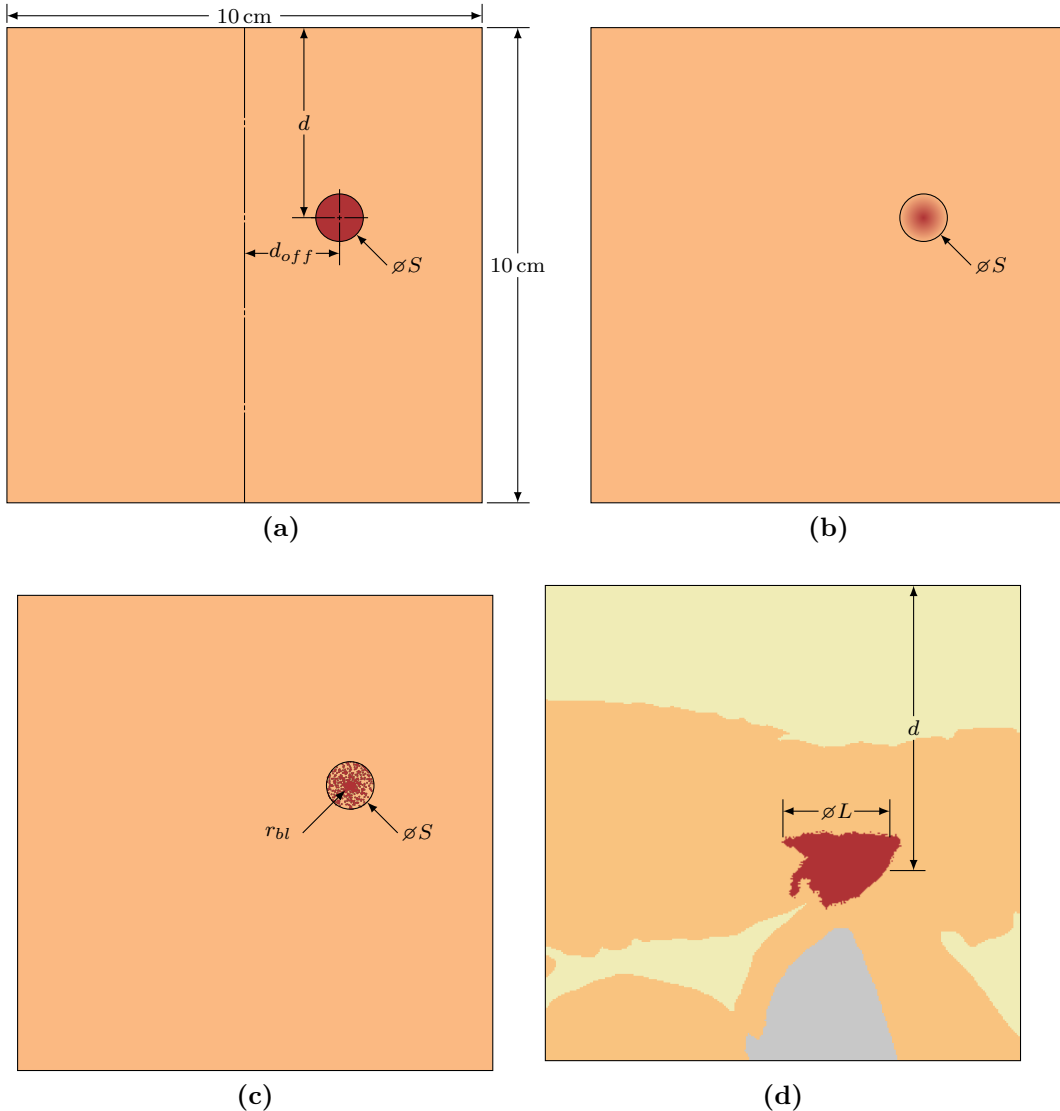


**Fig. 5.1:** Schematics of the lesion models that were investigated using shear wave speed quantification showing (a) a spherical hard-boundaried lesion, (b) a spherical blurred-boundary lesion, (c) a cluster of numerous small lesions composing a larger lesionous region, and (d) the geometry from an MRI-acquired deep tissue injury overlaid on a slice from the Visible Human Project such that the injury lesion was located immediately superior to an ischial tuberosity.

### 5.2.3 Model Validation

In order to validate the results presented in Section 5.3, a subset of the results were compared with experimental results obtained with a physical tissue mimicking phantom. The phantom used was the same CIRS Elasticity QA Phantom model 049 that was used in Chapter 3. The phantom models both

stiff and unstiff lesions at two different depths and lesion sizes. The material properties of the phantom are listed in Table 3.2. Both tissue and lesion shear wave speeds were acquired using a Siemens AG ACUSON S2000<sup>TM</sup> ultrasound system running the Virtual Touch<sup>TM</sup> Quantification unstiffware suite with a Siemens 9L4 transducer. Measures of relative lesion stiffness were calculated as per equations 5.12 in an identical fashion to the simulated lesion cases and experiments were carried out over 10 trials for each investigated nominal lesion stiffness ratio. The detailed experimental protocol that was followed for these validations is given in Section C.3 in Appendix C.

## 5.3 Results and Discussion

Following the procedure outlined in Section 5.2, k-space models of ultrasound acoustics and finite-element models of temporal soft tissue deformation were synthesized and the resulting shear wave speeds developed in the tissue were analyzed according to the method laid out in Section 5.3.2. These shear wave speeds were used to calculate the relative stiffnesses of a variety of lesions with varying parameters as described in Section 5.2.2 which were then used to numerically characterize the use of shear wave speed quantification for the detection of early deep tissue injuries. The results of this characterization are presented here.

### 5.3.1 Acoustic Radiation Force Impulse Simulations

Since the acoustic radiation force impulse simulations were run in exactly the same manner for shear wave speed quantification as in the ARFI imaging presented in Chapter 4, the results are identical—see Section 4.3.1 for the results. For completeness, the force distribution which generated the shear

waves studied in Section 5.3.2 is plotted in Fig. 5.2. against a schematic of the lesion in order to better visualize the shear wave speed quantification process. Fig. 5.2 shows the focal line of the shear wave speed quantification technique, along which the axial displacement of the tissue is continuously monitored in order to calculate the localized shear wave speed of the tissue. This focal line extends laterally from the focal point of the acoustic radiation force impulse through the lesion to the edge of the tissue domain.

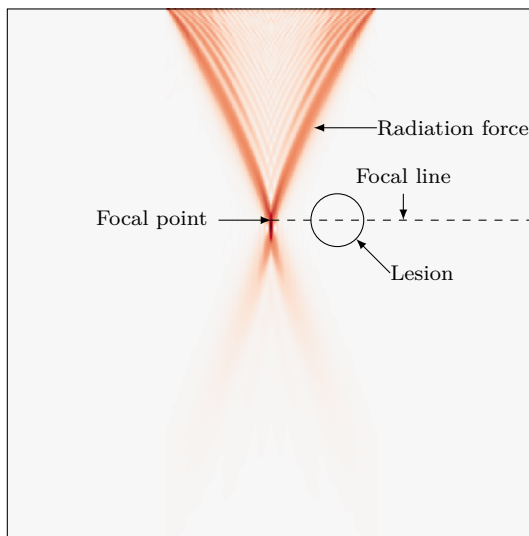


**Fig. 5.2:** A sample acoustic radiation force distribution shown with a schematic of the lesion's location and size in the simulated tissue domain. Note how the focal point is adjacent to the lesion, offset in this case by 1.25 cm. The focal line extends laterally from the focal point, through the lesion, to the edge of the tissue domain—this is the line that will be used to calculate shear wave speeds.

### 5.3.2 Sample Shear Wave Speed Measurement

Although measuring the shear wave speed of tissue may quantify the tissue stiffness through equation 5.11, the results presented here represent the measured stiffness ratio of lesions in order to present continuity with Chapters 3 and 4. In all cases where relative lesion stiffness is presented, it was calculated through comparison of the mean shear wave speed in the defined lesion region

with the mean shear wave speed outside of the lesion region along the path of the lateral shear wave radiation direction. Specific ratios may be calculated using equation 5.12 where  $E_{rel}$  is the relative stiffness ratio,  $\mu_l$  and  $\mu_t$  are Lamé's second parameter for the lesion and tissue respectively,  $c_{T,l}$  and  $c_{T,t}$  are the shear wave speeds in the lesion and tissue respectively, and  $\rho$  is the density of the tissue and assumed to be constant between the lesion and tissue.

$$c_T = \sqrt{\frac{\mu}{\rho}} \quad (5.12a)$$

$$c_T^2 \rho = \mu \quad (5.12b)$$

$$E_{rel} = \frac{\mu_l}{\mu_t} = \left( \frac{c_{T,l}}{c_{T,t}} \right)^2 \quad (5.12c)$$

In order to determine the velocity of generated shear waves, the ARFI load-induced displacement of the soft tissue must be tracked through time along a line passing through the focal point radiating laterally outward in the finite-element model of tissue deformation. A sample result of tissue displacement through time and along such a line is presented in Fig. 5.3 where the wave can be readily visualized through time, noting that the wave travels ever further from the centreline.

The results in Fig. 5.3 represent a finite subsample of the shear wave's propagation along the focal line. For a continuous representation of the shear wave propagation, the surface shown in Fig 5.4 may be constructed. In order to track the wave through both position and time, a contour line representing a constant displacement value may be extracted. For this work, a contour line representing the mean value of the displacement over the entire position-time domain was utilized and is portrayed in Fig. 5.5.

Fig. 5.6 represents the extracted contour line. This contour line now

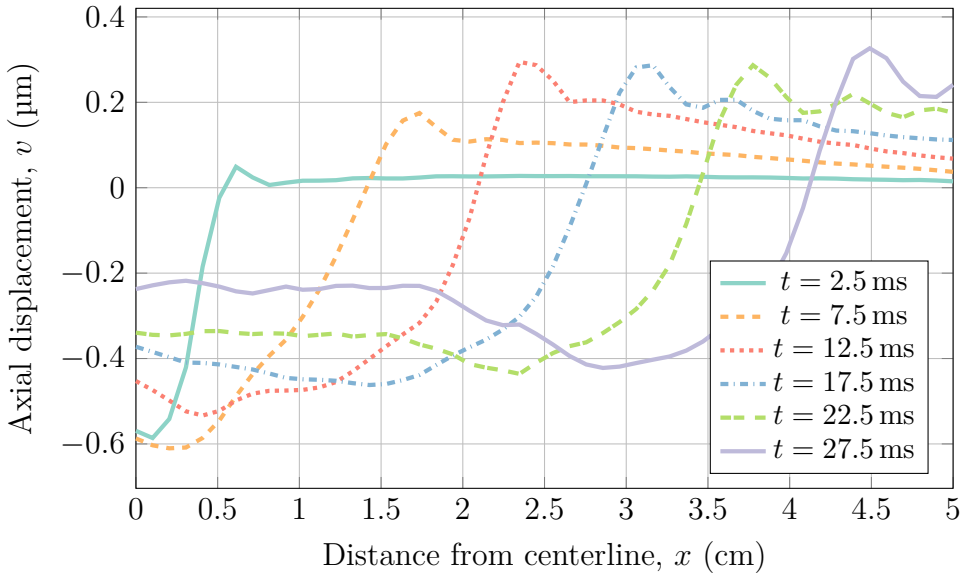


**Fig. 5.3:** Axial displacement induced by a shear wave traveling laterally across the focal line of an ARFI load. There is a stiff ( $E_{\text{rel}} = 3.2$ ) lesion with a diameter of 1 cm located 1.25 cm away from the centerline, with both the focal line and the lesion located at a depth of 4 cm from the surface.

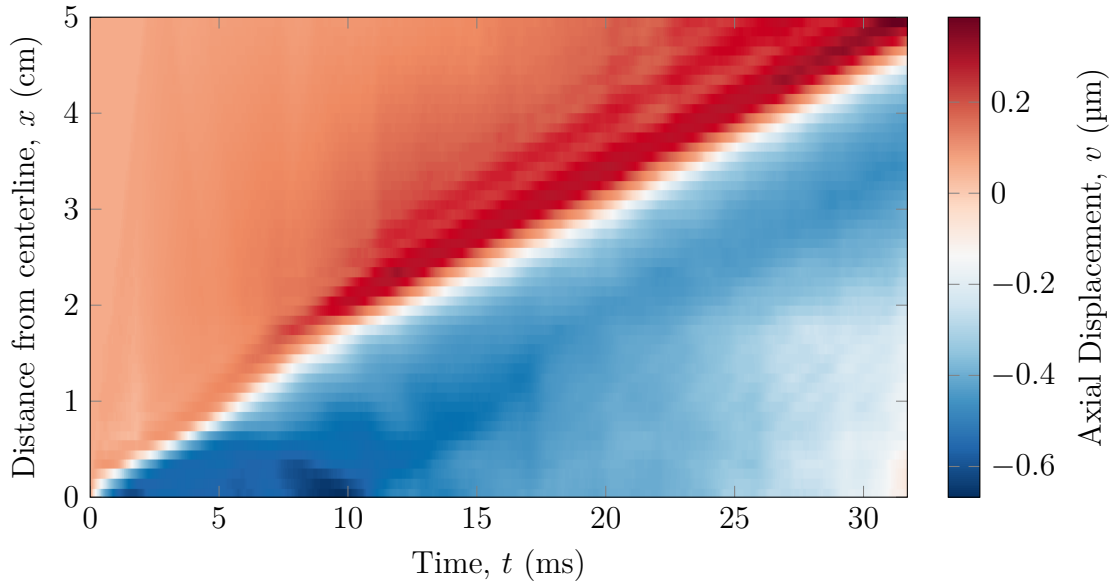


**Fig. 5.4:** Continuous surface plot of the shear wave induced axial displacement tracked through both time and distance from the transducer centreline. The sharp transition from negative to positive displacement marks the location of shear wave in time at any given location.

represents a position-time trace of the shear wave, from which the velocity of the wave may be calculated by differentiating the position of the wave with

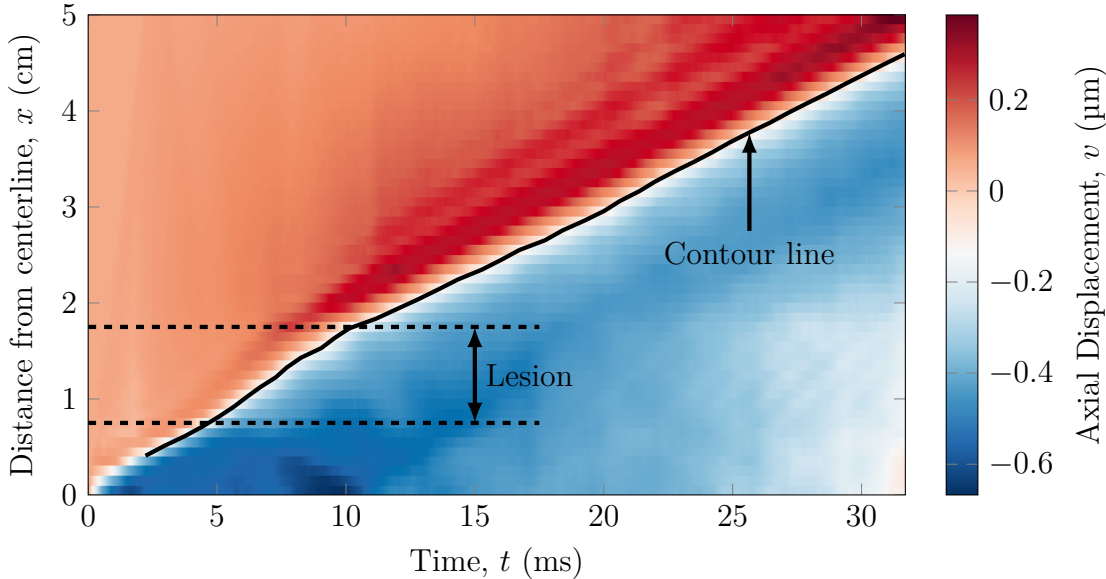


**Fig. 5.5:** Continuous surface plot of shear wave induced axial displacement highlighting a mean contour line representing the shear wave location as time progresses. By inspection, the slope of the contour line is greater within the lesionous region than outside of it, suggesting that the lesion is stiffer than the surrounding tissue.

respect to time as per equation 5.13. Care must be taken when numerically differentiating, as numerical errors are greatly amplified by differentiation. To combat this, a moving window average filter with a kernel of 5 mm was applied to the position-time curve before centre-difference differentiation was used to result in the shear wave speed graph given in Fig. 5.7. Sample source code used to extract and generate the shear wave speed plot is given in listing B.6 in Appendix B.

$$c_T = \frac{dx}{dt} \quad (5.13)$$

As is shown in Fig. 5.7, the speed of the shear wave within the lesion (which was in this case 3.2 times as stiff as the surrounding tissue) is substantially greater than the shear wave speed in the regular tissue. Note that instead of an impulse response at the boundaries of the lesion as might be expected, the shear wave speed reaches a peak value approximately halfway through the

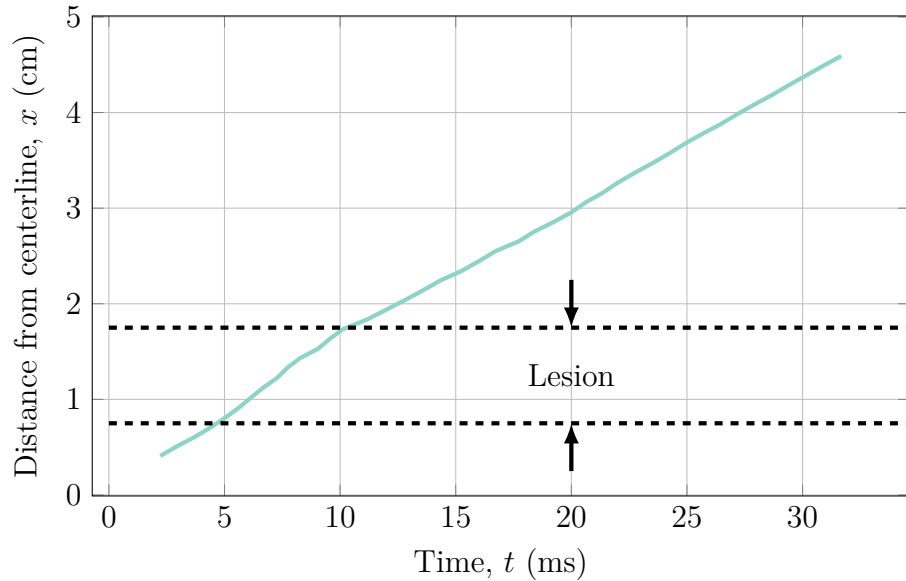


**Fig. 5.6:** The extracted shear wave position-time trace showing the location of the generated shear wave increases with time, albeit at different rates depending on the underlying tissue properties.

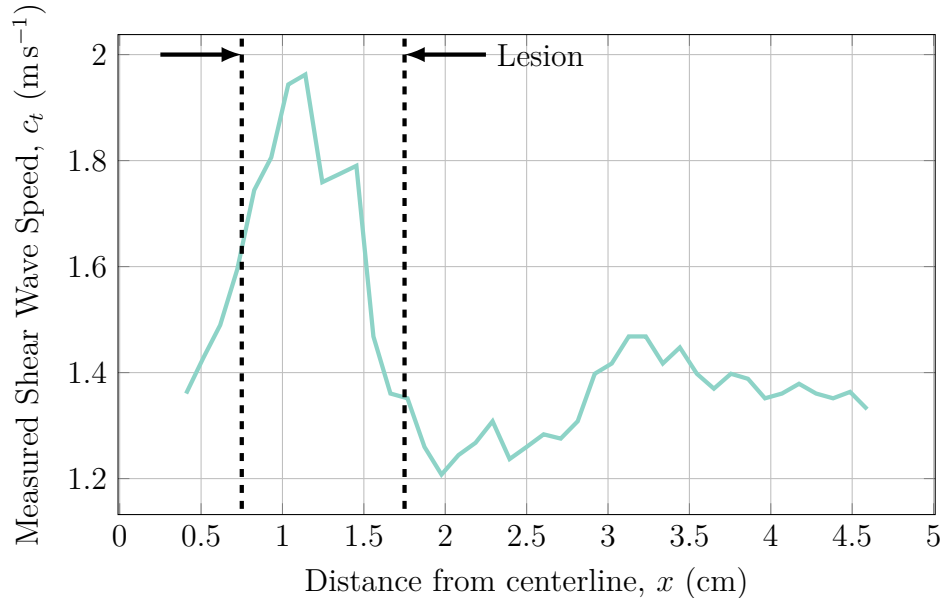


**Fig. 5.7:** Trace of the shear wave speed along the focal line through both lesionous and “healthy” tissue. The shear wave speed within the lesion is much greater than the shear wave speed through the “healthy” tissue, indicating that the lesion is significantly stiffer than the surrounding tissue. The shear wave speed was calculated as the numerical differentiation of the shear wave’s position through time.

lesion, indicating that the wave requires some finite amount of time to both speed up and slow down within the lesion, suggesting that the technique may have difficulty identifying small lesions as the shear wave speed will not be able to fully adjust to the lesion in the time it takes for the wave to completely pass through the lesion.

### 5.3.3 Lesion Detection Characterization

In order to determine the detection sensitivity of shear wave speed quantification with respect to lesion size, hard-boundaried spherical lesions with varying radii were interrogated using ARFI loads while the speed of the shear waves developed along the focal line were monitored. The ARFI loads were applied using a probing frequency of 2 MHz for 150  $\mu$ s with a source pressure of 3.35 MPa using an F-number of  $f/1.0$ . The lesions were located at a depth of 4 cm with an offset of 1.25 cm from the focal point of the ARFI load. The results of this characterization are given in Fig. 5.8. Lesions stiffness ratios were measured by calculating the maximum or minimum shear wave speed within the lesion if the shear wave speed within the lesion was greater than or less than the surrounding tissue respectively and the mean shear wave speed without the lesion and applying equation 5.10.

As can be seen in Fig. 5.8, small lesions with radii  $\leq 5.0$  mm are nearly impossible to detect—large changes in the true lesion stiffness ratio represent very minute changes in the measured lesion stiffness ratio for these small lesions. Conversely, large lesions are much easier to detect, portraying a nearly one-to-one or better mapping between the true and measured lesion stiffness ratios. This suggests that the larger a lesion is, the more readily it may be detected while smaller lesions are more difficult to detect with a lower limit of the lesion radius approaching 5.0 mm.

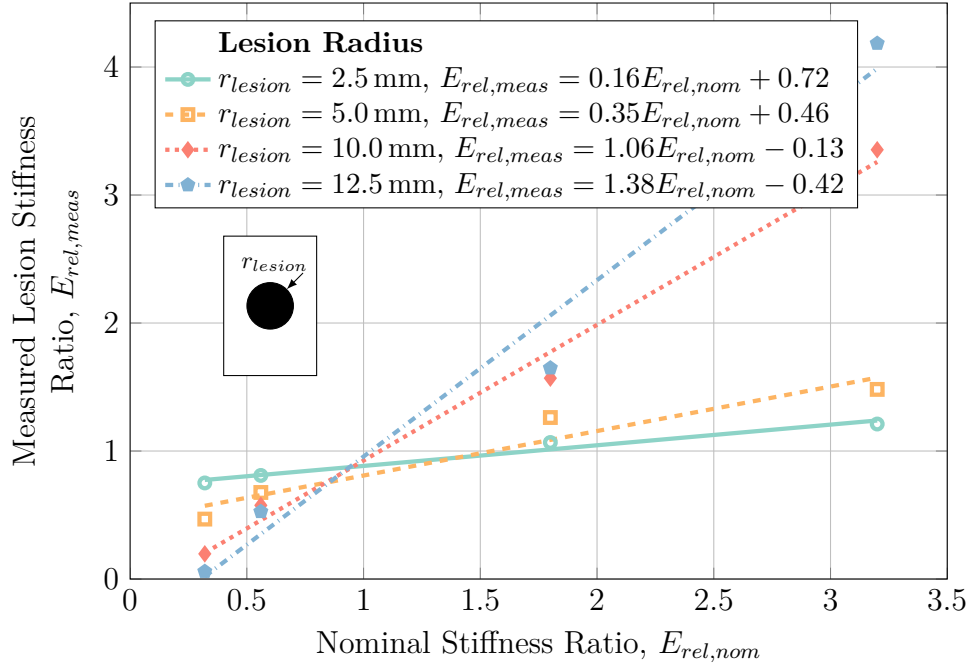


**Fig. 5.8:** Numerical characterization of the shear wave speed measured stiffness ratios acquired with varying lesion radii for a hard-boundaried lesion at a depth of 4 cm using an ARFI interrogation frequency of 2 MHz.

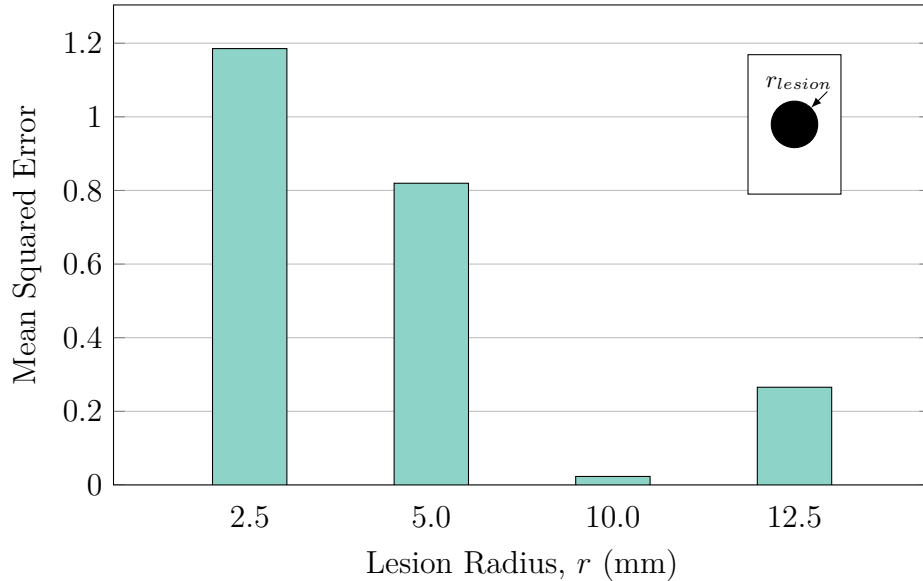


**Fig. 5.9:** Mean squared error between the true and measured lesion stiffness ratios for increasing lesion radii for a hard-boundaried lesion at a depth of 4 cm using an ARFI interrogation frequency of 2 MHz.

To further investigate these results, the mean-squared error associated with varying lesion size was calculated as per equation 4.17 with the results pre-

sented in Fig. 5.9. In Fig. 5.9, it is clear to see that the error associated with small lesions was significantly greater than with larger lesions. Interestingly, the largest lesions tested (with radii of 12.5 mm) presented greater error than lesions with radii of 10.0 mm. This increase in error may be largely attributed to the over-estimation of the lesion stiffness ratio for a stiff ( $3.2 \times$  basal stiffness) lesion with a radius of 12.5 mm seen in Fig. 5.8.

One of the key parameters used in shear wave speed quantification is the distance between the focal point of the acoustic radiation force and the lesion itself. In order to adequately generate fully-formed shear waves within the lesion, the focal point of acoustic radiation force should be located adjacent to the lesion. As can be seen in Fig. 5.10, regardless of the lesion offset distance, shear wave speed quantification is able to differentiate lesions from the tissue with reasonable accuracy. The largest exception to this generalization is for very stiff lesions for which the ARFI load is focused the farthest away from the lesion. It is hypothesized that the measured stiffness ratio of these lesions is underestimated because by the time the shear wave reaches the relatively far-away lesion, its energy has substantially dissipated, disallowing the wave to remain fully cohesive and speed up appropriately.

Fig. 5.11 portrays the mean squared error between the measured and true lesion stiffness ratios with increasing lesion offset distance. As Fig. 5.11 shows, a lesion offset of approximately 2.5 cm is ideal for quantifying lesion stiffness as it produces the least amount of error between the true and measured lesion stiffness ratios which confirms the notion that the shear wave needs some time to become fully developed as it travels through the tissue. Since the error between lesion offsets of 1.25 cm and 2.50 cm is nearly negligible, it is likely that the wave is able to become fully developed even earlier than 2.50 cm and lesion offsets as small as 1.25 cm may be used. The relatively large error

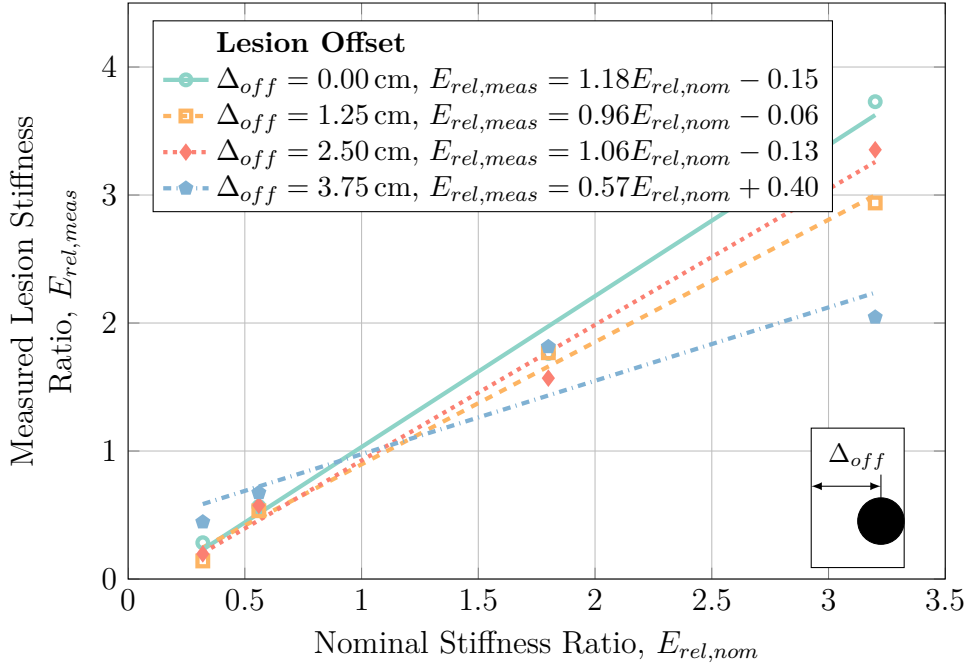


**Fig. 5.10:** Numerical characterization of the shear wave speed measured stiffness ratios acquired with varying lesion offsets for a hard-boundaried 0.5 cm radius lesion at a depth of 4 cm using an ARFI interrogation frequency of 2 MHz. The greatest error between the true and measured stiffness ratios occurred at the highest stiffness ratio of 3.2, with the large lesion offset underestimating the stiffness ratio and the negated lesion offset overestimating the stiffness ratio.

present for the largest lesion offset of 3.75 cm is largely due to the severe underestimation of the lesion stiffness for the stiffest lesion seen in Fig. 5.10.

Another key parameter relating to the detection of deep tissue injury lesions relates to the depth that the lesions may actually be detected—for example, in people with large amounts of body fat or muscle, the distance between the surface of the skin and the boney prominence where lesions are most likely to form may be very large compared to someone with very little amounts of body fat or muscle. In order to study the effect of lesion depth on the detection sensitivity of shear wave speed quantification, simulated lesions were placed at various depths ranging from 2 cm – 8 cm below the surface of the skin with the measured stiffness ratios for these lesions calculated and shown in Fig. 5.12.

As Fig. 5.12 shows, there is little dependence of shear wave speed quan-

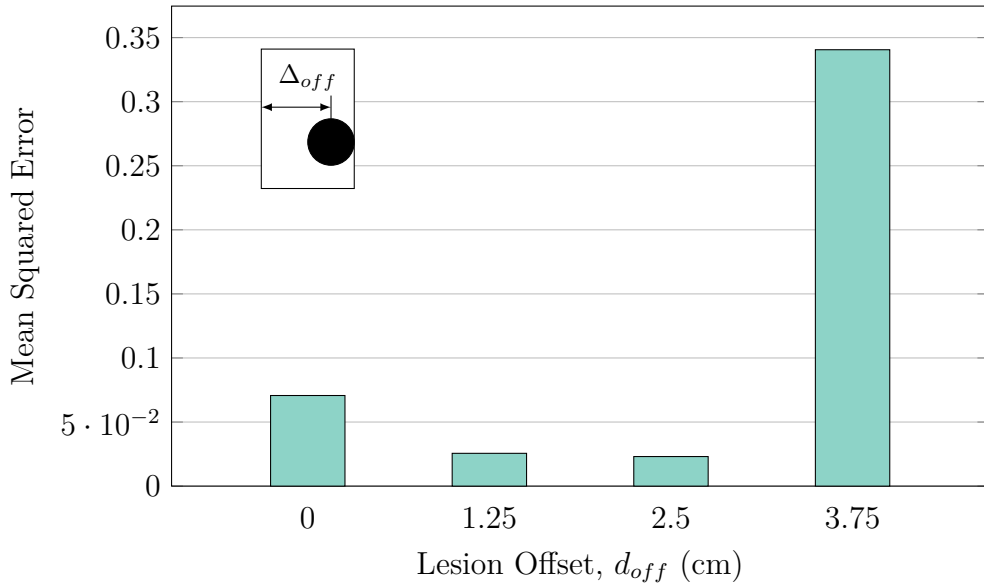


**Fig. 5.11:** Mean squared error between the true and measured lesion stiffness ratios for increasing lesion offsets for a hard-boundaried 0.5 cm radius lesion at a depth of 4 cm using an ARFI interrogation frequency of 2 MHz.

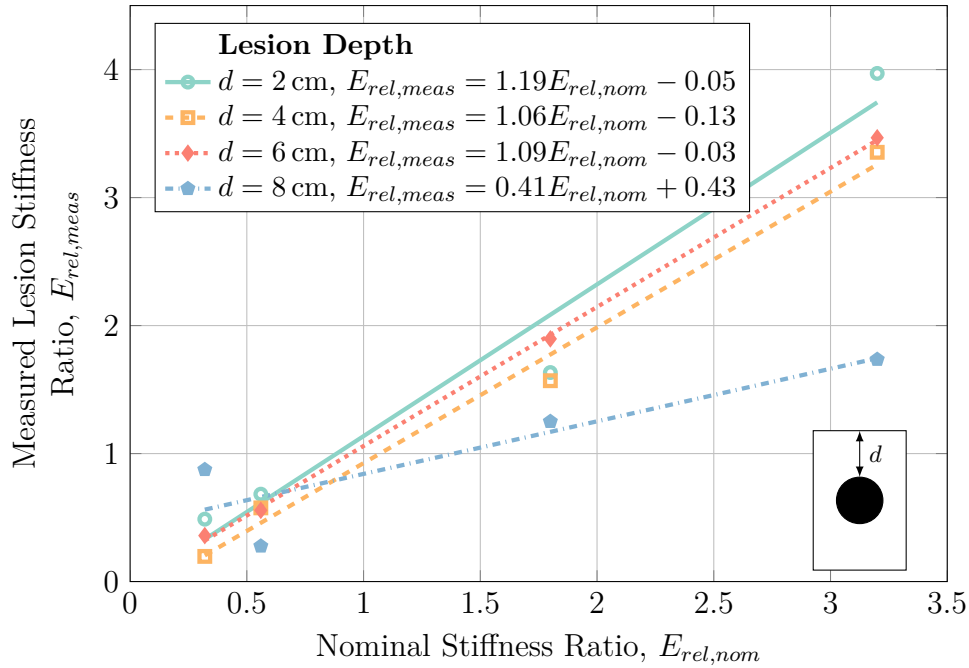


**Fig. 5.12:** Numerical characterization of the shear wave speed measured stiffness ratios acquired with varying lesion and focal point depths for a hard-boundaried 0.5 cm radius lesion with an offset of 2.50 cm using an ARFI interrogation frequency of 2 MHz.

tifications detection sensitivity for shallow to medium-depth lesions—lesions placed at a depth of 2 cm – 6 cm presented approximately equal detection curves. Of note in Fig. 5.12 is that deep lesions—lesions at a depth of 8 cm or more—are difficult to detect as the method is not very sensitive to these deeper lesions—both underestimating the stiffness of deep stiff lesions and overestimating the stiffness of deep unstiff lesions. The large error involved with attempting to measure the stiffness of deep lesions can be seen in Fig. 5.13 where the mean squared error for the various depths examined was calculated. In Fig. 5.13, the 8 cm deep lesions present a significantly greater amount of error than their shallower counterparts. Also of note is that the shallowest lesions investigated—lesions at a depth of 2 cm—presented with greater error than the mid-depth lesions. The source of this error largely lies in the overestimation of the stiff lesion stiffness seen in Fig. 5.12 which may be due to numerical errors in the models and calculations.

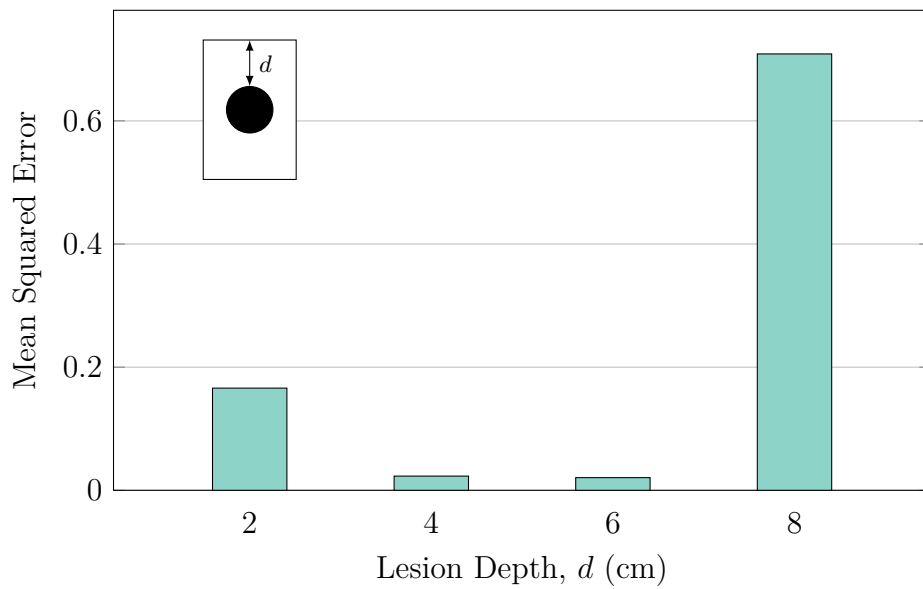


**Fig. 5.13:** Mean squared error between the true and measured lesion stiffness ratios for increasing lesion depths for a hard-boundaried 0.5 cm radius lesion with an offset of 2.50 cm using an ARFI interrogation frequency of 2 MHz.

Since deep tissue injury lesions are unlikely to be perfectly round and

hard-boundaried, three different models of lesion geometry were investigated—namely, lesions with blurred boundaries that “fade” into the surrounding tissue, clusters of small lesions that together make up a larger lesions region, and a lesion with MRI-acquired geometry [67] embedded in geometry obtained from a Visible Human slice [126]. Although the spherical hard-boundaried lesions may not represent all the intricacies of real deep tissue injuries, the general trends that result from analysing them may improve the general understanding of lesion detection behaviour.

In order to investigate the effect of blurring lesions into the background tissue, hard-boundaried spherical lesions were blurred with varying blur radii as described in Section 5.2.2. The results of this characterization are presented in Fig. 5.14. As can be seen in Fig. 5.14, the effect of blur radii on lesion detection ability is negligible as noted by how the detection curves of the lesions with varying blur radii are largely coincident.

This lack of reliance of detection sensitivity on blur radius is further portrayed by the mean squared error of the results, calculated in Fig. 5.15. While there are some minor differences in the error between the various blur radii—chiefly between blur radii of 2.5 mm and 5.0 mm—the scale of these differences lie within the range of numerical error and noise and so are not significant.

The fact that detection sensitivity does not decrease with increasing blur radii in shear wave speed quantification makes shear wave speed quantification a desirable tool for detecting deep tissue injury lesions as it means that even imperfect, newly-forming lesions can still be readily detected and monitored.

Beyond having boundaries that “fade” into the background tissue, deep tissue injury lesions may in fact be heterogeneous in nature with a large number of small lesions clustered together to form a larger lesionous region. To investigate this phenomenon, the effect of small clustered lesion density and

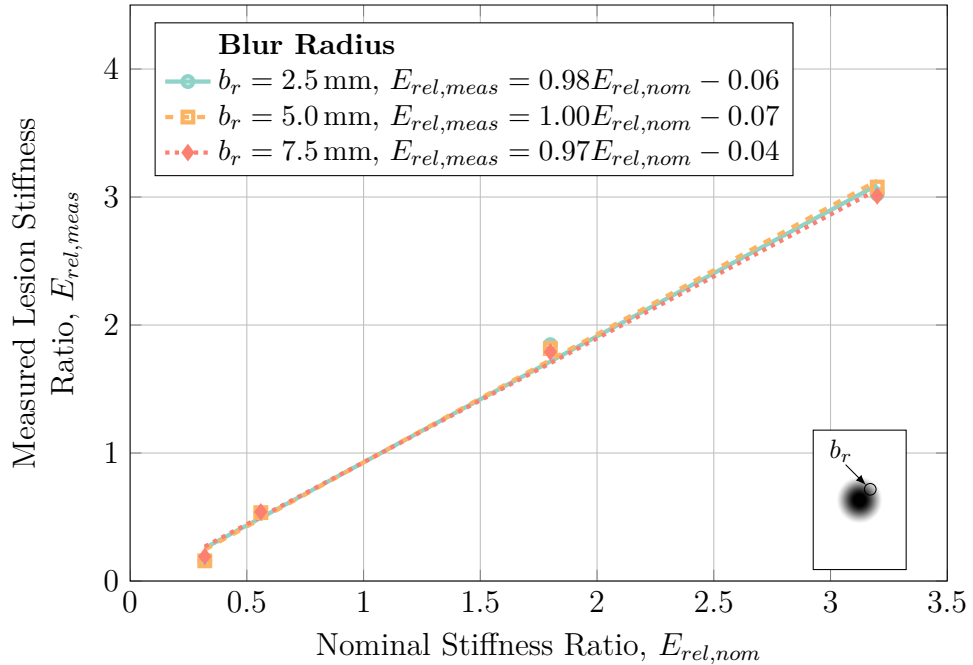


**Fig. 5.14:** Numerical characterization of the shear wave speed measured stiffness ratios acquired with varying lesion and focal point depths for a blurred 1.0 cm radius lesion with an offset of 1.25 cm at a depth of 4 cm using an ARFI interrogation frequency of 2 MHz.

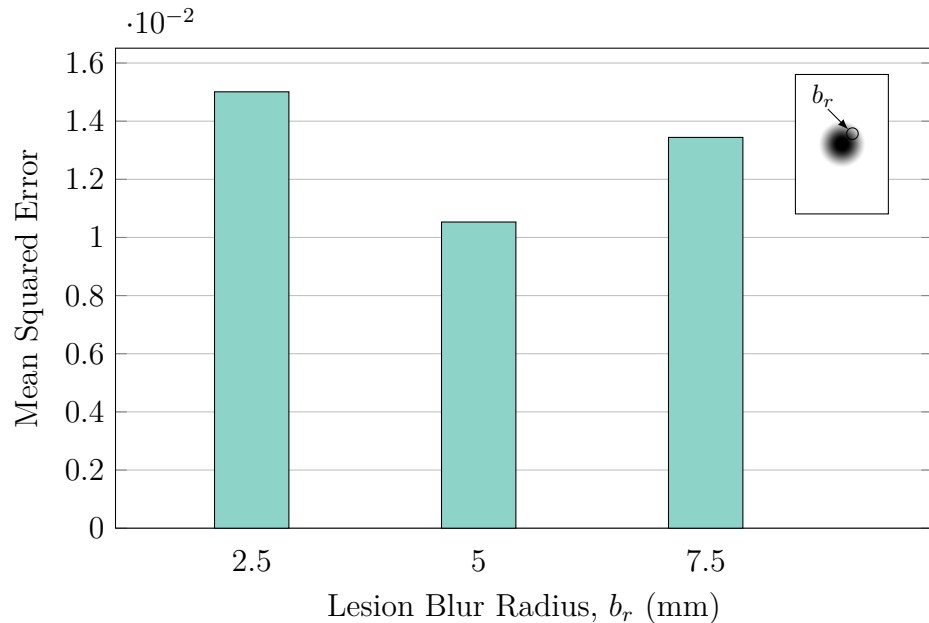


**Fig. 5.15:** Mean squared error between the true and measured lesion stiffness ratios for increasing lesion depths for a blurred 1.0 cm radius lesion with an offset of 1.25 cm at a depth of 4 cm using an ARFI interrogation frequency of 2 MHz.

individual radii were investigated using shear wave speed quantification. The effect of clustered lesion density was investigated as outlined in Section 5.2.2, the results of which are shown in Fig. 5.16.

As Fig. 5.16 shows, decreasing the cluster density generally results in a decreasing detection sensitivity with the least dense clusters both underestimating the stiffness of stiff lesions and overestimating the stiffness of unstiff lesions. This behaviour is somewhat expected—as the density of clustered lesions decreases, so too does the mean true stiffness of the lesionous region that is inspected due to the greater ratio of “healthy” tissue to lesionous tissue.

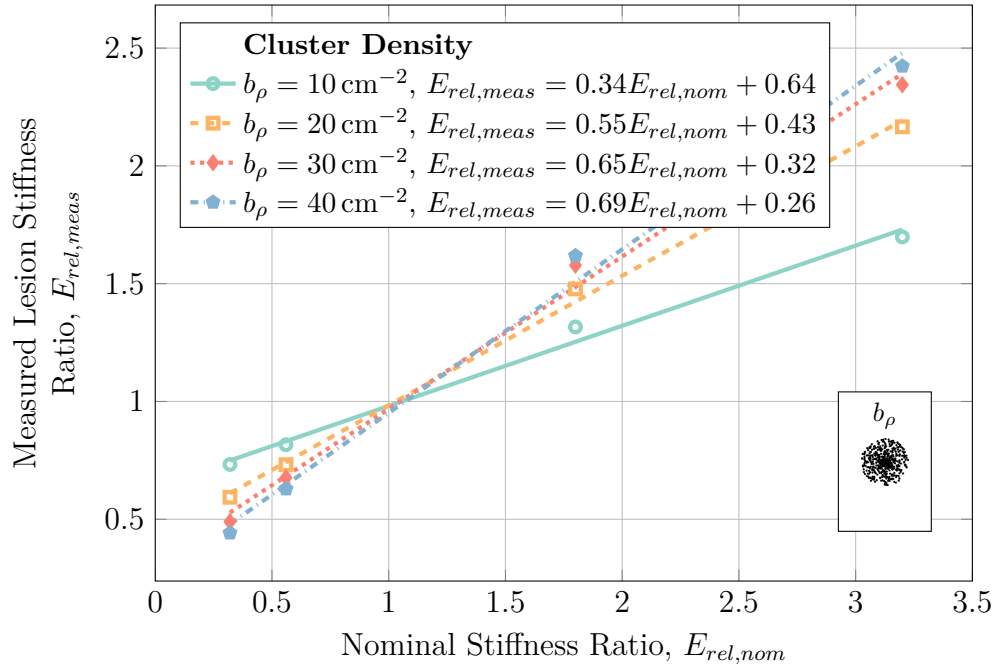


**Fig. 5.16:** Numerical characterization of the shear wave speed measured stiffness ratios acquired with varying cluster densities for clustered 1 mm radius lesions within a 1.0 cm radius with an offset of 1.25 cm at a depth of 4 cm using an ARFI interrogation frequency of 2 MHz.

This generalization is further portrayed by the mean squared error which is shown in Fig. 5.17. In Fig. 5.17, increasing cluster density results in monotonically decreasing error.

Beyond the cluster density, the size of individual clustered lesions within

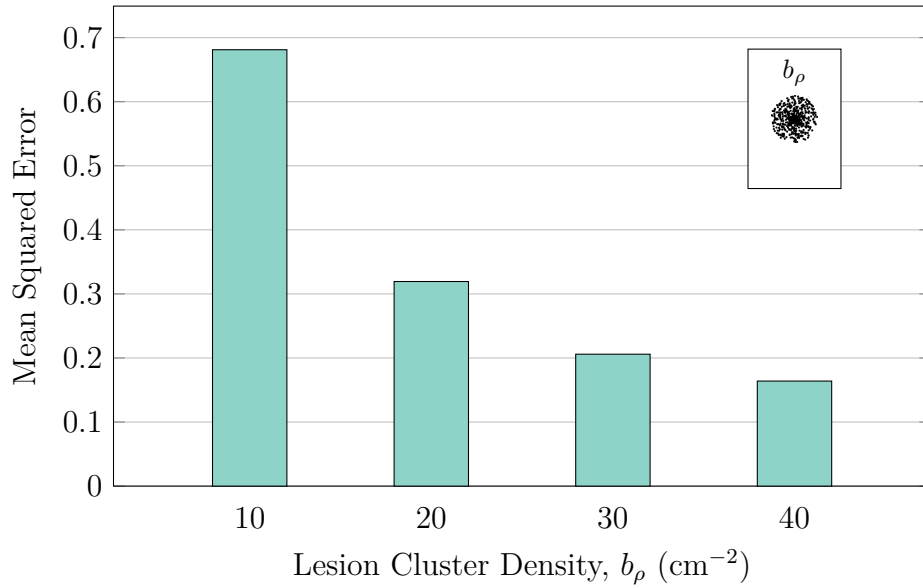


**Fig. 5.17:** Mean squared error between the true and measured lesion stiffness ratios for increasing lesion cluster density for clustered 1 mm radius lesions within a 1.0 cm radius with an offset of 1.25 cm at a depth of 4 cm using an ARFI interrogation frequency of 2 MHz.

the lesionous region may affect the detection sensitivity. To investigate this parameter, the radii of the individual lesions in the clustered lesion model were varied, with the results presented in Fig. 5.18. Fig. 5.18 shows how decreasing the individual clustered lesion radii results in decreases in the detection sensitivity. This is similar to the results presented in Fig. 5.16 in that decreasing the individual lesion radii results in a decrease of the ratio between lesionous tissue and healthy tissue within the lesionous region—the greater the proportion of lesionous tissue within the investigated region, the more accurate the detection of the lesionous region.

Again, this conclusion is corroborated by the mean squared error shown in Fig. 5.19. In Fig. 5.19, increasing the individual lesion radii results in a significant decrease in the stiffness measurement error in the lesionous region.

Finally, in order to place these characterizations within the context of a real deep tissue injury situated within the geometry of a real human soft tis-

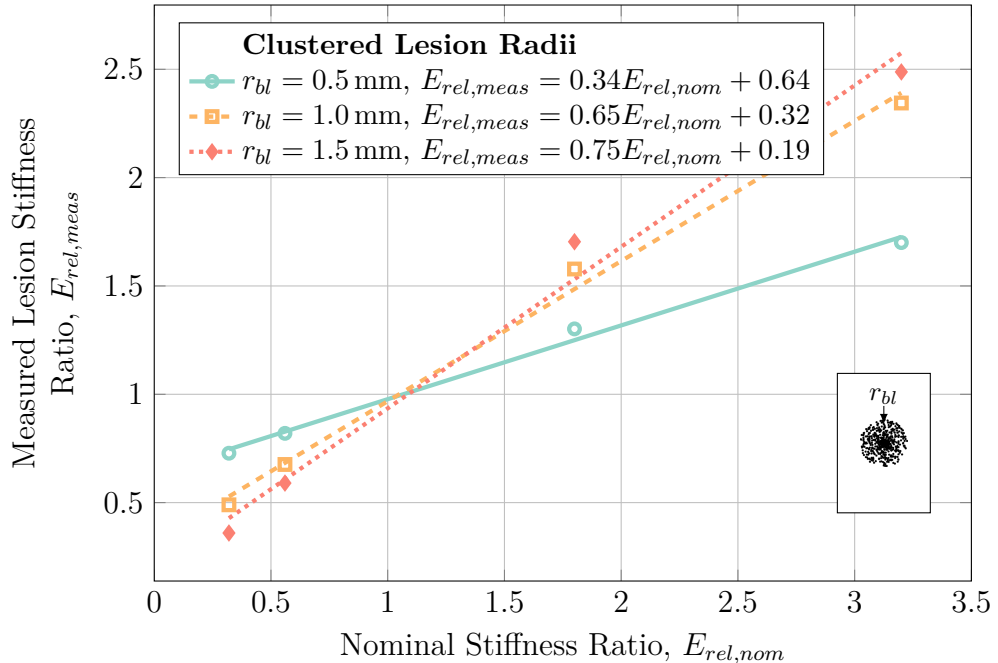


**Fig. 5.18:** Numerical characterization of the shear wave speed measured stiffness ratios acquired with varying clustered lesion radii for clustered lesions with a density of  $30 \text{ cm}^{-2}$  within a 1.0 cm radius with an offset of 1.25 cm at a depth of 4 cm using an ARFI interrogation frequency of 2 MHz.

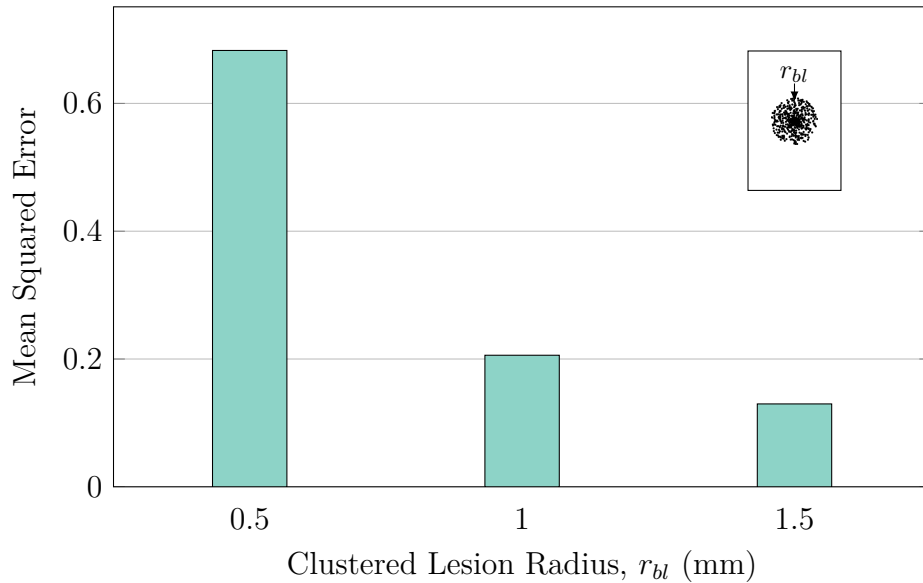


**Fig. 5.19:** Mean squared error between the true and measured lesion stiffness ratios for increasing clustered lesion radii for clustered lesions with a density of  $30 \text{ cm}^{-2}$  within a 1.0 cm radius with an offset of 1.25 cm at a depth of 4 cm using an ARFI interrogation frequency of 2 MHz.

sue domain, a numerical characterization of lesion size in the Visible Human lesion model outlined in Section 5.2.2 was carried out with the results portrayed in Fig. 5.20. Fig. 5.20 relates the change in detection sensitivity with different sized lesions and shows that small lesions (with “radii”  $\leq 5.0$  mm) are extremely difficult to detect as the stiffness of small stiff lesions is severely underestimated and the stiffness of small unstiff lesions is severely overestimated. These results align with what was seen in the spherical hard-boundaried lesion case presented in Fig. 5.8, indicating that the simplified spherical results generally hold true for the more complex geometry results.

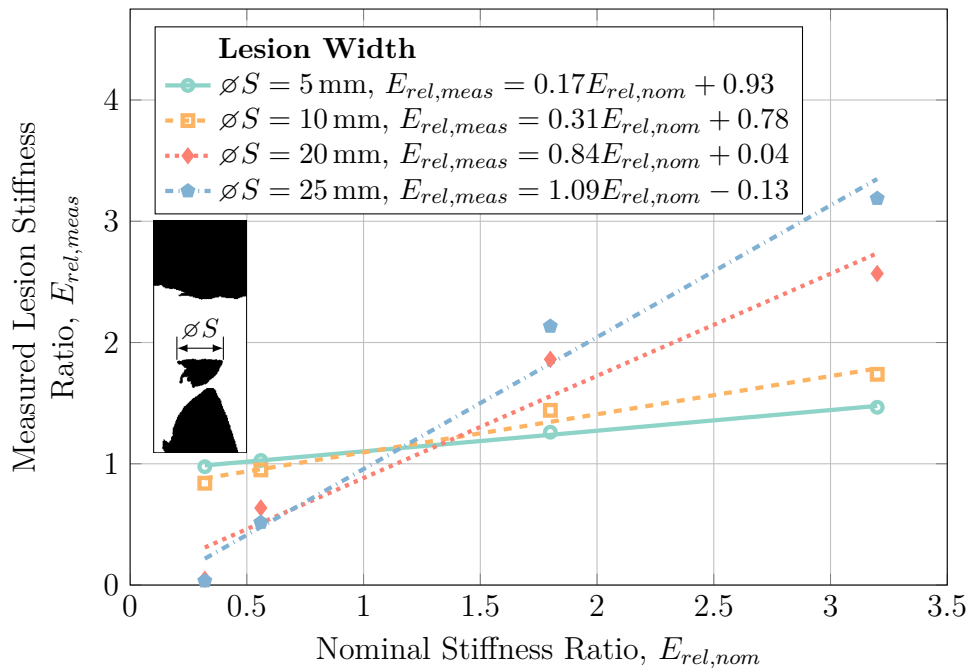


**Fig. 5.20:** Numerical characterization of shear wave speed measured stiffness ratio with changing lesion radii for MRI-acquired lesion geometry in a Visible Human model with an offset of 1.25 cm at a depth of 6 cm using an ARFI interrogation frequency of 2 MHz.

As expected from the results in Fig. 5.20, increasing the lesion radius results in monotonically decreasing measurement error as is shown in Fig. 5.21 with the least amount of measurement error present for the largest lesions. This means that relatively larger lesions will be easier to detect and accurately

quantify and may be due to the shear wave requiring some finite period of time to speed up or slow down with a lesionous region of tissue as discussed previously.

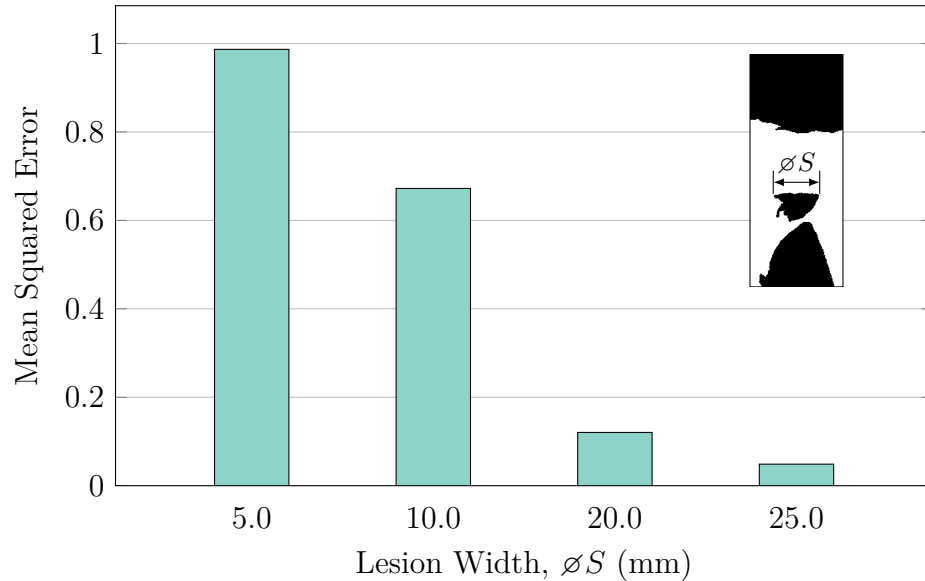


**Fig. 5.21:** Mean squared error between the true and measured lesion stiffness ratios for increasing lesion radii for MRI-acquired lesion geometry in a Visible Human model with an offset of 1.25 cm at a depth of 6 cm using an ARFI interrogation frequency of 2 MHz.

Numerical values for the characterization plots presented here are given in Section A.3 of Appendix A.

### 5.3.4 Physical Phantom Validation

In order to examine the validity of the simulations presented in Section 5.2.2 and the results presented in Section 5.3, experiments using a physical tissue mimicking phantom and an ultrasound machine were performed as described in Section 5.2.3. The results of these experiments are presented in Figs. 5.22 and 5.23 where the difference between the experimentally measured stiffness ratios of lesions were compared against their nominal and simulated stiffnesses respectively.

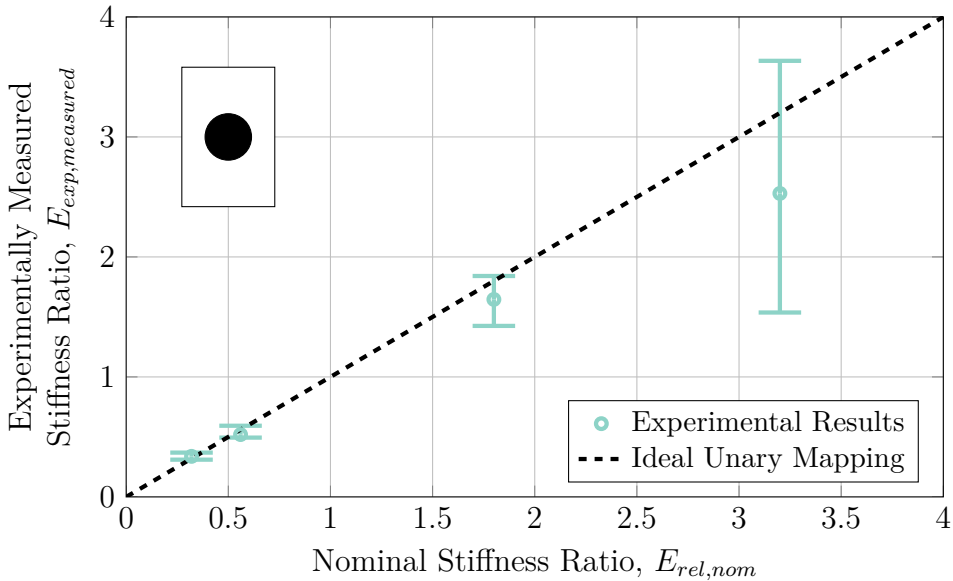


**Fig. 5.22:** Relation between nominally reported strain ratios of the tissue mimicking phantom and experimentally measured strain ratios for a lesion at a depth of 3.5 cm and diameter of 2.0 cm showing general agreement between simulated and experimental cases. Error bars represent the range of measurements acquired.

Fig. 5.22 shows the general agreement between the nominal and experimentally acquired lesion stiffness ratios. Of note is the increasing amount of measurement error associated with increasing nominal stiffness ratios and reflects the general underestimation of stiff lesion stiffness that was seen in the characterization of nearly all stiff lesions in Section 5.3. Further, the relatively large degree of error was due to the measurement of the shear wave speed within the lesion rather than variability in the shear wave speed of the surrounding tissue. Nonetheless, the experimentally-acquired values lay within error of the expected nominal stiffness ratios, so the experiment was considered to produce acceptable results to compare against the simulations. The results of this comparison are shown in Fig. 5.23 where the stiffness ratios acquired through simulation are compared against experimentally-acquired stiffness ratios of parametrically identical lesions.

As expected, there is nearly a one-to-one correspondence between the ex-

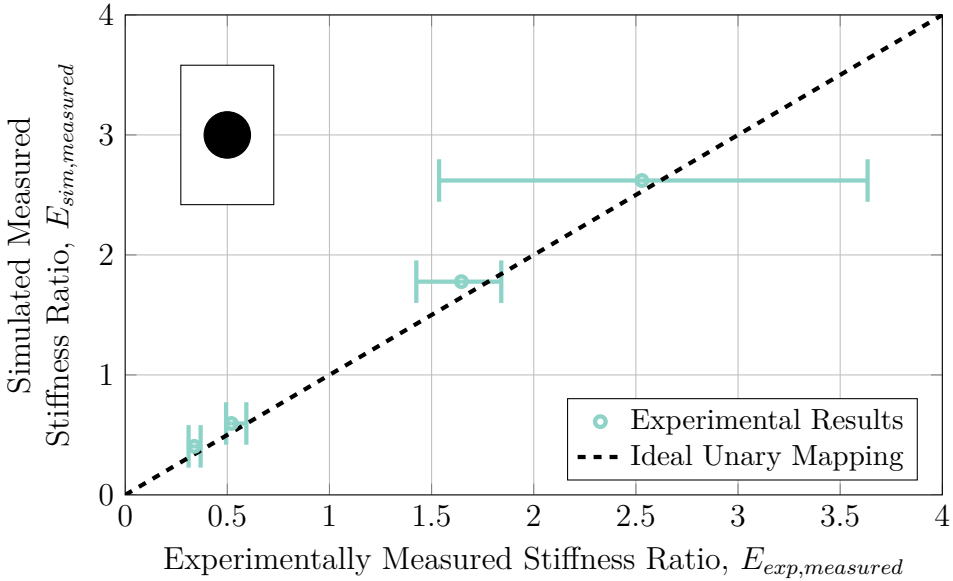


**Fig. 5.23:** Relation between simulated measured strain ratios and experimental measured strain ratios for a lesion at a depth of 3.5 cm and diameter of 2.0 cm showing general agreement between simulated and experimental cases.

perimentally measured lesion stiffness ratios and the simulated lesion stiffness ratios for the various lesions investigated. In all of the lesion cases studied, the simulated lesion stiffness ratio was slightly greater than the experimentally measured stiffness ratio. This suggests that the simulated models introduce a minor bias in the results, although as the correlation is linear this may be readily accounted for. Another key observation is that the underestimated lesion stiffness ratio for stiff lesions that was seen in Fig. 5.22 correlates well with the results obtained experimentally.

## 5.4 Conclusions

The results given in Section 5.3 represent a numerical characterization of the use of the ultrasound elastography technique of shear wave speed quantification toward the detection and monitoring of early and progressive deep tissue injuries. This work presents arguably the most useful technology for moni-

toring deep tissue injury progression as it provides quantitative measures of lesion stiffnesses as opposed to the qualitative measures provided by quasi-static elastography and acoustic radiation force impulse imaging.

The results presented here show that shear wave speed quantification is a viable tool for both detecting and monitoring deep tissue injuries, provided the injuries are in general greater than 1 cm in diameter and are closer to the surface of the skin than 8 cm. In order to provide the most accurate results, ARFI focal points should be located approximately 1.25 cm – 2.50 cm away from the desired region of interest, allowing the shear waves to fully develop before they pass through the lesion for measurement. Blurring the lesions had no appreciable effect on the detection sensitivity whatsoever, however clusters of small lesions comprising a larger lesionous region did—reducing the area ratio of lesionous tissue to that of healthy tissue consistently resulted in lower detection sensitivities. To relate the findings from the simpler model geometries, a simulated lesion with MRI-acquired geometry was placed in a cross-sectional slice of human tissue with geometry obtained from the Visible Human project. The results of the numerical characterizations were consistent with those found using a simpler, spherical model. Finally, the entire simulation pipeline was validated using a tissue mimicking phantom and an ultrasound machine capable of performing shear wave speed quantification where physical lesions presented similar results to their simulated counterparts.

With a firm understanding of the parameters that affect deep tissue injury detection using shear wave speed quantification, future work may entail investigating the use of shear wave speed quantification in both animal and human subjects who are either at an elevated risk of developing deep tissue injuries or are known to be suffering from such injuries. These steps will be necessary before the technique may be used in a clinical setting—an eventuality that will

hopefully result from this work.

# Chapter 6

## Conclusion

Pressure ulcers and deep tissue injuries are an incredible problem facing the health of society today. They arise most often as complications in the elderly and those with spinal cord injuries and present an extremely significant burden on both the health care system and individual patients alike. Deep tissue injuries are somewhat more insidious than pressure ulcers due to how they form—deep tissue injuries begin at the bone-muscle interface deep within tissue and aren't readily noticeable on the surface of the skin until they have broken through as late-stage pressure ulcers. Although DTI prevention and mitigation strategies do exist, their efficacy is highly variable and the treatments are largely untargeted blanket programs which may not adequately treat the needs of patients with formative DTI and may waste money on those without issue. Without a proper clinical diagnostic capability, the incidence of pressure ulcers and DTI has remained largely unchanged for decades. Currently, the only tool capable of detecting formative deep tissue injuries in their early stages—before they tunnel to the surface—is  $T_2^*$ -weighted MRI which images oxygen content (or lack thereof) as a proxy for tissue health. While MRI may be effective in research settings, it is hardly suitable for large-scale

clinical adoption due to the excessive monetary and temporal costs as well as it's lack of mobility and lack of ability to image people with critical medical implants such as pacemakers.

Ultrasound elastography is a relatively new imaging modality that has shown some promise toward the detection of early deep tissue injuries by imaging the stiffness changes that tissue undergoes beginning immediately after an injury has occurred—injured tissue shows 1.6-fold to 3.3-fold stiffening after the initial injury and after becoming necrotic shows stiffness below that of healthy tissue. There are three main technologies relating to ultrasound elastography: quasi-static elastography, acoustic radiation force impulse imaging, and shear wave speed quantification. Quasi-static ultrasound elastography is a technique whereby the deflection and deformation of acoustic scatterers embedded throughout soft tissue are tracked between externally-applied pre- and post- compression states. Regions of tissue which deform less than their surroundings are mechanically stiffer than their surroundings and may represent a formative deep tissue injury. Acoustic radiation force impulse imaging operates on much the same principle as this, however the externally-induced tissue deformation is generated through the application of acoustic radiation forces stemming from specialized pulses emitted from the ultrasound transducer itself. By generating tissue deformation in this manner, the repeatability and inter-operator reliability of diagnostic scans may be improved due to the automatic and computer-controlled nature of the acoustic radiation forces. While quasi-static ultrasound elastography and acoustic radiation force impulse imaging provide only qualitative measures of tissue stiffness relative to it's surroundings, shear-wave speed quantification can provide quantitative measures of tissue elasticity through the direct computation of a region of tissue's shear modulus by it's measured velocity and an assumed

tissue density. Shear-wave speed quantification tracks the velocity of shear waves generated using an acoustic radiation force as they pass through both diseased and healthy tissue using regular ultrasound tracking beams sampled at extremely high frequencies. Through these methods, it is expected that a clinical tool may be developed for not only detecting the early onset of deep tissue injuries but also for tracking their progress over time. The work completed here represents the first step in that goal and numerically characterized the use of all three techniques toward the detection of both early and late-stage deep tissue injuries.

## 6.1 Comparisons Between Methods

In the quest to understand the use of the various ultrasound elastography imaging modalities toward early detection of deep tissue injuries, the sensitivity of numerous parameters relating to each modality were studied. Amongst the studied parameters, a subset of studies are directly comparable between modalities—parameters such as lesion size, depth, blur radius, cluster density, and the use of “real-world” geometry were all examined at parametrically identical values. This allows the direct comparison between modalities and may lead to recommendations for future clinical use of ultrasound elastography.

### Simulated Lesions

Across the range of simulated lesions using the quasi-static elastography, ARFI imaging, and shear wave speed quantification modalities, hard boundaried lesions represent the most “basic” and general case used to investigate overarching lesion parameters such as overall size of the lesion and the depth at which it is placed. In order to compare the investigated modalities, a cross-section

of the data centred around a lesion with radius of 10 mm at a depth of 4 cm is shown in Fig. 6.1. In Fig. 6.1, it is clear to see that shear wave speed quantification is by far the most accurate of the three detection modalities with its characterization curve representing an almost ideal one-to-one mapping of measured stiffness to true stiffness. Quasi-static elastography and ARFI imaging resulted in less detection sensitivity and were not substantially different from each other.

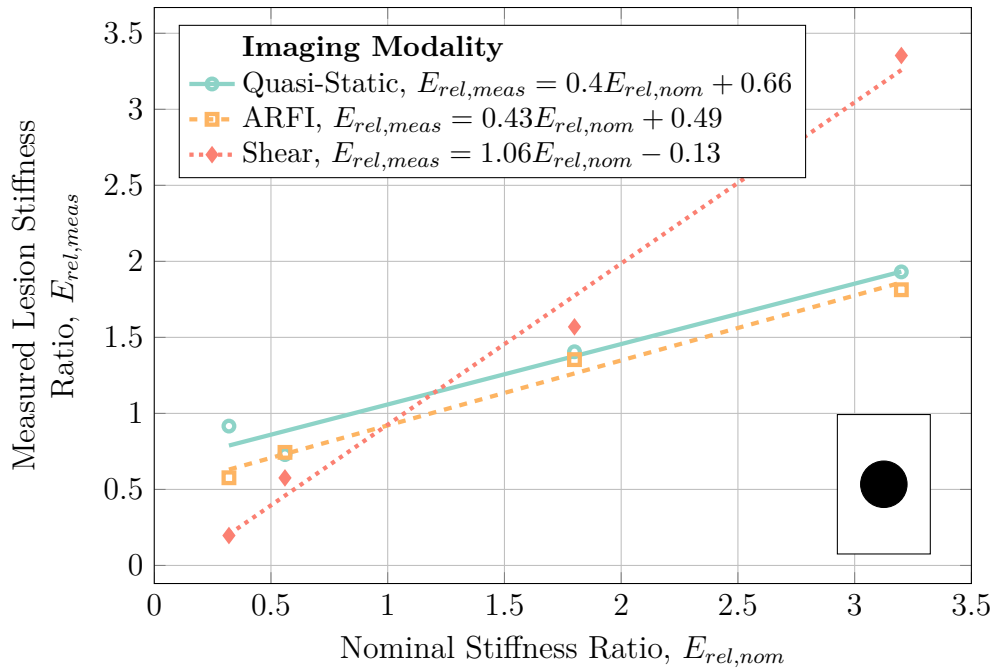


**Fig. 6.1:** Detection sensitivities of hard-boundaried spherical lesions with radii of 10 mm at a depth of 4 cm using quasi-static elastography, ARFI imaging, and shear wave speed quantification.

To further examine the error introduced by the various detection modalities, the percent difference between the expected true values of lesion stiffness and the measured lesion stiffness for the results seen in Fig. 6.1 are shown in Fig. 6.2. Fig. 6.2 shows that in across all lesion stiffnesses, shear wave speed quantification results in the least amount of error between the true and measured lesion stiffness. Errors across all the modalities were greatest for the least stiff lesions—those with stiffness ratios of 0.32. Errors involved with

ARFI imaging were slightly greater than for quasi-static imaging across the remaining investigated stiffness ratios. It is likely however that the slight increase in error associated with ARFI imaging may be worth the added benefit of increased reliability and repeatability. Beyond this, shear wave speed quantification is certainly recommended for detecting lesions if at all possible not only due to its nature of fully quantifying tissue stiffness rather than simply estimating it but also due to it's superior accuracy over quasi-static elastography and ARFI imaging.

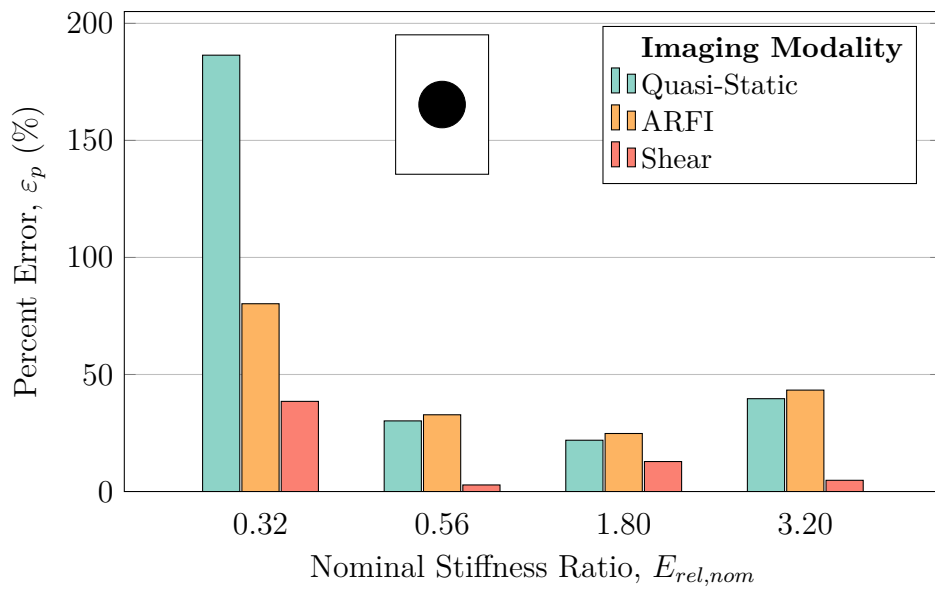


**Fig. 6.2:** Percent error of measured stiffness ratios for spherical lesions with radii of 10 mm at a depth of 4 cm across the three investigated modalities.

Since it is highly unlikely that real-world lesions will present as perfectly spherical, hard-boundaried lesions, different lesion geometries were studied. One such case is where a lesion will not have rigidly defined boundaries and may “fade” into the background healthy tissue. To investigate this, lesions with blurred boundaries that fade into the background were studied using all three elastography modalities. The characterization curves of a lesion with a radius of 10 mm which was blurred using a kernel blur radius of 7.5 mm

across the three modalities are given in Fig. 6.3. As expected, shear wave speed quantification again revealed itself to produce the most accurate results with a nearly one-to-one mapping between true and measured lesion stiffness. Quasi-static elastography and ARFI imaging paralleled each other however quasi-static elastography was generally unable to distinguish unstiff blurred lesions against the background, making ARFI imaging much more preferable than quasi-static elastography when examining late-stage DTI.

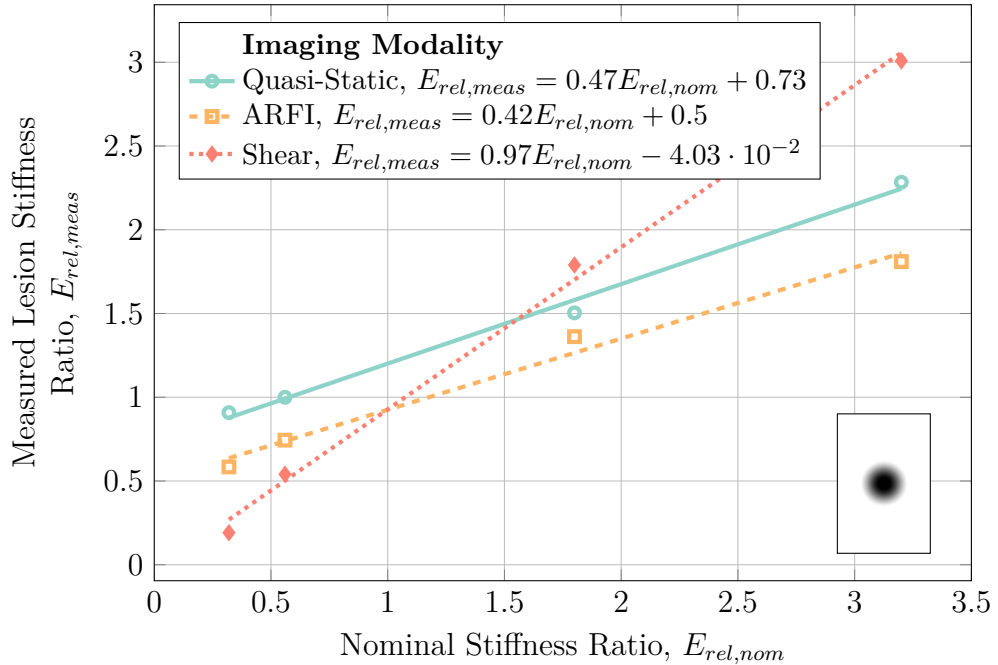


**Fig. 6.3:** Detection sensitivities of blurred-boundary spherical lesions with radii of 10 mm with blur radii of 7.5 mm using quasi-static elastography, ARFI imaging, and shear wave speed quantification.

Again as expected, shear wave speed quantification resulted in substantially less error for characterizing all stages of deep tissue injuries than both quasi-static elastography and ARFI imaging as Fig. 6.4 shows. Once again, the least stiff lesions that were investigated—those with a relative stiffness ratio of 0.32—were the most difficult to detect accurately and presented with the greatest amount of error. Of further note is that although quasi-static elastography was worse at accurately detecting unstiff deep tissue injury lesions than

ARFI imaging, quasi-static elastography portrayed less error when detecting stiff (early) deep tissue injury lesions. This suggests that quasi-static elastography is not well suited for detecting unstiff lesions and that the more reliable ARFI imaging should be used where possible if shear wave speed quantification cannot be used.

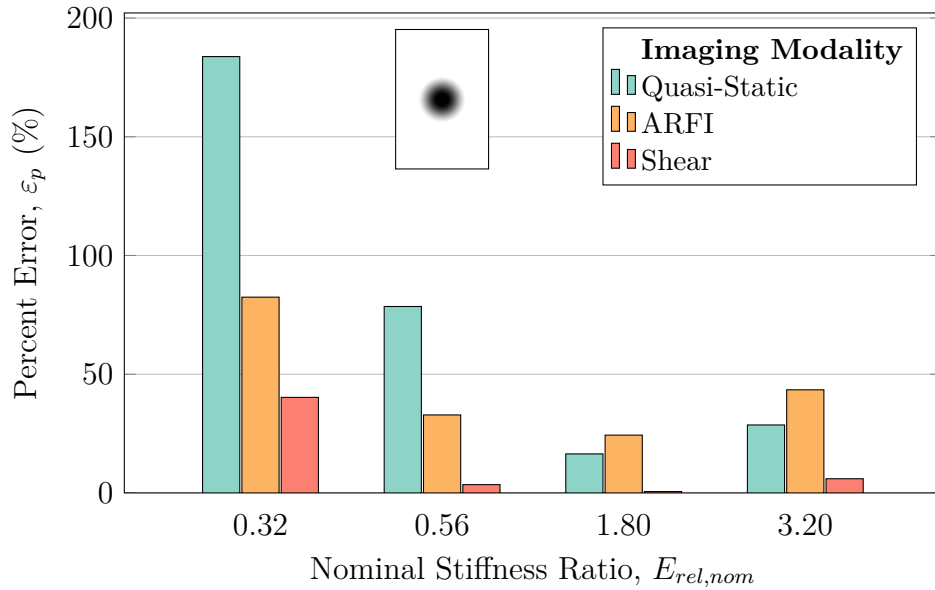


**Fig. 6.4:** Percent error of measured stiffness ratios for blurred lesions with radii of 10 mm and blur radii of 7.5 mm across the three investigated modalities.

Since lesionous regions may not be completely homogeneous regions of injured tissue, a model comprising numerous small lesions clustered together to form a greater lesionous region was developed. Fig. 6.5 shows a cross-section of the characterization curves for this model when small lesions with radii of 1 mm were clustered with a density of  $20 \text{ cm}^{-2}$ . Although none of the investigated modalities were able to distinguish individual lesions in the various cluster models, all were able to differentiate the lesionous region as a whole. Once again, shear wave speed quantification proved to be the most accurate method with its characterization curves coming the closest to a one-to-one mapping of true to measured stiffnesses. Of note in this case, however, is that

even shear wave speed quantification was still substantially less sensitive to lesions than an ideal case—all investigated modalities both over-estimated the stiffness of unstiff lesions and under-estimated the stiffness of stiff lesions.

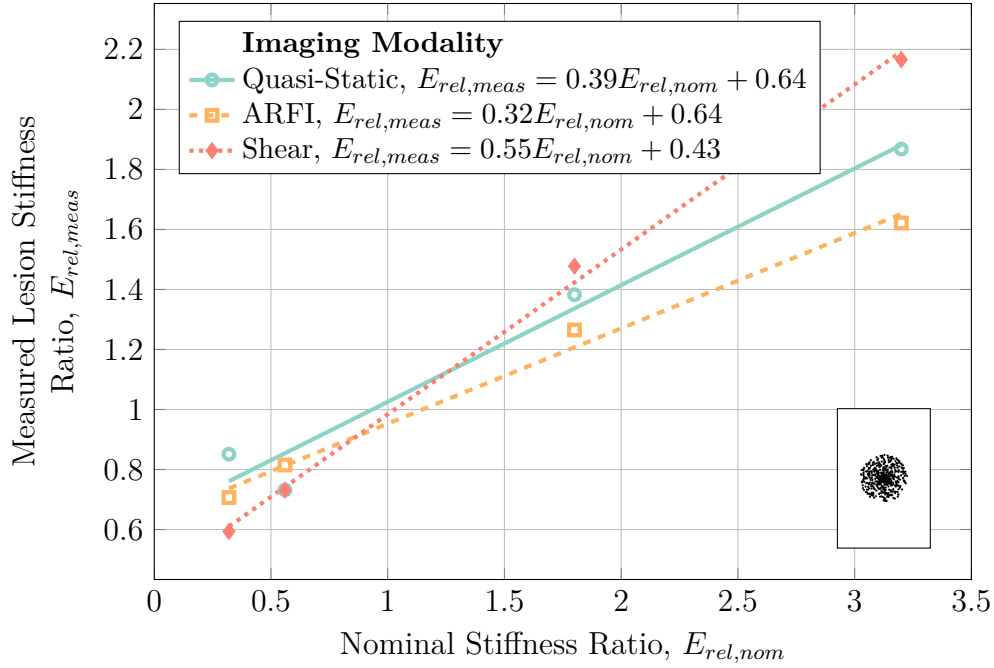


**Fig. 6.5:** Detection sensitivities of clustered lesions with a cluster density of  $20 \text{ cm}^{-2}$  and individual radii of 1 mm using quasi-static elastography, ARFI imaging, and shear wave speed quantification.

The lesser detection sensitivity with all investigated imaging modalities that was portrayed in Fig. 6.5 results in a greater amount of error across all imaging modalities and lesion stiffness ratios as seen in Fig. 6.6. For all but the least stiff of lesions, ARFI imaging had the greatest amount of error when attempting to detect these lesionous clusters, while shear wave speed quantification continued to generally produce the least amount of error. The overall increased error in this model is somewhat expected however, due to the nature of how the models were constructed and evaluated. In the clustered lesion models, only a portion of the lesionous region actually contains “injured” tissue—averaging out the true stiffness over the entire lesionous area would result in a less pronounced stiffness for that region, rather than the “spikes”

that are seen in the clustered model. This means that if such a lesionous region were to exist, the severity of the injury may not be adequately represented by *any* of the three imaging modalities. Further work should be done to examine this problem further and investigate any alternative technologies which may be able to adequately granularize clusters of small lesions.

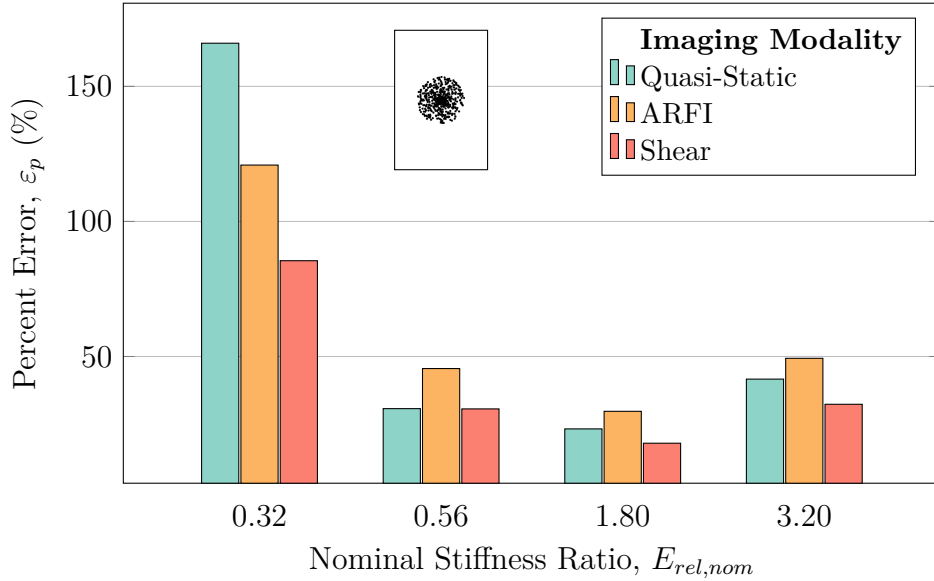


**Fig. 6.6:** Percent error of measured stiffness ratios for clustered lesions with a cluster density of  $20 \text{ cm}^{-2}$  and individual radii of 1 mm across the three investigated modalities.

The final major model to be evaluated across quasi-static elastography, ARFI imaging, and shear wave speed quantification was the use of geometry obtained from MRI scans of real deep tissue injuries in pigs which were then placed in a background of tissue with geometry obtained from the Visible Human project. The purpose of these models was to place the various simulation techniques in the context of detecting “real-world” deep tissue injury lesions. The characterization curves of the three investigated modalities for a lesion with a width of 20 mm located at a depth of 6 cm are given in Fig. 6.7. A lesion depth of 6 cm was chosen in these models as in the Visible Human tissue domain this depth placed the lesion to sit immediately

superior to the ischial tuberosity—a boney prominence often associated with deep tissue injuries. As Fig. 6.7 shows, shear wave speed quantification once again presented the most ideal detection sensitivity of the three modalities. Both quasi-static elastography and ARFI imaging were much less sensitive to lesions in this model, with unstiff lesions being almost impossible to detect using quasi-static elastography. A key differentiation in this Visible Human model from the hard-boundaried spherical model studied previously is that shear wave speed quantification grossly underestimated the stiffness of both the least stiff and stiffest lesions examined.

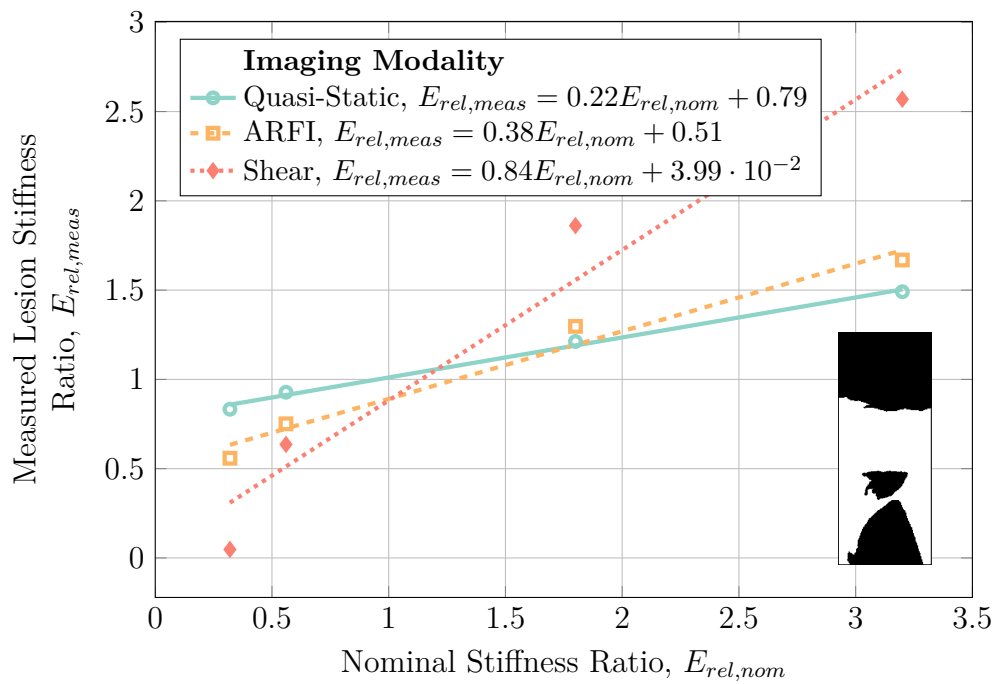


**Fig. 6.7:** Detection sensitivities of MRI-acquired Visible Human lesions with a width of 20 mm at a depth of 6 cm using quasi-static elastography, ARFI imaging, and shear wave speed quantification.

As Fig. 6.8 shows, the error for shear wave speed quantification is much greater for both very unstiff ( $E_{rel,nom} = 0.32$ ) and very stiff ( $E_{rel,nom} = 3.20$ ) lesions—the error for unstiff lesions even surpasses that of ARFI imaging for the first time. For all other nominal stiffness ratios, shear wave speed quan-

tification once again outperformed both quasi-static elastography and ARFI imaging. Although the use of more complicated geometry in the Visible Human project decreased the accuracy of shear wave speed quantification, it was once again the most sensitive and accurate of the investigated imaging modalities, suggesting it be used for quantifying deep tissue injuries if at all possible.

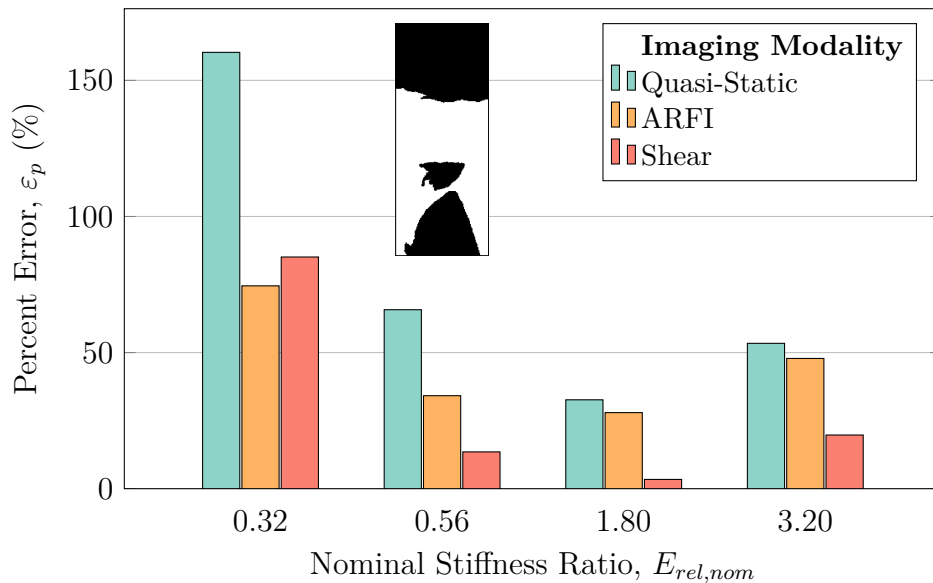


**Fig. 6.8:** Percent error of measured stiffness ratios for MRI-acquired Visible Human lesions with a width of 20 mm at a depth of 6 cm across the three investigated modalities.

## Experimental Validations

In the experiments that were performed with each of the three elastography modalities on a tissue mimicking phantom, all three methodologies were able to distinguish both hard and unstiff lesions with some degree of accuracy. However, the stiffest lesions that were examined—those with a nominal stiffness ratio of 3.2—presented the greatest error and variation in the results as seen in Fig. 6.9. In these experiments, both ARFI imaging and shear wave speed quantification score similarly, although the variation in the shear results was much greater than the variation in the ARFI experiments. Both ARFI imaging

and shear wave speed quantification showed relatively similar detection sensitivities with the major difference between the two being that ARFI imaging consistently over-estimated lesion stiffness as compared to shear wave speed quantification. Shear wave speed quantification was found to be the most accurate for unstiff lesions, while ARFI imaging performed marginally better with stiff lesions. Quasi-static elastography generally displayed the worst results, echoing what was seen in Section 6.1.

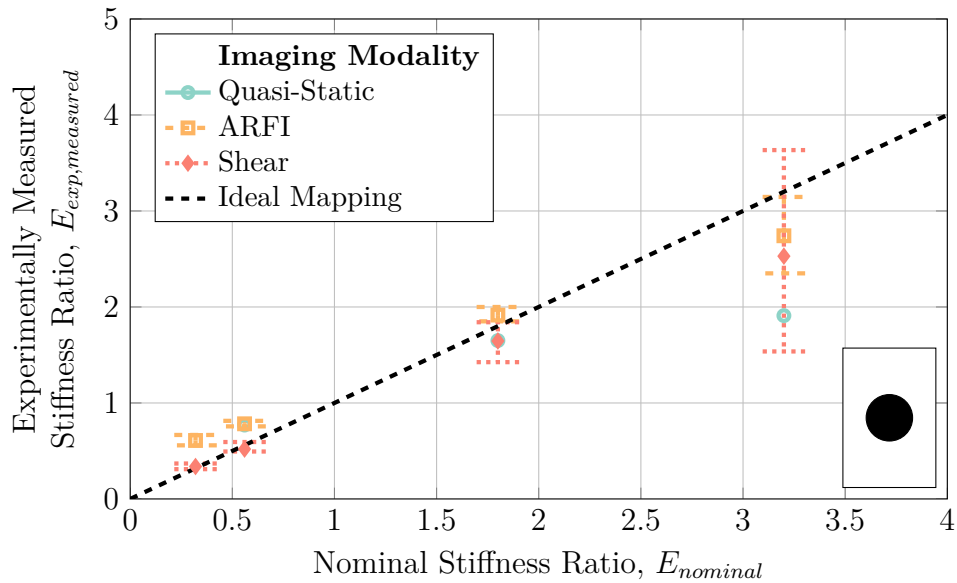


**Fig. 6.9:** Experimental results of the three methodologies investigated. ARFI imaging consistently overestimated the stiffness of the lesion compared to both quasi-static and shear wave speed quantification, which generally underestimated the stiffness of lesions.

By comparing the simulated results presented throughout this work to the parametrically identical results obtained through experiment, the accuracy of the simulations apart from the overall accuracy of the technique may be determined. These results are compared in Fig. 6.10 which shows a general agreement between experimentally measured stiffness ratios and their simulated counterparts for all but stiff ARFI imaging-acquired lesions. Since the simulation results for quasi-static elastography and shear wave speed quantification

fall within error of their experimental counterparts, these simulation paradigms may be deemed acceptable. Counter to this, the simulation-acquired stiffness ratios in ARFI imaging fall well below their experimental values, suggesting that the current ARFI imaging simulation methodology is insufficient in accurately reproducing real-world results and that future work is necessary to more closely align the ARFI imaging models with reality.

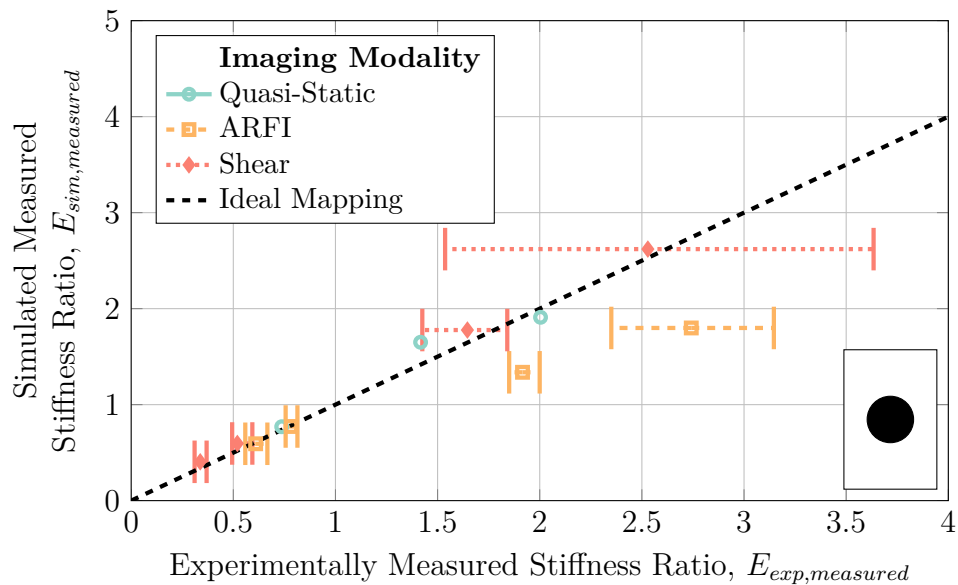


**Fig. 6.10:** Experimental validation of the simulation results across all three methodologies investigated. The quasi-static ultrasound elastography and shear wave speed quantification simulations most closely matched the results seen experimentally.

## 6.2 Recommendations and Future Work

The work presented in Chapters 3 – 5 represents a numerical characterization of three different ultrasound elastography imaging modalities: quasi-static ultrasound elastography, acoustic radiation force impulse imaging, and shear wave speed quantification. From the results presented in these chapters the critical parameters relating to detecting both formative and progressive deep tissue injuries across all three detection modalities were investigated. These

parameters included device-design specifics such as: frequency; transmit pressure; transducer size; etc, as well as physical lesion-specific parameters such as: depth; size; geometry; etc. Through the comparisons made in Section 6.1, it is clear that shear wave speed quantification is the ideal ultrasound elastography modality with regards to detecting deep tissue injuries. Not only is shear wave speed quantification a quantifiable technology which would allow clinicians to directly track the progression of an injury over time, but it was found to consistently provide the most accurate results compared to both quasi-static elastography and ARFI imaging. Shear wave speed quantification is not without its limits however, as the acoustic radiation force impulses which give rise to deformation deep within tissue may not be large enough to be readily detected by the ultrasound machine. To overcome these limitations, the ultrasonic transmission power may be increased and the interrogation frequency may be decreased, but such measures may only go so far and have profound tissue health implications. Further, since only specific, localized regions of tissue may be interrogated using shear wave speed quantification, quasi-static ultrasound elastography or ARFI imaging may be used to image much larger regions of tissue in order to search for specific regions of interest. Although such “fishing” expeditions may not provide truly accurate and quantifiable data, they may guide the use of shear wave speed quantification to provide a more complete picture of tissue health.

From the work presented here, it is fully expected that ultrasound elastography is capable of becoming a clinical tool to be used in the early detection and monitoring of deep tissue injuries. The adoption of this technology for such a venture would have wide-ranging consequences from potentially increasing quality of life of at-risk patients, to decreasing the financial burden on the health care system, to even providing future avenues for deep tissue

injury research—without a quality early deep tissue injury detection method, the bulk of deep tissue injury research focuses on late-stage ulcers for which treatments are often applied “too late”. With a firm understanding of the mechanics and principles involved with ultrasound elastography, the next stage in this technology’s development is to investigate its use in animal models where deep tissue injury lesions may be tightly controlled and the lesions can be co-investigated using MRI techniques. Once early deep tissue injury detection is well understood in living tissue, trials should move to at-risk human patients. Since ultrasound and subsequently ultrasound elastography are non-invasive tools with relatively inexpensive equipment, it is expected that clinical adoption will be swift once the technology is proven in human tissue. Although as of the time of writing there are commercially available ultrasound elastography systems, future work may also involve developing application-specific probes or even entire devices devoted to applying ultrasound elastography toward deep tissue injuries which can provide the necessary parameters to optimize detection and ease of use.

Ultrasound elastography is a powerful tool which through the numerical simulations performed in this work was found to be able to distinguish both early and late stage deep tissue injuries and may provide for the first ever clinical tool to reliably detect DTI with a thought toward improving patient care and quality of life.

# References

- [1] R. M. Allman, P. S. Goode, M. M. Patrick, N. Burst, and A. A. Bartolucci, “Pressure ulcer risk factors among hospitalized patients with activity limitation.,” *JAMA : the journal of the American Medical Association*, vol. 273, no. 11, pp. 865–870, Mar. 15, 1995, ISSN: 0098-7484.
- [2] C. A. Salzberg, D. W. Byrne, C. G. Cayten, P. van Niewerburgh, J. G. Murphy, and M. Viehbeck, “A new pressure ulcer risk assessment scale for individuals with spinal cord injury.,” *American journal of physical medicine & rehabilitation / Association of Academic Physiatrists*, vol. 75, no. 2, pp. 96–104, 1996, ISSN: 0894-9115.
- [3] N. Kanno, T. Nakamura, M. Yamanaka, K. Kouda, T. Nakamura, and F. Tajima, “Low-echoic lesions underneath the skin in subjects with spinal-cord injury.,” *Spinal cord*, vol. 47, no. 3, pp. 225–229, Mar. 2009, ISSN: 1362-4393. DOI: 10.1038/sc.2008.101.
- [4] A. Stekelenburg, D. Gawlitta, D. L. Bader, and C. W. Oomens, “Deep tissue injury: how deep is our understanding?” *Archives of physical medicine and rehabilitation*, vol. 89, no. 7, pp. 1410–1413, Jul. 2008, ISSN: 1532-821X. DOI: 10.1016/j.apmr.2008.01.012.
- [5] A. Gefen, N. Gefen, E. Linder-Ganz, and S. S. Margulies, “In vivo muscle stiffening under bone compression promotes deep pressure sores.,”

*Journal of biomechanical engineering*, vol. 127, no. 3, pp. 512–524, Jun. 2005, ISSN: 0148-0731.

- [6] S. Loerakker, E. Manders, G. J. Strijkers, K. Nicolay, F. P. Baaijens, D. L. Bader, and C. W. Oomens, “The effects of deformation, ischemia, and reperfusion on the development of muscle damage during prolonged loading.,” *Journal of applied physiology (Bethesda, Md. : 1985)*, vol. 111, no. 4, pp. 1168–1177, Oct. 14, 2011, ISSN: 1522-1601. DOI: 10.1152/japplphysiol.00389.2011.
- [7] J. Black, M. M. M. Baharestani, J. Cuddigan, B. Dorner, L. Edsberg, D. Langemo, M. E. E. Posthauer, C. Ratliff, G. Taler, and National Pressure Ulcer Advisory Panel, “National pressure ulcer advisory panel’s updated pressure ulcer staging system.,” *Advances in skin & wound care*, vol. 20, no. 5, pp. 269–274, May 2007, ISSN: 1527-7941. DOI: 10.1097/01.asw.0000269314.23015.e9.
- [8] C. V. Bouten, C. W. Oomens, F. P. Baaijens, and D. L. Bader, “The etiology of pressure ulcers: skin deep or muscle bound?” *Archives of physical medicine and rehabilitation*, vol. 84, no. 4, pp. 616–619, Apr. 2003, ISSN: 0003-9993. DOI: 10.1053/apmr.2003.50038.
- [9] C. W. Oomens, S. Loerakker, and D. L. Bader, “The importance of internal strain as opposed to interface pressure in the prevention of pressure related deep tissue injury.,” *Journal of tissue viability*, vol. 19, no. 2, pp. 35–42, May 2010, ISSN: 0965-206X. DOI: 10.1016/j.jtv.2009.11.002.
- [10] A. Stekelenburg, C. W. Oomens, G. J. Strijkers, K. Nicolay, and D. L. Bader, “Compression-induced deep tissue injury examined with magnetic resonance imaging and histology.” *Journal of applied physiology*

(Bethesda, Md. : 1985), vol. 100, no. 6, pp. 1946–1954, Jun. 2006, ISSN: 8750-7587. DOI: 10.1152/japplphysiol.00889.2005.

- [11] N. Aoi, K. Yoshimura, T. Kadono, G. Nakagami, S. Iizuka, T. Higashino, J. Araki, I. Koshima, and H. Sanada, “Ultrasound assessment of deep tissue injury in pressure ulcers: possible prediction of pressure ulcer progression.,” *Plastic and reconstructive surgery*, vol. 124, no. 2, pp. 540–550, Aug. 2009, ISSN: 1529-4242. DOI: 10.1097/prs.0b013e3181addb33.
- [12] M. Tanter, J. Bercoff, A. Athanasiou, T. Deffieux, J.-L. L. Gennisson, G. Montaldo, M. Muller, A. Tardivon, and M. Fink, “Quantitative assessment of breast lesion viscoelasticity: initial clinical results using supersonic shear imaging.,” *Ultrasound in medicine & biology*, vol. 34, no. 9, pp. 1373–1386, Sep. 2008, ISSN: 0301-5629. DOI: 10.1016/j.ultrasmedbio.2008.02.002.
- [13] K. König, U. Scheipers, A. Pesavento, A. Lorenz, H. Ermert, and T. Senge, “Initial experiences with real-time elastography guided biopsies of the prostate.,” *The Journal of urology*, vol. 174, no. 1, pp. 115–117, Jul. 2005, ISSN: 0022-5347. DOI: 10.1097/01.ju.0000162043.72294.4a.
- [14] L. Sandrin, B. Fourquet, J.-M. M. Hasquenoph, S. Yon, C. Fournier, F. Mal, C. Christidis, M. Ziol, B. Poulet, F. Kazemi, M. Beaugrand, and R. Palau, “Transient elastography: a new noninvasive method for assessment of hepatic fibrosis.,” *Ultrasound in medicine & biology*, vol. 29, no. 12, pp. 1705–1713, Dec. 2003, ISSN: 0301-5629.
- [15] E. Linder-Ganz and A. Gefen, “Mechanical compression-induced pressure sores in rat hindlimb: muscle stiffness, histology, and computa-

- tional models.,” *Journal of applied physiology (Bethesda, Md. : 1985)*, vol. 96, no. 6, pp. 2034–2049, Jun. 2004, ISSN: 8750-7587. DOI: 10.1152/japplphysiol.00888.2003.
- [16] L. R. Solis, A. B. Liggins, P. Seres, R. R. Uwiera, N. R. Poppe, E. Pehowich, R. B. Thompson, and V. K. Mushahwar, “Distribution of internal strains around bony prominences in pigs.,” *Annals of biomedical engineering*, pp. 1–19, Mar. 8, 2012, ISSN: 1521-6047. DOI: 10.1007/s10439-012-0539-y.
- [17] A. Gefen, “Deep tissue injury from a bioengineering point of view.,” *Ostomy/wound management*, vol. 55, no. 4, pp. 26–36, Apr. 2009, ISSN: 0889-5899.
- [18] J.-F. F. Deprez, E. Brusseau, J. Fromageau, G. Cloutier, and O. Basset, “On the potential of ultrasound elastography for pressure ulcer early detection.,” *Medical physics*, vol. 38, no. 4, pp. 1943–1950, Apr. 2011, ISSN: 0094-2405.
- [19] K. Beckrich and S. A. Aronovitch, “Hospital-acquired pressure ulcers: a comparison of costs in medical vs. surgical patients.,” *Nursing economic\$*, vol. 17, no. 5, pp. 263–271, 1999, ISSN: 0746-1739.
- [20] C. Russo, C. Steiner, and W. Spector, “Hospitalizations related to pressure ulcers among adults 18 years and older, 2006: statistical brief no. 64.,” *Agency for Health Care Policy and Research (US)*, Dec. 2008.
- [21] J. M. Zanca, D. M. Brienza, D. Berlowitz, R. G. Bennett, C. H. Lyder, and National Pressure Ulcer Advisory Panel, “Pressure ulcer research funding in america: creation and analysis of an on-line database.,” *Advances in skin & wound care*, vol. 16, no. 4, pp. 190–197, 2003, ISSN: 1527-7941.

- [22] D. K. Langemo, H. Melland, D. Hanson, B. Olson, and S. Hunter, “The lived experience of having a pressure ulcer: a qualitative analysis.,” *Advances in skin & wound care*, vol. 13, no. 5, pp. 225–235, 2000, ISSN: 1527-7941.
- [23] M. M. Baharestani, “The lived experience of wives caring for their frail, homebound, elderly husbands with pressure ulcers.,” *Advances in wound care : the journal for prevention and healing*, vol. 7, no. 3, May 1994, ISSN: 1076-2191.
- [24] M. C. C. de Freitas, A. B. F. B. Medeiros, M. V. C. V. Guedes, P. C. C. de Almeida, F. T. T. de Galiza, and J. d. M. d. e . M. Nogueira, “[pressure ulcers in the elderly: analysis of prevalence and risk factors].,” *Revista gaúcha de enfermagem / EENFUFRGS*, vol. 32, no. 1, pp. 143–150, Mar. 2011, ISSN: 0102-6933.
- [25] S. A. Aronovitch, “Intraoperatively acquired pressure ulcer prevalence: a national study.,” *Journal of wound, ostomy, and continence nursing*, vol. 26, no. 3, pp. 130–136, May 1999, ISSN: 1071-5754.
- [26] E. Jaul, “Assessment and management of pressure ulcers in the elderly: current strategies.,” *Drugs & aging*, vol. 27, no. 4, pp. 311–325, Apr. 1, 2010, ISSN: 1170-229X. DOI: 10.2165/11318340-00000000-00000.
- [27] Z. B. Niazi, C. A. Salzberg, D. W. Byrne, and M. Viehbeck, “Recurrence of initial pressure ulcer in persons with spinal cord injuries.,” *Advances in wound care : the journal for prevention and healing*, vol. 10, no. 3, pp. 38–42, 1997, ISSN: 1076-2191.
- [28] S. L. Garber and D. H. Rintala, “Pressure ulcers in veterans with spinal cord injury: a retrospective study.,” *Journal of rehabilitation research and development*, vol. 40, no. 5, pp. 433–441, 2003, ISSN: 0748-7711.

- [29] C. Campbell and L. C. C. Parish, “The decubitus ulcer: facts and controversies.,” *Clinics in dermatology*, vol. 28, no. 5, pp. 527–532, Sep. 2010, ISSN: 1879-1131. DOI: 10.1016/j.clindermatol.2010.03.010.
- [30] J. M. Black, L. E. Edsberg, M. M. Baharestani, D. Langemo, M. Goldberg, L. McNichol, J. Cuddigan, and National Pressure Ulcer Advisory Panel, “Pressure ulcers: avoidable or unavoidable? results of the national pressure ulcer advisory panel consensus conference.,” *Ostomy/wound management*, vol. 57, no. 2, pp. 24–37, Feb. 2011, ISSN: 1943-2720.
- [31] J. Maklebust, “Pressure ulcers: the great insult.,” *The Nursing clinics of North America*, vol. 40, no. 2, pp. 365–389, Jun. 2005, ISSN: 0029-6465. DOI: 10.1016/j.cnur.2004.09.015.
- [32] L. Gunningberg and N. A. Stotts, “Tracking quality over time: what do pressure ulcer data show?” *International journal for quality in health care : journal of the International Society for Quality in Health Care / ISQua*, vol. 20, no. 4, pp. 246–253, Aug. 2008, ISSN: 1353-4505. DOI: 10.1093/intqhc/mzn009.
- [33] C. T. Milne, D. Trigilia, T. L. Houle, S. Delong, and D. Rosenblum, “Reducing pressure ulcer prevalence rates in the long-term acute care setting.,” *Ostomy/wound management*, vol. 55, no. 4, pp. 50–59, Apr. 2009, ISSN: 0889-5899.
- [34] J. A. Witkowski and L. C. Parish, “Histopathology of the decubitus ulcer.,” *Journal of the American Academy of Dermatology*, vol. 6, no. 6, pp. 1014–1021, Jun. 1982, ISSN: 0190-9622.

- [35] S. M. Dinsdale, “Decubitus ulcers: role of pressure and friction in causation.,” *Archives of physical medicine and rehabilitation*, vol. 55, no. 4, pp. 147–152, Apr. 1974, ISSN: 0003-9993.
- [36] M. KOSIAK, “Etiology of decubitus ulcers.,” *Archives of physical medicine and rehabilitation*, vol. 42, pp. 19–29, Jan. 1961, ISSN: 0003-9993.
- [37] R. Labbe, T. Lindsay, and P. M. Walker, “The extent and distribution of skeletal muscle necrosis after graded periods of complete ischemia.,” *Journal of vascular surgery*, vol. 6, no. 2, pp. 152–157, Aug. 1987, ISSN: 0741-5214. DOI: 10.1067/mva.1987.avso060152.
- [38] P. E. Strock and G. Majno, “Microvascular changes in acutely ischemic rat muscle.,” *Surgery, gynecology & obstetrics*, vol. 129, no. 6, pp. 1213–1224, Dec. 1969, ISSN: 0039-6087.
- [39] M. Bliss and B. Simini, “When are the seeds of postoperative pressure sores sown?. often during surgery.,” *BMJ (Clinical research ed.)*, vol. 319, no. 7214, pp. 863–864, Oct. 2, 1999, ISSN: 0959-8138.
- [40] K. Ytrehus, O. Reikerås, N. Huseby, and R. Myklebust, “Ultrastructure of reperfused skeletal muscle: the effect of oxygen radical scavenger enzymes.,” *International journal of microcirculation, clinical and experimental / sponsored by the European Society for Microcirculation*, vol. 15, no. 4, pp. 155–162, 1995, ISSN: 0167-6865.
- [41] F. W. Blaisdell, “The pathophysiology of skeletal muscle ischemia and the reperfusion syndrome: a review.,” *Cardiovascular surgery (London, England)*, vol. 10, no. 6, pp. 620–630, Dec. 2002, ISSN: 0967-2109.
- [42] S. Tsuji, S. Ichioka, N. Sekiya, and T. Nakatsuka, “Analysis of ischemia-reperfusion injury in a microcirculatory model of pressure ulcers.,”

*Wound repair and regeneration*, vol. 13, no. 2, pp. 209–215, Mar. 2005,  
ISSN: 1067-1927. DOI: 10.1111/j.1067-1927.2005.130213.x.

- [43] R. Salcido, J. C. Donofrio, S. B. Fisher, E. K. LeGrand, K. Dickey, J. M. Carney, R. Schosser, and R. Liang, “Histopathology of pressure ulcers as a result of sequential computer-controlled pressure sessions in a fuzzy rat model.,” *Advances in wound care : the journal for prevention and healing*, vol. 7, no. 5, Sep. 1994, ISSN: 1076-2191.
- [44] G. E. Miller and J. Seale, “Lymphatic clearance during compressive loading.,” *Lymphology*, vol. 14, no. 4, pp. 161–166, Dec. 1981, ISSN: 0024-7766.
- [45] T. A. Krouskop, N. P. Reddy, W. A. Spencer, and J. W. Secor, “Mechanisms of decubitus ulcer formation—an hypothesis.,” *Medical hypotheses*, vol. 4, no. 1, pp. 37–39, 1978, ISSN: 0306-9877.
- [46] N. P. Reddy and G. V. Cochran, “Interstitial fluid flow as a factor in decubitus ulcer formation.,” *Journal of biomechanics*, vol. 14, no. 12, pp. 879–881, 1981, ISSN: 0021-9290.
- [47] B. Braden and N. Bergstrom, “A conceptual schema for the study of the etiology of pressure sores.,” *Rehabilitation nursing : the official journal of the Association of Rehabilitation Nurses*, vol. 12, no. 1, pp. 8–12, 1987, ISSN: 0278-4807.
- [48] A. S. Landsman, D. F. Meaney, R. S. Cargill, E. J. Macarak, and L. E. Thibault, “1995 william j. stickel gold award. high strain rate tissue deformation. a theory on the mechanical etiology of diabetic foot ulcerations.,” *Journal of the American Podiatric Medical Association*, vol. 85, no. 10, pp. 519–527, Oct. 1995, ISSN: 8750-7315.

- [49] C. V. Bouten, M. M. Knight, D. A. Lee, and D. L. Bade, “Compressive deformation and damage of muscle cell subpopulations in a model system.,” *Annals of biomedical engineering*, vol. 29, no. 2, pp. 153–163, Feb. 2001, ISSN: 0090-6964.
- [50] Y.-N. N. Wang, C. V. Bouten, D. A. Lee, and D. L. Bader, “Compression-induced damage in a muscle cell model in vitro.,” *Proceedings of the Institution of Mechanical Engineers. Part H, Journal of engineering in medicine*, vol. 219, no. 1, pp. 1–12, 2005, ISSN: 0954-4119.
- [51] K. K. Ceelen, A. Stekelenburg, S. Loerakker, G. J. Strijkers, D. L. Bader, K. Nicolay, F. P. Baaijens, and C. W. Oomens, “Compression-induced damage and internal tissue strains are related.,” *Journal of biomechanics*, vol. 41, no. 16, pp. 3399–3404, Dec. 5, 2008, ISSN: 0021-9290. DOI: [10.1016/j.jbiomech.2008.09.016](https://doi.org/10.1016/j.jbiomech.2008.09.016).
- [52] E. Linder-Ganz, N. Shabshin, Y. Itzchak, Z. Yizhar, I. Siev-Ner, and A. Gefen, “Strains and stresses in sub-dermal tissues of the buttocks are greater in paraplegics than in healthy during sitting.,” *Journal of biomechanics*, vol. 41, no. 3, pp. 567–580, 2008, ISSN: 0021-9290. DOI: [10.1016/j.jbiomech.2007.10.011](https://doi.org/10.1016/j.jbiomech.2007.10.011).
- [53] S. Portnoy, I. Siev-Ner, N. Shabshin, A. Kristal, Z. Yizhar, and A. Gefen, “Patient-specific analyses of deep tissue loads post transtibial amputation in residual limbs of multiple prosthetic users.,” *Journal of biomechanics*, vol. 42, no. 16, pp. 2686–2693, Dec. 11, 2009, ISSN: 1873-2380. DOI: [10.1016/j.jbiomech.2009.08.019](https://doi.org/10.1016/j.jbiomech.2009.08.019).
- [54] N. Slomka and A. Gefen, “Relationship between strain levels and permeability of the plasma membrane in statically stretched myoblasts.,”

*Annals of biomedical engineering*, vol. 40, no. 3, pp. 606–618, Mar. 7, 2012, ISSN: 1573-9686. DOI: 10.1007/s10439-011-0423-1.

- [55] S. Loerakker, L. R. Solis, D. L. Bader, F. P. Baaijens, V. K. Mushahwar, and C. W. Oomens, “How does muscle stiffness affect the internal deformations within the soft tissue layers of the buttocks under constant loading?” *Computer methods in biomechanics and biomedical engineering*, vol. 16, no. 5, pp. 520–529, 2013, ISSN: 1476-8259. DOI: 10.1080/10255842.2011.627682.
- [56] E. Linder-Ganz and A. Gefen, “Stress analyses coupled with damage laws to determine biomechanical risk factors for deep tissue injury during sitting.,” *Journal of biomechanical engineering*, vol. 131, no. 1, Jan. 2009, ISSN: 0148-0731. DOI: 10.1115/1.3005195.
- [57] T. Nagel, S. Loerakker, and C. W. Oomens, “A theoretical model to study the effects of cellular stiffening on the damage evolution in deep tissue injury.,” *Computer methods in biomechanics and biomedical engineering*, vol. 12, no. 5, pp. 585–597, Oct. 2009, ISSN: 1476-8259. DOI: 10.1080/10255840902788603.
- [58] A. Gefen and E. Linder-Ganz, “[diffusion of ulcers in the diabetic foot is promoted by stiffening of plantar muscular tissue under excessive bone compression].,” *Der Orthopäde*, vol. 33, no. 9, pp. 999–1012, Sep. 2004, ISSN: 0085-4530. DOI: 10.1007/s00132-004-0701-9.
- [59] D. DiMaio and Vincent, “Rigor mortis,” in *Forensic Pathology, Second Edition (Practical Aspects of Criminal and Forensic Investigations)*, V. J. Geberth, Ed., 2nd ed. CRC Press, Jun. 28, 2001, pp. 26–28, ISBN: 084930072X.

- [60] S. Portnoy, Z. Yizhar, N. Shabshin, Y. Itzchak, A. Kristal, Y. Dotan-Marom, I. Siev-Ner, and A. Gefen, “Internal mechanical conditions in the soft tissues of a residual limb of a trans-tibial amputee.,” *Journal of biomechanics*, vol. 41, no. 9, pp. 1897–1909, 2008, ISSN: 0021-9290. DOI: [10.1016/j.jbiomech.2008.03.035](https://doi.org/10.1016/j.jbiomech.2008.03.035).
- [61] K. Vanderwee, M. H. Grypdonck, D. De Bacquer, and T. Defloor, “Effectiveness of turning with unequal time intervals on the incidence of pressure ulcer lesions.,” *Journal of advanced nursing*, vol. 57, no. 1, pp. 59–68, Jan. 2007, ISSN: 0309-2402. DOI: [10.1111/j.1365-2648.2006.04060.x](https://doi.org/10.1111/j.1365-2648.2006.04060.x).
- [62] S. E. Rich, D. Margolis, M. Shardell, W. G. Hawkes, R. R. Miller, S. Amr, and M. Baumgarten, “Frequent manual repositioning and incidence of pressure ulcers among bed-bound elderly hip fracture patients.,” *Wound repair and regeneration*, vol. 19, no. 1, pp. 10–18, 2011, ISSN: 1524-475X. DOI: [10.1111/j.1524-475x.2010.00644.x](https://doi.org/10.1111/j.1524-475x.2010.00644.x).
- [63] T. A. Krouskop, P. S. Noble, J. Brown, and R. Marburger, “Factors affecting the pressure-distributing properties of foam mattress overlays.,” *Journal of rehabilitation research and development*, vol. 23, no. 3, pp. 33–39, Jul. 1986, ISSN: 0748-7711.
- [64] B. Pham, L. Teague, J. Mahoney, L. Goodman, M. Paulden, J. Poss, J. Li, L. Ieraci, S. Carcone, and M. Krahn, “Early prevention of pressure ulcers among elderly patients admitted through emergency departments: a cost-effectiveness analysis.,” *Annals of emergency medicine*, vol. 58, no. 5, Nov. 2011, ISSN: 1097-6760. DOI: [10.1016/j.annemergmed.2011.04.033](https://doi.org/10.1016/j.annemergmed.2011.04.033).

- [65] L. Rafter, “Evaluation of patient outcomes: pressure ulcer prevention mattresses.,” *British journal of nursing (Mark Allen Publishing)*, vol. 20, no. 11, 2011, ISSN: 0966-0461.
- [66] S. Gyawali, L. Solis, S. L. L. Chong, C. Curtis, P. Seres, I. Kornelsen, R. Thompson, and V. K. Mushahwar, “Intermittent electrical stimulation redistributes pressure and promotes tissue oxygenation in loaded muscles of individuals with spinal cord injury.,” *Journal of applied physiology (Bethesda, Md. : 1985)*, vol. 110, no. 1, pp. 246–255, Jan. 2011, ISSN: 1522-1601. DOI: 10.1152/japplphysiol.00661.2010.
- [67] L. R. Solis, E. Twist, P. Seres, R. B. Thompson, and V. K. Mushahwar, “Prevention of deep tissue injury through muscle contractions induced by intermittent electrical stimulation after spinal cord injury in pigs.,” *Journal of applied physiology (Bethesda, Md. : 1985)*, vol. 114, no. 2, pp. 286–296, Jan. 15, 2013, ISSN: 1522-1601. DOI: 10.1152/japplphysiol.00257.2012.
- [68] N. Greer, N. A. Foman, R. MacDonald, J. Dorrian, P. Fitzgerald, I. Rutks, and T. J. Wilt, “Advanced wound care therapies for nonhealing diabetic, venous, and arterial ulcers: a systematic review.,” *Annals of internal medicine*, vol. 159, no. 8, pp. 532–542, Oct. 15, 2013, ISSN: 1539-3704. DOI: 10.7326/0003-4819-159-8-201310150-00006.
- [69] R. L. Longe, “Current concepts in clinical therapeutics: pressure sores.,” *Clinical pharmacy*, vol. 5, no. 8, pp. 669–681, Aug. 1986, ISSN: 0278-2677.
- [70] H. Brem, D. M. Nierman, and J. E. Nelson, “Pressure ulcers in the chronically critically ill patient.,” *Critical care clinics*, vol. 18, no. 3, pp. 683–694, Jul. 2002, ISSN: 0749-0704.

- [71] B. Biglari, A. Büchler, T. Reitzel, T. Swing, H. J. Gerner, T. Ferbert, and A. Moghaddam, “A retrospective study on flap complications after pressure ulcer surgery in spinal cord-injured patients.,” *Spinal cord*, vol. 52, no. 1, pp. 80–83, Jan. 12, 2014, ISSN: 1476-5624. DOI: 10.1038/sc.2013.130.
- [72] I. Bales and T. Duvendack, “Reaching for the moon: achieving zero pressure ulcer prevalence, an update.,” *Journal of wound care*, vol. 20, no. 8, Aug. 2011, ISSN: 0969-0700.
- [73] M. Thompson, “Reducing pressure ulcers in hip fracture patients.,” *British journal of nursing (Mark Allen Publishing)*, vol. 20, no. 15, 2011, ISSN: 0966-0461.
- [74] D. Carson, K. Emmons, W. Falone, and A. M. M. Preston, “Development of pressure ulcer program across a university health system.,” *Journal of nursing care quality*, Sep. 10, 2011, ISSN: 1550-5065. DOI: 10.1097/ncq.0b013e3182310f8b.
- [75] D. Norton, R. McLaren, and A. N. Exton-Smith, *An Investigation Of Geriatric Nursing Problems In Hospital*, 5. London, UK: Churchill Livingstone, Jul. 1975, vol. 77, pp. 317+. DOI: 10.1016/s0033-3506(63)80071-2.
- [76] B. J. Braden and N. Bergstrom, “Predictive validity of the braden scale for pressure sore risk in a nursing home population.,” *Research in nursing & health*, vol. 17, no. 6, pp. 459–470, Dec. 1994, ISSN: 0160-6891.
- [77] M. Lindgren, M. Unosson, A.-M. M. Krantz, and A.-C. C. Ek, “A risk assessment scale for the prediction of pressure sore development: reliability and validity.,” *Journal of advanced nursing*, vol. 38, no. 2, pp. 190–199, Apr. 2002, ISSN: 0309-2402.

- [78] I. Fromantin, M. C. Falcou, A. Baffie, C. Petot, R. Mazerat, C. Jaouen, L. Téot, and d. Rycke, “Inception and validation of a pressure ulcer risk scale in oncology.,” *Journal of wound care*, vol. 20, no. 7, Jul. 2011, ISSN: 0969-0700.
- [79] U. Källman and M. Lindgren, “Predictive validity of 4 risk assessment scales for prediction of pressure ulcer development in a hospital setting.,” *Advances in skin & wound care*, vol. 27, no. 2, pp. 70–76, Feb. 2014, ISSN: 1538-8654. DOI: 10.1097/01.asw.0000439059.72199.41.
- [80] Y. J. J. Lee, S. Park, J. Y. Y. Kim, C. G. G. Kim, and S. K. K. Cha, “[clinical nurses’ knowledge and visual differentiation ability in pressure ulcer classification system and incontinence-associated dermatitis].,” *Journal of Korean Academy of Nursing*, vol. 43, no. 4, pp. 526–535, Aug. 2013, ISSN: 2093-758X. DOI: 10.4040/jkan.2013.43.4.526.
- [81] J. M. Levine, E. A. Ayello, K. M. Zulkowski, and J. Fogel, “Pressure ulcer knowledge in medical residents: an opportunity for improvement.,” *Advances in skin & wound care*, vol. 25, no. 3, pp. 115–117, Mar. 2012, ISSN: 1538-8654. DOI: 10.1097/01.asw.0000412908.43335.46.
- [82] J. Wardlaw, M. Brazzelli, H. Miranda, F. Chappell, P. McNamee, G. Scotland, Z. Quayyum, D. Martin, K. Shuler, P. Sandercock, and M. Dennis, “An assessment of the cost-effectiveness of magnetic resonance, including diffusion-weighted imaging, in patients with transient ischaemic attack and minor stroke: a systematic review, meta-analysis and economic evaluation.,” *Health technology assessment (Winchester, England)*, vol. 18, no. 27, pp. 1–368, Apr. 2014, ISSN: 2046-4924.

- [83] G. K. von Schulthess and P. Veit-Haibach, “Workflow considerations in PET/MR imaging.,” *Journal of nuclear medicine : official publication, Society of Nuclear Medicine*, May 1, 2014, ISSN: 1535-5667.
- [84] N. Johnson, L. Sorenson, L. Bennetts, K. Winter, S. Bryn, W. Johnson, M. Glissmeyer, J. Garreau, and D. Blanchard, “Breast-specific gamma imaging is a cost effective and efficacious imaging modality when compared with MRI.,” *American journal of surgery*, vol. 207, no. 5, pp. 698–701, May 2014, ISSN: 1879-1883.
- [85] E. Sloth and T. Karlsmark, “Evaluation of four non-invasive methods for examination and characterization of pressure ulcers.,” *Skin research and technology : official journal of International Society for Bioengineering and the Skin (ISBS) [and] International Society for Digital Imaging of Skin (ISDIS) [and] International Society for Skin Imaging (ISSI)*, vol. 14, no. 3, pp. 270–276, Aug. 2008, ISSN: 1600-0846. DOI: [10.1111/j.1600-0846.2008.00290.x](https://doi.org/10.1111/j.1600-0846.2008.00290.x).
- [86] T. Higashino, G. Nakagami, T. Kadono, Y. Ogawa, S. Iizaka, H. Koyanagi, S. Sasaki, N. Haga, and H. Sanada, “Combination of thermographic and ultrasonographic assessments for early detection of deep tissue injury.,” *International wound journal*, Nov. 22, 2012, ISSN: 1742-481X. DOI: [10.1111/j.1742-481x.2012.01117.x](https://doi.org/10.1111/j.1742-481x.2012.01117.x).
- [87] C. Gehin, E. Brusseau, R. Meffre, P. M. Schmitt, J. F. Deprez, and A. Dittmar, “Which techniques to improve the early detection and prevention of pressure ulcers?” *Conference proceedings : ... Annual International Conference of the IEEE Engineering in Medicine and Biology Society. IEEE Engineering in Medicine and Biology Society. Conference*

- ence, vol. 1, pp. 6057–6060, 2006, ISSN: 1557-170X. DOI: 10.1109/ iembs.2006.259506.
- [88] A. Gefen, K. J. Farid, and I. Shaywitz, “A review of deep tissue injury development, detection, and prevention: shear savvy.,” *Ostomy/wound management*, vol. 59, no. 2, pp. 26–35, Feb. 2013, ISSN: 1943-2720.
- [89] J.-F. F. Deprez, G. Cloutier, C. Schmitt, C. Gehin, A. Dittmar, O. Basset, and E. Brusseau, “3D ultrasound elastography for early detection of lesions. evaluation on a pressure ulcer mimicking phantom.,” *Conference proceedings : ... Annual International Conference of the IEEE Engineering in Medicine and Biology Society. IEEE Engineering in Medicine and Biology Society. Conference*, vol. 2007, pp. 79–82, 2007, ISSN: 1557-170X. DOI: 10.1109/ iembs.2007.4352227.
- [90] R. Beetham, “Biochemical investigation of suspected rhabdomyolysis.,” *Annals of clinical biochemistry*, vol. 37 ( Pt 5), pp. 581–587, Sep. 2000, ISSN: 0004-5632.
- [91] J. M. Sauret, G. Marinides, and G. K. Wang, “Rhabdomyolysis.,” *American family physician*, vol. 65, no. 5, pp. 907–912, Mar. 1, 2002, ISSN: 0002-838X.
- [92] W. H. Bagley, H. Yang, and K. H. Shah, “Rhabdomyolysis.,” *Internal and emergency medicine*, vol. 2, no. 3, pp. 210–218, Oct. 2007, ISSN: 1828-0447. DOI: 10.1007/s11739-007-0060-8.
- [93] J. F. Greenleaf, M. Fatemi, and M. Insana, “Selected methods for imaging elastic properties of biological tissues.,” *Annual review of biomedical engineering*, vol. 5, no. 1, pp. 57–78, 2003, ISSN: 1523-9829. DOI: 10.1146/annurev.bioeng.5.040202.121623.

- [94] Hippocrates, “On the articulations. the genuine works of hippocrates.,” *Clinical orthopaedics and related research*, no. 400, pp. 19–25, Jul. 2002, ISSN: 0009-921X.
- [95] E. Brusseau, C. Perrey, P. Delachartre, M. Vogt, D. Vray, and H. Erment, “Axial strain imaging using a local estimation of the scaling factor from RF ultrasound signals.,” *Ultrasonic imaging*, vol. 22, no. 2, pp. 95–107, Apr. 2000, ISSN: 0161-7346.
- [96] P. Hoskins, K. Martin, and A. Thrush, Eds., *Diagnostic Ultrasound Physics and Equipment*. Cambridge, UK: Cambridge University Press, 2010, ISBN: 978-0-521-75710-2.
- [97] T. Karlas, C. Pfrepper, J. Wiegand, C. Wittekind, M. Neuschulz, J. Mössner, T. Berg, M. Tröltzscher, and V. Keim, “Acoustic radiation force impulse imaging (ARFI) for non-invasive detection of liver fibrosis: examination standards and evaluation of interlobe differences in healthy subjects and chronic liver disease.,” *Scandinavian journal of gastroenterology*, vol. 46, no. 12, pp. 1458–1467, Dec. 2011, ISSN: 1502-7708. DOI: [10.3109/00365521.2011.610004](https://doi.org/10.3109/00365521.2011.610004).
- [98] R. L. Maurice, J. Ohayon, Y. Frétigny, M. Bertrand, G. Soulez, and G. Cloutier, “Noninvasive vascular elastography: theoretical framework.,” *IEEE transactions on medical imaging*, vol. 23, no. 2, pp. 164–180, Feb. 2004, ISSN: 0278-0062. DOI: [10.1109/tmi.2003.823066](https://doi.org/10.1109/tmi.2003.823066).
- [99] R. J. Dickinson and C. R. Hill, “Measurement of soft tissue motion using correlation between a-scans.,” *Ultrasound in medicine & biology*, vol. 8, no. 3, pp. 263–271, 1982, ISSN: 0301-5629.

- [100] L. S. Wilson and D. E. Robinson, “Ultrasonic measurement of small displacements and deformations of tissue.,” *Ultrasonic imaging*, vol. 4, no. 1, pp. 71–82, Jan. 1982, ISSN: 0161-7346.
- [101] E. J. Chen, J. Novakofski, W. K. Jenkins, and W. D. O’Brien, “Young’s modulus measurements of soft tissues with application to elasticity imaging,” *IEEE Transactions on Ultrasonics, Ferroelectrics, and Frequency Control*, vol. 43, no. 1, pp. 191–194, Jan. 1996, ISSN: 08853010.
- [102] G. Treece, J. Lindop, L. Chen, J. Housden, R. Prager, and A. Gee, “Real-time quasi-static ultrasound elastography,” *Interface Focus*, Apr. 20, 2011. DOI: [10.1098/rsfs.2011.0011](https://doi.org/10.1098/rsfs.2011.0011).
- [103] J. Ophir, I. Céspedes, H. Ponnekanti, Y. Yazdi, and X. Li, “Elastography: a quantitative method for imaging the elasticity of biological tissues.,” *Ultrasonic imaging*, vol. 13, no. 2, pp. 111–134, Apr. 1991, ISSN: 0161-7346.
- [104] J.-F. F. Deprez, E. Brusseau, C. Schmitt, G. Cloutier, and O. Basset, “3D estimation of soft biological tissue deformation from radio-frequency ultrasound volume acquisitions.,” *Medical image analysis*, vol. 13, no. 1, pp. 116–127, Feb. 2009, ISSN: 1361-8423. DOI: [10.1016/j.media.2008.07.003](https://doi.org/10.1016/j.media.2008.07.003).
- [105] J. Meunier and M. Bertrand, “Ultrasonic texture motion analysis: theory and simulation.,” *IEEE transactions on medical imaging*, vol. 14, no. 2, pp. 293–300, 1995, ISSN: 0278-0062. DOI: [10.1109/42.387711](https://doi.org/10.1109/42.387711).
- [106] T. Varghese, “Quasi-Static ultrasound elastography.,” *Ultrasound clinics*, vol. 4, no. 3, pp. 323–338, Jul. 2009, ISSN: 1556-858X. DOI: [10.1016/j.cult.2009.10.009](https://doi.org/10.1016/j.cult.2009.10.009).

- [107] P.-E. Austrell, B. Enquist, A. Heyden, and S. Spanne, “Contact free strain measurement using MATLAB image processing toolbox,” Lund, Sweden.
- [108] E. Brusseau, J. Kybic, J.-F. F. Deprez, and O. Basset, “2-D locally regularized tissue strain estimation from radio-frequency ultrasound images: theoretical developments and results on experimental data.,” *IEEE transactions on medical imaging*, vol. 27, no. 2, pp. 145–160, Feb. 2008, ISSN: 0278-0062. doi: [10.1109/tmi.2007.897408](https://doi.org/10.1109/tmi.2007.897408).
- [109] K. R. Nightingale, R. W. Nightingale, M. L. Palmeri, and G. E. Trahey, “A finite element model of remote palpation of breast lesions using radiation force: factors affecting tissue displacement.,” *Ultrasonic imaging*, vol. 22, no. 1, pp. 35–54, Jan. 2000, ISSN: 0161-7346.
- [110] K. R. Nightingale, M. L. Palmeri, R. W. Nightingale, and G. E. Trahey, “On the feasibility of remote palpation using acoustic radiation force.,” *The Journal of the Acoustical Society of America*, vol. 110, no. 1, pp. 625–634, Jul. 2001, ISSN: 0001-4966.
- [111] K. Nightingale, M. S. S. Soo, R. Nightingale, and G. Trahey, “Acoustic radiation force impulse imaging: in vivo demonstration of clinical feasibility.,” *Ultrasound in medicine & biology*, vol. 28, no. 2, pp. 227–235, Feb. 2002, ISSN: 0301-5629.
- [112] K. Nightingale, R. Bentley, and G. Trahey, “Observations of tissue response to acoustic radiation force: opportunities for imaging.,” *Ultrasonic imaging*, vol. 24, no. 3, pp. 129–138, Jul. 2002, ISSN: 0161-7346.
- [113] M. L. Palmeri, K. D. Frinkley, L. Zhai, M. Gottfried, R. C. Bentley, K. Ludwig, and K. R. Nightingale, “Acoustic radiation force impulse

- (ARFI) imaging of the gastrointestinal tract.,” *Ultrasonic imaging*, vol. 27, no. 2, pp. 75–88, Apr. 2005, ISSN: 0161-7346.
- [114] R. S. Lazebnik, “Tissue strain analytics: virtual touch tissue imaging and quantification,” Siemens Medical Solutions, USA, INC., Mountain View, CA USA, Tech. Rep., Oct. 2008.
- [115] G. F. Pinton, J. J. Dahl, and G. E. Trahey, “Rapid tracking of small displacements with ultrasound.,” *IEEE transactions on ultrasonics, ferroelectrics, and frequency control*, vol. 53, no. 6, pp. 1103–1117, Jun. 2006, ISSN: 0885-3010.
- [116] “Guidelines for the safe use of diagnostic ultrasound,” Tech. Rep., 2001.
- [117] “Information for manufacturers seeking marketing clearance of diagnostic ultrasound systems and transducers,” Food and Drug Administration, Tech. Rep., Sep. 9, 2008.
- [118] K. Nightingale, S. McAleavey, and G. Trahey, “Shear-wave generation using acoustic radiation force: in vivo and ex vivo results.,” *Ultrasound in medicine & biology*, vol. 29, no. 12, pp. 1715–1723, Dec. 2003, ISSN: 0301-5629.
- [119] J. Bercoff, M. Tanter, and M. Fink, “Supersonic shear imaging: a new technique for soft tissue elasticity mapping.,” *IEEE transactions on ultrasonics, ferroelectrics, and frequency control*, vol. 51, no. 4, pp. 396–409, Apr. 2004, ISSN: 0885-3010.
- [120] R. Cao, Z. Huang, T. Varghese, and G. Nabi, “Tissue mimicking materials for the detection of prostate cancer using shear wave elastography: a validation study.,” *Medical physics*, vol. 40, no. 2, Feb. 2013, ISSN: 0094-2405. DOI: [10.1118/1.4773315](https://doi.org/10.1118/1.4773315).

- [121] K. Arda, N. Ciledag, E. Aktas, B. K. K. Aribas, and K. Köse, “Quantitative assessment of normal soft-tissue elasticity using shear-wave ultrasound elastography.,” *AJR. American journal of roentgenology*, vol. 197, no. 3, pp. 532–536, Sep. 2011, ISSN: 1546-3141. DOI: 10.2214/ajr.10.5449.
- [122] K. Chen, A. Yao, E. E. Zheng, J. Lin, and Y. Zheng, “Shear wave dispersion ultrasound vibrometry based on a different mechanical model for soft tissue characterization.,” *Journal of ultrasound in medicine*, vol. 31, no. 12, pp. 2001–2011, Dec. 2012, ISSN: 1550-9613.
- [123] C. Amador, M. W. Urban, S. Chen, and J. F. Greenleaf, “Loss tangent and complex modulus estimated by acoustic radiation force creep and shear wave dispersion.,” *Physics in medicine and biology*, vol. 57, no. 5, pp. 1263–1282, Mar. 7, 2012, ISSN: 1361-6560. DOI: 10.1088/0031-9155/57/5/1263.
- [124] T. Glozman and H. Azhari, “A method for characterization of tissue elastic properties combining ultrasonic computed tomography with elastography.,” *Journal of ultrasound in medicine*, vol. 29, no. 3, pp. 387–398, Mar. 2010, ISSN: 1550-9613.
- [125] F. Lv, J. Tang, Y. Luo, Y. Ban, R. Wu, J. Tian, T. Yu, X. Xie, and T. Li, “Muscle crush injury of extremity: quantitative elastography with supersonic shear imaging.,” *Ultrasound in medicine & biology*, vol. 38, no. 5, pp. 795–802, May 2012, ISSN: 1879-291X. DOI: 10.1016/j.ultrasmedbio.2012.01.010.
- [126] T. U. S. National Library of Medicine, *Visible human project*, 1994.

- [127] J. C. Bamber and R. J. Dickinson, “Ultrasonic b-scanning: a computer simulation.,” *Physics in medicine and biology*, vol. 25, no. 3, pp. 463–479, May 1980, ISSN: 0031-9155.
- [128] T. A. Krouskop, T. M. Wheeler, F. Kallel, B. S. Garra, and T. Hall, “Elastic moduli of breast and prostate tissues under compression,” *Ultrasonic Imaging*, vol. 20, no. 4, pp. 260–274, Oct. 1, 1998, ISSN: 1096-0910. DOI: [10.1177/016173469802000403](https://doi.org/10.1177/016173469802000403).
- [129] A. P. Choi and Y. P. Zheng, “Estimation of young’s modulus and poisson’s ratio of soft tissue from indentation using two different-sized indentors: finite element analysis of the finite deformation effect.,” *Medical & biological engineering & computing*, vol. 43, no. 2, pp. 258–264, Mar. 2005, ISSN: 0140-0118.
- [130] A. D. Martin, M. Z. Daniel, D. T. Drinkwater, and J. P. Clarys, “Adipose tissue density, estimated adipose lipid fraction and whole body adiposity in male cadavers.,” *International journal of obesity and related metabolic disorders : journal of the International Association for the Study of Obesity*, vol. 18, no. 2, pp. 79–83, Feb. 1994, ISSN: 0307-0565.
- [131] J. Y. Rho, R. B. Ashman, and C. H. Turner, “Young’s modulus of trabecular and cortical bone material: ultrasonic and microtensile measurements.,” *Journal of biomechanics*, vol. 26, no. 2, pp. 111–119, Feb. 1993, ISSN: 0021-9290.
- [132] R. Shahar, P. Zaslansky, M. Barak, A. A. Friesem, J. D. Currey, and S. Weiner, “Anisotropic poisson’s ratio and compression modulus of cortical bone determined by speckle interferometry,” *Journal of Biome-*

- chanics*, vol. 40, no. 2, pp. 252–264, Jan. 2007, ISSN: 00219290. DOI: 10.1016/j.jbiomech.2006.01.021.
- [133] Y. Zheng, W. W. Lu, Q. Zhu, L. Qin, S. Zhong, and J. C. Leong, “Variation in bone mineral density of the sacrum in young adults and its significance for sacral fixation.,” *Spine*, vol. 25, no. 3, pp. 353–357, Feb. 1, 2000, ISSN: 0362-2436.
- [134] B. E. Treeby, J. Jaros, A. P. Rendell, and B. T. Cox, “Modeling non-linear ultrasound propagation in heterogeneous media with power law absorption using a k-space pseudospectral method.,” *The Journal of the Acoustical Society of America*, vol. 131, no. 6, pp. 4324–4336, Jun. 2012, ISSN: 1520-8524. DOI: 10.1121/1.4712021.
- [135] R. T. Beyer, “The parameter B/A,” in *Nonlinear Acoustics*, M. F. Hamilton and D. T. Blackstock, Eds. Melville: Acoustical Society of America, 2008, pp. 25–39.
- [136] W. Nyborg, “Acoustic streaming,” in *Physical Acoustics*, W. Mason, Ed. New York: Academic Press Inc., 1965, vol. IIB, ch. 11, pp. 265–331.
- [137] C. Then, T. J. Vogl, and G. Silber, “Method for characterizing viscoelasticity of human gluteal tissue.,” *Journal of biomechanics*, vol. 45, no. 7, pp. 1252–1258, Apr. 30, 2012, ISSN: 1873-2380. DOI: 10.1016/j.jbiomech.2012.01.037.
- [138] L.-L. L. Gras, D. Mitton, P. Viot, and S. Laporte, “Viscoelastic properties of the human sternocleidomastoideus muscle of aged women in relaxation.,” *Journal of the mechanical behavior of biomedical materials*, vol. 27, pp. 77–83, Nov. 2013, ISSN: 1878-0180. DOI: 10.1016/j.jmbbm.2013.06.010.

- [139] X. Wang, J. A. Schoen, and M. E. Rentschler, “A quantitative comparison of soft tissue compressive viscoelastic model accuracy.,” *Journal of the mechanical behavior of biomedical materials*, vol. 20, pp. 126–136, Apr. 2013, ISSN: 1878-0180. DOI: 10.1016/j.jmbbm.2013.01.007.
- [140] C. Then, J. Menger, G. Benderoth, M. Alizadeh, T. J. Vogl, F. Hübner, and G. Silber, “A method for a mechanical characterisation of human gluteal tissue.,” *Technology and health care*, vol. 15, no. 6, pp. 385–398, 2007, ISSN: 0928-7329.
- [141] E. L. Madsen, H. J. Sathoff, and J. A. Zagzebski, “Ultrasonic shear wave properties of soft tissues and tissuelike materials.,” *The Journal of the Acoustical Society of America*, vol. 74, no. 5, pp. 1346–1355, Nov. 1983, ISSN: 0001-4966.

# Appendix A

## Data Tables

### A.1 Quasi-Static Ultrasound Elastography

**Table A.1:** Data for Fig. 3.9

$r_{lesion}$ (mm)	$E_{rel,nom}$			
	0.32	0.56	1.80	3.20
2.5	0.84	0.92	1.09	1.20
5.0	0.77	0.83	1.22	1.48
10.0	0.92	0.73	1.41	1.93
12.5	0.92	0.70	1.47	2.10

**Table A.3:** Data for Fig. 3.11

$h$ (cm)	$E_{rel,nom}$			
	0.32	0.56	1.80	3.20
1.25	0.70	0.72	1.53	2.11
2.50	0.92	0.70	1.47	2.10
3.75	0.81	0.69	1.49	2.13

**Table A.4:** Data for Fig. 3.12

$f$ (MHz)	$E_{rel,nom}$			
	0.32	0.56	1.80	3.20
2	0.67	0.72	1.47	2.06
4	0.92	0.70	1.47	2.10
8	0.71	0.69	1.47	2.09

**Table A.2:** Data for Fig. 3.10

$d$ (cm)	$E_{rel,nom}$			
	0.32	0.56	1.80	3.20
3.5	0.91	0.74	1.42	2.00
6.5	0.80	0.71	1.51	2.19
8.5	0.87	0.70	1.49	2.14
10.0	0.92	0.70	1.47	2.10

**Table A.5:** Data for Fig. 3.13

$\varepsilon_{app}$ (%)	$E_{rel,nom}$			
	0.32	0.56	1.80	3.20
2.5	0.85	0.77	1.40	1.98
5.0	0.92	0.70	1.47	2.10
10.0	1.34	0.93	1.35	1.20

**Table A.6:** Data for Fig. 3.14

$\delta_{sep}$	$E_{rel,nom}$			
(cm)	0.32	0.56	1.80	3.20
1.25	0.78	0.86	1.18	1.40
1.50	0.77	0.86	1.19	1.39
1.75	0.76	0.85	1.19	1.41
2.00	0.75	0.84	1.20	1.42

**Table A.11:** Data for Fig. 3.22

$d$	$E_{rel,nom}$			
(cm)	0.32	0.56	1.80	3.20
6.5	0.68	0.75	1.13	1.46
6.75	0.77	0.81	1.18	1.51
7.25	0.76	0.88	1.25	1.59

**Table A.7:** Data for Fig. 3.16

$b_r$	$E_{rel,nom}$			
(mm)	0.32	0.56	1.80	3.20
1.0	0.93	0.69	1.49	2.17
2.5	0.93	0.87	1.51	2.24
5.0	0.91	1.00	1.52	2.30
7.5	0.91	1.00	1.50	2.28

**Table A.8:** Data for Fig. 3.17

$b_\rho$	$E_{rel,nom}$			
(cm $^{-2}$ )	0.32	0.56	1.80	3.20
10	0.78	0.79	1.29	1.66
20	0.85	0.73	1.38	1.87
30	0.86	0.71	1.42	1.96
40	0.76	0.71	1.43	1.99

**Table A.9:** Data for Fig. 3.19

$r_{bl}$	$E_{rel,nom}$			
(mm)	0.32	0.56	1.80	3.20
0.5	0.72	0.82	1.25	1.58
1.0	0.86	0.71	1.42	1.96
1.5	0.90	0.72	1.44	2.01

**Table A.10:** Data for Fig. 3.20

$\phi L$	$E_{rel,nom}$			
(cm)	0.32	0.56	1.80	3.20
0.5	1.15	1.17	1.17	1.26
1.0	1.01	1.09	1.21	1.28
2.0	0.83	0.93	1.21	1.49
2.5	0.76	0.88	1.25	1.59

## A.2 Acoustic Radiation Force Impulse Imaging

**Table A.12:** Data for Fig. 4.4

Depth, $d_f$ (cm)	Body Force at Focal Point, $F_{b,f}$ ( $\text{kN m}^{-3}$ )			
	f = 1 MHz	f = 2 MHz	f = 4 MHz	f = 6 MHz
1	151.5	194.0	122.1	128.5
2	113.0	97.9	83.1	29.2
3	81.7	46.9	33.2	13.3
4	57.3	24.2	12.2	2.2
5	40.7	12.8	4.0	0.2
6	29.6	7.2	0.8	0.0
7	21.8	4.2	0.1	0.0
8	16.3	2.5	0.0	0.0
9	12.4	1.5	0.0	0.0

**Table A.13:** Data for Fig. 4.5

Frequency, $f$ (MHz)	Body Force at Focal Point, $F_{b,f}$ ( $\text{kN m}^{-3}$ )		
	$w_{active} = 4 \text{ cm}$	$w_{active} = 8 \text{ cm}$	$w_{active} = 10 \text{ cm}$
1.0	55.3	85.0	96.6
1.5	19.1	25.9	24.7
2.0	15.3	18.0	12.5
3.0	16.4	10.2	5.6
4.0	1.0	0.3	0.1

**Table A.14:** Data for Fig. 4.6

$n_c$	$F_{b,f}$ ( $\text{kN m}^{-3}$ )
3	0.2
100	2.6
300	7.2
500	7.3
700	7.3

**Table A.15:** Data for Fig. 4.5

Depth, $d_f$ (cm)	Body Force at Focal Point, $F_{b,f}$ (kN m $^{-3}$ )				
	$P = 4$ MPa	$P = 5$ MPa	$P = 6$ MPa	$P = 7$ MPa	$P = 8$ MPa
3	66.7	103.5	147.8	199.3	257.5
4	34.4	53.5	76.6	103.4	133.9
5	18.1	28.2	40.4	54.5	70.6
6	10.3	16.0	22.9	30.9	40.0
9	2.1	3.3	4.7	6.4	8.3

**Table A.16:** Data for Fig. 4.8

Depth, $d_f$ (cm)	Spatial-Peak Pulse-Average Intensity, $I_{SPPA}$ (W cm $^{-2}$ )			
	$f = 1$ MHz	$f = 2$ MHz	$f = 4$ MHz	$f = 6$ MHz
1	1,992	1,705	1,399	1,465
2	1,400	749	388	347
3	982	321	182	140
4	673	154	151	137
5	478	117	146	110
6	352	95	142	118
7	265	103	128	120
8	206	79	126	106
9	165	64	159	100

**Table A.17:** Data for Fig. 4.9

Depth, $d_f$ (cm)	Maximum Induced Tissue Displacement, $ v _{max}$ (μm)			
	$f = 1$ MHz	$f = 2$ MHz	$f = 4$ MHz	$f = 6$ MHz
1	3.10	3.29	3.87	3.77
2	2.90	1.93	1.70	1.52
3	2.47	1.13	0.76	0.52
4	1.83	0.63	0.30	0.18
5	1.40	0.37	0.15	0.10
6	1.15	0.22	0.09	0.08
7	1.07	0.13	0.05	0.07
8	0.85	0.08	0.00	0.00
9	0.58	0.05	0.00	0.00

**Table A.18:** Data for Fig. 4.10

Depth, $d_f$ (cm)	Maximum Induced Tissue Displacement, $ v _{max}$ ( $\mu\text{m}$ )				
	$P = 4 \text{ MPa}$	$P = 5 \text{ MPa}$	$P = 6 \text{ MPa}$	$P = 7 \text{ MPa}$	$P = 8 \text{ MPa}$
3	1.61	2.52	3.62	4.93	6.44
4	0.90	1.40	2.02	2.75	3.59
5	0.52	0.81	1.17	1.60	2.09
6	0.31	0.49	0.70	0.95	1.24
9	0.07	0.10	0.15	0.20	0.26

**Table A.19:** Data for Fig. 4.11

Frequency, $f$ (MHz)	Maximum Induced Tissue Displacement, $ v _{max}$ ( $\mu\text{m}$ )		
	$P = 4 \text{ MPa}$	$P = 6 \text{ MPa}$	$P = 8 \text{ MPa}$
1	1.83	4.10	7.28
2	0.31	0.70	1.24
4	0.14	0.36	0.79
6	0.12	0.33	0.73

**Table A.20:** Data for Fig. 4.12

$r_{lesion}$ (mm)	$E_{rel,nom}$			
	0.32	0.56	1.80	3.20
2.5	0.80	0.87	1.21	1.50
5.0	0.60	0.76	1.34	1.78
10.0	0.58	0.74	1.35	1.81
12.5	0.57	0.74	1.37	1.84

**Table A.22:** Data for Fig. 4.16

$b_r$ (mm)	$E_{rel,nom}$			
	0.32	0.56	1.80	3.20
2.5	0.58	0.74	1.36	1.81
5.0	0.58	0.74	1.36	1.82
7.5	0.58	0.74	1.36	1.81

**Table A.21:** Data for Fig. 4.14

$d$ (cm)	$E_{rel,nom}$			
	0.32	0.56	1.80	3.20
2	0.57	0.76	1.32	1.74
4	0.58	0.74	1.35	1.81
6	0.53	0.71	1.35	1.81
8	0.57	0.75	1.35	1.79

**Table A.23:** Data for Fig. 4.18

$b_\rho$ ( $\text{cm}^{-2}$ )	$E_{rel,nom}$			
	0.32	0.56	1.80	3.20
10	0.77	0.85	1.22	1.52
20	0.71	0.82	1.27	1.62
30	0.66	0.79	1.30	1.69
40	0.63	0.77	1.32	1.74

**Table A.24:** Data for Fig. 4.20

$r_{bl}$ (mm)	$E_{rel,nom}$			
	0.32	0.56	1.80	3.20
0.5	0.85	0.91	1.15	1.37
1.0	0.66	0.79	1.30	1.69
1.5	0.60	0.75	1.34	1.78

**Table A.25:** Data for Fig. 4.22

$\phi L$ (cm)	$E_{rel,nom}$			
	0.32	0.56	1.80	3.20
0.5	0.91	0.95	1.09	1.24
1.0	0.75	0.87	1.21	1.47
2.0	0.56	0.75	1.30	1.67
2.5	0.56	0.75	1.31	1.69

### A.3 Shear Wave Speed Quantification

**Table A.26:** Data for Fig. 5.8

$r_{lesion}$	$E_{rel,nom}$			
(mm)	0.32	0.56	1.80	3.20
2.5	0.75	0.81	1.07	1.21
5.0	0.47	0.68	1.26	1.48
10.0	0.20	0.58	1.57	3.35
12.5	0.06	0.53	1.65	4.18

**Table A.30:** Data for Fig. 5.16

$b_\rho$	$E_{rel,nom}$			
(cm $^{-2}$ )	0.32	0.56	1.80	3.20
10	0.73	0.82	1.32	1.70
20	0.59	0.73	1.48	2.17
30	0.49	0.68	1.58	2.34
40	0.44	0.63	1.62	2.42

**Table A.27:** Data for Fig. 5.10

$\Delta_{off}$	$E_{rel,nom}$			
(cm)	0.32	0.56	1.80	3.20
0.00	0.28	0.57	1.76	3.73
1.25	0.14	0.53	1.77	2.94
2.50	0.20	0.58	1.57	3.35
3.75	0.45	0.67	1.81	2.05

**Table A.31:** Data for Fig. 5.18

$r_{bl}$	$E_{rel,nom}$			
(mm)	0.32	0.56	1.80	3.20
0.5	0.73	0.82	1.32	1.70
1.0	0.59	0.73	1.48	2.17
1.5	0.49	0.68	1.58	2.34

**Table A.32:** Data for Fig. 5.20

$\varnothing L$	$E_{rel,nom}$			
(cm)	0.32	0.56	1.80	3.20
0.5	0.98	1.03	1.26	1.47
1.0	0.84	0.95	1.44	1.74
2.0	0.05	0.64	1.86	2.57
2.5	0.03	0.52	2.13	3.19

**Table A.28:** Data for Fig. 5.12

$d$	$E_{rel,nom}$			
(cm)	0.32	0.56	1.80	3.20
2	0.49	0.68	1.63	3.97
4	0.20	0.58	1.57	3.35
6	0.36	0.56	1.90	3.47
8	0.87	0.28	1.25	1.74

**Table A.29:** Data for Fig. 5.14

$b_r$	$E_{rel,nom}$			
(mm)	0.32	0.56	1.80	3.20
2.5	0.16	0.53	1.85	3.02
5.0	0.16	0.53	1.82	3.08
7.5	0.19	0.54	1.79	3.01

# Appendix B

## Source Code

### B.1 Quasi-Static Ultrasound Elastography

**Listing B.1:** Sample code used to simulate b-mode ultrasound images through the convolution of a simulated scattering center distribution with the point spread function of an ultrasound pulse.

```
1 % generate normally distributed noise across the domain
2 rng(domainSeed);
3 backgroundMap = 1 + noiseMagnitude * randn([Ny, Nx]);

5 % transform the background map into the domain -1 -> 1
6 backgroundMap = (backgroundMap - min(min(backgroundMap))) / (
7     max(max(backgroundMap)) - min(min(backgroundMap)));
8 backgroundMap = 2 * backgroundMap - 1;

9 % if a finite-element model of tissue compression is being used
10 ,
11 % compress the background map
12 if model ~= 0
13     % extract the resultant degrees of freedom from the model
14     [x, y, u, v] = extractUV([transducerWidth, depth], size(
15         backgroundMap), model);

16     % generate the domain over which interpolation will occur
17     [xx, yy] = meshgrid(x, y);

18     % interpolate the data to deform it
19     backgroundMap = interp2(xx, yy, backgroundMap, xx - u, yy - v
20         , 'spline', mean(mean(backgroundMap)));
21 end

% use a cosine function to create the point-spread function
% shape in the axial direction
```

```

23 | xpsf = linspace(-windowWidth / 2, windowHeight / 2, 1 *
24 |     pointsPerWaveLength);
25 | ypsf = linspace(0, 4 * wavelength, 2 * pointsPerWaveLength);
26 | [xmpsf, ympsf] = meshgrid(xpsf, ypsf);
27 | psf = cos(2 * pi * frequency * ympsf / waveSpeed);
28 |
29 | % apply a lateral gaussian "filter" to the signal
30 | mu = 0;
31 | sigma = windowHeight / 4;
32 | gauss = (1 / (sigma * sqrt(2 * pi))) * exp(-(xmpsf - mu) .^ 2 /
33 |     (2 * sigma ^ 2));
34 | psf = psf .* gauss;
35 |
36 | % apply an axial gaussian "filter" to the signal
37 | mu = 2 * wavelength;
38 | sigma = wavelength * 2;
39 | gauss = (1 / (sigma * sqrt(2 * pi))) * exp(-(ympsf - mu) .^ 2 /
40 |     (2 * sigma ^ 2));
41 | gauss = (gauss - min(min(gauss))) / (max(max(gauss)) - min(min(
42 |     gauss)));
43 | psf = psf .* gauss;
44 |
45 | % normalize it to -1 -> 1
46 | psf = (psf - min(min(psf)))/(max(max(psf)) - min(min(psf)));
47 | psf = 2 * psf - 1;
48 |
49 | % convolve the scattering map with the point spread function
50 | bmode = conv2(backgroundMap, psf);
51 |
52 | % crop the image to the appropriate size
53 | sz = size(bmode);
54 | bmode = bmode(int32(floor((sz(1) - pointDepth) / 2)) : int32(
55 |     floor((sz(1) - pointDepth) / 2) + pointDepth - 1), int32(
56 |     floor((sz(2) - numElements) / 2)) : int32(floor((sz(2) -
57 |         numElements) / 2) + numElements - 1));
58 |
59 | % apply classical ultrasound post-processing
60 | % the signal is currently oscillating a high frequency
61 | % - extract the envelope of the signal
62 | bmode = envelopeDetection(bmode)';
63 | % apply log compression to allow to be readily viewed
64 | bmode = logCompression(bmode, 3, true);
65 |
66 | % normalize it to 0 -> 1
67 | bmode = (bmode - min(min(bmode))) ./ (max(max(bmode)) - min(min(
68 |     bmode)));

```

**Listing B.2:** Sample code used to generate displacement maps under quasi-static deformation

```

2 | function model = compression(parameters)
3 | % import COMSOL features
4 | import com.comsol.model.*
5 | import com.comsol.model.util.*

```

```

6 % create the model
7 model = ModelUtil.create('Model');
8 model.modelPath('compression');
9 model.modelNode.create('mod1');
10 model.geom.create('geom1', 2);
11 model.mesh.create('mesh1', 'geom1');
12 model.physics.create('solid', 'SolidMechanics', 'geom1');
13 model.study.create('std1');
14 model.study('std1').feature.create('stat', 'Stationary');
15 model.study('std1').feature('stat').activate('solid', true);

16 % set parameters in the model
17 model.param.set('modelWidth', sprintf('%f[m]', parameters.
18     domainWidth));
19 model.param.set('modelDepth', sprintf('%f[m]', parameters.
20     domainDepth));
21 model.param.set('appliedStrain', sprintf('%f', parameters.
22     appliedStrain));
23 model.param.set('compression', 'modelDepth*appliedStrain');
24 model.param.set('basalStiffness', sprintf('%f[Pa]', 
25     parameters.basalStiffness));
26 model.param.set('stiffnessRatio', sprintf('%f', parameters.
27     lesionStiffnessRatio));
28 model.param.set('lesionStiffness', 'basalStiffness*
29     stiffnessRatio');
30 model.param.set('lesionExtraStiffness', 'lesionStiffness -
31     basalStiffness');
32 model.param.set('density', sprintf('%f[kg/m^3]', parameters.
33     density));
34 model.param.set('poissonsRatio', sprintf('%f', parameters.
35     poisonsRatio));

36 % deal with the human model case
37 if strcmpi(cell2mat(parameters.caseCategory), 'human') == 1
38     model.param.set('fatStiffness', '80[kPa]');
39     model.param.set('boneStiffness', '18.6[GPa]');
40     model.param.set('fatExtraStiffness', 'fatStiffness -
41         basalStiffness');
42     model.param.set('boneExtraStiffness', 'boneStiffness -
43         basalStiffness');

44 % import our stiffness image
45 model.func.create('im1', 'Image');
46 model.func('im1').set('filename', sprintf('compression/
47     stiffnessMap_%03d.png', caseIndex));
48 model.func('im1').importData;
49 model.func('im1').set('xmin', sprintf('%f', (-parameters.
50     domainWidth / 2)));
51 model.func('im1').set('xmax', sprintf('%f', (parameters.
52     domainWidth / 2)));
53 model.func('im1').set('ymax', sprintf('%f', parameters.
54     domainDepth));
55 model.func('im1').set('inplace', 'off');

```

```

44     model.func('im1').set('scaling', 'manual');
45     model.func('im1').set('manualexpr', 'r');
46     model.func('im1').set('funcname', 'lesionMap');
47     model.func.duplicate('im2', 'im1');
48     model.func.set('funcname', 'boneMap');
49     model.func.set('manualexpr', 'b');
50     model.func.duplicate('im3', 'im2');
51     model.func.set('funcname', 'fatMap');
52     model.func.set('manualexpr', 'g');
53 else
54     % import our stiffness image
55     model.func.create('im1', 'Image');
56     model.func('im1').set('funcname', 'stiffnessMap');
57     model.func('im1').set('filename', sprintf('compression/
58 stiffnessMap_%03d.png', caseIndex));
59     model.func('im1').importData;
60     model.func('im1').set('xmin', sprintf('%f', (-parameters.
61 domainWidth / 2)));
62     model.func('im1').set('xmax', sprintf('%f', (parameters.
63 domainWidth / 2)));
64     model.func('im1').set('ymax', sprintf('%f', parameters.
65 domainDepth));
66 end

68 % define the model geometry
69 model.geom('geom1').feature.create('r1', 'Rectangle');
70 model.geom('geom1').feature('r1').setIndex('size', ,
71     'domainWidth', 0);
72 model.geom('geom1').feature('r1').setIndex('size', ,
73     'domainDepth', 1);
74 model.geom('geom1').feature('r1').setIndex('size', ,
75     'modelWidth', 0);
76 model.geom('geom1').feature('r1').setIndex('size', ,
77     'modelDepth', 1);
78 model.geom('geom1').feature('r1').setIndex('pos', ,
79     '-modelWidth/2', 0);
80 model.geom('geom1').run;

82 % set the material properties
83 model.physics('solid').feature('lemm1').set(
84     'NearlyIncompressible', 1, '1');
85 model.physics('solid').feature('lemm1').set('E_mat', 1, ,
86     'userdef');

88 % deal with the human model case
89 if strcmpi(cell2mat(parameters.caseCategory), 'human') == 1
90     model.physics('solid').feature('lemm1').set('E', 1, ,
91         basalStiffness + (fatMap(x, modelDepth - y) *
92             fatExtraStiffness) + (lesionMap(x, modelDepth - y) *
93                 lesionExtraStiffness) + (boneMap(x, modelDepth - y) *
94                     boneExtraStiffness));
95 else
96     model.physics('solid').feature('lemm1').set('E', 1, ,
97         basalStiffness+(stiffnessMap(x,modelDepth-y)*
98             stiffnessExtraStiffness));

```

```

    lesionExtraStiffness));
82 end

84 model.physics('solid').feature('lemm1').set('nu_mat', 1, ,
85     userdef);
model.physics('solid').feature('lemm1').set('nu', 1, ,
86     poissonsRatio);
model.physics('solid').feature('lemm1').set('rho_mat', 1, ,
87     userdef);
model.physics('solid').feature('lemm1').set('rho', 1, ,
88     density);

% set the boundary conditions
90 model.physics('solid').feature.create('fix1', 'Fixed', 1);
model.physics('solid').feature('fix1').selection.set([2]);
92 model.physics('solid').feature.create('displ1', 'Displacement1',
93     1);
model.physics('solid').feature('displ1').selection.set([3]);
94 model.physics('solid').feature('displ1').set('Direction', 2, ,
95     1);
model.physics('solid').feature('displ1').set('U0', 2, ,
96     -compression);

% create the mesh
98 model.mesh('mesh1').feature.create('ftri1', 'FreeTri');
model.mesh('mesh1').feature('size').set('hauto', '1');
100 model.mesh('mesh1').run;

% setup the study and run it
102 model.sol.create('sol1');
103 model.sol('sol1').study('std1');
model.sol('sol1').feature.create('st1', 'StudyStep');
105 model.sol('sol1').feature('st1').set('study', 'std1');
model.sol('sol1').feature('st1').set('studystep', 'stat');
108 model.sol('sol1').feature.create('v1', 'Variables');
model.sol('sol1').feature('v1').set('control', 'stat');
110 model.sol('sol1').feature.create('s1', 'Stationary');
model.sol('sol1').feature('s1').feature.create('fc1', ,
111     FullyCoupled);
model.sol('sol1').feature('s1').feature.remove('fcDef');
113 model.sol('sol1').attach('std1');

114 model.sol('sol1').runAll;
115
116 end

```

**Listing B.3:** Sample code used to estimate the lateral and axial strain along a given scanline of a pre- and post- compression b-mode image using quasi-static ultrasound elastography.

```

% calculate the number of windows along this scanline
2 M = maxX / deltaAx;

4 % these variables will return the alpha and tau coefficients
% along this scanline

```

```

6  alpha = [];
7  tau = [];
8
9  % loop through every window along this scanline
10 for m = 1:M
11    % calculate the locations of the two windows to start the
12    % search from
13    pr1 = m .* deltaAx;
14    pr2 = sum(deltaAx ./ alpha);
15
16    % extract the window in the uncompressed image
17    x1 = linspace(pr1, pr1 + L, numPoints);
18    r1 = interp1(1 : length(I1), I1, x1, 'linear', 'extrap');
19
20    % initialize search variables
21    alphas = maxAlpha:-0.001:1;
22    taus = zeros(size(alphas));
23    correlations = zeros(size(alphas));
24
25    % loop through the possible values of alpha
26    for i = 1 : length(alphas)
27      % keep track of which scanline gives us the best
28      % correlation
29      columnCorrelations = [];
30
31      % loop through the adjacent scanlines
32      for c = (column - columnRadius) : (column + columnRadius)
33        % make sure we have a valid scanline
34        if (c < 1) || (c > columns)
35          continue;
36        end
37
38        % extract the window in the compressed image
39        x2 = linspace(round(pr2), round(pr2) + round(L),
40        numPoints);
41        r2 = interp1(1:length(I2(:, c)), I2(:, c), x2, 'linear',
42        'extrap');
43
44        % get the correlation for the two windows
45        columnCorrelations = [columnCorrelations, Correlate(r1,
46        r2)];
47      end
48
49      % pick the scanline that had the best correlation for this
50      % alpha
51      c = -columnRadius : column + columnRadius;
52      [correlations(i), mindx] = min(columnCorrelations);
53      taus(i) = c(mindx);
54    end
55
56    % employ a-priori smoothing to the data
57    % in case of errant outliers
58    [~, mindx] = min(correlations);
59    if abs(alphas(mindx) - alpha(length(alpha))) > 0.02

```

```

54     alpha = [alpha; alpha(length(alpha))];
55     tau = [tau; tau(length(tau))];
56 else
57     alpha = [alpha; alphas(mindex)];
58     tau = [tau; taus(mindex)];
59 end
60 end

```

## B.2 Acoustic Radiation Force Impulse Imaging

**Listing B.4:** Sample code used in conjunction with the K-Wave Toolbox to simulate acoustic radiation force body loads generated by an ultrasonic transducer.

```

1 % calculate the best grid size for computational efficiency
2 % taking into account Nyquist so that appropriate sampling is
3 % used
4 dx = medium.sound_speed / (2 * probingFrequency);
5 dy = dx;
6 Nx = bestFactor(domainDepth / dx + (2 * PML_X_SIZE)) - (2 *
7     PML_X_SIZE);
8 Ny = bestFactor(domainWidth / dy + (2 * PML_Y_SIZE)) - (2 *
9     PML_X_SIZE);
10 dx = domainDepth / Nx;
11 dy = domainWidth / Ny;

12 % make the grid!
13 kGrid = makeGrid(Nx, dx, Ny, dy);

14 % create the time array
15 kGrid.t_array = makeTime(kGrid, medium.sound_speed, [] ,
16     pulseCycles / probingFrequency);

17 % beam-form the data
18 % create indices for our elements
19 numActiveElements = Ny;
20 elementIndices = -(numActiveElements - 1) / 2 : (
21     numActiveElements - 1) / 2;

22 % calculate time delays for a steered and focussed beam
23 elementWidth = dy;
24 delayTimes = focalDepth / medium.sound_speed * (1 - sqrt(1 + (
25     elementIndices * elementWidth ./ focalDepth) .^ 2)); % [s]

26 % convert the delays to be in units of time points
27 delayTimes = delayTimes - min(delayTimes);
28 delayTimes = delayTimes ./ kGrid.dt;

29 % use the k-wave toolbox's function "toneBurst" to create the
30 % signal
31 inputSignal = toneBurst(1 / kGrid.dt, probingFrequency,
32     pulseCycles, 'SignalOffset', delayTimes);

```

```

32 % scale the signal by the source pressure
33 source.p = sourcePressure .* inputSignal;
34
35 % truncate the input signal to the appropriate length
36 source.p = source.p(:, 1:length(kGrid.t_array));
37
38 % make only the nodes along the top boundary apply pressure to
39 % the domain
40 source.p_mask = zeros([Nx, Ny]);
41 source.p_mask(1, 1 : (numActiveElements)) = 1;
42
43 % tell the k-wave toolbox to record the pressure and intensity
44 % for
45 % the entire domain, continuously
46 sensor.mask = ones(Nx, Ny);
47 sensor.record = {'I', 'p'};
48
49 % set up simulation settings
50 inputArgs = {'PlotSim', false, 'PMLInside', false, 'PlotPML',
51             false, 'PMLSize', [PML_X_SIZE, PML_Y_SIZE], 'DataCast',
52             'single', 'DataRecast', true, 'DisplayMask', 'off'};
53
54 % run the simulation
55 sensorData = kspaceFirstOrder2D(kGrid, medium, source,
56                                 inputArgs{:});
57
58 % reshape the output data to make sense
59 Ix = reshape(sensorData.Iy, [Nx, Ny, kGrid.Nt]);
60 Iy = reshape(sensorData.Ix, [Nx, Ny, kGrid.Nt]);
61 P = reshape(sensorData.p, [Nx, Ny, kGrid.Nt]);
62
63 % calculate body forces
64 alpha = (attenuationCoefficient * 100 * probingFrequency / 1e6)
65             / (20 / log(10));
66 Fx = 2 * alpha .* Ix ./ soundSpeed;
67 Fy = -2 * alpha .* Iy ./ soundSpeed;

```

**Listing B.5:** Sample code used to simulate time-dependent displacement of viscoelastic soft tissue as a response to acoustic radiation force impulse loads applied to it.

```

1 function model = relaxation(parameters)
2     % import COMSOL features
3     import com.comsol.model.*
4     import com.comsol.model.util.*
5
6     % create the model
7     model = ModelUtil.create('Model');
8     model.modelPath('ARFI');
9     model.name('relaxation.mph');
10
11    % set parameters in the model
12    model.param.set('domainWidth', sprintf('%f[m]', parameters.
13        domainWidth));

```

```

13 model.param.set('domainDepth', sprintf('%f[m]', parameters.
    domainDepth));
14 model.param.set('focalDepth', sprintf('%f[mm]', parameters.
    focalDepth));
15 model.param.set('timeStep', sprintf('%f[us]', parameters.
    timeStep));
16 model.param.set('loadTime', sprintf('%f[us]', parameters.
    loadTime));
17 model.param.set('listenTime', sprintf('%f[ms]', parameters.
    listenTime));
18 model.param.set('focalY', 'domainDepth-focalDepth');
19 model.param.set('dFocalY', 'focalY/1[m]');
20 model.param.set('stiffnessRatio', sprintf('%f', parameters.
    stiffnessRatio));
21 model.param.set('cutoffAmplitude', sprintf('%f', parameters.
    cutoffAmplitude));

23 % load interpolation files for both geometry
24 % and initial acoustic radiation force
25 model.modelNode.create('mod1');
26 model.func.create('int1', 'Interpolation');
27 model.func.create('int2', 'Interpolation');
28 model.func.create('step1', 'Step');
29 model.func.create('im1', 'Image');
30 model.func('int1').set('funcs', {'Fx' '1'});
31 model.func('int1').set('source', 'file');
32 model.func('int1').set('filename', 'ARFI/Fx.txt');
33 model.func('int1').set('struct', 'grid');
34 model.func('int1').set('defvars', 'on');
35 model.func('int1').set('extrap', 'value');
36 model.func('int1').set('argunit', 'm');
37 model.func('int1').set('fununit', 'N/(m^3)');
38 model.func('int2').set('funcs', {'Fy' '1'});
39 model.func('int2').set('source', 'file');
40 model.func('int2').set('filename', 'ARFI/Fy.txt');
41 model.func('int2').set('struct', 'grid');
42 model.func('int2').set('defvars', 'on');
43 model.func('int2').set('extrap', 'value');
44 model.func('int2').set('argunit', 'm');
45 model.func('int2').set('fununit', 'N/(m^3)');
46 model.func('step1').set('location', 'loadTime');
47 model.func('step1').set('from', '1');
48 model.func('step1').set('to', '0');
49 model.func('step1').set('smoothactive', false);
50 model.func('im1').set('funcname', 'stiffnessMap');
51 model.func('im1').set('filename', 'ARFI/stiffnessMap.png');
52 model.func('im1').set('xmin', '-domainWidth/2');
53 model.func('im1').set('xmax', 'domainWidth/2');
54 model.func('im1').set('ymax', 'domainDepth');
55 model.func('im1').set('extrap', 'value');

57 % create the geometry
58 model.geom.create('geom1', 2);
59 model.geom('geom1').feature.create('r1', 'Rectangle');

```

```

61     model.geom('geom1').feature.create('r2', 'Rectangle');
62     model.geom('geom1').feature('r1').set('pos', {'0' '0'});
63     model.geom('geom1').feature('r1').set('size', {'domainWidth/2
64         ' domainDepth'});
65     model.geom('geom1').feature('r2').set('pos', {'domainWidth/2
66         '0'});
67     model.geom('geom1').feature('r2').set('size', {'domainWidth/8
68         ' domainDepth});
69     model.geom('geom1').run;
70
71     % set up material properties
72     model.material.create('mat1');
73     model.material('mat1').propertyGroup.create('KG', 'Bulk
74         modulus and shear modulus');
75     model.material('mat1').propertyGroup('def').set('density', '
76         1060');
77     model.material('mat1').propertyGroup('KG').set('K', '');
78     model.material('mat1').propertyGroup('KG').set('G', '');
79     model.material('mat1').propertyGroup('KG').set('K', '
80         stiffnessRatio*515.656[kPa]');
81     model.material('mat1').propertyGroup('KG').set('G', '
82         stiffnessRatio*1032[Pa]');
83
84     % set up the physics
85     % including boundary and 'initial' conditions
86     % fix the bottom of the domain
87     model.physics.create('solid', 'SolidMechanics', 'geom1');
88     model.physics('solid').feature.create('fix1', 'Fixed', 1);
89     model.physics('solid').feature('fix1').selection.set([2 5]);
90     model.physics('solid').feature('fix1').name('bottom hold');
91
92     % prevent motion in the vertical direction at the top
93     % boundary
94     model.physics('solid').feature.create('disp1', 'Displacement1
95         ', 1);
96     model.physics('solid').feature('disp1').selection.set([3 6]);
97     model.physics('solid').feature('disp1').set('Direction', {'0'
98         ; '1'; '0'});
99     model.physics('solid').feature('disp1').name('top hold');

100
101    % the ARFI is a body load
102    model.physics('solid').feature.create('bl1', 'BodyLoad', 2);
103    model.physics('solid').feature('bl1').selection.set([1]);
104    model.physics('solid').feature('bl1').set('FperVol', {'Fx(x,y
105        )*step1(t[1/s])'; 'Fy(x,y)*step1(t[1/s])'; '0'});
106    model.physics('solid').feature('bl1').set('Ftot', {''; 'Fy(x,
107        y)*step1(t[1/s])*10^2'; '0'});
108    model.physics('solid').feature('bl1').name('ARFI load');

109
110    % make the model symmetric
111    model.physics('solid').feature.create('sym1', 'SymmetrySolid'
112        , 1);
113    model.physics('solid').feature('sym1').selection.set([1]);

```

```

101 % use a viscoelastic tissue model
model.physics('solid').feature.create('vmm1', ,
    'ViscoelasticModel', 2);
model.physics('solid').feature('vmm1').selection.all;
model.physics('solid').feature('vmm1').set('K_mat', 'userdef',
    );
model.physics('solid').feature('vmm1').set('K', '(515.656 [
    kPa]) * (1 + (stiffnessMap(x, y) * (stiffnessRatio - 1)))');
model.physics('solid').feature('vmm1').set('G_mat', 'userdef',
    );
model.physics('solid').feature('vmm1').set('G', '(1032 [Pa])
    * (1 + (stiffnessMap(x, y) * (stiffnessRatio - 1)))');
model.physics('solid').feature('vmm1').set('Branch', {'1'; '2
    ', '2'});
model.physics('solid').feature('vmm1').set('Gi', {'(791 [Pa])
    * (1 + (stiffnessMap(x, y) * (stiffnessRatio - 1)))';
    '(66.5 [Pa]) * (1 + (stiffnessMap(x, y) * (stiffnessRatio -
    1)))'; '(628 [mPa]) * (1 + (stiffnessMap(x, y) * (
    stiffnessRatio - 1)))'});
model.physics('solid').feature('vmm1').set('tau', {'2 [s]'; '40
    [s]'; '80 [s]'});
model.physics('solid').feature('vmm1').set(
    'NearlyIncompressible', '1');

113 % create the mesh
model.mesh.create('mesh1', 'geom1');
model.mesh('mesh1').feature.create('ftri1', 'FreeTri');
model.mesh('mesh1').feature.create('map1', 'Map');
model.mesh('mesh1').feature('size').set('hauto', 3);
model.mesh('mesh1').feature('map1').active(false);
model.mesh('mesh1').feature('map1').set('adjustedgdistr',
    true);
model.mesh('mesh1').run;

121 % set up a probe at the focal point
model.result.table.create('tbl1', 'Table');
model.result.table.create('tbl2', 'Table');
model.probe.create('pdom1', 'DomainPoint');
model.probe('pdom1').model('mod1');
model.coordSystem.create('pml1', 'geom1', 'PML');
model.coordSystem('pml1').selection.set([2]);
model.probe('pdom1').set('coords2', {'0' 'domainDepth-
    focalDepth'});
model.probe('pdom1').feature('ppb1').set('probename', 'focalPointDisplacement');
model.probe('pdom1').feature('ppb1').set('table', 'tbl1');
model.probe('pdom1').feature('ppb1').set('window', 'window1');
model.result.table('tbl1').name('Probe Table 1');
model.result.table('tbl2').comments('Global Evaluation 1 (t)');
model.result.table('tbl2').comments('Global Evaluation 2 (t)');

133 % create a transient study

```

```

137 model.study.create('std1');
138 model.study('std1').feature.create('time', 'Transient');
139
140 % set up the solution parameters
141 model.sol.create('sol1');
142 model.sol('sol1').study('std1');
143 model.sol('sol1').attach('std1');
144 model.sol('sol1').feature.create('st1', 'StudyStep');
145 model.sol('sol1').feature.create('v1', 'Variables');
146 model.sol('sol1').feature.create('t1', 'Time');
147 model.sol('sol1').feature('t1').feature.create('fc1', ,
148     FullyCoupled);
149 model.sol('sol1').feature('t1').feature.create('st1', ,
150     StopCondition);
151 model.sol('sol1').feature('t1').feature.remove('fcDef');
152 model.sol('sol1').attach('std1');
153 model.sol('sol1').feature('st1').name('Compile Equations:
154     Time Dependent');
155 model.sol('sol1').feature('st1').set('studystep', 'time');
156 model.sol('sol1').feature('v1').set('control', 'time');
157 model.sol('sol1').feature('v1').feature('mod1_u').set(
158     'scalemethod', 'manual');
159 model.sol('sol1').feature('v1').feature('mod1_u').set(
160     'scaleval', '1e-2*0.0640312423743285');
161 model.sol('sol1').feature('t1').set('tlist', 'range(0,
162     timeStep,loadTime+listenTime)');
163 model.sol('sol1').feature('t1').set('fieldselection', 'mod1_u
164     ');
165 model.sol('sol1').feature('t1').set('atolmethod', {'mod1_u' ,
166     'global' 'mod1_solid_qXX3' 'global' 'mod1_solid_qXY2' ,
167     'global' 'mod1_solid_qXY3' 'global' 'mod1_solid_qXX1' ,
168     'global' ...
169     'mod1_solid_qXX2' 'global' 'mod1_solid_qYY3' 'global' ,
170     'mod1_solid_qYY2' 'global' 'mod1_solid_qYY1' 'global' ,
171     'mod1_solid_qXY1' 'global' ...
172     'mod1_solid_pw' 'global'});
173 model.sol('sol1').feature('t1').set('atol', {'mod1_u' '1e-3'
174     'mod1_solid_qXX3' '1e-3' 'mod1_solid_qXY2' '1e-3' ,
175     'mod1_solid_qXY3' '1e-3' 'mod1_solid_qXX1' '1e-3' ...
176     'mod1_solid_qXX2' '1e-3' 'mod1_solid_qYY3' '1e-3' ,
177     'mod1_solid_qYY2' '1e-3' 'mod1_solid_qYY1' '1e-3' ,
178     'mod1_solid_qXY1' '1e-3' ...
179     'mod1_solid_pw' '1e-3'});
180 model.sol('sol1').feature('t1').set('atoludot', {'mod1_u' '1e
181     -3' 'mod1_solid_qXX3' '1e-3' 'mod1_solid_qXY2' '1e-3' ,
182     'mod1_solid_qXY3' '1e-3' 'mod1_solid_qXX1' '1e-3' ...
183     'mod1_solid_qXX2' '1e-3' 'mod1_solid_qYY3' '1e-3' ,
184     'mod1_solid_qYY2' '1e-3' 'mod1_solid_qYY1' '1e-3' ,
185     'mod1_solid_qXY1' '1e-3' ...
186     'mod1_solid_pw' '1e-3'});
187 model.sol('sol1').feature('t1').set('atoludotactive', {
188     mod1_u 'off' 'mod1_solid_qXX3' 'off' 'mod1_solid_qXY2' ,
189     off' 'mod1_solid_qXY3' 'off' 'mod1_solid_qXX1' 'off' ...
190     'mod1_solid_qXX2' 'off' 'mod1_solid_qYY3' 'off' ,

```

```

169     mod1_solid_qYY2' 'off' 'mod1_solid_qYY1' 'off' ,
170     mod1_solid_qXY1' 'off' ...
171     'mod1_solid_pw' 'off'});
172 model.sol('sol1').feature('t1').set('timemethod', 'genalpha')
173     ;
174 model.sol('sol1').feature('t1').set('tstepsgenalpha', 'manual
175     ');
176 model.sol('sol1').feature('t1').set('timestepgenalpha', 'timeStep');
177 model.sol('sol1').feature('t1').set('plot', 'on');
178 model.sol('sol1').feature('t1').set('plotgroup', 'pg2');
179 model.sol('sol1').feature('t1').feature('fc1').set('plot', 'on');
180 model.sol('sol1').feature('t1').feature('fc1').set('plotgroup
181     ', 'pg2');

% add a stop condition to stop the simulation when the tissue
182     has relaxed
183 model.sol('sol1').feature('t1').feature('st1').set('stopcond'
184     , 'if(t > 0.003 && mod1.focalPointDisplacement <
185         cutoffAmplitude, -1, 1)');

% create data sets to evaluate later:
186 % * The displacement at the focal point over time
187 % * The displacement along an axial line going through the
188     focal point
189 % * The displacement along a lateral line going through the
190     focal point
191 model.result.dataset.create('cpt1', 'CutPoint2D');
192 model.result.dataset.create('cln1', 'CutLine2D');
193 model.result.dataset.create('cln2', 'CutLine2D');
194 model.result.dataset.create('dset2', 'Solution');
195 model.result.dataset('dset2').set('probetag', 'pdom1');
196 model.result.dataset.create('cpt2', 'CutPoint2D');
197 model.result.dataset('cpt2').set('probetag', 'pdom1');
198 model.result.dataset('cpt2').set('data', 'dset2');
199 model.result.numerical.create('pev1', 'EvalPoint');
200 model.result.numerical('pev1').set('probetag', 'ppb1');
201 model.result.numerical.create('gev1', 'EvalGlobal');
202 model.result.numerical('gev1').set('probetag', 'none');
203 model.result.create('pg1', 'PlotGroup1D');
204 model.result('pg1').set('probetag', 'none');
205 model.result('pg1').feature.create('ptgr1', 'PointGraph');
206 model.result.create('pg2', 'PlotGroup2D');
207 model.result('pg2').feature.create('surf1', 'Surface');
208 model.result.create('pg3', 'PlotGroup1D');
209 model.result('pg3').set('probetag', 'none');
210 model.result('pg3').feature.create('lngr1', 'LineGraph');
211 model.result.create('pg4', 'PlotGroup1D');
212 model.result('pg4').set('probetag', 'none');
213 model.result('pg4').feature.create('lngr1', 'LineGraph');
214 model.result.create('pg5', 'PlotGroup1D');
215 model.result('pg5').set('probetag', 'window1');
216 model.result('pg5').feature.create('tblp1', 'Table');

```

```

211     model.result('pg5').feature('tblp1').set('probetag', 'ppb1');
213     model.result.dataset('cpt1').name('Focal Point');
215     model.result.dataset('cpt1').set('pointx', '0');
216     model.result.dataset('cpt1').set('pointy', 'dFocalY');
217     model.result.dataset('cln1').name('Lateral Cut');
218     model.result.dataset('cln1').set('genpoints', {'-domainWidth
219         /2' : domainDepth - focalDepth, 'domainWidth/2' :
220             domainDepth - focalDepth});
221     model.result.dataset('cln2').name('Axial Cut');
222     model.result.dataset('cln2').set('genpoints', {'0' :
223         domainDepth, '0' : '0'});
224     model.result.dataset('dset2').name('Probe Solution 2');
225     model.result.dataset('cpt2').set('pointy', 'focalY');
226     model.result.numerical('gev1').set('table', 'tbl2');
227     model.result.numerical('gev1').set('expr', 't');
228     model.result.numerical('gev1').set('unit', 's');
229     model.result.numerical('gev1').set('descr', 'Time');
230     model.result.numerical('gev1').set('dataseries', 'maximum');
231     model.result.numerical('pev1').setResult;
232     model.result.numerical('gev1').setResult;
233     model.result('pg1').name('Focal Point Relaxation');
234     model.result('pg1').set('data', 'cpt1');
235     model.result('pg1').set(' xlabel', 'Time (ms)');
236     model.result('pg1').set(' ylabel', 'Displacement (m)');
237     model.result('pg1').set(' xlabelactive', false);
238     model.result('pg1').set(' ylabelactive', false);
239     model.result('pg1').feature('ptgr1').set('descractive', true)
240         ;
241     model.result('pg1').feature('ptgr1').set('descr', 'Displacement');
242     model.result('pg1').feature('ptgr1').set('titletype', 'manual');
243     model.result('pg1').feature('ptgr1').set('title', 'Focal
244         Point Relaxation');
245     model.result('pg1').feature('ptgr1').set('xdata', 'expr');
246     model.result('pg1').feature('ptgr1').set('xdataexpr', 't');
247     model.result('pg1').feature('ptgr1').set('xdataunit', 'ms');
248     model.result('pg1').feature('ptgr1').set('xdatadescr', 'Time');
249     model.result('pg2').name('Surface Displacement');
250     model.result('pg3').name('Displacement of Axial Focal Cut');
251     model.result('pg3').set('data', 'cln2');
252     model.result('pg3').set(' xlabel', 'Depth (m) (m)');
253     model.result('pg3').set(' ylabel', 'Total displacement (m)');
254     model.result('pg3').set(' xlabelactive', false);
255     model.result('pg3').set(' ylabelactive', false);
256     model.result('pg3').feature('lngr1').set('xdata', 'expr');
257     model.result('pg3').feature('lngr1').set('xdataexpr',
258         'domainDepth - y');
259     model.result('pg3').feature('lngr1').set('xdatadescractive', true);
260     model.result('pg3').feature('lngr1').set('xdatadescr', 'Depth
261         (m)');
262     model.result('pg3').feature('lngr1').set('legend', true);

```

```

    model.result('pg4').name('Displacement of Lateral Focal Cut')
    ;
255 model.result('pg4').set('data', 'cln1');
model.result('pg4').set(' xlabel', 'x-coordinate (m)');
257 model.result('pg4').set(' ylabel', 'abs(v) (m)');
model.result('pg4').set('legendpos', 'lowerright');
259 model.result('pg4').set(' xlabelactive', false);
model.result('pg4').set(' ylabelactive', false);
261 model.result('pg4').feature('lngr1').set('expr', 'abs(v)');
model.result('pg4').feature('lngr1').set('descr', 'abs(v)');
263 model.result('pg4').feature('lngr1').set('xdata', 'expr');
model.result('pg4').feature('lngr1').set('xdataexpr', 'x');
265 model.result('pg4').feature('lngr1').set('xdatadescr', 'x-
    coordinate');
model.result('pg4').feature('lngr1').set('legend', true);
267 model.result('pg5').name('Probe 1D Plot Group 5');
model.result('pg5').set(' xlabel', 't');
269 model.result('pg5').set(' ylabel', 'Total displacement, Point
    Probe Expression 1');
model.result('pg5').set('windowtitle', 'Probe Plot 1');
271 model.result('pg5').set(' xlabelactive', false);
model.result('pg5').set(' ylabelactive', false);
273 model.result('pg5').feature('tblp1').name('Probe Table Graph
    1');

275 % initiate the domain probe we defined earlier
model.probe('pdom1').genResult([]);
277
% set the timestepping for the solution
279 model.study('std1').feature('time').set('tlist', 'range(0,
    timeStep,loadTime+listenTime)');
model.study('std1').feature('time').set('plot', 'on');
281 model.study('std1').feature('time').set('plotgroup', 'pg2');

283 % run the model
model.sol('sol1').runAll;
285 end

```

### B.3 Shear Wave Speed Quantification

**Listing B.6:** Sample code used to calculate the speed of a shear wave generated by an ARFI force along a lateral line traversing the focal point of the applied force.

```

1 % extract the displacement along a lateral line traversing the
   focal point
% throughout the complete simulation time
3 [x, t, lateralCut] = getLateralFocalCutDisplacement(model);

5 % use the mean value of the displacement through time and
   location
% as the isoline value to track
7 targetValue = mean(mean(lateralCut));

```

```

9  % loop along the x-coordinates of the dataset
10 points = NaN(length(x), 2);
11 % ignore the first 4 data points which lie within the width of
12 % the
13 for xi = 5 : length(x)
14     % find the point in time where the displacement at the given
15     % x-coordinate
16     % crosses the target value previously established
17     for ti = 2 : length(t)
18         if (lateralCut(ti, xi) < targetValue) && (lateralCut(ti -
19             1, xi) >= targetValue)
20             % if the cross-over point was found, store it and
21             % continue with
22             % the next x-coordinate
23             points(xi, :) = [t(ti), x(xi)];
24             ti = length(t);
25             break;
26         end
27     end
28 end

29 % remove NaNs from the dataset
30 points = points(~any(isnan(points), 2), :);

31 % differentiate to get shear velocity
32 % (use a center-weighted moving window average filter first
33 % otherwise the data will become unusable)
34 Ct = diff(smooth(points(:, 2))) ./ diff(smooth(points(:, 1)));
35 x = linspace(min(points(:, 2)), max(points(:, 2)), length(Ct));

```

# Appendix C

## Experimental Protocols

Each of the protocols detailed here were carried out on a Siemens ACUSON S2000<sup>TM</sup> portable ultrasound machine with a Siemens 9L4 transducer on a CIRS Elasticity QA Phantom model 049 as shown in Fig. C.1.

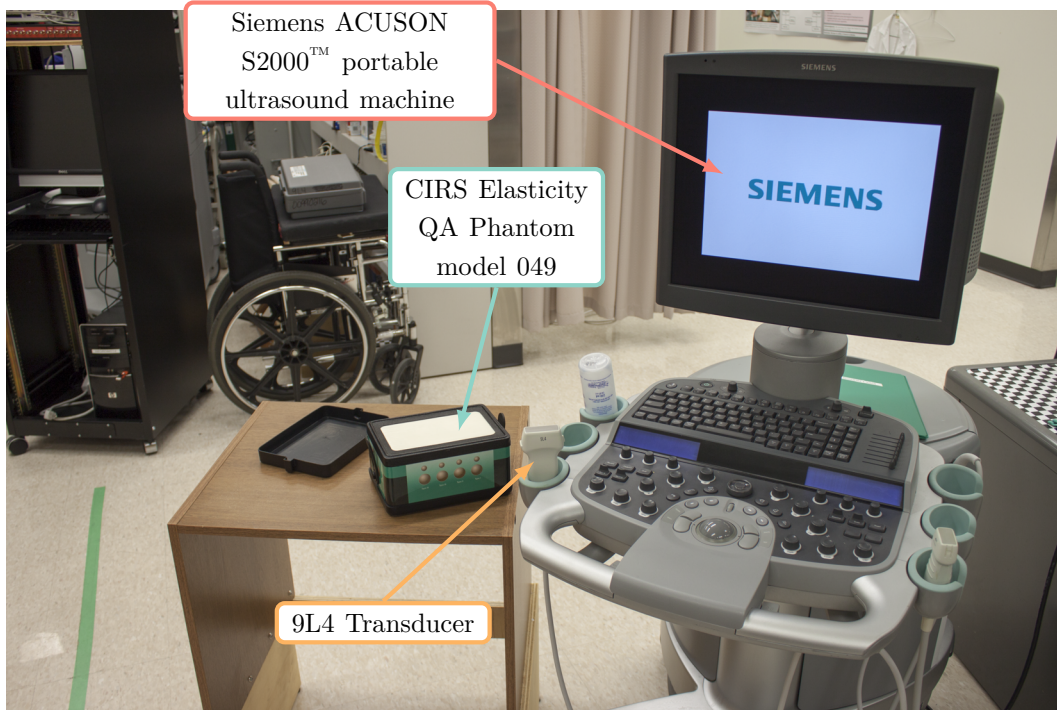


**Fig. C.1:** Experimental setup showing the ultrasound machine, probe, and phantom model.

## C.1 Quasi-Static Ultrasound Elastography

1. Apply a layer of ultrasound gel to the active transducer area
2. Begin a new “2D” imaging sequence on the machine using the “Breast” preset
3. Position the transducer for the desired lesion
  - (a) Note the planar location of the lesion denoted on the sides of the phantom model
  - (b) Place the active component on the surface of the phantom model
  - (c) Align the transducer so as to intersect the lesion’s planar location in a perpendicular manner
4. Adjust the depth of the image to reach the full domain depth of the phantom model (approximately 7.5 cm)
5. Save the current screen
6. Manually indent the transducer into the tissue by approximately 0.5 cm
7. Save the current screen
8. Repeat steps 3 – 7 until all desired images have been acquired
9. Export the images to “USB in PC format”
10. Import the images into MATLAB®
  - (a) Crop the images so only the imaged domain is visible
11. Process the cropped images using a strain estimation algorithm

## C.2 Acoustic Radiation Force Impulse Imaging

1. Apply a layer of ultrasound gel to the active transducer area
2. Begin a new “2D” imaging sequence on the machine using the “Breast” preset
3. Position the transducer for the desired lesion
  - (a) Note the planar location of the lesion denoted on the sides of the phantom model
  - (b) Place the active component on the surface of the phantom model

- (c) Align the transducer so as to intersect the lesion's planar location in a perpendicular manner
4. Adjust the depth of the image to reach the full domain depth of the phantom model (approximately 7.5 cm)
  5. Using the ultrasound machine's trackball, select the "Virtual Touch imaging" button
  6. Ensure the elastogram colour map is a gradient from black to white
  7. Using the trackball and the "Next" button, adjust the position and size of the region of interest in order to fully capture the lesion and surrounding tissue
  8. Press the "Update" button and hold the transducer as motionless as possible while the scan completes
  9. Save the current screen
  10. Wait for the cooling process to complete then press the "Freeze" button to unfreeze the image
  11. Repeat steps 3 – 10 until all desired images have been acquired
  12. Export the images to "USB in PC format"
  13. Import the images into MATLAB®
  14. Calculate the stiffness ratios by comparing the mean brightness of the elastograms inside the lesion to the mean brightness of the elastograms in an identical area located superior to the lesion

### C.3 Shear Wave Speed Quantification

1. Apply a layer of ultrasound gel to the active transducer area
2. Begin a new "2D" imaging sequence on the machine using the "Breast" preset
3. Position the transducer for the desired lesion
  - (a) Note the planar location of the lesion denoted on the sides of the phantom model
  - (b) Place the active component on the surface of the phantom model
  - (c) Align the transducer so as to intersect the lesion's planar location in a perpendicular manner

4. Adjust the depth of the image to reach the full domain depth of the phantom model (approximately 7.5 cm)
5. Using the ultrasound machine's trackball, select the “Virtual Touch Quantification imaging” button
6. Using the trackball, position the region of interest within the lesionous region
7. Press the “Update” button and hold the transducer as motionless as possible while the scan completes
8. Record the shear wave speed ( $V_s$ ) of the interrogated region
9. Wait for the cooling process to complete then press the “Freeze” button to unfreeze the image
10. Using the trackball, position the region of interest outside the lesionous region
11. Press the “Update” button and hold the transducer as motionless as possible while the scan completes
12. Record the shear wave speed ( $V_s$ ) of the interrogated region
13. Wait for the cooling process to complete then press the “Freeze” button to unfreeze the image
14. Repeat steps 3 – 13 until all desired lesions have been investigated